UNIVERSITÀ DEGLI STUDI DI NAPOLI FEDERICO II

DOCTORAL THESIS

An investigation on the vibroacoustic behavior of systems in similitude

Author:
Alessandro CASABURO
Supervisors:
Prof. Sergio DE ROSA
Prof. Francesco FRANCO
Dr. Giuseppe PETRONE

External reviewers:
Prof. Elisabetta MANCONI
Prof. Tobias MELZ

A thesis submitted in fulfillment of the requirements
for the degree of Doctor of Philosophy
in the
Pasta-Lab
Dipartimento di Ingegneria Industriale

July 7, 2021

"*I was just guessing at numbers and figures / Pulling the puzzles apart"*

Coldplay, *The Scientist*

"*May the days be aimless. Let the seasons drift. Do not advance the action according to a plan.*"

Don DeLillo, *White Noise*

"*Quello che devo fare.*"

Luther Blissett, *Q*

Abstract

Similitude theory allows engineers to establish the necessary conditions to design a scaled - up or down - model of a full-scale prototype structure. In recent years, the research on similitude methods, which allow to design the models and establish similitude conditions and scaling laws, has grown so that many obstacles associated with full-scale testing, such as cost and setup, may be overcome. This thesis aims at, on the one hand, expanding the possibilities of similitude methods by means of their application to new structural configurations; on the other hand, at the investigation of new approaches. Therefore, similitude conditions and scaling laws of thin aluminium plates with clamped-free-clamped-free boundary conditions, first, and aluminium foam sandwich plates with simply supported and free-free boundary conditions, then, are derived. Particularly, two sets of conditions are derived for the sandwich plates: the first by expliciting all the geometrical and material properties, the second by combining some parameters into just one with physical meaning, that is, the bending stiffness. These conditions and laws are successively validated by means of dynamic experimental tests, in which reconstructions of the natural frequencies and the velocity response of the prototype are attempted. Also the prediction of the radiated acoustic power is performed for the sandwich plates. All the tests highlight that these laws do not work fine when the models are distorted, i.e., when the similitude conditions are not satisfied. Therefore, the potentialities of machine learning are investigated and used to establish degrees of correlation between similar systems, without invoking governing equations and/or solution schemes. In particular, artificial neural networks are used in order to predict the dynamic characteristics, first, and the scaling parameters, then, of beams, as test (since they do not exhibit distorted models), and plates. In the latter case, the predictions of the artificial neural networks are validated by the results provided by the experimental tests. The networks prove to be robust to noise, very helpful in predicting the response characteristics, and identifying the model type. Finally, the similitude methods are used as a tool for supporting, and eventually validating, noisy experimental measurements, not for predicting the prototype behavior. In this way, they can help to understand if a set of measurements is reliable or not. Therefore, the sandwich plates are analysed with digital image correlation cameras. Then, with the help of an algorithm for blind source separation, the force spectra and velocity responses are reconstructed. It is demonstrated that the similitude results are coherent with the quality of the experimental measurements, since the curves overlap when the spatial patterns are recognizable. Instead, when the displacement field is too polluted by noise, the reconstruction exhibits discrepancies. This proves that the application of similitude methods should not be underestimated, especially in the light of the expanding range of approaches which can extract important information from noisy observations.

Contents

List of Figures

List of Tables

List of Abbreviations

ABS	**A**diabatic **B**anding **S**hear
AI	**A**rtificial **I**ntelligence
ANN	**A**rtificial **N**eural **N**etwork
ASMA	**A**symptotical **S**caled **M**odal **A**nalysis
BPANN	**B**ack **P**ropagation **N**eural **N**etworks
BSS	**B**lind **S**ource **S**eparation
CAD	**C**omputer **A**ided **D**esign
CFCF	**C**lamped-**F**ree-**C**lamped-**F**ree
CLT	**C**lassical **L**aminate **T**heory
CMA	**C**lassic **M**odal **A**nalysis
CNN	**C**onvolutional **N**eural **N**etwork
DA	**D**imensional **A**nalysis
DBN	**D**eep **B**elief **N**etwork
DIC	**D**igital **I**mage **C**orrelation
DLT	**D**istorted **L**ay-up **T**echnique
DOE	**D**esign **O**f **E**xperiments
DOF	**D**egree **O**f **F**reedom
GOE	**G**aussian **O**rthogonal **E**nsemble
EDA	**E**nergy **D**istribution **A**nalysis
EFG	**E**lement-**F**ree **G**alerkin
EM	**E**nergy **M**ethod (based on conservation of energy)
EMA	**E**xperimental **M**odal **A**nalysis
ESM	**E**mpirical **S**imilarity **M**ethod
FE	**F**inite **E**lement
FEA	**F**inite **E**lement **A**nalysis
FDM	**F**used **D**eposition **M**ethod
FEM	**F**inite **E**lement **M**ethod
FML	**F**iber **M**etal **L**aminate
GMM	**G**aussian **M**ixture **M**odel
GSA	**G**lobal **S**ensitivity **A**nalysis
GUI	**G**raphical **U**ser **I**nterface
HMM	**H**idden **M**arkov **M**odel
JAD	**J**oint **A**pproximated **D**iagonalization
kNN	**k**-**N**earest-**N**eighbor
LaRC	**La**ngley **R**esearch **C**enter

LDV	**L**aser **D**oppler **V**ibrometer
LHS	**L**eft **H**and **S**ide
LSA	**L**ocal **S**ensitivity **A**nalysis
MAC	textbfModal **A**ssurance **C**riterion
MSE	**M**ean **S**quared **E**rror
MSTA	**M**ean **S**quared **t**ransfer **A**dmittance
MLT	**M**ass, **L**ength, **T**ime (base of DA)
MOF	**M**odal **O**verlap **F**actor
NASA	**N**ational **A**eronautics and **S**pace **A**dministration
NASTRAN	**NA**SA **STR**uctural **AN**alysis
OMA	**O**perational **M**odal **A**nalysis
PC	**P**rincipal **C**omponent
PCA	**P**rincipal **C**omponent **A**nalysis
PME	**P**hase-based **M**otion **E**stimation
PSD	**P**ower **S**pectral **D**ensity
RBF	**R**adial **B**asis **F**unction
RHS	**R**ight **H**and **S**ide
RMS	**R**oot **M**ean **S**quared
RNN	**R**ecurrent **N**eural **N**etworks
RP	**R**apid **P**rototyping
SA	**S**ensitivity **A**nalysis
SAMSARA	**S**imilitude and **A**symptotic **M**odels for **S**tructural-**A**coustic **R**esearch **A**pplications
SEA	**S**tatistical **E**nergy **A**nalysis
SHM	**S**tructural **H**ealth **M**onitoring
SL	**S**tereo**L**ithography
SOBI	**S**econd-**O**rder **B**lind **I**dentification
SPL	**S**ound **P**ressure **L**evel
STAGE	**S**imilitude **T**heory **A**pplied to **G**overning **E**quations
SVM	**S**upport **V**ector **M**achines
TSM	**T**raditional **S**imilarity **M**ethod
VOODOO	**V**ersatile **O**ffset **O**perator for the **D**iscrete **O**bservation of **O**bjects

Physical Constants

Air density	$\rho_0 = 1.225$ kg/m^3
Speed of sound	$c_0 = 343$ m/s

For us, the living

Chapter 1

Introduction

Experimental testing is a fundamental step in the design of a product. In fact, theoretical and numerical approaches are valuable tools, yet their predictions must be validated by extensive sets of experimental tests before going to production. This way, whether applied to the validation of a simple or complex system, one achieves the desired reliability, performance, and safety. The seminal work on structural similitudes by Simitses and Rezaeepazhand (Simitses and Rezaeepazhand, 1993) may help to illustrate the experimental effort required: the final static tests of the Lockheed C-141A airlifter needed 8 wing tests, 17 fuselage tests, and 7 empennage tests.

Crashworthiness evaluation is another fitting example, requiring both full-scale and drop tests. Furthermore, errors, focusing on unexpected phenomena or other unforeseen events may lead to the necessary repetition of some tests. Unfortunately, full-scale experimental testing is expensive, in terms of both cost and time and, sometimes, the implementation is not straightforward (for example, when the test article has too large or small dimensions); in extreme cases, the usefulness of the acquired data cannot justify the required effort. For these reasons, in order to bypass many of the problems listed, it is useful to design a scaled (up or down) model of the full-scale system (also called *prototype*), that can be tested at significantly lower cost and with less difficulty. However, even if the scaling procedure is carried out perfectly, the model is still another structure which static and dynamic responses do not coincide with those of the prototype. As a consequence, the recovery – or reconstruction – of the prototype response is not guaranteed.

Actual savings of money and time provided by the use of scaled models are proved by Holmes and Sliter (Holmes and Sliter, 1974). The authors estimate savings between 1/3 and 1/4 the cost of the full-scale building and testing for a single crash test. The time required is reduced by 1/3 and more if also model fabrication is taken into account. Therefore, an entire experimental program, with a mixture of subscale and full-scale models, would lead to greater economy in both financial and temporal terms.

Moreover, the problems do not concern only the experimental field. In fact, analytical and numerical simulations may be computationally prohibitive. For instance, De Rosa and Franco (De Rosa and Franco, 2008b) point out that, in order to estimate with acceptable degree of accuracy the response of a plate subjected to a Turbulent

Boundary Layer (TBL) excitation, both structure and fluid should be discretised with meshes, having different sizes, which should be linked with an interpolation matrix, leading to a computationally demanding procedure. This problem may be bypassed through similitude theory, moving towards analytical or numerical domains which resolution would be more efficient.

Similitude theory provides the conditions to design a scaled model of a full-scale system and to predict the prototype's structural response from the scaled results. The tools used are the similitude methods.

This work moves along two parallel directions. On the one hand, to expand the application of classical similitude theory, by deriving and experimentally validating the similitude conditions and scaling laws for thin and sandwich plates. In particular, the conditions and laws of clamped-fixed-clamped-fixed thin plates are derived, and it is demonstrated that they are the same if the boundary conditions change. Therefore, it is the geometry that dictates the behavior in similitude, first. Then, simply supported sandwich plates are investigated, since their dynamic behavior in similitude has not been studied yet. On the other hand, new applications are investigated, namely the application of machine learning, in order to overcome the typical limits of classical similitude theory (i.e., partial similitudes), and the use of systems in similitude to validate experimental measurements.

With reference to Fig. 1.1, this thesis is structured as follows. Chapter 2 reports a thorough literature review, in which the main methods and their applications are provided, with a particular attention to the results concerning 2D structures (that is, plates), the advantages and disadvantages of any approach.

Chapter 3 provides the theoretical framework on the similitude method used, explains how the similitude conditions and scaling laws of the main dynamic characteristics are derived, and gives an overview of the machine learning methods herein adopted.

Chapter 4 is dedicated to the experimental validation of the scaling laws for CFCF thin plates and simply supported sandwich plates. The natural frequencies and velocity response of both structural configurations are reconstructed, demonstrating that the prediction of the prototype behavior is no more possible if the similitude conditions are not satisfied. Moreover, only for the sandwich configuration, it is shown that the number of similitude conditions can be reduced if many parameters are gathered just in one, physically meaningful; in addition, also the radiated acoustic power is reconstructed. Then, the same scaling laws are used with free-free sandwich plates, in order to demonstrate, again, the validity of the set for boundary conditions other than those used to derive the laws themselves.

Chapter 5 concerns the application of machine learning methods (namely, artificial neural networks and principal component analysis) to similitude fields, investigating the prediction capabilities and potentialities of this computer science branch and the effective usefulness. Particularly, two problems are faced: prediction of dynamic characteristics starting from the scaling characteristics, and vice versa. This is done for both one-dimensional (i.e., beams) and two-dimensional structural configurations.

In Chapter 6, similitude theory is applied as means for verifying the reliability of a set of noisy experimental data. With the only knowledge of panels data and the measurements, an algorithm is used to extract the spectra of the excitation forces and check whether the input information is coherently retained or not into noisy data. Then, the quality of the experimental estimation of the displacements measured with digital image correlation technique is validated by means of similitude theory. The process is carried out with numerical simulations, first, and real plates, then.

Chapter 7 is the last one. In here, the conclusions are drawn, briefly summarizing the results of this work and providing ideas for further developments.

All the experimental activities discussed in this work were carried out in collaboration with Facultad de Ciencias Físicas y Matemáticas, Universidad de Chile, in Santiago de Chile (Chile), during two secondments in 2019 supervised by Prof. V. Meruane. Part of the theoretical framework was developed during a three-months long collaboration in 2020 with École Centrale de Lyon, in Lyon (France), under the supervision of Prof. M. Ichchou.

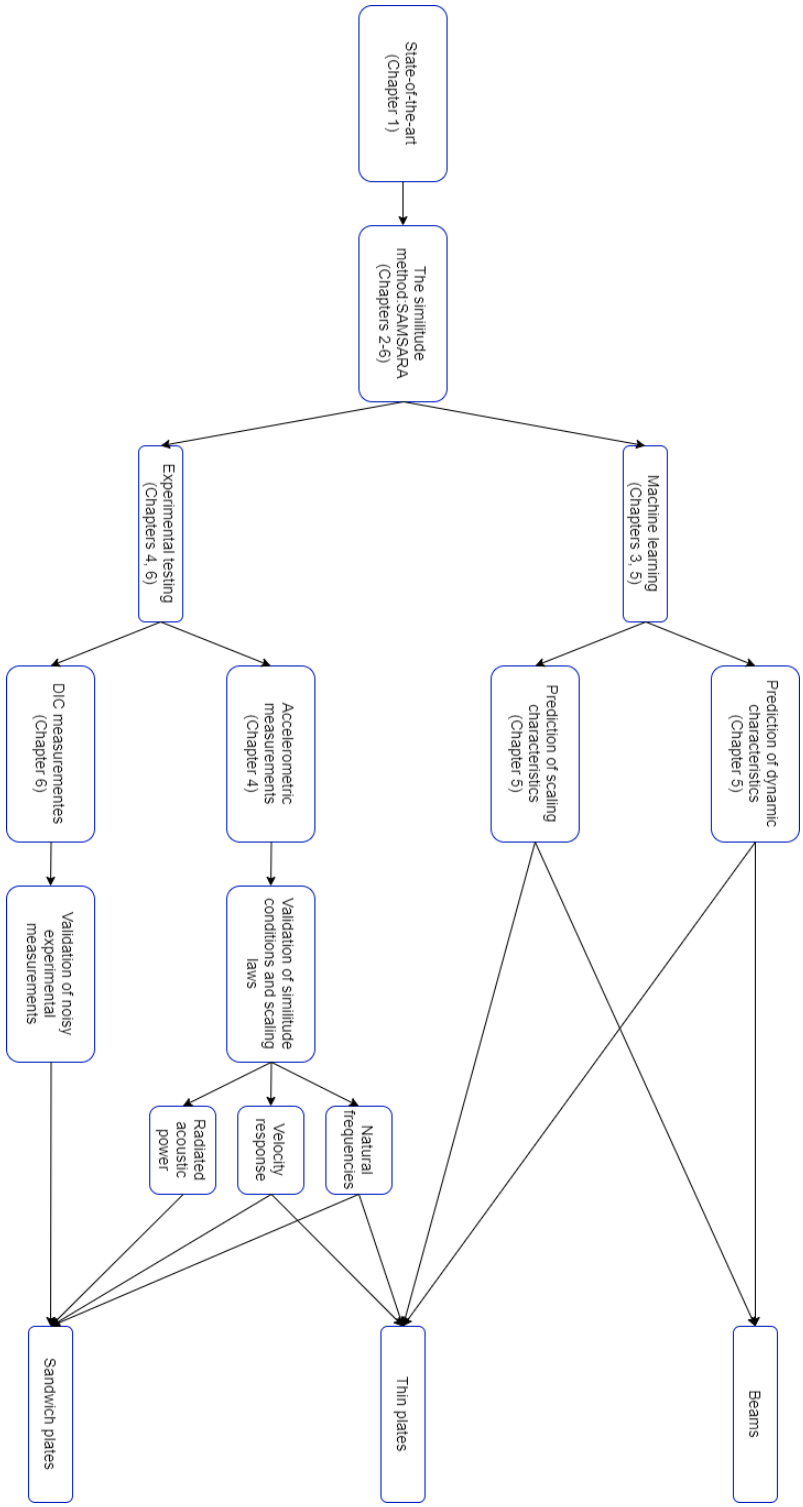

FIGURE 1.1: Thesis flowchart.

Chapter 2

Literature review

The aim of this chapter is to provide a comprehensive review of similitude methods applied to structural engineering. Few related reviews have been published up to now: the first dates back to the early 2000s (Simitses, Starnes Jr, and Rezaeepazhand, 2000) and focuses, after an historical review, on the the analysis of composite test articles by means of similitude theory applied to the governing equations of plates and shells. Not only this work is the first review on the topic, but also it explains some key terminology related to similitude theory that lacks precise definition, specifically *scaling* (or *scale*) and *size effects*. Generally, scale effects describe changes in the response to external causes due to changes in the geometric dimensions of a structure (or a structural component); size effects concern changes of strength and stiffness of the material as a consequence of the physical scaling process. According to Wissmann (Wissmann, 1968), when a size effect occurs, a physical phenomenon gains importance in a model due to differences in size of the model and the prototype. Notwithstanding these definitions, the terminology scale effects are used also to refer to effects of size in many articles. In order to avoid any ambiguity, from now on, the terminology size effects will be used exclusively to describe the effects of physical scaling.

A comprehensive review is also provided by Coutinho et al. (Coutinho, Baptista, and Rodrigues, 2016), which combines historical, methodological and application insights to reconstruct the evolution of similitude theory. Then, Zhu et al. (Zhu et al., 2017) reviewed vibration problems of plates and shells using similitude theory based on the governing equations and sensitivity analysis. Recently, Casaburo et al. provided two review works on the topic: the first is organized in terms of test articles and engineering applications (Casaburo et al., 2019), while the other focuses on the similitude of plates in vibroacoustic field (Casaburo et al., 2020). Rosen (Rosen, 1989) surveyed the literature in the late 1980s, underlining commonalities and relationships among all the scientific fields in which similitudes are applied. Literature presents other limited reviews, as the one on scaling models in marine structures (Vassalos, 1999), the work by Cagliostro (Cagliostro, Florence, and Abrahamson, 1979) on the structural response of liquid metal fast breeder reactor vessels to hypothetical core disruptive accidents, and the article by Saito and Kuwana (Saito and Kuwana, 2017) on scale modeling applied to vibroacoustics.

This chapter is organized as follows. First, a short historical review is provided, in

which some information is given about the first publications, manuals and textbooks dealing with the topic. Then, similitude theory is formally defined and several similitude methods are surveyed, focusing on their relative advantages and disadvantages. Section 2.3, the core of the chapter, is divided into several subsections. In order to provide a functional perspective on the topic, the discussion around the applications is categorized in terms of test articles, so that all the contributions to a topic scattered across time and research fields are organized in a new presentation. Therefore, each subsection of Section 2.3 is focused on the application of similitude methods to a particular test article (beams, plates, and cylinders). Section 2.4 is dedicated to the use of the theory in the study of more complex structures across several engineering fields.

An useful synopsis of the reviewed articles is provided in Appendix A, in which the references are categorized in three tables in terms of methods, test article, and engineering field.

2.1 Short historical review

According to Zhu et al. (Zhu et al., 2017), the first reference to similitude theory dates back to the 18th century, as Galilei and Weston (Galilei and Weston, 1730) state that size and strength of an object do not decrease in the same ratio: if dimensions decrease, the strength increases. Curiously, Galilei and Weston are already facing the problem of size effects in the 18th century. However, the first work in which scientific models based on dimensional analysis are discussed is due to Rayleigh (Rayleigh, 1915). According to Macagno (Macagno, 1971), Rayleigh's work aims at underlining the importance of similitude approach in engineering field. However, thirty years have to pass before similitude methods receives enough attention in this field, namely in the NACA technical report by Goodier and Thomson (Goodier and Thomson, 1944) and the book by Goodier (Goodier, 1950). In these publications, dimensional analysis is applied, for the first time, with a systematic procedure to both simple and complex problems: materials with nonlinear stress-strain characteristics or plastic behavior, buckling, and large deflections.

In the following years, several textbooks are written on the topic. Simitses et al. (Simitses, Starnes Jr, and Rezaeepazhand, 2000) cite many publications (Murphy, 1950; Langhaar, 1951; Charlton, 1954; Pankhurst, 1964; Gukhman, 1965), in which dimensional analysis is at the base of similitudes and modeling. Similitude conditions are derived by means of both dimensional analysis an approach based on governing equations by Kline (Kline, 1965). Then, this latter method is accurately treated by Szucs (Szucs, 1980), while a complete chapter is dedicated to dimensional analysis by Singer (Singer, Arbocz, and Weller, 1997). Coutinho et al. (Coutinho, Baptista, and Rodrigues, 2016) provide good alternatives to the previous references, such as the works by Baker et al. (Baker, Westine, and Dodge, 1991) and Sonin (Sonin, 2001); furthermore, other manuals have the objective of explaining dimensional analysis (Harris and Sabnis, 1999; Szirtes, 2007; Tan, 2011), even though other methods have been already introduced and successfully applied. Finally, Kuneš (Kuneš, 2012)

gives a wider interpretation of modeling concept, while Zohuri (Zohuri, 2012) provides a perspective on classic dimensional analysis, deepening the topic further (Zohuri, 2017), going beyond Buckingham's Π Theorem and approaching self-similar solutions.

Fig. 2.1 reports an overview of similitude methods in time. The methods on the vertical axis - which details will be given in further sections - are Dimensional Analysis (DA), Similitude Theory Applied to Governing Equations (STAGE), Energy Method based on the conservation of energy (EM), Asymptotical Scaled Modal Analysis (ASMA), Similitude and Asymptotic Models for Structural-Acoustic Research Applications (SAMSARA), Empirical Similarity Method (ESM), and Sensitivity Analysis (SA). The horizontal bars represent the range of years in which each method has been used.

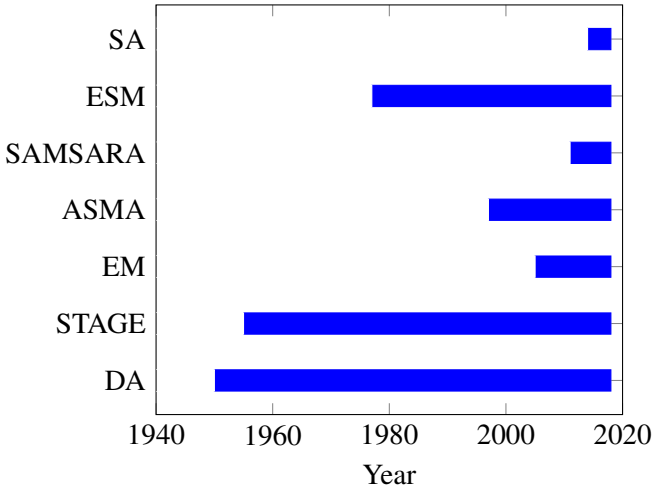

FIGURE 2.1: Time overview of similitude methods.

The development and application of similitude methods has not followed a linear path in terms of test articles. In fact, contrary to expectations, these method have not been applied to simple test articles first and more complicated ones later. For example, as already reported above, in the first relevant application of similitude theory to engineering (Goodier and Thomson, 1944), the authors first provide an extensive theoretical study on general structures (isotropic, composite, linear, and nonlinear), then they employ dimensional analysis to buckled thin square plates in shear, with and without holes. After many years, dimensional analysis is then applied to a stiffened panel by Mazzariol et al. (Mazzariol et al., 2010). Governing equations are used by Frostig and Simitses (Frostig and Simitses, 2004) to investigate sandwich panels. It is up to Morton (Morton, 1988) the first application of similitude concept to beams, in which the author employs dimensional analysis. Some years later, Hamada and Ramakrishna (Hamada and Ramakrishna, 1995) conduct the first analysis of unstiffened cylinders in similitude; oddly, Sato et al. have already studied stiffened cylinders by

means of dimensional analysis in a previous work (Sato, Vecchio, and Andre, 1989). An overview of progress in applying similitude methods to different test articles is given in Fig. 2.2. Again, the bars illustrate the time range in which analyses concerning the corresponding test articles were published.

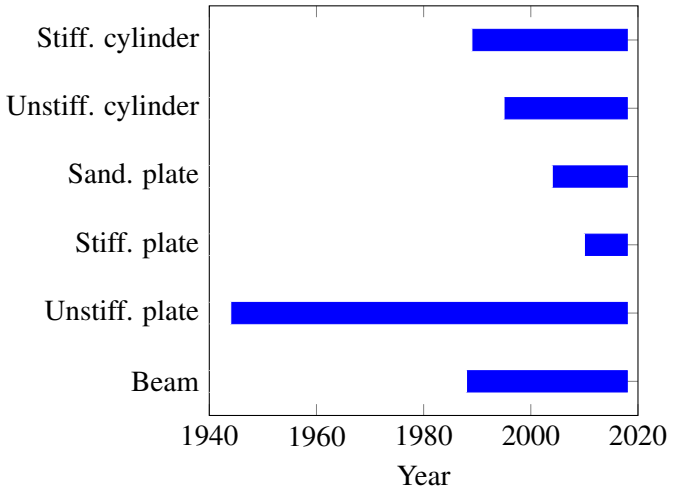

FIGURE 2.2: Time overview of test articles.

Before concluding this short historical overview, a mention to two historically relevant works is needed. Both are dedicated to similitude applied to shells.

The first is an analysis conducted by Ezra (Ezra, 1962), motivated by a peculiar behavior of shells for which, under certain conditions, they can sustain pressures much more larger than the static buckling pressure value, yet, when applying a pressure rapidly for a long time, the structures carries less than it would statically. Therefore, the author applies dimensional analysis to determine the buckling of a thin shell model. Such a structure has arbitrary shape and is subjected to an impulsive pressure load which duration is not short enough to be considered as a pure impulse, nor long enough to be considered static pressure. He shows that, if prototype and model have similar materials, consistent predictions require that the magnitude of the applied pressure must be the same while the duration must be scaled proportionally. If magnitude and duration cannot be controlled, then a complete similitude can be achieved by a suitable choice of the model material.

The second relevant work is by to Soedel (Soedel, 1971), in which the author derives the similitude conditions for free and forced vibrations of shells from Love's equations. Because shells are characterized by both in-plane and transverse oscillations, when deriving exact similitude conditions from governing equations the thickness is not independent from the surface geometry. However, decoupling membrane and bending effects allows to derive two sets of approximate conditions in which the thickness is independent of the surface geometry. The choice of the set is dictated by the relative dominance of membrane and bending effects.

Finally, it is worth mentioning some works by Sterrett concerning similitude and, more generally, model in a wider manner. The epistemological setting of these articles may help to explain the concepts underlying similitude theory. In the first work (Sterrett, 2002), the main topic is the application of fundamental laws to scale modeling: according to the author, scale modeling must not mediate between an abstract/theoretical world and a phenomenological one, but rather to give insights into phenomena, so that it is possible to tell what happens in a situation that is not directly observable by means of another situation that can be observed. In other works, a direct insight into dimensional analysis and Buckingham's Π Theorem applied to both geometrical and physical similitudes is given (Sterrett, 2009), the usefulness of models is underlined (Sterrett, 2015a), showing how new areas of applications and investigative research have been found. This topic is further developed in other articles (Sterrett, 2005; Sterrett, 2014; Sterrett, 2015b).

2.2 Similitude methods

Similitude theory is a branch of engineering sciences which allows to determine the conditions of similitude between two or more systems. The full-scale system is known as *prototype*, while the scaled (up or down) one is the *model*. When a model satisfies the similitude conditions, it is expected to have - qualitatively - the same response of the prototype. For this reason these methods are very useful: designing and investigating scaled models would allow to overcome all the problems associated with full-scale testing (may it be experimental or numerical).

A remark about the terminology is necessary, as some authors refer to *similitude*, while others to *similarity*. In fact, both terms are used interchangeably in the literature although with a slight difference: similarity is closer to the usage in fields of mathematics (self-similarity solutions, for example), as the application by Polsinelli and Levent Kavvas (Polsinelli and Levent Kavvas, 2016), in which Lie scaling methodology is introduced. This approach performs symmetry analysis of the governing differential equations basing on Lie groups - special structures leading to invariant transformations. An extensive treatise on the topic is given by Bluman and Cole (Bluman and Cole, 1974). In this thesis, only the word similitude is used.

Similitude and similitude conditions are two fundamental concepts which need a clear explanation before going further with the description of the several similitude methods.

A first distinction of similitudes can be made according to the parameters taken into account; thus, it is possible to have

- *Geometric similitude*, when the geometrical characteristics are scaled.
- *Kinematic similitude*, when homologous particles lie at homologous points at homologous times (Baker, Westine, and Dodge, 1991). By recalling the ratio between space and time, it follows that kinematic similitude is achieved, simply, when homologous particles have homologous velocities.

- *Dynamic similitude*, when homologous parts of a system are subject to homologous net forces.

Baker et al. (Baker, Westine, and Dodge, 1991) clarify that the term homologous means *corresponding but not necessarily equal values*.

Langhaar (Langhaar, 1951) gives a formal definition of kinematic similitude, also introducing the concept of scale factor:

> The function f' is similar to function f, provided the ratio f'/f is a constant, when the functions are evaluated for homologous points and homologous times. The constant λ = f'/f is called the scale factor for the function f.

However, there are other types of similitudes that can be defined, beyond those listed above. For example, Baker et al. (Baker, Westine, and Dodge, 1991) add constitutive similitude to the list, achieved when the stress-strain curves of prototype and model, or the constitutive properties of these materials, are in similitude. However, in general, only geometric, kinematic, and dynamic similitudes are considered, so that is is possible to say that two systems are similar if they share the aforementioned characteristics.

A useful definition of similitude conditions in given by Szucs (Szucs, 1980):

> The sufficient and necessary condition of similitude between two systems is that the mathematical model of the one be related by a biunique transformation to that of the other.

Therefore, considering two vectors X_p and X_m of N parameters, respectively, of the prototype and the model, then they are related one to each other as

$$X = [\Lambda]\widehat{X} \quad \text{or} \quad \widehat{X} = [\Lambda]^{-1}X, \tag{2.1}$$

where the hat symbol $\widehat{\ }$ denotes the model parameter. Matrix $[\Lambda]$ is written as:

$$[\Lambda] = \begin{bmatrix} \lambda_{x_1} & 0 & \dots & 0 \\ 0 & \lambda_{x_2} & \dots & 0 \\ \vdots & \vdots & \ddots & \vdots \\ 0 & 0 & \dots & \lambda_{x_N} \end{bmatrix} \tag{2.2}$$

which performs a transformation between the mathematical models for the prototype and scaled model. The diagonal matrix provides the simplest form of transformation.

The diagonal elements of matrix Λ are the scale factors of the parameter x_i (where i = 1, 2, ..., N), that in this thesis are defined as

$$\lambda_{x_i} = \frac{\widehat{x_i}}{x_i}, \tag{2.3}$$

although other authors use the inverse formulation.

Another distinction among similitudes can be performed in terms of similitude conditions:

- *True model*: all the conditions are fulfilled; a complete similitude is achieved.
- *Adequate model*: first-order conditions, i.e., the conditions related to the main parameters, are fulfilled; a first-order similitude is achieved.
- *Distorted model*: at least one of the first-order conditions is not satisfied; a partial similitude is achieved.

The difference between true and adequate models is of relevance especially when dimensional analysis is used, as special insights into a problem can be used to reason that some of the conditions are of "second-order" importance.

To clarify this concept, Harris and Sabnis (Harris and Sabnis, 1999) provide an interesting example: in rigid frame problems, axial and shearing forces are of second-order importance relative to bending moments as far as deformations are concerned. Therefore, it may be adequate to model the moment of inertia but not the cross-sectional areas of members.

Thus, the difference between true and adequate models relies clearly on the choice of parameters that are accounted for when deriving the similitude conditions. For those methods working according to other principles (such as STAGE and SAM-SARA, introduced further), such a difference is absent and the concepts of true and adequate models can be joined.

When a system is scaled, the scaling effects, such as the change in response of the structure due to geometric scaling procedure, must be taken into account. There are some application, like impact response, in which size effects must also be considered; they arise as change in material properties (such as strength and stiffness) due to the scaling procedure. Simitses et al. (Simitses, Starnes Jr, and Rezaeepazhand, 2000) cite a workshop on the topic (Jackson, 1993) in which, on the one hand, all the attendees agree on the fact that size effect on stiffness is almost nonexistent but, on the other hand, disagree about is influence on strength.

Several similitude methods can be found in literature; their working principles, advantages and disadvantages are presented in the following subsections. These points are also summarized in table 2.1.

2.2.1 Dimensional Analysis (DA)

Dimensional analysis, or Traditional Similarity Method [TSM, as Coutinho et al. (Coutinho, Baptista, and Rodrigues, 2016) refer to], is based on the definition of a set of dimensionless parameters governing the phenomenon under investigation. It relies on the concept of dimensional homogeneity, that is, an equation describing a physical phenomenon must have both sides with the same dimensions. As a matter of

TABLE 2.1: Overview of similitude methods.

	Advantages	**Disadvantages**
DA	Simple Useful when governing equations are not known	Experienced analyzer is needed Great effort in deriving the conditions Trial-and-error approach Non-dimensional groups may have little physical meaning
STAGE	Similitude conditions are more specific Conditions have physical meaning Scale factors can be applied to both governing equations and solutions	Governing equations must be known Effort in deriving the conditions It cannot be implemented in an algorithm
EM	The procedure is more straightforward than involving the field equations Same level of generality and results of STAGE	Effort in deriving the conditions Problems occur when prototype and model are made of different materials
ASMA	Reduced computational time Applicable to FE analysis It can be implemented in an algorithm	It works well only for global response
SAMSARA	Structural response completely achieved for replicas It can be implemented in an algorithm	Structural response partially achieved for avatars
ESM	Transformation matrix is derived empirically	Additional manufacturing and testing
SA	Reduced effort in deriving similitude conditions It can be implemented in an algorithm Sensitivity-based scaling laws do not need prior knowledge of the structural scaling behavior	It is not based on physical equations Computationally expensive

Note: Table A.1 in Appendix A gives the corresponding references.

fact, these concepts are gathered in Buckingham's Π Theorem (Buckingham, 1914). Let K fundamental dimensions describe the N physical variables $P_1, P_2, ..., P_N$, it is supposed that these variables can be related through the functional relation

$$f_1(P_1, P_2, ..., P_N) = 0. \tag{2.4}$$

Eq. 2.4 may be rewritten in terms of $(N-K)$ dimensionless products, called Π products, as

$$f_2(\Pi_1, \Pi_2, ..., \Pi_{N-K}) = 0, \tag{2.5}$$

where each Π product is a dimensionless product of $K+1$ physical variables so that, without loss of generality, it is possible to write

$$\begin{cases} \Pi_1 = f_3(P_1, P_2, ..., P_{K+1}) \\ \Pi_2 = f_4(P_1, P_2, ..., P_{K+2}) \\ \dots \\ \Pi_{N-K} = f_{N-K+2}(P_1, P_2, ..., P_K, P_N) \end{cases}. \tag{2.6}$$

In most of the applications $K = 3$, being the fundamental dimensions mass, length, and time (which constitutes the MLT - Mass, Length, Time - base). The repeating variable P_i ($i = 1, 2, ..., K$) must include all the K fundamental dimensions, while each dependent variable of interest should appear in just one Π product.

A complete similitude is achieved with dimensional analysis when all the dimensionless Π products are scaled in such a way that they are equal for both model and prototype, which means

$$\widehat{\Pi}_j = \Pi_j, \tag{2.7}$$

for each value of $j = 1, 2, ..., (N-K)$.

If at least one condition is not satisfied, then the model is distorted. However, it is possible to simplify the procedure by considering only the first-order conditions, neglecting, therefore, the difference between a true and an adequate model even when using dimensional analysis.

There are some applications in which dimensional analysis does not involve Buckingham's Π Theorem directly and the scaling laws are determined by defining just one scale factor, then expressing the model/prototype ratio of parameters as a power law of this scale factor. Because this step requires dimensional consistency, this approach can be regarded as another version of dimensional analysis.

In conclusion, the described method is simple to apply and useful for those systems without a set of governing equations, such as complex or new systems. Nonetheless, a phenomenologically meaningful choice of parameters is required. In fact, on the one hand, taking into account a parameter with low or no influence on the phenomenon would complicate the derivation of the Π terms unnecessarily. On the other hand, ignoring an important parameter would lead to incomplete, and maybe wrong,

conclusion. Hence, using dimensional analysis would require an experienced analyzer and a deep knowledge of the problem. Moreover, Π terms may be not unique, which leads to a trial-and-error approach and, therefore, to a significant calculation effort; besides, not all the Π terms have physical meaning and, generally, the characteristic equations of the phenomena under observation can be formulated only in an incomplete form. Finally, the procedure is not structured, so it cannot be easily implemented into an algorithm (Coutinho, Baptista, and Rodrigues, 2016; Casaburo et al., 2020).

2.2.2 Similitude Theory Applied to Governing Equations (STAGE)

Second only to dimensional analysis, STAGE is another common method used to derive the similitude conditions. Kline (Kline, 1965) is the first to introduce this method.

STAGE is applied directly to the field equations of the system, including initial and boundary conditions, characterizing the system in terms of its variables and parameters. Because systems in similitude are governed by equivalent sets of field equations and conditions, the similitude conditions may be derived by defining the scale factors and comparing the equations of both prototype and scaled model, as direct consequence of the invariance defined by Szucs (Szucs, 1980) and expressed by Eq. 2.1. The derived conditions relate geometric (length, width, thickness, etc.), structural (in terms of assembly), excitation (force amplitude, force phase, excitation frequency, etc.), and material properties (Young's modulus, Poisson's ratio, mass density, etc.) of the system to its response. Also in this case, satisfying all these conditions lead to complete similitude; not fulfilling only one of them leads to a similitude at best partial.

STAGE allows a certain application flexibility, as the similitude conditions can be derived by introducing the scale factors into the solutions (exact or approximate) of the field equations (Simitses and Rezaeepazhand, 1993) or directly into the equation themselves, in dimensional (Ungbhakorn, 2001) and non-dimensional (Torkamani, Jafari, and Navazi, 2008) form. In the latter case, the scale factors that appear in the scaling laws (derived from the governing equations for the prototype and the model), are called *explicit scale factors*. Those factors that disappear in the scaling laws but relate to the boundary condition and the excitation mechanisms are called *implicit scale factors* and need to be suitably defined in order to obtain a complete set of similitude conditions and, therefore, the complete similitude. As an example, Wu (Wu, 2003), while investigating the scaled models of an elastically restrained flat plate under dynamic load, sets the scale factors of length, width, thickness, and displacement as explicit factors. Those for translational and rotational springs, excitation frequency, moving-load speed, damping ratios, and natural frequencies are implicit scale factors. Up to now, no one has investigated partial similitudes in which the distortions are introduced by changing the boundary conditions between prototype and model.

The advantage of STAGE is allowing to derive a set of conditions more specific than those obtained with DA, because they are equation driven and, therefore, the relationships are "forced" by the governing equations, implying that they have a physical meaning and that the procedure is more structured with respect to the one used with DA. However, such a procedure lacks of a standard action sequence, thus STAGE, as DA, cannot be implemented in an algorithm. Moreover, the applications are limited to systems which set of field equation is known and the derivation of the similitude conditions still requires a certain calculation effort.

2.2.3 Energy methods

Besides DA and STAGE, that can be considered as the classic methods, other approaches have been proposed successively. Two of them fall into the energy approaches. One exploits the principle of conservation of energy (Kasivitamnuay and Singhatanadgid, 2005), the other is known as ASMA (De Rosa, Franco, and Mace, 2005).

Energy Method based on the principle of conservation of energy (EM)

The EM (Kasivitamnuay and Singhatanadgid, 2005) is based on the conservation of energy, according to which the strain energy U stored in the structure is equal to the sum of kinetic energy T and the work made by external forces W, assuming that there is no energy loss (in terms of heat and chemical reactions). Denoting with X_i, Y_j, Z_k the complete sets of properties (geometric ones, material ones, etc.) related to each type of energy then the principle can be explicited as

$$U(X_i) = W(Y_j) + T(Z_k), \tag{2.8}$$

which includes the structural domain, the applied loads, and the boundary conditions. Hence, the system is considered as a whole and there is no need to determine the explicit and implicit scale factors separately.

The similitude conditions are derived by scaling all the considered energies simultaneously, obtaining a scaled energy equation. The prototype equation of energy Eq. 2.8 becomes

$$U(\widehat{X}_i\lambda_i) - W(\widehat{Y}_j\lambda_j) - T(\widehat{Z}_k\lambda_k) = 0, \tag{2.9}$$

which can be rewritten as

$$\phi(\lambda_i)U(\widehat{X}_i) - \chi(\lambda_j)W(\widehat{Y}_j) + \Phi(\lambda_k)T(\widehat{W}_k) = 0, \tag{2.10}$$

where $\phi(\lambda_i)$, $\chi(\lambda_j)$, and $\Phi(\lambda_k)$ are functional relationships among scale factors.

The complete similitude is achieved when the principle of conservation is satisfied, which implies that, for the model under analysis, from Eqs. 2.9–2.10,

$$U(\widehat{X}_i) - W(\widehat{Y}_j) - T(\widehat{Z}_K) = 0 \iff \phi(\lambda_i) = \chi(\lambda_j) = \Phi(\lambda_k). \tag{2.11}$$

In conclusion, EM turns out to be more straightforward than STAGE as it provides the scaling factors even when the structure is made of several components, while keeping the same level of generality and obtaining the same conditions. However, a certain calculation effort is still required, especially when complex systems are considered, and problems may occur when prototype and model are made of different materials.

Asymptotical Scaled Modal Analysis (ASMA)

The Asymptotic Scaled Modal Analysis (ASMA) method is conceived to deal with the problem of spatial mesh typical of dynamic analyses executed with the Finite Element Method (FEM). As a matter of fact, FEM is the best numerical tool for structural analysis, however its computational cost becomes overwhelming as frequency increases. In fact, the spatial mesh is frequency dependent, thus the higher the frequency range of the analysis, the smaller the mesh dimension. Moreover, since the Nyquist sampling theorem (Nyquist, 1928) must be taken into account, the maximum frequency of the analysis must be fixed equal to, at least, twice the maximum frequency of interest, leading to a considerable increase of computational time. The main aim of ASMA is, therefore, to reduce the spatial extent in order to save time during simulations.

The method is first defined invoking the Statistical Energy Analysis (SEA) (De Rosa et al., 1997) with the objective of defining a scaled finite element model representing the energy exchange for increasing excitation frequency. The main idea is to reduce the extension of the spatial dimensions not involved in energy transmission, so that the original finite element mesh can be maintained, and, at the same time, to increase artificially the damping level in order to keep the same energy level of the prototype. ASMA is the formally justified without involving SEA (De Rosa, Franco, and Mace, 2005) but using the Energy Distribution Analysis [EDA (Mace, 2003)], which defines the way the scaled model can represent the main response. All the linear dimensions g not involved in the structural energy transmission are scaled down with a scale factor $\sigma < 1$, so that the scaled dimension becomes

$$\widehat{g} = \sigma g. \tag{2.12}$$

This operation moves the natural frequencies to higher frequency, thus, in order to keep the same energy level, damping must be scaled-up by means of another scale factor, ε, so that the scaled damping is

$$\widehat{\eta} = \varepsilon \eta. \tag{2.13}$$

The mode shapes are retained if the boundary conditions and the material of prototype and model do not change.

The solution of the dynamic problem with ASMA allows a reduction of both the Degrees Of Freedom (DOFs) and eigenvalues to be extracted. This opens the way to several possibilities of computational time saving:

- Same number of DOFs and eigensolutions: no computational advantage, but ASMA can represent the response at higher frequencies.
- Same number of DOFs, reduced number of eigensolutions: a certain computational advantage is acquired with dynamic response obtained, at least, in the same frequency range of the prototype.
- Reduced number of DOFs and eigensolutions: the number of DOFs is tailored in order to obtain both an appreciable computational advantage and the correct dynamic response in the same frequency range of the prototype.

By definition, the method is applicable to Finite Element Analysis (FEA) but, in general, it can be implemented in any Finite Element (FE) solver and any type of algorithm. ASMA can be applied to any structural operator for which the real or complex modal base (natural frequencies, mode shapes, and damping) is known, as it is based on modal expansion. Furthermore, it does not require a reference solution, thus a prior analysis of the prototype is not required. On the other hand, the response is evaluated meaningfully only for the global frequency response, being the local information lost due to the artificially increased value of damping. Nonetheless, the response is perfectly replicated when averaged on both acquisition and excitation points.

Finally, ASMA can be seen as a modulator of the original modal base that allows the analysis of the response of a structure in the frequency domain where the response is meaningful (De Rosa and Franco, 2008a).

2.2.4 Similitude and Asymptotic Models for Structural-Acoustic Research Applications (SAMSARA)

In a work by De Rosa et al. (De Rosa, Franco, and Polito, 2011), a new similitude method is proposed, justified by EDA, in order to enlarge the number of parameters to achieve a complete similitude and to investigate the possibility to define similitude conditions for acoustic-structural systems. Successively formalized in another work (De Rosa et al., 2012), the method is called SAMSARA and it is a generalization of the modal approach used in the ASMA method to define the scaling laws.

At a first stage, in order to reproduce the dynamic response by means of similitude it is necessary to satisfy some conditions:

- Material does not change, as any modification would alter the distribution of natural frequencies.
- The boundary conditions do not change.
- The system is excited by a concentrated harmonic force acting at the same dimensionless [or homologous, according to the definition of Baker et al. (Baker, Westine, and Dodge, 1991)] location.

- The structural damping is such that the system response can be obtained by using the real mode shapes and the undamped natural frequencies. More complicated models, based on complex mode shapes, do not add further contributions to theory development and results.

These assumptions are necessary since changes in the modal base, when SAMSARA is applied, must be limited. However, these are not limitations of the method but points to be explored in further developments.

When using SAMSARA method, the model is called *replica* if all the geometrical dimensions of the structure are scaled by the same scale factor. Instead, a distorted model is called *avatar*. To obtain a complete similitude, all the similitude conditions - which must not involve necessarily all the geometrical parameters - must be satisfied. A replica is, therefore, a true model because it fulfills all the conditions, although other scale factors, which do not appear into the scaling conditions, are involved.

In order to clarify, plates in similitude can be considered. A plate is geometrically characterized by width, length, and thickness, therefore scaling all these dimensions with the same scale factors leads to a true model and to a replica. However, the similitude condition for a complete similitude requires that length and width scale equally (De Rosa, Franco, and Meruane, 2015): thickness is a free parameter [as already demonstrated by Soedel (Soedel, 1971)]. Satisfying the conditions leads to a *proportional sides* model, which is another true model. In conclusion, to achieve a complete similitude is sufficient fulfilling the similitude conditions (proportional sides), however involving other parameters does not affect the similitude (replica).

When investigating systems in complete similitude, the prototype mode shapes appear at different natural frequencies in the model (for example, higher frequencies if the model is scaled down), but the succession of modes is retained. The energy given by the excitation spreads in a model according to a certain succession of modes with perturbed natural frequencies. By applying a *remodulation*, such succession of modes can be brought back to prototype ones. In this way, the response of the structure is reconstructed. This approach does not work with avatars, because the modes succession is distorted and the remodulation process does not keep trace of this.

An advantage of SAMSARA is that it directly involves modal parameters, such as natural frequencies and damping, which means that their scale factors are defined; this can be considered as the main novelty of the approach. Differently from ASMA, which provides only mean responses, SAMSARA can furnish even local responses. Moreover, it can be implemented in an algorithm.

2.2.5 Empirical Similarity Method (ESM)

In the field of Rapid Prototyping (RP), DA is the most used similitude method. However, some issues related to the difference in material properties between prototype and model, sensitivity to distortions, too restrictive use of information, and dependence of cost and time on geometrical complexity, has led Cho and Wood (Cho and

Wood, 1997) to propose the Empirical Similarity Method (ESM). It is based on testing a specimen pair: one specimen - the prototype specimen - has simple geometric features fabricated through RP, the other - the product specimen - is fabricated through the actual prediction process. By measuring the state vectors of this pair and the scaled structure obtained through rapid prototyping, a state transformation is derived in which the scale factors are replaced by weighting factors.

On the one hand, the empirical transformation matrix can be considered as the advantage of ESM, on the other hand additional specimen pairs are needed, which leads to additional manufacturing and testing.

2.2.6 Sensitivity Analysis (SA)

Sensitivity analysis, which can be defined as the study of how uncertainty in the output of a system can be related to uncertainties in the input of the same system, has been applied recently to structural similitude. Global Sensitivity Analysis (GSA) is applied when the global behavior is of interest, while Local Sensitivity Analysis (LSA) is applied when the response is studied at a particular point of the parameter space with a differential approach.

The first application of SA to the derivation of similitude conditions is up to Luo et al. (Luo et al., 2015). The authors enunciate the following four principles to get distorted laws:

- *Principle 1*: In distorted scaling laws, if parameter j is directly reflected in the governing equation, the index k of the scaling factor λ_j^k can be directly determined from the governing equations.
- *Principle 2*: In the sensitivity analysis, if sensitivity's absolute values satisfy $|\Phi_a| > |\Phi_b|$ in distorted scaling laws, the index relation of scaling factors λ_a^α and λ_b^β is $|\alpha| > |\beta|$. Here, Φ_a and Φ_b are the sensitivities (i.e., the change rates) of the natural frequency with respect to geometrical parameters a and b.
- *Principle 3*: If $\Phi_j > 0$, λ_j is positively proportional to λ_ω (the scale factor of the natural frequencies) in the distorted scaling law; conversely, λ_j is inversely proportional to λ_ω if sensitivity $\Phi_j < 0$.
- *Additional principle*: In the distorted scaling law, the index ratio $\alpha : \beta$ of scaling factors λ_a^α and λ_b^β is approximate to the ratio of the sensitivity $\alpha : \beta \approx \Phi_a : \Phi_b$.

The first three principles are used to derive approximate distorted scaling laws, i.e., scaling laws for distorted models that return a high percentage of error between the natural frequency of the distorted model and the predicted natural frequency. The additional principle is used to derive accurate distorted scaling laws which return an error lower than approximate laws (typically within 5%).

Adams et al. (Adams, Bös, and Melz, 2016) give a statistical application of GSA by employing, first, a 2^k ($k = 3$, in this case) full factorial design to study the effects on

the response of the structure to changes in input parameters, then derive sensitivity-based scaling laws through a multiple quadratic regression.

In another work, Adams et al. (Adams et al., 2018) apply LSA and derive the following expression for the k-th response of the model, $Y_k^{(m)}$,

$$Y_k^{(m)} = Y_k^{(p)} \prod_{i=1}^{N} (\lambda_{X_j})^{\alpha_{j,k}}, \tag{2.14}$$

that is, as the product of the prototype response $Y_k^{(p)}$ and N linearly independent scale factors λ_{X_j} (where X_j is a design parameter of the system, like geometrical, material, etc.), each one weighted by an unknown power $\alpha_{j,k}$.

The approach is directly deduced from Buckingham's Π Theorem, according to which DA can be used to derive the weighting terms $\alpha_{j,k}$. The novelty of the method proposed relies on the application of SA to derive these exponents, which can be written as

$$\alpha_{j,k} = \frac{\ln\left(Y_k^{(+)}\right) - \ln\left(Y_k^{(-)}\right)}{\ln\left(\lambda_{X_j}^{(+)}\right) - \ln\left(\lambda_{X_j}^{(-)}\right)}, \tag{2.15}$$

where the symbols (+) and (-) indicate the scaling up and down procedures, respectively.

As a consequence, SA does not require the derivation of dimensionless groups, as in DA, or to compare the equations of prototype and model, as in STAGE or SAMSARA. Briefly, it does not provide similitude-based scaling laws, but sensitivity-based ones obtained by just knowing the scale factors and the responses and using Eqs. 2.14-2.15, without any prior knowledge of the scaling behavior and with minimum effort. However, this characteristic makes both GSA and LSA lacking of physical insight into the problem that may lead one to overlook some important phenomena. Furthermore, too complex systems may lead to prohibitive computational costs and inefficient procedure.

2.2.7 Methods summary

As shown in this brief introduction to similitude methods, despite the increasing complexity of modern applications and the emerging methods, DA and STAGE are still the most used approaches.

According to DA, the similitude conditions are derived by defining sets of non-dimensional ratios - the Π terms - through the investigation of the reference parameters. It is not based on the knowledge of some equation (like the governing equations, or more specific ones), which makes the method employable in a wide range of applications, even very complex ones, even though a great amount of manual calculations may be needed. For instance, DA is used a lot in fluid dynamics in order to find the

non-dimensional numbers representing the main characteristics of a fluid (Mach number, Reynolds number, Peclet number and many others are non-dimensional ratios) by comparing dimensional groups with their own physical meaning.

DA is a very useful tool when the analyzer is experienced on the topic or when the governing equations are unknown or too complex to be solved analytically or numerically. As the choice of parameters is up to the analyzer, it can be exploited in order to understand the influence of a particular parameter on the phenomenon under observation.

STAGE is the second, most used method and it is based on the definition of scale factors successively substituted into the governing equations in order to derive the similitude conditions. On the one hand, this requires knowing the field equation; on the other hand, the conditions obtained are more specific and the method itself lacks the trial-and-error approach which is one of the drawbacks characterizing DA. Generally, when the governing equations are known, it is better to employ STAGE and DA.

Conservation of energy is the foundation of EM introduced by Kasivitamnuay and Singhatanadgid (Kasivitamnuay and Singhatanadgid, 2005). Once the strain energy, the kinetic energy, and the work of the (possibly multicomponent) structure have been evaluated, the scaling conditions are derived keeping the same results and level of generality of STAGE. Despite being more straightforward than STAGE, the EM procedure is still affected by a certain effort when dealing with complex structures.

ASMA and SAMSARA are the first methods addressing the similitude theory toward an automatic procedure, because both of them can be implemented in an algorithm.

ASMA is introduced because computational costs can sometimes be prohibitive; its purpose is to scale down the spatial domain by means of a scale factor. Since the energy level must be retained, an artificial increased damping is introduced. However, this damping limits the analysis to the global frequency response. Therefore, ASMA is expected to produce a good level of accuracy only for the mean response of a structure. Thus, the method is suitable for computationally expensive analyses where the analyzer is interested only in the mean response or in the response at high frequency range. Moreover, ASMA is useful in evaluating how SEA energy influence coefficients (both direct and indirect) are affected by changes in the Modal Overlap Factor (MOF).

SAMSARA applications exploit scale factors, just like STAGE. Modal parameters are also involved in the scaling procedure. Differently from ASMA, SAMSARA provides the local response, too. From this, with multiple acquisitions, the mean response can be reconstructed. SAMSARA is also very useful when studying structural dynamics and acoustic-structural systems.

ESM is used in RP applications. It derives a state transformation between a specimen pair and the scaled structure obtained through RP. Its introduction is due to the need of overcoming the problems of DA applied to RP, such as differences in material properties and sensitivity to distortions. Additional manufacturing is the main

disadvantage of the method.

SA is the last step, up to now, toward an automatic approach, especially in terms of scaling laws derivation, because it can be implemented into an algorithm. It is divided into GSA and LSA, according to the purpose. Its automatic nature allows to derive the sensitivity-based scaling laws without knowing the scaling behavior of the system *a priori* but, at the same time, it is not based on physical relationships. Moreover, it can become computationally expensive.

2.3 Applications of similitude methods

Similitude theory has been applied in many engineering branches to elementary structures such as beams, plates, and cylinders, which may occur as stand-alone systems or form the basic structural components of more complex ones [for example, pressure vessels (Hu, 2000; Shi and Gao, 2001)]. In this section, the applications of similitude theory to these systems is reviewed.

First of all, the application of similitude methods has concerned several structural fields, such as static and dynamic behavior, impact response, and damage.

The analysis of dynamic response focuses on identifying the natural frequencies and the mode shapes of a structure, since this information is fundamental for investigating fluid-structure interaction and other vibroacoustic phenomena, such as the response of a structure to a TBL excitation, which is an important source of vibration and noise, as the stochastic pressure distribution associated with the turbulence excites significantly the structural response and radiated acoustic power. For fluid-interaction problems like this, there are some computational issues related to the fact that solutions are typically lost above the structural/aerodynamic coincidence frequency, even if the mesh is built to simulate the dynamics at very high frequencies, that is, very small structural wavelengths. This opens the way to other concerns associated with dynamic response, i.e., the prediction capability at each frequency range at acceptable computational costs (De Rosa and Franco, 2008b).

Impacts are a branch of dynamic response of particular engineering interest, as large, short-duration forces may produce damage that can affect the load carrying capacities of a structure. There are many examples in which the resistance of structures to penetration or perforation has primary importance: design of a structure to resist wall perforation by a high velocity projectile, containment of fragments or projectiles generated by possible accidents in nuclear reactors, the threat of the so-called wind-generated missiles, containment of fragments generated in aircraft turbine engine disintegration, bird impacts on aircraft, etc (Magness and Farrand, 1990; Sorensen et al., 1991; Anderson, Jr., Mullin, and Kuhlman, 1993; Rosenberg, Kreif, and Dekel, 1997).

For metallic materials, this damage involves plastic deformation and wear in contact zone (Rosenberg, Kreif, and Dekel, 1997; Zhao, 1998; Oshiro and Alves, 2004), while it takes the form of fiber failure, matrix cracking, and delamination for composites (Morton, 1988; Jackson and Fasanella, 1989; Jackson, 1990; McKown, Cantwell,

and Jones, 2008). Things become more complicated when distinguishing between structures localizing the damage and those for which damage is more widespread. In structures with significant flexibility, multiple collisions may happen and a large amount of energy is released as vibrations. For rigid bodies, impactor and body vibrations are negligible and deformations are confined to the vicinity of the contact region.

These few observations demonstrate the complexity of impact problems, as they involve many phenomena that must be accounted for, ranging from inertial effects to material response to varying strain-rate and thermal loading, and material failure and stability. Particularly, scaling strain-rate dependence is challenging. In fact, because of it, the material increases its resistance as the impact load is applied. The model/prototype ratio of dynamic stress, representing how the static flow stress changes when there is a varying strain-rate, is no longer invariant. When dealing with similitudes, this translates into distortions because strain-rate phenomena do not support scaling, at least not with the usual, geometric scaling procedures (Oshiro and Alves, 2004).

In addition to dynamic behavior, similitude theory is commonly applied to the analysis of static behavior, too, which often schedules the loading of the test article until failure. Being known that size effects have a strong influence on failure mechanisms and the ultimate strength of the structure, and because statistical models or fracture mechanics theories fail to explain these effects, experimental tests result to be very useful for understanding the limits of validity of similitudes (Asl et al., 2016b; Asl et al., 2017a; Asl et al., 2017c; Asl et al., 2018).

Since their introduction more than sixty years ago, composite materials have received significant attention, being an interesting and useful alternative to the classic, isotropic engineering materials, thanks to their lightness and resistance capabilities. An important example is aeronautic field, in which, being both stiffness-to-weight and strength-to weight ratios important properties, composite materials are used for load-bearing aircraft structures such as the upper fuselage of A380 Airbus (Vlot, 2001).

With respect to isotropic materials, such as metal alloys, composite materials non-trivial interactions between micro- and macro-structural properties. As an example, there are several ways in which a composite material undergoes damage (fiber fracture, delamination, and matrix cracking), or the emergence of size effects. These are all phenomena that start at the microscopic scale and then evolve, eventually, to the macroscopic level of laminate.

These considerations suggest that both the micro- and macro-structures of a laminated composite should be scaled. However, such a procedure is never executed due to its practical complexity, therefore only the macrostructure is considered when similitude conditions are derived. This approach leads to some obstacles, as the descriptions of notch and strain-rate sensitivity, for example, are strongly dependent on the microscopic characteristics of a composite material. Notably, notch sensitivity is strong in quasi-isotropic laminates, yet weak in unidirectional laminates subject to traction in the fiber direction. Strain-rate sensitivity depends on fiber and matrix materials; glass

and Kevlar fibers are rate-sensitive, as the epoxy resin matrix, while carbon fibers are not rate-sensitive. Moreover, the degree of sensitivity depends on the lay-up and the rate of loading may affect the damage mechanisms. The interaction among all these factors may easily lead to scaling conflicts, therefore scaling a composite laminate is an operation to carry out carefully. Indeed, testing is required to establish guidelines and to underline those size effects which are not modeled by any scaling procedure.

The wide usage of laminated composites is limited only by their susceptibility to impact damage that can reduce the compressive strength even if such damage is not visible (at the naked eye). Characterizing impact phenomena become, therefore, necessary because the response of composites is complex, involving localized out-of-plane loading, possible strain-rate effects, and the interaction of several failure models.

There are many works (Kellas and Morton, 1992b; Rezaeepazhand and Simitses, 1993; Rezaeepazhand, Simitses, and Starnes, Jr., 1995a; Rezaeepazhand, Simitses, and Starnes, Jr., 1995b; Simitses and Rezaeepazhand, 1995; Rezaeepazhand, Simitses, and Starnes, Jr., 1996a; Rezaeepazhand, Simitses, and Starnes, Jr., 1996b; Rezaeepazhand and Simitses, 1997; Simitses, Rezaeepazhand, and Sierakowski, 1997; Wisnom and Atkinson, 1997; Johnson et al., 1998; Johnson et al., 2000; Simitses, 2001; Frostig and Simitses, 2004; Carrillo and Cantwell, 2007a; Carrillo and Cantwell, 2007b; Rezaeepazhand and Wisnom, 2009; Rezaeepazhand and Yazdi, 2011; Yazdi and Rezaeepazhand, 2011a; Yazdi and Rezaeepazhand, 2012; Yazdi, 2013) showing that a key parameter in scaling composite materials is the stacking sequence. Literature provides three scaling approaches, namely: ply-level scaling, sublaminate scaling, and general reduction of the number of plies. Ply-level scaling consists in adjusting the number of plies in a group having the same orientation; thickness is scaled and the stacking sequence is retained. Sublaminate-level scaling involves basic sublaminates, stacked together, so that thicker laminates are formed. The general reduction of the number of plies is self-explanatory.

Obviously, each scaling strategy has significant consequences on the response of the composite specimen, as studied in many works (Wisnom and Atkinson, 1997; Johnson et al., 1998; Johnson et al., 2000; Carrillo and Cantwell, 2007a; Carrillo and Cantwell, 2007b) which demonstrate how ply-level scaling applied only to thickness or to all the geometric dimensions (respectively known as one- and three-dimensional scaling) leads to a decreasing tensile strength with increasing size. The increasing severity of edge delamination and debonding are the main causes of this behavior, as they create stress concentrations that lower the strength of hybrid materials. On the other hand, two-dimensional ply-level scaling, i.e., area scaling, exhibits an increased tensile strength for larger samples. In this case, delamination affects smaller specimens because the relative width of the delaminated zone is greater. The severity of delamination varies due to the Poisson's ratio mismatches between the materials. Sublaminate-level scaling affects area scaling significantly, as it reduces the tendency of smaller models to fail earlier.

The remainder of the section is organized in several subsections (2.3.1–2.3.3),

one for each type of structure. For each subsection, a further partition is made in terms of applications, highlighting the commonalities in results and the novelties of the applied methods. The following contents are summarized in Table 2.2. The rows show, on the left, the test article, on the right the method, while the columns separate the applications in terms of used procedures (theoretical and experimental) and each box is filled with the material.

TABLE 2.2: Overview of test articles, procedures, methodologies and materials used in similitude methods

	Analytical/Numerical	**Experimental**	**Method**
Beam	Aluminium	Aluminium	ASMA
	Aluminium, Brass, Composite, Magnesium alloy, Steel, Titanium, Tungsten alloy	Composite, Steel	DA
	Aluminium, Steel	–	EM
Unstiffened plate	Aluminium, Composite	Aluminium	ASMA
	Aluminium, Composite, Steel	Aluminium, Composite, PVC, Steel	DA
	Aluminium, Steel	–	EM
	Aluminium	Aluminium	SAMSARA
	Steel	–	SA
	Aluminium, Composite, Magnesium alloy	Composite	STAGE
	Aluminium, Steel	Aluminium, Steel	STAGE + SA
Stiffened plate	Steel	Steel	DA
	Aluminium	–	STAGE
Sandwich plate	–	Composite + PMI (polymethacrylimide)	DA
	TC4 Titanium alloy + General rubber	–	STAGE
Unstiffened cylinder	Steel	Aluminium, Composite, Concrete, Steel	DA
	Aluminium	–	SAMSARA
	Steel	Steel	STAGE
	Aluminium	–	STAGE + SA
Stiffened cylinder	Composite	–	EM
	Aluminium	–	SAMSARA
	Aluminium, Steel	Aluminium, Steel	STAGE

Note: Table A.2 in Appendix A gives the corresponding references.

In the following sections, only the most relevant works are discussed in detail. The analytical details are provided for those analyses that are meaningful for the results presented in this thesis. A complete list of works is provided by Tables A.1–A.2 in Appendix A, in which the references for both methods and test articles are indicated.

2.3.1 Beams

Beams and bars are structural models constituting the main elements of frames, as well as subcomponents of more complex systems, such as stiffeners in a stiffened cylinder or spar caps and shear webs in wind turbine blades. Similitude methods have been applied to investigate both the static and dynamic behavior, failure, and impact response of beams.

Failure analysis

An important contribution to similitude theory is provided by the extensive experimental and numerical tests made by Jackson and Fasanella (Jackson and Fasanella, 1989) and Jackson (Jackson, 1990), which aim at investigating the behavior to failure of composite beams. In particular, six scaled models of a graphite-epoxy composite beam with unidirectional, angle- and cross-ply, quasi-isotropic stacking sequence, from 1/6 to full-scale, are subjected to both static and dynamic (impulsive) eccentric axial compression. The test articles were chosen because of the possibility of achieving large bending deflections promoting global failure away from the supported ends.

The prototype is scaled with DA, and the results highlight many important characteristics of scaled models, especially in terms of size effects, that reoccur in several subsequent works. The main experimental results are:

- In static tests, the scaled load and strain responses depend on the laminate stacking sequence and on the number of 0° plies in the laminate. the responses scale well in unidirectional and cross-ply laminates, which means that these models do not exhibit size effects. Conversely, for angle-ply and quasi-isotropic laminates, the responses deviate from those predicted with similitude theory because the beam stiffness is altered by damage.

- In static tests, all laminates exhibit a significant size effect in strength: as the size of the beam decreases - especially cross-ply beams - normalized loads, end displacements, and strains at failure increase. In dynamic tests, quasi-isotropic small models are more severely damaged.

- For dynamic tests, the predictions provided by scaled models are good for unidirectional laminates, but inconsistent for cross-, angle-ply, and quasi-isotropic ones, again mainly due to the size effects.

- In static tests, only the scaled models of cross-ply beams exhibit size effects in failure mechanism (while fiber fracture was not present in larger models).

In static and dynamic tests, failure modes are the same for the same stacking sequence, independently of specimen scale.

- Test data from beams belonging to the same laminate family and with same scaled size indicate similar load and strain responses in both static and dynamic tests. The failure locations due to both static and dynamic loading are nearly identical, with the exception of cross-ply laminates. It is therefore possible to retrieve important information on the global dynamic response of structures from simple static testing of scaled models.

- Bending stiffness is not affected by size for unidirectional, cross-ply, and quasi-isotropic laminates; angle-ply laminates exhibit greater stiffness as the size decreases.

In addition to specific observations about scaled composite beams, these works underline the problem of size effects which arise as noticeable departures from the predictions of similitude methods in actual experimental tests.

Static analysis

Asl et al. dedicate many works (Asl et al., 2016b; Asl et al., 2017a; Asl et al., 2017c; Asl et al., 2018) to static tests on composite beams, in which composite I-beams are investigated analytically, numerically, and experimentally in the framework of sub-component analysis for sub-component testing; the beams are equivalent to the spar caps and shear webs of wind turbine blades. STAGE is applied to derive the similitude conditions. The novelty of these works relies on the use of partial similitude. In fact, it is possible theoretically to achieve complete similitude by applying ply-level scaling and keeping the same aspect ratio. However, when the laminate thickness is supposed to scale down below the range in which there is no integer number of lamina left in the stack up, ply-level scaling is no more achievable (and reducing the lamina thickness is not an available option). Ply-level scaling is applicable only to specific lamination schemes but the possibility of keeping the same lay-up in the scaled models (as in the prototype) is limited by manufacturing constraints, since only fabrics with specific thicknesses are available in industry. It is therefore likely that the outcome due to manufacturing issues is a partial similitude. Thus, aiming for a good prediction of prototype behavior using partial similitudes, Asl et al. (Asl et al., 2016b; Asl et al., 2017a; Asl et al., 2017c; Asl et al., 2018) introduce a permutation algorithm which searches for the potential model having ply schemes with overall laminate thickness less than that of the prototype. By means of the definition of error to find the lay-up that works best with the derived scaling laws, then such a lay-up is used for predictions. This algorithm is called Distorted Lay-up Technique (DLT) and the tests demonstrate that the results exhibit errors smaller than 6% - and are, therefore, satisfactory - also with distorted models. It is worth noting that, as the number of layers in a model decreases, the probability of finding an accurate model

decreases, thus there is a limited amount of scaling that can be performed with DLT. The advantage of this technique is that it is applicable to other geometries and ply schemes.

DLT is used in a recent work (Asl et al., 2018) to test experimentally a prototype and nine models (three small, three medium, three large) having different lay-ups in a four-point bending test. According to the results, the strain field of the small beams is representative of those of the medium and large models: the prescribed loads described by similitude analysis work accurately across different scales. This implies that a certain strain level for a composite beam geometry with specific scale and lay-up can be accurately replicated in a smaller model with a different lay-up. Therefore, a scaled model may facilitate and expedite the fatigue testing process for large composite structures, leading to reduced costs and times.

In another experimental campaign (Asl et al., 2017a), analytical and numerical results are verified by a three-point bending test measured with Digital Image Correlation (DIC) executed on a composite beam in order to reproduce flapwise bending. The results of these tests confirm those already obtained previously by Jackson and Fasanella (Jackson and Fasanella, 1989) and Jackson (Jackson, 1990) about the absence of size effects: the bending stiffness of particular lay-ups is not affected by scaling. However, it has to be noted that the predictions are very good because the study is carried out in the elastic range, before yielding or failure appeared.

Frequency response

Asl et al. (Asl et al., 2017b) provide more insights on stiffness behavior with size by means of another experimental investigation concerning the response of three models (small, medium, and large) of a free-free beam excited with an impact hammer. The comparisons among the models show that the Frequency Response Functions (FRFs) agree; however, a certain decorrelation arises, increasing as moving towards higher frequencies. This is due to the flexural stiffness, which is dominating over those modes associated with shear, at low frequencies. Therefore, the first two peaks - for example - exhibit a good correlation because, as already noted (Jackson, 1990; Asl et al., 2017a), bending stiffness is not affected by scaling. At higher frequencies, shear becomes dominant and, as the FRFs decorrelation increases in this case, it is possible to conclude that shear stiffness is affected by scaling. Rotary inertia has a similar influence, which shifts the frequencies of larger models to lower values.

The advantages of ASMA are demonstrated by studying the structural dynamic behavior by De Rosa et al. (De Rosa et al., 1997) and De Rosa and Franco (De Rosa and Franco, 2010). Six in-line rods are investigated in the first work, two flexural aluminium beams and two sets of, respectively, two and four in-line rods are analysed in the second work. ASMA proves to be a valuable tool with respect to SEA and Classic Modal Analysis (CMA). Particularly, a comparison with the latter highlights how ASMA provides good predictions only at high frequencies as it captures an average energetic behavior. Nonetheless, it demonstrates the actual advantage of dealing with

scaled domains or with the same number of DOFs across a larger frequency range (De Rosa et al., 1997). ASMA is also used to evaluate the coupling loss factors providing acceptable results in regions of low, medium, and high MOF (De Rosa and Franco, 2010).

Impact response

As previously noted, the investigation of dynamic behavior due to impacts is challenging to approach, especially within a rigorous theoretical framework. The number of physical properties which need characterization with analytical models is quite large, and equally large is the number of parameters within these models. Many works provided in literature focused on the need to reduce such a number of parameters to a smaller, more manageable set and, more importantly, to introduce quantities that would allow comparison of results obtained for systems with similar geometries, boundary conditions, and loads.

Before Jackson and Fasanella (Jackson and Fasanella, 1989) and Jackson (Jackson, 1990), similar size effects were already described by Morton (Morton, 1988) while investigating experimentally the impact at the center of a composite beam of a free-falling mass. Small specimens were found to be stronger than larger ones and thus able to carry larger post-damage loads, while, the larger the specimen, the lower the impact velocity causing damage.

It is still up to Morton (Morton, 1988) the interesting experimental observation for which smaller specimens seem to exhibit smaller impact duration than larger ones. However, the reason may not be a size effect but rather the fact that the articles exhibiting this behavior are made of the same material (carbon fibers in an epoxy matrix) coming from another, older batch. This underlines the typical experimental problem in which the results, on the one hand, may be important and highlighting hidden phenomena but, on the other hand, must be treated carefully.

As evidence of this, McKown et al. (McKown, Cantwell, and Jones, 2008) present another example of results possibly polluted by improper experimental procedures in which Fiber Metal Laminate (FML) beams and plates are studied with DA. While some results, like the good agreement with predictions of load and deflections in both static (four-point bend flexure) and dynamic (low velocity impacts) tests, or the persistence of failure mechanisms, are consistent with previous works, on the other hand, the flexural yield forces of the 1/4-scale model are said to be 15% smaller than those of other models. This may be a size effect or, alternatively, the consequence of incorrect alignment of the smallest specimens on the test supports, which is a particularly difficult task. It is important to underline that, in this investigation, only geometrical scaling has been performed, therefore the approach may not work when higher strain-rates are considered.

The dynamic plastic response of bodies subject to impacts is the main focus of Zhao (Zhao, 1998), who uses DA to find a unique, dimensionless number to describe

these phenomena. Such a number is called response number, it is given by the product of Johnson's damage number (Johnson, 1972) and the geometrical influence of the structure, and takes into account three aspects: load inertia, material resistance, and structure geometry. In the cited work, it is demonstrated that the response number is suitable for representing the plastic response of beams and plates for many boundary and loading conditions. It also considers second-order effects such as finite deflections, transverse shear, strain-rate sensitivity (which makes the Zhao's work an early contribution addressing this phenomenon), and dynamic tearing.

The response number is the product of a similitude parameter in impact dynamics and a term related to the geometry of the structure. This leads to different forms of the response number as the loading conditions change. This consideration led to the formulation of a generalization of the response number to cover other forms of dynamic plastic failure, such as bifurcation buckling problems (Zhao, 1999). This application was expanded by other authors to more geometries, including circular and quadrilateral plates (Hu, 2000), and generalized the technique to different types of shells (Shi and Gao, 2001). These works are the evidence that the response number is quite useful to study the dynamic plastic response and failure of structures (beams, plates, shells, etc.) subject to large dynamic loading.

Christoforou and Yigit (Christoforou and Yigit, 1998; Christoforou and Yigit, 2009) have the same aim, thus they introduce dimensionless numbers, analytically or numerically obtainable according to the complexity of the system, in order to reduce the number of parameters characterizing impacts. The importance of their work relies on the fact that their results provide both physical insights and a tool for generalizing and correlating experimental results through the use of minimum data and model tests. In fact, different structures - such as beams and plates - made from different materials, under different boundary conditions and impacts, yet having the same values of non-dimensional numbers, share the same normalized responses. This makes possible to scale the impact responses among different systems. However, similitude is achievable only during the initial response or, more generally, before the mechanical waves are reflected back by the structure interfaces (because, after a such reflection, beams and plates exhibit different dynamics). Therefore, on the one hand, the global response scales well in terms of impact force and deflection; on the other hand, the local responses scale well only in terms of force. This aspect cannot be generalized among different structures, as the transition region between global and local behavior is not captured accurately by the dimensionless number.

The size effects are the aim of Pintado and Morton (Pintado and Morton, 1994). The authors focus on graphite-epoxy composite beams under three-point bending vertical impact loading. Lack of similitude is up to two sources: constant gravitational acceleration and non-scaling of stacking sequence. However, the former introduces small errors in model behavior, thus it can be neglected. It is the latter that leads to greater discrepancies. By applying Buckingham's Π Theorem, it is noticed that a complete similitude is achievable only with ply-level scaling; sublaminate-level

scaling leads to partial similitudes. This behavior can be explained physically: ply-level scaling allows to keep both in-plane and flexural moduli of the structure, while sublaminate-level scaling changes the flexural stiffness of the laminate.

However, a correction factor allows, under certain circumstances, to adjust the distortion introduced by sublaminate-level scaling. Pintado and Morton use DA based on bending stiffness to derive this factor but, because Classical Laminate Theory (CLT) predicts inaccurate values of this stiffness, the correction factor is evaluated with experimental data. These countermeasures against distortions allow to replicate results already seen (Morton, 1988; Jackson and Fasanella, 1989; Jackson, 1990): smaller models exhibit higher energy thresholds and fail at higher loads. In certain cases, the discrepancy in terms of failure scaled load is of 25%.

Nonetheless, the source of the size effects is not clear to the authors, who propose two possible explanations:

- Presence of a critical defect in the material. Because the distribution of defects of any size is uniform in the volume of the structure, the probability of finding a critical defect in larger specimens is higher than in smaller ones.
- the size dependence of strength is driven by fracture mechanism principles. For example, the authors refer to the fracture model of Laws and Dvorak (Laws and Dvorak, 1988) for cross-ply laminates in which the stresses necessary to produce first ply failure depend on the absolute size. Therefore, larger specimens are weaker than smaller ones.

However, these explanations are incomplete. Kellas and Morton (Kellas and Morton, 1992b) demonstrate that the dependence of strength on size can be inverted for certain lay-ups and loading conditions. In fact, even though in-plane moduli are equal for specimens with both ply- and sublaminate-level scaling, the tensile strength of ply level laminates decreases as the specimen size and thickness increase. Using sublaminate-level scaling on angle-ply laminates, instead, the tensile strength increases with size.

The interpretability of results is emphasized also by Pintado and Morton (Pintado and Morton, 1994), as the outcomes from their tests are not easy to compare when scaled because DA does not allow the derivation of a unique set of Π products. The choice of bending stiffness-based DA leads to significant size effects; using, instead, an approach which neglects the lack of similitude in stacking sequence limits the size effects.

There are several works focused on geometric scaling issues and non-scaling effects in terminal ballistics. For example, Sorensen et al. (Sorensen et al., 1991) analyze penetration mechanics and potential benefits of high velocity for both monolithic and segmented penetrators. Anderson et al. (Anderson, Jr., Mullin, and Kuhlman, 1993) perform two-dimensional numerical simulations to demonstrate that the strain-rate sensitivity of the flow stress in the target material can generate some non-scaling effects in the penetration depths of long rods. However, the differences between a full-

and 1/10-scaled model amount to 5%, which is small enough to be neglected. Magness and Farrand (Magness and Farrand, 1990) present experimental results showing that, for both tungsten alloy and depleted uranium penetrators, simple scaling does not exist. Moreover, penetration capabilities for both materials are significantly improved by increasing the penetrator scale. The primary aim of the authors is to demonstrate that such a size effect depends on target properties. However, the comparison of results between two different targets does not show differences (size effects are the same), thus the authors are forced to admit that the results do not single out any definite source for the scale dependency of their tests.

The research made by Rosenberg et al. (Rosenberg, Kreif, and Dekel, 1997) is motivated by these previous works on terminal ballistics. They share the goal with Magness and Farrand (Magness and Farrand, 1990), but their assumption is that size effects depend on the properties of the penetrator, not on those of the target. More precisely, failure mode is the cause of the lack of geometric scalability: geometric scaling should hold for ductile penetrators (like copper), while semi-brittle penetrators (like tungsten alloy or depleted uranium) may perform better at full scale because of their different mode of failure. The authors provide some experimental observations to support their idea: copper penetrators exhibit a perfect scaling of penetration depth, while tungsten alloy ones lead to 10% of discrepancy. As a matter of fact, the latter type of penetrators are more prone to early failure at their interface with the target, while the former, being very ductile metal, creates a relatively wide crater due to hydrodynamic nature of its penetration process. Moreover, while copper penetrators create totally clean craters, those made of tungsten alloy are full of debris. All these characteristics highlight a totally different mechanism of penetration and erosion which the authors think to be at the base of differences in scaling behavior. Moreover, the authors' assumptions are supported analytically, as the main cause of such non-scalability is traced to the plastic zone size parameter. Semi-brittle materials exhibit large values of this parameter that, consequently, exhibit different failure mechanisms at different scales. To give an example, as the penetrator dimensions increase, the plastic zone ahead of cracks becomes smaller, which leads to more brittle failure.

Alves, Oshiro and their collaborators focus on the application of DA to overcome the difficulties due to strain-rate sensitivity (Oshiro and Alves, 2004; Alves and Oshiro, 2006a; Alves and Oshiro, 2006b; Oshiro and Alves, 2009; Oshiro et al., 2011; Oshiro and Alves, 2012). The authors propose a new approach to DA (Oshiro and Alves, 2004) which allows to overcome the distortion problems in impact phenomena. Instead of using a MLT base, the authors propose the VSG (initial impact velocity, dynamic yielding stress, and impact mass) base. However, the new novelty of the work relies on the compensation of the distortion due to rate-sensitivity by means of the definition a new model/prototype impact velocity ratio without taking directly into account the constitutive model of the material. Two types of structures are analyzed: a clamped beam subject to an impulsive velocity and a Calladine model (two plates clamped together) under axial impact. The results show that the technique is robust,

scaling different types of structures with different behaviors and undergoing different phases of motion with errors below 1%. Strain-rate choice may be the source of discrepancy, as it is constant through the whole motion for beams, while only during the final phase of motion in plates. This implies that not all the motion stages can be corrected at the same time.

The success of the method proposed by Alves and Oshiro (Oshiro and Alves, 2004) motivates the authors to expand the approach and to demonstrate that the VSG base is versatile and overcomes some experimental constraint. For example, the authors first consider a scaling based on the impact mass rather than the initial impact velocity (Alves and Oshiro, 2006b), obtaining very good results and achieving even effectively zero error. Then, the same scale factor is changed in order to take into account models made of different materials (Alves and Oshiro, 2006a). This study is motivated by size effects [which can occur as discussed previously (()morton1988, jackson1989, jackson1990)] affecting the behavior of the models in such a way that material properties change when models are very small or very large with respect to the prototype. The constitutive curve changes, therefore inaccurate predictions result when inferring prototype behavior from that of a model. The proposed method is able to reconstruct the response of the prototype - made of mild steel - from that of a model - made of aluminium - with an error smaller than 3%. However, the authors specify that the method works only when it is assumed that the wave speed is the same in both prototype and models, otherwise there would be changes in the model response when elastic effects are important (but, in this work, these effects are ignored).

All the previous approaches have a common problem: the choice of representative strain-rate, of which an average value is chosen, although the estimation of such an average value is not always easy to carry out. Therefore, this consideration leads to the further expansion of the VSG method (Oshiro and Alves, 2009), consisting in the change of the constitutive law choice: using Norton-Hoff law instead of Cowper-Symonds one. Actually, the strain-rate is described as in the previous works, however the new law allows an exact scaling without prior knowledge of the structural response. As a consequence, the already small errors obtained with the previous approach are now totally removed.

Geometric effects are considered in addition to strain-rate effects by Oshiro and Alves (Oshiro and Alves, 2012), so that the complexity of scaled models, whose dimensions are flawlessly scaled, can be considered. According to the authors, geometric and strain-rate distortions can be dealt with separately. For the geometry, an exponential scaling law is used, however some residual errors appear since the exponent is difficult to determine.

Finally, Oshiro et al. (Oshiro et al., 2011) apply the VSG-based method in an experimental test on a T-cross section beam made of low carbon steel 1006 subjected to a quasi-static loading. The robustness of the VSG technique is noticeable when comparisons are made with the results obtained with the MLT-based approach.

2.3.2 Plates

Plates are the most investigated structural element, thanks to the wide range of practical applications and the extensive literature. Plates have many engineering applications: as upper and lower skins in wing boxes, spar caps of a wind turbine blade near to its maximum chord, as well as engine blades can be regarded as cantilever plates. Coated plates can be used as aircraft panel covered with a damping material that can reduce the flutter caused by airflow (Friedmann, 2004) and on ocean platforms. They are also used as propeller blades, vibrations adaptors, and to achieve anti-scour performance (Bachynski, Motley, and Young, 2012; Young, 2010).

Simitses and coworkers give a significant contribution to the study of laminated plates in similitude, thanks to the several applications and the fundamental results obtained (Simitses and Rezaeepazhand, 1992; Rezaeepazhand and Simitses, 1993; Simitses and Rezaeepazhand, 1993; Rezaeepazhand, Simitses, and Starnes, Jr., 1995a; Rezaeepazhand, Simitses, and Starnes, Jr., 1995b; Simitses and Rezaeepazhand, 1995; Simitses, 2001; Frostig and Simitses, 2004; Rezaeepazhand and Wisnom, 2009; Rezaeepazhand and Yazdi, 2011; Yazdi and Rezaeepazhand, 2011a; Yazdi and Rezaeepazhand, 2012). These investigations cover a wide range of loading conditions and structural configurations: bending of laminated, cross-ply orthotropic beamplates (Simitses and Rezaeepazhand, 1992; Simitses and Rezaeepazhand, 1993; Simitses, 2001), buckling and free vibrations of laminated cross-ply orthotropic beamplates (Simitses and Rezaeepazhand, 1993; Rezaeepazhand, Simitses, and Starnes, Jr., 1995b), symmetric laminated angle-ply plates (Rezaeepazhand and Simitses, 1993; Rezaeepazhand, Simitses, and Starnes, Jr., 1995a; Rezaeepazhand, Simitses, and Starnes, Jr., 1995b; Simitses and Rezaeepazhand, 1995), delaminated beamplates (Rezaeepazhand and Wisnom, 2009) and sandwich plates (Frostig and Simitses, 2004), flutter of symmetric angle-ply (Rezaeepazhand and Yazdi, 2011), antisymmetric cross-ply (Yazdi and Rezaeepazhand, 2011a), and delaminated cross-ply and quasi-isotropic, laminated plates (Yazdi and Rezaeepazhand, 2012). All these works aim at analyzing complete similitudes and, above all, to find the scaling conditions leading to the best predictions if partial similitudes are considered. The authors apply STAGE to the solutions of governing equations and boundary conditions.

The results obtained by Simitses and coworkers are consistent with the observations made in Sections 2.3–2.3.1. To achieve a true model, a laminated composite must satisfy at least these two conditions: the conservation of stacking sequence and material properties. These conditions are satisfied, respectively, by performing ply-level scaling and designing the model with the same material properties of the prototype. However, some particular configurations require additional conditions. For instance, mode shapes must be retained for cross-ply (Rezaeepazhand, Simitses, and Starnes, Jr., 1995b; Yazdi and Rezaeepazhand, 2011a) and delaminated (Rezaeepazhand and Wisnom, 2009) laminates.

On the other hand, partial similitudes make unfeasible to deduce a general behavior because each system, with its own geometry, loading, and boundary conditions, is

sensitive in its own way to a particular set of design parameters. This makes mandatory the separated analysis of each system. Nonetheless, some commonalities can be identified, as in some applications (Simitses and Rezaeepazhand, 1992; Simitses and Rezaeepazhand, 1993; Simitses, 2001) a distortion in number of plies still leads to good predictions of maximum deflection and stress provided that the right scaling law is chosen. Furthermore, the experimental validations made by Simitses and Rezaeepazhand (Simitses and Rezaeepazhand, 1992) show that STAGE fails in predicting any type of damage.

It can be helpful to show how some of the conditions are derived in these works for plates. The simplest case concerns an isotropic plate with uniform cross section and subject to a uniform transverse load Q (Simitses and Rezaeepazhand, 1993). Its governing differential equation is

$$\frac{\partial^4 w}{\partial x^4} + 2\frac{\partial^4 w}{\partial x^2 \partial y^2} + \frac{\partial^4 w}{\partial y^4} = \frac{Q}{D}, \tag{2.16}$$

wherein w is the displacement in the direction orthogonal to the xy plane - where the plate lies - and D is the bending stiffness.

A prototype and its model are governed by the same equation, therefore, assuming that Eq. 2.16 refers to the full-scale pate, it is possible to write, for the model,

$$\frac{\partial^4 \widehat{w}}{\partial \widehat{x}^4} + 2\frac{\partial^4 \widehat{w}}{\partial \widehat{x}^2 \partial \widehat{y}^2} + \frac{\partial^4 \widehat{w}}{\partial \widehat{y}^4} = \frac{\widehat{Q}}{\widehat{D}}. \tag{2.17}$$

Eq. 2.17 can be rewritten in terms of scale factors and the prototype parameters as

$$\left(\frac{\lambda_w}{\lambda_x^4}\right)\frac{\partial^4 w}{\partial x^4} + \left(\frac{\lambda_w}{\lambda_x^2 \lambda_y^2}\right) 2\frac{\partial^4 w}{\partial x^2 \partial y^2} + \left(\frac{\lambda_w}{\lambda_y^4}\right)\frac{\partial^4 w}{\partial y^4} = \left(\frac{\lambda_Q}{\lambda_D}\right)\frac{Q}{D}. \tag{2.18}$$

Eq. 2.16 and Eq. 2.18 are the same if the terms in parenthesis in the last equation are all equal, i.e.,

$$\frac{\lambda_w}{\lambda_x^4} + \frac{\lambda_w}{\lambda_x^2 \lambda_y^2} + \frac{\lambda_w}{\lambda_y^4} = \frac{\lambda_Q}{\lambda_D}\frac{Q}{D}, \tag{2.19}$$

and complete similitude is achieved when Eq. 2.19 is completely satisfied, which leads to the similitude condition

$$\lambda_x = \lambda_y. \tag{2.20}$$

Eq. 2.19 allows to derive three expressions for the orthogonal deflection scale factor λ_w:

$$\lambda_w = \frac{\lambda_Q \lambda_x^4}{\lambda_D}, \tag{2.21}$$

$$\lambda_w = \frac{\lambda_Q \lambda_x^2 \lambda_y^2}{\lambda_D}, \tag{2.22}$$

$$\lambda_w = \frac{\lambda_Q \lambda_y^4}{\lambda_D}, \tag{2.23}$$

that are absolutely equivalent and, therefore, ensure a perfect prediction of the prototype behavior, when Eq. 2.20 is satisfied. Conversely, not fulfilling the similitude condition makes Eqs. 2.21–2.23 different and yields to different results, none of which is ensured to be a good prediction. It is important to underline that the procedure herein presented should be completed by also considering the boundary conditions.

Other articles (Rezaeepazhand and Simitses, 1993; Rezaeepazhand, Simitses, and Starnes, Jr., 1995b; Simitses, 2001), which objective is to understand to which extent it is possible to push distortions before the prototype behavior is totally unrecoverable, are interesting example for laminated configurations. In the case of angle-ply plates, assuming that prototype and model have similar mode shapes - which implies that they can be well approximated by the same number of terms in the series obtained by applying Galerkin procedure to the solution of the characteristic equation - the scale factors associated to the integers characterizing this series are

$$\lambda_m = \lambda_n = \lambda_p = \lambda_q = \lambda_{A_{mn}} = 1, \tag{2.24}$$

where m and n are the number of half waves in x and y directions, respectively, p and q are integer indices of the Galerkin procedure, associated to the coefficient A_{mn}.

Then, five scaling laws for the non-dimensional frequency Ω are derived:

$$\lambda_\Omega^2 = \frac{\lambda_{D_{11}}}{\lambda_{E_{22}} \lambda_h^3 \lambda_{\mathcal{AR}}^4}, \tag{2.25}$$

$$\lambda_\Omega^2 = \frac{\lambda_{D_{12}}}{\lambda_{E_{21}} \lambda_h^3 \lambda_{\mathcal{AR}}^2}, \tag{2.26}$$

$$\lambda_\Omega^2 = \frac{\lambda_{D_{22}}}{\lambda_{E_{22}} \lambda_h^3}, \tag{2.27}$$

$$\lambda_\Omega^2 = \frac{\lambda_{D_{16}}}{\lambda_{E_{22}} \lambda_h^3 \lambda_{\mathcal{AR}}^3}, \tag{2.28}$$

$$\lambda_\Omega^2 = \frac{\lambda_{D_{26}}}{\lambda_{E_{22}} \lambda_h^3 \lambda_{\mathcal{AR}}}, \tag{2.29}$$

where the terms E_{ij} and D_{ij} are the laminate Young's moduli and flexural stiffnesses, h is the total plate thickness, and $\mathcal{AR}$ is the plate aspect ratio. The Eqs. 2.25–2.29 depend only on material properties and the total number of plies, not on the thickness of the single ply. All of them must be satisfied simultaneously to achieve a complete similitude.

By introducing a parameter β, linked only to the number of plies N_p,

$$\beta = \frac{3N_p^2 - 1}{N_p^3}, \tag{2.30}$$

and assuming plies with same thickness, same material properties and fiber orientation, complete similitude requires

$$\lambda_{\mathcal{AR}}^{-2} = \lambda_{\mathcal{AR}}^2 = \frac{\lambda_\beta}{\lambda_{\mathcal{AR}}} = \lambda_\beta \lambda_{\mathcal{AR}} = 1 \tag{2.31}$$

Satisfying all the Eqs. 2.25–2.29 leads necessarily to

$$\lambda_\beta = \lambda_{\mathcal{AR}} = 1. \tag{2.32}$$

Therefore, a true model is obtainable if length and width of the panel scale in the same way, as well as the total number of plies does not change, that is, as previously revealed, ply-level scaling. Interestingly, thickness is not directly involved into the scaling procedure, thus it is a free parameter.

Instead, for cross-ply configurations, the dimensionless frequency scales as

$$\lambda_\Omega^2 = \frac{\lambda_{D_{11}} \lambda_m^4}{\lambda_{E_{22}} \lambda_h^3 \lambda_{\mathcal{AR}}^4}, \tag{2.33}$$

$$\lambda_\Omega^2 = \frac{\lambda_{D_{12}} \lambda_m^2 \lambda_n^2}{\lambda_{E_{21}} \lambda_h^3 \lambda_{\mathcal{AR}}^2}, \tag{2.34}$$

$$\lambda_\Omega^2 = \frac{\lambda_{D_{22}} \lambda_n^4}{\lambda_{E_{22}} \lambda_h^3}, \tag{2.35}$$

thus complete similitude requires

$$\lambda_m^4 = \lambda_m^2 \lambda_n^2 \lambda_{\mathcal{AR}}^2 = \lambda_n^4, \tag{2.36}$$

that is satisfied if and only if

$$\begin{cases} \lambda_m = \lambda_n \\ \lambda_{\mathcal{AR}} = 1 \end{cases}. \tag{2.37}$$

Once again, the aspect ratio of the plate must be retained and, in addition, the numbers of half waves must scale in the same way.

The tests highlight that angle-ply laminated plates are very sensitive to scaling procedures different from ply-level one, leading to the aspect ratio scale factor $\lambda_{\mathcal{AR}}$ value adapting to correct the distortion, often requiring unsuitable design conditions. On the other hand, cross-ply constructions exhibit less sensitivity to changes in the number of plies, which implies less constrictions in design phase.

Concerning buckling load, its estimation is very sensitive to the number of plies - and, therefore, thickness - and aspect ratio (Rezaeepazhand and Simitses, 1993; Simitses and Rezaeepazhand, 1993; Rezaeepazhand, Simitses, and Starnes, Jr., 1995a; Simitses and Rezaeepazhand, 1995). However, it is still possible to obtain good predictions by changing the number of plies of the model provided that it is not too low (Simitses and Rezaeepazhand, 1993) or by modulating the aspect ratio (Rezaeepazhand and Simitses, 1993; Rezaeepazhand, Simitses, and Starnes, Jr., 1995a; Simitses and Rezaeepazhand, 1995).

Good matches with the prototype behavior are much more difficult to achieve when there are distortions in the material properties. Discrepancies vary between 5% and 30% depending on the chosen scaling law if the model is made of isotropic material (like metal and plastic) and between 15% and 20% if it is made of fiber-reinforced material (Simitses and Rezaeepazhand, 1993). Conserving the stacking sequence and the number of plies, the choice of a proper fiber-reinforced material for the model allows a good prediction of the buckling load without modulating the aspect ratio. To give an example, when the prototype is made of Kevlar/epoxy composite, good accuracy is achieved when the model is made of boron/epoxies, boron/polymider, and most of the graphite/epoxies materials. Conversely, glass/epoxy is not a good choice. When the model is made of isotropic material, modulating the aspect ratio still makes possible an accurate prediction of the buckling load. (Rezaeepazhand and Simitses, 1993; Rezaeepazhand, Simitses, and Starnes, Jr., 1995a; Simitses and Rezaeepazhand, 1995).

When determining the flutter speed in aerodynamic applications, good predictions are obtainable although distortions in thickness, fiber orientation, and aspect ratio. In contrast, the discrepancies increase as the Mach number increase. However, it is likely that such a phenomenon does not depend on the scaling procedure but to the aerodynamic theory used, as Rezaeepazhand and Yazdi (Rezaeepazhand and Yazdi, 2011) and Yazdi et al. (Yazdi and Rezaeepazhand, 2011a) apply the quasi-steady aerodynamic theory, valid for $M < \sqrt{5}$. It is therefore expectable a loss of accuracy at higher Mach numbers.

Complete similitudes require two more conditions if delamination is taken into account: the buckling modes (local for both thin and large delaminations) and the delamination position must be retained. In fact, when the delamination length is too low or the delamination position is too close to the plate midplane, there is a loss of accuracy precisely because the modes are no more local but global or mixed, thus the conservation of the modes is no more observed (Rezaeepazhand and Wisnom, 2009; Yazdi and Rezaeepazhand, 2012).

The works until now reviewed consisted in STAGE applied to the solutions of governing equations. In similar investigations (Ungbhakorn, 2001; Singhatanadgid and Ungbhakorn, 2002; Singhatanadgid and Ungbhakorn, 2003; Ungbhakorn and Singhatanadgid, 2003c; Singhatanadgid and Ungbhakorn, 2005; Singhatanadgid and Na Songkhla, 2008), STAGE is applied no more to solutions but to governing equations directly, deriving more general scaling conditions and laws because independent from

boundary conditions. These studies can be seen as a natural continuation of the previous works of Simitses, Rezaeepazhand, and their collaborators (Simitses and Rezaeepazhand, 1992; Rezaeepazhand and Simitses, 1993; Simitses and Rezaeepazhand, 1993; Rezaeepazhand, Simitses, and Starnes, Jr., 1995a; Rezaeepazhand, Simitses, and Starnes, Jr., 1995b; Simitses and Rezaeepazhand, 1995; Simitses, 2001; Frostig and Simitses, 2004; Rezaeepazhand and Wisnom, 2009; Rezaeepazhand and Yazdi, 2011; Yazdi and Rezaeepazhand, 2011a; Yazdi and Rezaeepazhand, 2012).

Also in this case, several configurations and loading conditions are considered: buckling of symmetric cross-ply (Ungbhakorn, 2001), antisymmetric cross- and angle-ply laminated plates (Ungbhakorn and Singhatanadgid, 2003c) subject to biaxial loading, symmetric plates under normal in-plane loading (Singhatanadgid and Ungbhakorn, 2003), polar orthotropic clamped annular plate under compression and torsional load, and free vibrations of antisymmetric cross- and angle-ply laminated plates (Singhatanadgid and Ungbhakorn, 2002).

These works confirm many of the results already seen, like the requirement of ply-level scaling for complete similitude. The authors point out that, physically, this implies retaining the flexural stiffness of the plates when scaling plates. As a matter of fact, limiting the distortions of flexural stiffness leads to good results because. For this reason, by changing the model material from Kevlar/epoxy to E-glass/epoxy, the accuracy of the predictions decrease, while the discrepancies are very low when switching from a stainless steel material to aluminium, as their flexural stiffnesses are very close (Simitses and Rezaeepazhand, 1995; Singhatanadgid and Ungbhakorn, 2005). Further confirmations are given when considering distortions in extensional, bending, and bending-extension stiffnesses: the discrepancies are always higher when the flexural stiffness is changed (Singhatanadgid and Ungbhakorn, 2002).

Singhatanadgid and Na Songkhla (Singhatanadgid and Na Songkhla, 2008) perform experimental tests on vibrating thin plates and, as seen seen in other works (Morton, 1988; McKown, Cantwell, and Jones, 2008), one of the main aspects is the difficulty of experimental testing. In fact, the results of the test made on plates with different boundary conditions highlight inconsistencies between the theoretical and the experimental predictions. However, these outcomes are, likely, due to imperfections in reproducing the boundary conditions, as analyses on free plates - the simplest boundary condition to realize - exhibit good theoretical/experimental matches.

Frequency response

Although DA is the oldest and most used similitude method, there are few interesting applications to the analysis of the frequency response of plates; one of these is due to Ciappi et al. (Ciappi et al., 2012). The aim of the authors is to define dimensionless parameters so that scaling laws for excitation frequency and Power Spectral Density (PSD) can be derived. In fact, such a dimensionless representation should provide a universal expression for the structural response of systems excited by a TBL, which induced vibrations in elastic structures are the source of the major noise in transport

engineering (naval, aerospace, and automotive). The test article under analysis is a thin, flat elastic plate without prestresses wetted over one face by a stationary TBL. The flow is incompressible and without pressure gradient.

This work is a demonstration of the experience needed, as the authors identify eleven dimensionless parameters governing the problem, but, by means of a thorough analysis of this set, it is demonstrated that not all the groups are useful. The authors conclude that the only dimensionless ratios important for deriving a non-dimensional form of the displacement PSD are those involving the pressure distribution PSD. Particularly, they derive three dimensionless equations of the displacement PSD by using a particular form of non-dimensional frequency, plus another one from energy considerations. The comparisons of four experimental tests - performed at different conditions in both wind tunnel and towing tank - are plotted on reference axes reporting the values of dimensionless frequency, on the horizontal axis, and one of the dimensionless formulations of displacement PSD. The experimental data are shown to collapse very close to each other, proving that the proposed representations allow an estimate of displacement PSD in the whole frequency range, revealing to be useful for preliminary predictive steps. Particularly, the equation derived by energy considerations links non-dimensional frequency and acceleration with just one, simple equation, which provides a quick estimate of structural response in the entire frequency range. On the other hand, the other equations provide a good response estimation when the damping is hard to identify (for example, when the plate is part of a greater structure, like a ship or an airplane).

The other application of DA to the investigation of the frequency response of plates is the work of He et al. (He et al., 2020), in which the problem of middle-frequency regions is addressed. In fact, SEA method, meant to give consistent results in high MOF regions, would not work in a proper frequency range. Moreover, the phase information is lost. FE approach, instead, is able to provide the phase information but its application outside the low modal density ranges becomes computationally inefficient. Therefore, the authors decide to apply the coupling wave FE-SEA hybrid method, combining the advantages of both the methods and suitable for the middle frequency range. The final aim of the work is to study the coupling between solar arrays and a satellite, however the method is first tested on a 2-plates assembly, where the subsystems with low modal density are modeled with FE approach, while those at high modal density are scaled with SEA approach. Both the plates are made of aluminium, and the excited plate is the deterministic one, while the receiver plate is the statistical one. Under the assumption of consistent material, unchanged damping (the internal loss factor is smaller than 0.1, thus the assumption is reasonable as the differences between the system are quite small), and broadband concentrated force, the authors define three fundamental scaling laws: one for the force PSD [in which, in accordance with other works previously mentioned (Rezaeepazhand and Simitses, 1993; Rezaeepazhand, Simitses, and Starnes, Jr., 1995b; Simitses, 2001) it is assumed that the geometrical dimensions of the plates scale in the same way], and two for the velocity response, which scales differently according to the type of subsystem (FE

or SEA). The predictions of the Root Mean Squared (RMS) responses are consistent. However, SEA introduces uncertainties, therefore the reconstructions of the response become less precise for increasing frequency. Moreover, the excited plate provides better predictions than the receiver because of the power loss in the hybrid line connection.

The advantages of ASMA are illustrated in two works. In the first one, De Rosa et al. (De Rosa, Franco, and Mace, 2005) analyze a two-plates assembly joined at right angle by means of ASMA, no more justified with SEA but EDA. The experiments are conducted by exciting one plate - the driver - and acquiring the response on the other - the receiver. Length and width of both plates are scaled down as

$$\begin{cases} \widehat{a} = \sigma a \\ \hat{b} = \sigma b \end{cases}, \tag{2.38}$$

where a and b are the lenght and width of one plate, respectively.

As a consequence, the j-th natural radial frequency ω_j scales as

$$\widehat{\omega}_j = \frac{\omega_j}{\sigma^2}. \tag{2.39}$$

In order to keep similar modal characteristics, dynamic scaling must be introduced. Thus another scale factor $\varepsilon < 1$ is introduced purposefully and the damping η_j scales as

$$\widehat{\eta}_j = \frac{\eta_j}{\varepsilon}. \tag{2.40}$$

EDA parameters must be scaled, too. Particularly, the spatial correlation between two modes must not change, therefore the cross-mode partecipation factors ψ_{jk} must remain the same:

$$\widehat{\psi}_{jk} = \psi_{jk}. \tag{2.41}$$

When characterizing frequency, instead, the auto-modal power mobilities Γ_{jj} scale as

$$\widehat{\Gamma}_j j = \varepsilon\sigma\widehat{\Gamma}_{jj}. \tag{2.42}$$

Concerning the cross-modal power mobilities Γ_{jk}, they can assume both large and small values, if the modes overlap or not, respectively. This leads to different functions of the scale factors σ and ε, i.e., different scaling procedures. In particular:

$$\widehat{\Gamma}_{jk,large} = \varepsilon\sigma^2\Gamma_{jk,large}, \tag{2.43}$$

$$\widehat{\Gamma}_{jk,small} = \frac{\sigma^2}{\varepsilon}\Gamma_{jk,small}. \tag{2.44}$$

Eqs. 2.43–2.44 show how the large terms scale in the same way of the auto-modal power mobilities, thus the small terms are the only ones which do not scale according to the rule $\sigma^2\varepsilon$.

When scaling the response of a system, or a directly excited subsystem belonging to a generic assembly, any value $0 < \sigma < 1$ can be chosen. Moreover, it can be demonstrated that assuming $\sigma = \varepsilon$ is a good approximation and returns acceptable results.

Under these hypotheses, the energy terms of interest (input power P_{IN}, kinetic energy T, EDA energy coefficients A_{rs}, and mean squared velocity V_m^2) scale as

$$\widehat{P}_{IN}^{(s)} = P_{IN}^{(s)}, \tag{2.45}$$

$$\widehat{T}^{(r)} = \varepsilon\sigma^2 T^{(r)} = \sigma^3 T^{(r)}, \tag{2.46}$$

$$\widehat{A}_{rs} = \varepsilon\sigma^2 A_{rs} = \sigma^3 A_{rs}, \tag{2.47}$$

$$\widehat{V}_m^2 = \varepsilon V_m^2 = \sigma V_m^2, \tag{2.48}$$

where the superscripts (s) and (r) indicate the source and receiver plates, respectively.

According to Eq. 2.45, the input power is not scaled. On the analytical side, this results is due to scale factors erasing each other; on the physical side, it is coherent with the energy redistribution, among the modes, imposed to the energy terms (EDA coefficients, damping, etc.) through the scale factors.

The computational saving searched can be obtained by scaling the number of modes N_M as

$$\widehat{N}_M = \sigma^2 N_M, \tag{2.49}$$

which gives the number of modes required in the scaled response. This choice is motivated by the decreasing modal density when the plate area is reduced. However, $\widehat{N}_M$ gives the minimum number of modes required. In fact, one can choose not to scale such a number and push the dynamic analysis of the model to further frequencies. In this regard, the scale factors act as a frequency modulator, controlling the width of the frequency window in which the model yields acceptable predictions.

The application of ASMA to the two-plates assembly shows that the predictions are good when the MOF μ is high enough to expect a global response, which means in the same range of validity of SEA. On the one hand, the response of the source plate is well reconstructed, because it is dominated by the power input, which in turn is related to the auto-modal power mobility, with which ASMA works fine. On the other hand, the predictions on the receiving system exhibits some approximations, yet the response is still acceptable [this is in accordance with the work due to He et al. (He et al., 2020)]. However, a noticeable computational saving is obtained, passing

from 400 (driver) and 320 (receiver) points in the prototype assembly to 60 and 48 points in the model assembly.

These results are successively strengthened in other investigations on the dynamic behavior of plates (De Rosa and Franco, 2008a; De Rosa, Franco, and Polito, 2011), assemblies of two-plates (De Rosa and Franco, 2008a; De Rosa and Franco, 2010), and three-plates (Martini, De Rosa, and Franco, 2004; De Rosa and Franco, 2010).

The second important work on ASMA concerns a panel excited by a TBL load (De Rosa and Franco, 2008b). Usually, the dynamic response is well estimated above the structural/aerodynamic coincidence frequency by discretizing both structure and fluid with meshes of different scales, successively linked with an interpolation matrix. This procedure is very time consuming, however, this problem can be bypassed with ASMA, which introduces a mesh with a scaled size for both the structural and aerodynamic operators, recovering the global response with an acceptable approximation. Of course, the local response is not well reproduced. Furthermore, a comparison with results obtained by means of FEM demonstrate that FEA diverges above the coincidence region due to the spatial aliasing of TBL correlation lengths. ASMA, instead, provides accurate results because the minimum scaled flexural wavelength is still smaller than TBL correlation length.

Two extensions to ASMA are provided by Li (Li, 2010a; Li, 2010b). First, SEA is combined with Skudrzyk's mean value Theorem (Skudrzyk, 1966) to derive, first, a general scaling law, then specific laws for a flexural plate (Li, 2010a). Modal density θ is used as control factor and scales as

$$\lambda_\theta = \sqrt{\frac{\lambda_\rho}{\lambda_E}\frac{\lambda_A}{\lambda_h}} < 1, \tag{2.50}$$

where ρ is the mass density, E is the elastic modulus, A is the plate area and h the plate thickness. This scale factor is used to simulate high frequency dynamics with coarse FE models; this is expressed by the condition $\lambda_\theta < 1$, as scaling down the modal density scale factor leads to a reduction of the computational cost.

The results show that both local and global responses are accurately estimated when the control factor is closer to one, that is, modal density of the prototype close to the model modal density. Even though the method is developed for global responses, it works fine for local responses, too.

In the other work (Li, 2010b), Li determines the scaling laws by using random process theory and assuming the Gaussian Orthogonal Ensemble (GOE) and that the mode shapes are random quantities. The test article is a thin flat plate with randomly placed masses attached, which leads to the definition of auxiliary requirements to assure the reduction in modal density and boosting the frequency analysis. The plate is excited by an harmonic force and the ensemble statistics (mean and variance) of the mean squared velocities of the model are well estimated. Furthermore, the model retains the ensemble size of the system.

SAMSARA is applied for the first time by De Rosa et al. (De Rosa et al., 2012) to investigate the response of an elastic homogeneous plate in contact with an acoustic cavity (a parallelepiped filled with fluid). Firstly, it is assumed that global mode shapes ϕ_j remain unaffected, i.e.,

$$\widehat{\phi}_j = \phi_j, \tag{2.51}$$

which implies that the mode shapes do not need to be posed in similitude. Moreover, it ensures that the excitation and measurement points, acting at the same dimensionless coordinates in both prototype and model, have the same behavior. Consequently, as already seen with ASMA in Eq. 2.32, also the cross-mode participation factors do not scale.

Concerning the auto-power mobilities, they scale as

$$\widehat{\Gamma}_{jj} = \frac{1}{\lambda_\eta \lambda_\omega^2} \Gamma_{jj}. \tag{2.52}$$

The cross terms involve different dependencies from the scaling parameters even in SAMSARA; therefore, they cannot be posed in direct similitude. The large terms and the small ones must be separated as

$$\widehat{\Gamma}_{jk,large} = \frac{1}{\lambda_\eta \lambda_\omega^2} \Gamma_{jk,large}, \tag{2.53}$$

$$\widehat{\Gamma}_{jk,small} = \frac{\lambda_\eta}{\lambda_\omega^2} \Gamma_{jk,small}. \tag{2.54}$$

With respect to ASMA, SAMSARA allows to introduce the scale factors of the parameters directly involved into the equations, which makes easier to provide a physical explanation. On the one hand, large values of damping help to increase the overlap between modes, therefore the small cross-power mobilities are proportional to damping. On the other hand, when the modes already overlap, to increase such an overlap requires a negligible amount of damping. However, damping is fundamental when the resonant response of each mode and the cross-modal power mobility must be reduced. Thus, large cross-power mobilities must be inversely proportional to damping.

More generally, the role of the cross-modal terms is not well reproduced when $\lambda_\eta \neq 1$. A complete similitude necessarily requires unchanged damping between prototype and model.

The spectral density force function S_{FF} - i.e., the excitation - and other EDA parameters already met in ASMA (Eqs. 2.45–2.51) scale as

$$\widehat{S}_{FF} = \frac{\lambda_F}{\lambda_M} S_{FF}, \tag{2.55}$$

$$\widehat{P}_{IN} = \frac{\lambda_F^2}{\lambda_\omega \lambda_M} P_{IN}, \tag{2.56}$$

$$\widehat{T}^{(r)} = \frac{\lambda_F^2}{\lambda_M \lambda_\eta \lambda_\omega^2} T^{(r)}. \tag{2.57}$$

As already seen in other works (Rezaeepazhand and Simitses, 1993; Rezaeepazhand, Simitses, and Starnes, Jr., 1995b; Simitses, 2001), the condition for the plate complete similitude is to keep unitary the aspect ratio scale factor ($\lambda_{\mathcal{AR}} = 1$). For the sake of simplicity, the authors represent the global modes as uncoupled structural and acoustic bases, thus the natural frequencies of the plate and the fluid volume, still uncoupled and retaining the material properties, scale as

$$\lambda_\omega^{plate} = \frac{\lambda_h}{\lambda_a^2}, \tag{2.58}$$

$$\lambda_\omega^{fluid} = \frac{1}{\lambda_a}, \tag{2.59}$$

in which all the sides of the parallelepiped cavity scale as the sides of the plate.

However, the system as a whole is still coupled and such a coupling can be expressed by the ratio Λ between the plate and fluid natural frequencies of the same mode order.

$$\Lambda = \frac{\omega_j^{plate}}{\omega_j^{fluid}}. \tag{2.60}$$

In order to keep the relative distribution of natural frequencies, the ration Λ must not change between prototype and model, i.e., $\lambda_\Lambda = 1$. This leads also to the additional conditions for which the plate thickness and area must not change. A complete similitude is investigated; after the remodulation in frequency, the prototype behavior is perfectly reconstructed.

In a successive work (De Rosa, Franco, and Meruane, 2015), replica and proportional sides models of simply supported plates are investigated; In both cases, a good reconstruction of the dynamic response is obtained. Therefore, as mentioned above, a good prediction of the prototype response does not require the scaling of all the structural dimensions (i.e., to perform a complete geometrical scaling), it is simply necessary to satisfy the similitude conditions. Avatars are analyzed for the first time in this work. The tests underline that the response estimation is acceptable until the distortion is limited. It is herein proposed the definition of a metric representative of the similitude degree. In this first attempt, the scale factor of the modal density is used,

$$\lambda_\theta = \frac{\lambda_a \lambda_b}{\lambda_h}, \tag{2.61}$$

that is Eq. 2.50 rewritten under the assumption of unchanged material properties and explicit area scale factor. On the one hand, the results are coherent when avatars are considered: the scale factor increases as the distortion increases. However, they are

totally incoherent with true models. For instance, a replica and a proportional sides model, quite close in terms of similitude degree, exhibit values of λ_θ equal to 0.33 and 8, respectively. Therefore, modal density turns out to be not a a good estimator of similitude degree.

New insights are obtained in the application of SAMSARA to cantilever plates due to Meruane et al. (Meruane, De Rosa, and Franco, 2015). Numerical and experimental comparisons exhibit good matches also when avatars are used. However, the high frequency range is characterized, in all cases, by significant discrepancies due to damping, as the numerical models assume constant damping for both prototype and models ($\zeta = 0.005$). Particularly, simulations with damping ratio ζ equal to 0.001 and 0.0075 are made. The results show that, indeed, while the experimental results of the prototype are closer to the numerical simulations at $\zeta = 0.001$, those provided by the replica are closer to the numerical results at $\zeta = 0.0075$. A possible explanation may be linked to the added damping due to the boundary condition, which sums to the classical internal dissipation mechanisms of the plate. Furthermore, the results of the experimental tests are close to the numerical results in regions at low modal density. In fact, apparently, the size of the plates affects the response in regions at high modal density. This leads to perform other tests with two different proportional sides models one with dimensions twice those of the prototype (proportional large), the other with dimensions halved (proportional small). The comparisons between the responses show that similitudes work well when the frequency range contains enough poles among which the energy can be distributed. This explanation is highlighted by the fact that the predictions provided by the proportional large model are quite close to the reference one, while those provided by the proportional small model are not. In fact, being tested in the same frequency range of the prototype, it exhibits fewer poles, thus larger discrepancies, because many natural frequencies have moved further. Therefore, these outcomes are in line with the results of Li (Li, 2010a), as the modal density must be kept as unchanged as possible.

Finally, Hausdorff distance is tested as similitude metric and the results are encouraging, being coherent with the types of similitudes: the distances evaluated for replica and proportional sides model are close enough, and they increase as distortions increase.

In the last two works (De Rosa, Franco, and Meruane, 2015; Meruane, De Rosa, and Franco, 2015), the role of modal density in similitudes is highlighted. In fact, it is first concluded that the modal density is not a reliable similitude index as it does not allow an acceptable interpretation of replica and proportional sides behaviors. Therefore, it cannot be generalized to all types of similitude (De Rosa, Franco, and Meruane, 2015). Conversely, Meruane et al. (Meruane, De Rosa, and Franco, 2015) remark that modal density must be retained in order to reconstruct the prototype response. This seems contradictory, because the values of modal density, in a given frequency range, for replica and proportional sides are different, yet both of them well predict the full-scale structure behavior. A further apparent contradiction arises from the observation that, by definition, the replica model can act as a prototype for

the proportional sides model. Actually, both the conclusions are true and in accordance between them. The modal density represents the number of resonating modes in a given frequency range (that can be changed according to the model considered), thus it is a quantitative information. Two models of the same prototype may have the same modal density, i.e., the same number of modes in a certain frequency range, but one may be a replica, the other an avatar. In fact, distortions can change the succession of modes, that is a qualitative information, and the response is no longer reconstructed although the modal density is the same. The quantitative condition allows the redistribution of the energy in the right number of poles, while the qualitative condition ensures that the succession of such poles is kept.

The scaling of radiated acoustic power of a simply supported panel is attempted by Robin et al. (Robin, De Rosa, and Berry, 2016), which is not a straightforward operation, since the presence of the radiation resistance matrix entails the definition of a new scaling condition for the frequency, namely

$$\lambda_\omega \lambda_d = 1, \tag{2.62}$$

where d is the distance between two elementary radiators. Moreover, a new frequency scale factor is proposed, which is an attempt, not derived from equations, of finding a law which leads to an acceptable avatar:

$$\lambda_\omega = \frac{2}{\lambda_a + \lambda_b}, \tag{2.63}$$

in which the 2 at the numerator leads to the replica scaling law when the condition $\lambda_a = \lambda_b$ is satisfied.

Applying Eqs. 2.62–2.63, experiments made on a proportional sides model show that the resonance peaks of the radiated power are well reconstructed in the range 100-1000 Hz, while underestimated/overestimated (according to which plate is used as reference) above 1000 Hz.

The scaling of radiated acoustic power is further deepened by Berry et al. (Berry et al., 2020), who apply SAMSARA in order to examine the similitude laws for the vibroacoustic response of rectangular orthotropic panels radiating sound in a semi-infinite light fluid medium. Particularly, the acoustic response in similitude is studied from the far-field and the near-field points of view. It is interesting to underline that the proportional sides assumption is necessary for scaling all the dynamic parameters (natural frequency, vibration response, near- and far-field acoustic responses); far-field pressure is always scalable, while near-field radiation can be scaled exactly only in specific situations. The laws are then validated with experimental tests involving plates with several dimensions and made of different materials.

SAMSARA is applied by Franco et al. (Franco et al., 2019) in analyzing the response of a plate under TBL excitation described by Corcos model. The whole engineering problem is transformed into a new domain by scaling the excitation, structural and transmitted vibration, and the structural noise. The increased complexity of the test case is reflected by a series of new similitude conditions. In fact, in addition to the

typical assumptions of SAMSARA, like unchanged damping and spatial dependence of the analytical mode shapes (De Rosa et al., 2012; De Rosa, Franco, and Meruane, 2015; De Rosa, Franco, and Meruane, 2015), it is also assumed that the reduced frequency is the same in both the x and y directions. This hypothesis ensures that the ratios appearing into the Corcos model, $\frac{\omega\xi_x}{U_c}$ and $\frac{\omega\xi_y}{U_c}$ (where ξ_x and ξ_y are the streamwise and spatial separations, while U_c is the convective velocity), do remain constant between the prototype and the model. This is a mandatory requirement to scale the correlation area accordingly to the structural domain if the Corcos coefficients assume fixed values. However, the basic constraint for complete similitude is expressed in terms of joint acceptances between two modes, derived under the assumption of similar auto-spectral densities.

For a simply supported plate, it is possible to scale the cross-spectral densities if the Corcos coefficients are constant and the scaling law is valid for all the TBL models using the same coherence functions (i.e., with separate space variables), because the joint acceptances, and their scaling law, are ruled by the choice of coherence function of TBL model. Furthermore, it is also possible to take into account changes of material.

The predictions are compared in terms of the ratio of auto-spectral densities of acceleration with respect to the auto-spectral density of wall pressure distribution due to TBL, versus frequency. The curves overlap for both aluminium and acrylic cast plates. The analytical results are strengthened by the experimental measurements of the auto-spectral densities, even though they are noisier (however, such a noise is independent from SAMSARA, as it is due to experimental uncertainties and measurement processing). It is further demonstrated that, because the TBL load acts as an uncorrelated pressure field for increasing frequency, the solution is less affected by acceptance integrals. Therefore, in the high frequency region, the condition related to the reduced frequency is no more a mandatory constraint.

Finally, numerical analyses are carried out also for more complex configurations, such as composite plates. The eigensolutions sequence is not affected if thickness and, most importantly, the stacking sequence are unchanged, which means performing ply-level scaling [as many authors already stated (Kellas and Morton, 1992b; Rezaeepazhand and Simitses, 1993; Rezaeepazhand, Simitses, and Starnes, Jr., 1995a; Rezaeepazhand, Simitses, and Starnes, Jr., 1995b; Simitses and Rezaeepazhand, 1995; Rezaeepazhand, Simitses, and Starnes, Jr., 1996a; Rezaeepazhand, Simitses, and Starnes, Jr., 1996b; Rezaeepazhand and Simitses, 1997; Simitses, Rezaeepazhand, and Sierakowski, 1997; Wisnom and Atkinson, 1997; Johnson et al., 1998; Johnson et al., 2000; Simitses, 2001; Frostig and Simitses, 2004; Carrillo and Cantwell, 2007a; Carrillo and Cantwell, 2007b; Rezaeepazhand and Wisnom, 2009; Rezaeepazhand and Yazdi, 2011; Yazdi and Rezaeepazhand, 2011a; Yazdi and Rezaeepazhand, 2012; Yazdi, 2013)]. In fact, proportional sides models provide perfect matches also changing the thickness; conversely, modifying the lay-up generates distortions.

This type of analysis is further developed by Franco et al. (Franco et al., 2020), applying SAMSARA to stiffened plates. In particular, the plates are characterized by

stiffeners - represented as beams - with Z and C cross-sections at the same time. The presence of the stiffening makes achieving complete similitude harder, as distortions are introduced by the terms linked to the bending stiffness of the beams. Also the smearing approach leads to some discrepancies, because such a formulation requires that the spacing between the stiffeners is small compared with the distance between vibration nodes. However, this work highlights an interesting point: the scale factor of frequency is not constant in all the frequency range, even though the sequence of the structural modes is not altered. Through numerical models (but also experimental, potentially), the function $\lambda_{\omega_{mn}}(\omega)$ can be reconstructed by means of a polynomial interpolation. However, the predictions are acceptable, although they exhibit some discrepancies moving towards high frequencies; this is due to the indeterminacy linked to the remodulation of the function $\lambda_{\omega_{mn}}(\omega)$, which has not a physical meaning.

The scaling behavior of plates excited by TBL is the study subject of Xiaojian et al. (Xiaojian et al., 2016), too, who propose a method very similar to SAMSARA. The novelty of the work is the method used to determine the frequency offset between low and high frequency regions. The numerical and experimental predictions prove to be good, although some slight discrepancies between them (it is not known if these errors are due to the approximated experimental fixing conditions or to the thickness effect that strongly affects the vibration response).

Luo et al. (Luo et al., 2013) propose an innovative approach in dealing with partial similitudes. In fact, the authors first apply STAGE to derive the scale factors, then evaluate the applicable structure size interval to determine accurate distorted scaling laws. The procedure consists in fixing the discrepancy value that must be returned by partial similitudes, designed by changing the structural parameters. The method is applied to a variety of test articles: simply supported plates numerically (Luo et al., 2013) and experimentally (Luo et al., 2014c) investigated, and to coated thin plates (Luo et al., 2016b). SA is then introduced to support STAGE to determine accurate distorted scaling laws (Luo et al., 2016b). The operating principles are summarized in four points (listed in Sec. 2.2.6) which link the design scale factors to the sensitivities of the system. The method is used to investigate thin walled plates (Luo et al., 2016b) and annular thin plates (Luo et al., 2015).

However, SA does not just support existing similitude methods like STAGE (Luo et al., 2015; Luo et al., 2016b), but can also be used to derive its own similitude conditions and scaling laws, as Adams et al. (Adams, Bös, and Melz, 2016; Adams et al., 2018) show. In the first work (Adams, Bös, and Melz, 2016), GSA is used to derive sensitivity-based scaling laws. GSA considers the design parameters space as a whole and allows to evaluate the effect of each parameter as well as their interactions. The test article herein investigated is a simply supported aluminium plate; the response parameters observed are the natural frequencies and the Mean Squared Transfer Admittance (MSTA). Design Of Experiments (DOE) is first used to determine the effects of the design parameters, employing multiple quadratic regression, too. Then, the assumption of natural frequencies and MSTA quadratically modeled is made. Complete geometrical scaling leads to satisfactory agreements, while changing the thickness

leads to significant error in predicting MSTA, which ranges from 21% to 85%. This implies that quadratic modeling is not sufficient; in fact, a fourth order model would be more suitable.

In Adams et al. (Adams et al., 2018), LSA is applied, which is based on differentiating the system under analysis at a particular point in the parameter space by performing a first-order sensitivity analysis. This procedure leads to the derivation of power-law sensitivity-based scaling laws. In this work, three cases are presented: an analytical study of a simply supported plate which behavior is described by Kirchhoff theory, a numerical, FE analysis of the same test article described with Mindlin-Reissner theory, and the investigation of a generic car undercarriage.

Two things are of particular interest. The first is the values of the exponents provided by SA, which leads to a frequency scale factor equal to

$$\lambda_\omega = \lambda_a^{-2}\lambda_h^1, \tag{2.64}$$

that is the same law obtained with SAMSARA (Eq. 2.58).

The second interesting thing is the case of the plate described by Mindlin-Reissner theory, as it highlights the pitfalls of sensitivity-based scaling laws, namely their mathematical origin. In fact, while similitude-based laws keep the physical meaning of the phenomenon under analysis, sensitivity-based laws are instead obtained by means of a mathematical procedure, therefore lacking of any link to the physical behavior of the system. This is why, when analyzing the Mindline-Reissner plate, SA tends to overestimate both natural frequencies and MSTA, because it does not take into account the influence of thickness. At high frequencies, the mode shapes also change.

Coutinho et al. (Coutinho, Baptista, and Rodrigues, 2018) introduce an interesting modification of STAGE, based on a modular approach which leads to scaling relationships as general and structured as possible because of their organization into modules. These modules are derived by applying STAGE to the most basic equations: the governing equation derived from elasticity theory, force and moments resultant written as integrals of stress fields, stress-strain and strain-displacements relations, and displacement field. In this way, it is possible to obtain flexible groups of scaling laws that can be efficiently re-used in a multilevel methodology. Using basic, general equations, no simplifying assumption is made, thus the scaling relationships obtained are as general as possible and applicable also to complex systems that lack of governing equations. This approach is a big step forward in similitude field, as all the previous approaches consider just specific cases and the similitude conditions are derived for each one of them, with great effort of the analyzer. Instead, the method proposed by Coutinho et al. derives the modular scaling laws just once and shows how they can be assembled to solve more complex problems (e.g., acoustic and thermal). The modular approach is applied to analyze a stiffened aluminium plate with pinned edges. The similitude conditions and scaling laws are derived for both the plate and the beam structural operators; those for the stiffened plate system are obtained by imposing the continuity of displacements and internal forces at the interfaces. The predictions provided by this approach are very good.

Impact response

Geometrical scaling is the most single one when DA is applied. However, it is not always sufficient for all the loading phenomena; for example, it is not for impact loading, which may produce fracture and effects of strain rate that do not scale with geometry. These limits of geometrical scaling are the subject of a series of works aimed at studying the impact response of plates (Nettles, Douglas, and Estes, 1999; Ambur et al., 2005; Sutherland and Guedes Soares, 2007; Viot et al., 2008; Xu et al., 2016).

Nettles et al. (Nettles, Douglas, and Estes, 1999) execute several experimental tests on composite plates subject to transverse load. The results underline the increased scaled load of small models with respect to the prototype and other phenomena, therefore confirming observations done in other works (Morton, 1988; Jackson and Fasanella, 1989; Jackson, 1990). However, new phenomena are highlighted, like the dents due to impacts that do not scale well and the smaller, with respect to the prototype, scaled delamination area of the model (passing from 32 to 16 plies leads to a change of 71%). Moreover, a longer matrix splitting induces a change into the delamination shape when the number of stacks increases (the shape changes from circular to a more elongated shape).

Ambur et al. (Ambur et al., 2005) focus on the effects of delamination and fiber failure. The authors execute impact experimental tests on six flat and curved composite panels, with two geometrically scaled sizes. The tests show significant size effects. The results suggest that the impact energy absorption appears to depend on the approach used to scale the laminate. In fact, flat panels, subjected to low damage impacts and scaled with the ply level procedure, are less resistant than the sublaminate-level scaled panels. On the other hand, when subjected to high damage impacts, the ply-level scaled panels are more damage resistant than the sublaminate-level scaled ones (which absorb more energy through local fiber failure). When the panels are curved, sublaminate-level scaling induces less damage resistance than ply-level scaling. Moreover, damage mode and extent are influenced and, as expected, scaled-up models exhibit more damage with respect to the prototype.

Sutherland and Guedes Soares (Sutherland and Guedes Soares, 2007) investigate an orthotropic plate made of a marine composite material and struck by a mass. Buckingham's Π Theorem is used to derive the similitude conditions. However, the derived scaling laws work fine only in the elastic range, as deviations are observed due to size effects: in larger specimens, the fiber failure occurs at relatively lower load and displacements [as already seen in other works (Nettles, Douglas, and Estes, 1999; Ambur et al., 2005). Larger plates exhibit limited stiffening effects and, when the specimens have thinner woven ravings, higher strain-rate results.

Viot et al. (Viot et al., 2008) and Xu et al. (Xu et al., 2016) also underline the limits of geometrical scaling and the general smaller resistance to damage of large test articles.

The *sequential* similitude method is proposed by Shokrieh and Askari (Shokrieh and Askari, 2013) for analyzing the scaling of buckling problems of structures previously impacted, therefore structures already damaged before being subjected to buckling load. Sequential similitude defines scaling laws in two consecutive steps:

1. Step one: the similitude method is first applied in the case of impact loading to produce similar damaged areas in all the plates.

2. Step two: the similitude is developed between plates under buckling loading without considering the effect of initial damages on buckling equations. The damaged plates are introduced in the buckling problem by setting the initial condition of the structure to the ultimate situation of the corresponding impacted plate.

STAGE is the similitude method used in these steps and the structures investigated are three carbon/epoxy composite plates. The predictions from the models are accurate even for impacts in the inelastic region: all the plates have damaged regions and their damage patterns are similar. Buckling loads and mode shapes are predicted with small errors.

Blasts scaling can be regarded as a particular type of impact problem, and they are studied in some articles (Jacob et al., 2004; Neuberger, Peles, and Rittel, 2007a; Neuberger, Peles, and Rittel, 2007b; Neuberger, Peles, and Rittel, 2009; Noam, Dolinski, and Rittel, 2014). The blast is a destructive wave of highly compressed air, typically produced by an explosion. Blasts are characterized by high accelerations, which allow to neglect other types of accelerations, for example, that of gravity. This assumption simplifies the derivation of the scaling laws, since gravitational acceleration is one of those phenomena that are not geometrically scalable. However, a structure undergoing blasts also exhibits other types of non-geometrically scalable phenomena, like fracture failure and rate-sensitivity.

Neuberger et al. apply DA to investigate the response of plates subjected to explosions in free air (Neuberger, Peles, and Rittel, 2007a), due to buried charges (Neuberger, Peles, and Rittel, 2007b), and the springback of a circular plate under TNT blast (Neuberger, Peles, and Rittel, 2009). The blasts are scaled with the Hopkinson method, also known as "cube root " method (Baker, Westine, and Dodge, 1991), based on the assumption that self-similar blast waves are produced at identical scaled distances when two explosive charges of similar geometries and explosive, but different weight, are detonated in the same atmosphere. Therefore this leads to introduce a scaled distance, a characteristic time of the blast, and an impulse.

When circular plates are subject to close-range large blasts (Neuberger, Peles, and Rittel, 2007a), the models are geometrically scaled and the normalized midpoint deflections and stresses scale well as a function of scaled time when using both a rate-insensitive bilinear and a rate-sensitive material model. Changes in material properties due to changes in material thickness are introduced to emulate possible manufacturing problems. In this case, there is a certain discrepancy in the predictions of both

midpoint deflection and stresses, reaching values of 7% for the peak values. Plasticity, which is a nonlinear phenomenon, scales well, as proved by the matches between experimental and numerical tests. This is not surprising, because, as already reviewed by Rosenberg et al. (Rosenberg, Kreif, and Dekel, 1997), geometric scaling holds for ductile penetrators and any deviation from this scaling should be attributed to the failure mechanism at the penetrator's head, not to the target properties [as suggested by Magness and Farrand (Magness and Farrand, 1990)].

In the second part of the investigation (Neuberger, Peles, and Rittel, 2007b), the authors consider the case in which a clamped circular plate is subject to blasts due to large buried spherical charges. Also in this study, changes in thickness lead to discrepancies in the numerical results. Moreover, the experimental/numerical comparisons show slight disagreements when the scaled distance decreases; the source may be tha change of material properties because of thickness variation. These works prove that the problem of determining the dynamic response of a structure subject to blasts is well scaled.

However, Noam et al. (Noam, Dolinski, and Rittel, 2014) underline that the method used by Neuberger et al. (Neuberger, Peles, and Rittel, 2007a; Neuberger, Peles, and Rittel, 2007b; Neuberger, Peles, and Rittel, 2009) works just for the structural response without addressing potential fracture failure. Moreover, Jones (Jones, 1989) states that it is not possible to scale failure in blast loaded structures when using fracture-mechanics based (fracture toughness) considerations. Therefore, Noam et al. (Noam, Dolinski, and Rittel, 2014) aim at providing an alternative approach based on two scalable competitive fracture criteria so that the blast scaling approach can be fully treated. The similitude method used is DA and it is coupled with the following failure criteria:

1. Strain energy density criterion: this describes adiabatic shear and is derived from the considerations of Rittel et al. (Rittel, Wang, and Merzer, 2006), according to which the dynamic failure energy can be viewed as a failure criterion when adiabatic shear is considered (adiabatic shear banding failure, or ASB failure).

2. Maximum principal stress criterion: this is introduced because the authors do not know if the blasts induce ASB failure. The criterion states that failure occurs when a maximum principal stress, developed in an element, is greater than the ultimate tensile stress of the material. Although this is a typical brittle fracture criterion, the authors are not interested in describing the differences of various types of fracture (like Rosenberg et al. (Rosenberg, Kreif, and Dekel, 1997) do), they just want to represent the fragmentation, that is, the creation of new surfaces.

Both criteria undergo complete scaling if the material is assumed to be rate-insensitive, as proved by numerical results of air plates under air blasts due to spherical charge. When the meshes are fine and medium, the normalized dimensions of the

cracks and the von Mises stresses are comparable; some slight differences appear but they are negligible. Because the fracture is triggered when the maximum stress criterion is satisfied, it is possible to consider it as a good alternative to fracture-mechanics based criteria when the problem has to be scaled.

Finally, the extensive experimental campaign made by Jacob et al. (Jacob et al., 2004) is worth mentioning. There, quadrangular plates are subjected to impacts and both charge (diameter and height) and plate (thickness and aspect ratio) geometries are changed. However, since different combinations of charge and plate properties return a multitude of responses and interactions, the authors introduce a parameter for localized loading of quadrangular plates in order to simplify such complexity. It is a modification of a dimensionless parameter previously introduced by Nurick and Martin (Nurick and Martin, 1989a; Nurick and Martin, 1989b) and it is useful to evaluate the midpoint deflection for many loading conditions and plate geometries. Numerical and experimental tests prove that the introduction of such a parameter leads to a good estimation of the midpoint deflection.

2.3.3 Cylinders

Cylinders are another type of widely used structural element, as they are used to model tubes, aeronautical structures like fuselages (especially stiffened cylinders), or other types as containers and tanks. They are also used as casks for the storage, transportation, or final disposal of irradiated nuclear reactor fuel (Sato, Vecchio, and Andre, 1989), gasholder barrels (Yu and Li, 2016), and riser tube for fluid drilling operations (Chouchaoui and Ochoa, 1999; Chouchaoui, Parks, and Ochoa, 1999).

Buckling and frequency response

As done for laminated plates, STAGE is applied also to composite cylinders (Rezaeepazhand, Simitses, and Starnes, Jr., 1996a; Rezaeepazhand, Simitses, and Starnes, Jr., 1996b; Simitses, Rezaeepazhand, and Sierakowski, 1997; Rezaeepazhand and Simitses, 1997; Ungbhakorn and Singhatanadgid, 2003a; Ungbhakorn and Singhatanadgid, 2003b; Ungbhakorn and Wattanasakulpong, 2007; Yazdi, 2013), for which the conditions to obtain complete similitude are the same of the plates (in terms of lay-up), plus the conservation of the curvature parameter (squared length over the product between thickness and radius). Therefore, it is expected a great sensitivity when varying the length, the radius or the thickness of the cylinder. Of course, a true model allows for perfect reconstruction of the prototype behavior.

Rezaeepazand et al. investigate the predictive capabilities of STAGE in free vibration problems of symmetric cross-ply laminated cylindrical shells with single (Rezaeepazhand, Simitses, and Starnes, Jr., 1996a) and double (Rezaeepazhand and Simitses, 1997) curvature. Distortions in stacking sequence are allowed only if the number of plies is odd; accuracy increases if the number of plies of the prototype increases. Retaining the mode shapes allows for acceptable predictions of the dimensionless frequency even for changing length and radius. Conversely, the investigation of flutter

boundaries (Ungbhakorn and Singhatanadgid, 2003a) shows how length distortions generate errors up to 20%. The response is more sensitive to variations in radius than in length (Rezaeepazhand, Simitses, and Starnes, Jr., 1996a) and the Gaussian curvature also affects considerably the estimations (Rezaeepazhand and Simitses, 1997). Moreover, it is important to underline that retaining a mode shape is a simple matter only from the theoretical point of view, as it is enough to impose and respect the similitude condition. This is not so easy to obtain during an experimental test.

Other investigations due to Rezaeepazhand et al. also seek to determine the buckling load of cross-ply laminated cylindrical shell under axial compression (Rezaeepazhand, Simitses, and Starnes, Jr., 1996b) and lateral loading (Rezaeepazhand and Simitses, 1997). Again, distortions in the stacking sequence allow good predictions of the buckling load, while the sensitivity to variations in radius leads to high discrepancies, even if the distortions are small. Instead, changing the length leads to good results even if the mode shapes are not kept. Moreover, Simitses et al. (Simitses, Rezaeepazhand, and Sierakowski, 1997) note that more accurate predictions result from an increase in length than from a decrease; however, when the length reaches very low values, the buckling load is well estimated even if the mode shapes change.

Tabiei et al. (Tabiei, Sun, and Simitses, 1997) propose a variation of STAGE in a work that can be considered as a continuation of the investigation made on the buckling behavior of cross-ply laminated cylindrical shells under lateral pressure (Simitses, Rezaeepazhand, and Sierakowski, 1997). The proposed variation consists in a curve fitting technique involving scale factors as a function of other scale factors. The considered factors do not need to be derived from equations, it is enough to consider those that bring to the sought distorted model. The fitted model captures, indeed, higher-order terms reducing, therefore, the inaccuracies, with respect to the classical scaling laws.

Ungbhakorn et al. investigated the buckling and free vibrations of antisymmetric angle-ply (Ungbhakorn and Singhatanadgid, 2003a), symmetric cross-ply (Ungbhakorn and Singhatanadgid, 2003b), and antisymmetric cross-ply (Ungbhakorn and Wattanasakulpong, 2007) laminated circular cylindrical shells. They show how neglecting the bending-extension coupling effects leads to small errors, typically smaller than 1%, while neglecting the extensional and flexural effects leads to higher errors, from 33% for the buckling load up to 100% and 200% for the natural frequencies.

These works allow to infer some information that confirm the results already obtained by scaling laminated plates. Firstly, the distortions in stacking sequence are the only one allowed; then, it is not necessary to fulfill the conditions associated to the coupled extensional-bending stiffness, but it is important to fulfill those related to the flexural stiffness. Therefore, the response of the system is sensitive to the number of plies, i.e., thickness. Finally, the varying sensitivity with, for instance, length in different systems proves that it is not easy to deduce a general behavior.

Yu and Li (Yu and Li, 2016) investigate prestressed, stiffened cylindrical panels and shells using an approach similar to the EM (Kasivitamnuay and Singhatanadgid, 2005). Specifically, the authors relate the total energy of prototype and model by

means of a functional relationship between transformation parameters. Complete similitude leads to perfectly predicted buckling loads, unaffected by changes in aspect ratio and curvature; as long as the wavenumbers are retained, natural frequencies and mode shapes are well reconstructed, too. Changing the stiffener material leads to design equivalent stiffeners that support a very good prediction of both buckling load and natural frequencies, with errors smaller than 3%. Also changes in material are acceptable, as long as Poisson's ratio does not vary excessively: if the model deviates too much from the prototype, the discrepancies become significant.

A cylinder filled with air is investigated by means of SAMSARA by De Rosa et al. (De Rosa et al., 2012). According to the scaling laws, variations of thickness and area of the cylinder lead to a modification of both structural and acoustic natural frequencies distributions. Therefore, for this type of acoustic-elastic systems, the structural and acoustic poles scale with different laws. Furthermore, if a complete similitude is desired, damping must be kept, too, as its change would allow a good reconstruction of the mean response only. The similitude conditions are violated on purpose by De Rosa et al. (De Rosa, Franco, and Polito, 2012) so that avatars of thin aluminium cylindrical shells can be investigated. According to the scaling laws, length, radius, and thickness should vary in the same way. In this article, instead, length and radius vary according to scaling laws different from that of the thickness. As a matter of fact, this choice seems to affect only the first axial-radial modes. However, the distortions alter not only the natural frequencies but also their distribution, so a partial reconstruction of the response is feasible only in particular frequency ranges. As also proved in a successive work (De Rosa and Franco, 2015), the smaller the distortion, the higher the prediction accuracy.

When investigating orthogonally stiffened cylinders (De Rosa and Franco, 2015), the smeared stiffness approach can be adopted, so that the rigidity properties of the stiffeners are spread along an equivalent, continuous cylinder having the same geometrical properties as the prototype. Since the stiffeners decrease the modal density, there is an improvement in the agreement between prototype and avatar [for the same reason previously illustrated (Meruane, De Rosa, and Franco, 2015)]. Some analyses are made by changing the number and area of the stiffeners, too, which leads to good local results when the MOF is low, and good results only in the average sense when the MOF is high.

Longitudinally and orthogonally stiffened cylinders are numerically analyzed with the aid of SAMSARA by Petrone et al. (Petrone et al., 2017). The results for replicas and avatars are coherent with previous works (De Rosa et al., 2012; De Rosa, Franco, and Polito, 2012; De Rosa and Franco, 2015). However, the novelty of the work relies on the use of several scaling laws to describe the behavior of avatars. Thus, two different frequency scaling laws are derived *a posteriori* and are used to define the frequency ranges of validity of the laws. The results do exhibit an error lower than the case in which just one scaling law is used. The identification of a confidence band shows that the low frequency range dictates the confidence interval, because the greater errors (maximum 35%) are placed in the low frequency range. Thus, it is hard

to reconstruct the local response.

Also Torkamani et al. (Torkamani, Jafari, and Navazi, 2008; Torkamani et al., 2009) study orthogonally stiffened cylinders, applying STAGE to the non-dimensional solutions of governing equations. Also in this case, the stiffened structure is substituted by a smeared one and, therefore, until the wavelength is greater than the spacing between stiffeners, accurate predictions can be obtained.

Scaling of stiffened cylinders is not a trivial matter because manufacturing constraints may limit the production of stiffening elements or shell thicknesses that fulfill the scaling conditions, thus Torkamani et al. suggest some approaches to bypass the problem. Equivalent stiffeners can be designed so that the same mode shapes are kept. Only the cross section is changed; shell material and geometry, stiffener material and distribution, boundary conditions and loading are kept. The conditions show that the equivalent stiffener is obtained by conserving the cross-sectional area, the moment of inertia, the polar moment of inertia, and the eccentricity. The most simple equivalent stiffener has a T-shaped cross section.

Instead, to circumvent the thickness limitations, both shell and stiffeners can be designed with different materials having better formability. The thickness of the stiffeners can be changed keeping, at the same time, the shape of the cross section. Another approach for scaling thickness is based on the modification of the number of stiffeners. However, lowering too much such a number leads to inaccurate predictions, because the smearing theory is used.

The numerical predictions are validated by experimental tests, in which the prototype is made of aluminium and presents Z-shaped ribs and Ω-shaped stringers; a one-third model is made of steel alloy and has equivalent T-shaped ribs and stringers. All the cylinders are free on both edges. The predictions are very good: the response peaks coincide although some small errors, which can be attributed to the non-linearities of the model.

Impact response

Until now, cylinders made of isotropic or composite materials have been reviewed. The analysis of Sato (Sato, Vecchio, and Andre, 1989), instead, involves concrete cylinders, providing, therefore, an interesting insight into the scaling behavior of material not commonly tested. Particularly, the authors perform experimental tests on four thick-walled concrete cylinders with circumferential and tie reinforcements made of steel. The objective is to investigate the damage modes and extent generated by impacts on three scaled-down models. These are expected to be the same for the prototype and models. Indeed, the damage modes are similar, as the models exhibit the formation of a shear plug at the impact point, crushing of the concrete of the inner surface, flexural cracking of the outer surface, and cracking of both surfaces. Conversely, the damage extent differs between the models and the prototype. The main results can be summarized as follows:

1. The end cover spalling decreases as the model size decreases. The source of this phenomenon finds difficulties in modeling the micro-aspects of concrete that governs fracture toughness; very high strain-rate sensitivity is observed in the smaller models resulting in high tensile strength and lower-than-expected deceleration forces in smaller models.

2. Smaller models exhibit a reduced extent of concrete crushing damage, because strain rate increases the concrete compressive strength and, maybe, also enhances the properties of the steel reinforcements.

3. Deceleration peak and strain-rate are consistent with the scaling laws.

4. The increase of compressive strength in models leads to underpredicted footprint widths; cracks are sometimes overpredicted, sometimes underpredicted. However, the predictions are good, even though these slight differences.

5. Outside cracking spacing is overpredicted, while the inside spacing is underpredicted.

In conclusion, the models are more severely cracked. The results exhibit different behaviors: crack data, generally, agrees with the scaling laws but is susceptible to impact randomness of concrete scaling. Because of such randomness, the study of scaled models should involve more specimens so that a good statistical response can be obtained.

Jiang et al. (Jiang, Wang, and Zhang, 2006) investigate size effects in cylinders, too, by performing experimental quasi-static compression and impact tests on thin walled mild steel circular tubes that are geometrically scaled, but without scaling impact velocities and mass. Strain rate affects both quasi-static and impact tests and its influence is stronger in the smaller models. Other experimental tests were conducted by Tarfaoui et al. (Tarfaoui et al., 2007), focusing on low velocity impact to simulate the dynamics of underwater impacts. In this case, the observed damage consists in local crushing of the resin at the point of contact with the projectile, without fiber failure. The scaling laws are obtained with DA and can predict the dynamic response, although underestimate the error. Larger tubes are more damaged.

2.3.4 Summary of similitude theory applications

The reviewed articles demonstrate the wide applicability of similitude methods, in terms of engineering fields, loading conditions, and materials.

DA has proven to be the best method when it comes to deal with impact problems. As a matter of fact, geometrical scaling allows good predictions of the prototype behavior until the plastic threshold, and even beyond if the damages are not too accentuated and the material has a limited rate-sensitivity. However, the scaling procedure fails when failure occurs and damages and rate-sensitivity are not negligible. In these cases, DA exhibits a strong versatility: switching from MLT to a VSG-based method

(Oshiro and Alves, 2004), as well as other applications (Christoforou and Yigit, 1998; Zhao, 1998), prove that, by means of a suitable choice of the dimensional parameters that constitute the dimensionless groups, some limits of geometrical scaling can be circumvented. However, these considerations again underline the need of an experienced analyzer (of the subject under examination). Knowing the underlying theory is also important for distinguishing inaccuracies due to the limits of such a theory from those of the adopted similitude method. A perfect example is provided by the works due to Rezaeepazhand and Yazdi (Rezaeepazhand and Yazdi, 2011) and Yazdi and Rezaeepazhand (Yazdi and Rezaeepazhand, 2011a), in which the discrepancies in the predictions of prototype behavior may come from the application of quasi-steady aerodynamic theory outside its validity boundaries.

Nonetheless, literature demonstrates that similitude methods do not allow one to bypass all of these limits at the same time. In fact, on the one hand, in the works by Neuberger et al. (Neuberger, Peles, and Rittel, 2007a; Neuberger, Peles, and Rittel, 2007b) plasticity scales accurately when not considering fracture; on the other hand, Noam et al. (Noam, Dolinski, and Rittel, 2014) are able to scale fracture in terms of failure criteria hat scale well only under the assumption of rate-insensitive material. Moreover, DA does not provide a unique set of Π-terms, which leads to interpretability problems, as highlighted by Pintado and Morton (Pintado and Morton, 1994). In conclusion, the versatility of DA is not always an advantage.

STAGE is less versatile than DA, but the scaling process has a more easily interpretable physical meaning because they derive from the governing equations. However, also STAGE has its inconveniences. First, prototype static and dynamic behavior may often be predicted by means of partial similitude in an acceptable way when an accurate set of governing equations is provided. However, since a certain scale factor may take different alternative forms, when partial similitudes are considered, it is a good practice to investigate all of them, because some may give good predictions, others may not. For instance, the laws obtained by Asl et al. (Asl et al., 2017a) for the transverse deflection of a beam have two forms, one of which underpredicts the prototype behavior, while the other overpredicts it. Generally, each equation has its own limited applicability range of values of the design parameters. This consideration highlights the importance of the determination of the applicable size interval (Luo et al., 2013; Luo et al., 2014c; Luo et al., 2016b).

Such a limited validity of the scaling laws is a point in common between STAGE and SAMSARA. While the conditions provided by STAGE are valid in intervals of the design parameters, those provided by SAMSARA are valid in frequency intervals. Indeed, it has also been demonstrated that different laws allow good estimation of the dynamic response in particular frequency ranges (Petrone et al., 2017).

However, whereas DA has proven to be versatile, STAGE has been shown to be prone to some interesting variations, such as the modular approach by Coutinho et al. (Coutinho, Baptista, and Rodrigues, 2018), the determination of size applicable intervals (Luo et al., 2013; Luo et al., 2014c; Luo et al., 2016b), and the support of SA (Luo et al., 2015; Luo et al., 2016b).

The methods until now recapitulated aim at reconstructing the response characteristics in order to save costs and time in the experimental procedures. ASMA introduces another point of view, which is computational time saving in numerical simulations in those frequency ranges that make FE analysis unusable. The method cannot substitute SEA, which has better prediction capabilities, but it is still useful in those cases in which analytical solutions are not available and FE models still represent the best tools. ASMA proves to be an efficient method to fulfill the meshing requirements in fluid-structure interaction problems thereby avoiding a prohibitive computational time (De Rosa and Franco, 2008b).

SA has demonstrated to be a method that can support already existing methods, such as STAGE (Luo et al., 2015; Luo et al., 2016b), or can work stand-alone, allowing the derivation of sensitivity-based scaling laws (Adams, Bös, and Melz, 2016; Adams et al., 2018). GSA is useful to obtain the effects of the parameters and their combinations on the structural response, even for complex systems. LSA represents a first order derivative, which means that the system is linearized in the vicinity of the current design point. Therefore, a certain accuracy is expected in a limited range, typically $\pm 5\%$. Conversely, similitude-based laws allow, instead, an application in a wider range; assuming a complete similitude, the range over which the field equations are valid.

Suitable sensitivity-based laws can always provide fitting predictions, but their origin is mathematical, thus they totally lose sight of the physical aspects of the problem. Nonetheless, the method is further step toward the automation of the scaling procedure. Comparing the similitude-based laws with those sensitivity-based, it is possible to conclude that each method has its own advantages and disadvantages so that they are balanced.

A common point of many similitude methods is the inability to predict size effects, that is, the change of strength properties of specimens when their size changes. Usually, the smaller the structure, the more resistant it is. However, this is not a general rule, as evidenced in some works (Sato, Vecchio, and Andre, 1989; Kellas and Morton, 1992b). Something similar happens in the frequency domain, as highlighted by Li (Li, 2010b) and Meruane et al (Meruane, De Rosa, and Franco, 2015). The size decrease of the model moves the modes to higher frequencies, so analyzing their structural response in the same frequency range of the prototype would lead to inaccurate predictions. Modal density is at the base: it must be retained as much as possible in order to reconstruct an acceptable response.

Size effects are not predictable by similitude methods, but they can be experimentally observed, even though the matter is not so simple, as an improper setup may pollute the results (Morton, 1988) to the point that it is not possible to distinguish if the error originates from an improper experimental procedure or a physical phenomenon not taken into account by the scaling laws (Xiaojian et al., 2016). Experimental tests are also useful to investigate the validity of theoretical assumptions, as Meruane et al. (Meruane, De Rosa, and Franco, 2015) do. In this work, as previously seen, the constant damping assumption among models is shown to not be exactly fulfilled.

Finally, all the similitude methods have dealt with partial similitudes. All the authors, in fact, unanimously agree that complete similitude at some point becomes unfeasible from the manufacturing point of view. As long as the distortion is limited, that is acceptable, or even mandatory, assumption in the manufacturing error framework, since the predictions have an acceptable accuracy. Nevertheless, the study of partial similitudes is still important.

2.4 Complex structures and other fields of application

Similitude theory has also dealt with complex structures, often made of several subcomponents, such as satellites, launch vehicles, spacecrafts, aircrafts, ships, and buildings. This section has, therefore, the main objective of demonstrating the actual usefulness of similitude theory by providing examples of industrial engineering in which the methods until now reviewed have been applied. The following fields are considered:

1. *Aerospace engineering*: investigations on static and dynamic behavior of structures such as spacecrafts, aircrafts, satellites, and other components. Beyond some typical applications of similitude theory, two branches stand out for their peculiar characteristics: aeroelastic and thermal similitudes.

2. *Civil engineering*: applications investigating the dynamic response of buildings and physical infrastructure, especially when subject to seismic phenomena.

3. *Impact engineering*: investigations of short-lasting events caused by collision between two bodies, characterized by rapid induced motion and deformation, release of high kinetic energy and, often, damage of the impacted structure.

4. *Rapid Prototyping*: applications to quick fabrication techniques supported by Computer Aided Design (CAD).

5. *Naval and marine engineering*: applications to study naval structures and marine installations.

A complete reference list of the works is given in Table A.3, while Fig. 2.3 illustrates the application of similitude methods over the years (on the horizontal axis) to complex structures in the listed engineering fields (on the vertical axis).

2.4.1 Aerospace engineering

Aerospace engineering has exploited similitude methods for a long time. In fact, from the early 1960s, NASA (National Aeronautics and Space Administration) Langley Research Center (LaRC) investigated the structural response of space vehicles such as landers, launchers, spacecrafts, and their subcomponents, which full-size dimensions were very large. Therefore, considering the limitations of ground facilities, many tests

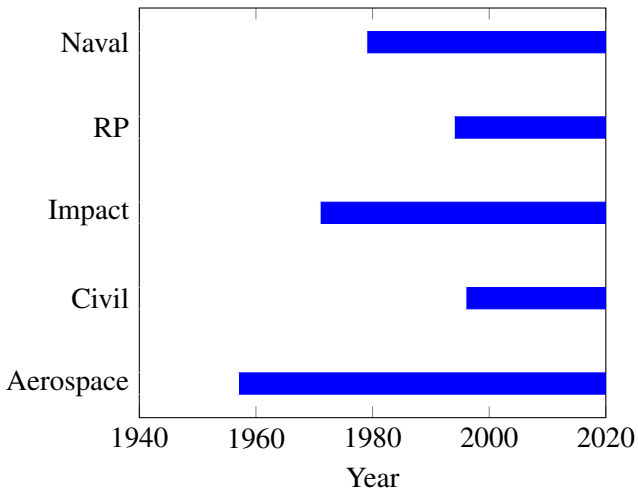

FIGURE 2.3: Time overview of engineering fields

were feasible only using scaled models. A comprehensive review about the relevant LaRC technical reports is provided by Horta and Kvaternik (Horta and Kvaternik, 2000).

These works are not based on a complete similitude theory and its limits, neither differences between prototype and model behavior are analyzed. Similitude methods are used as a tool to investigate - theoretically and experimentally - the static and dynamic behavior of structures, sloshing phenomena into fuel tanks, and to understand the most suitable analyses and the most convenient construction philosophies. Particularly, experimental tests are often used to validate new analytical models or structural simulation software [for example, the first versions of NASTRAN (NASA STRucture ANalysis) FE solver]. Different scale sizes are used, from 1/5 to 1/10 or more, sometimes applying hybrid scaling (in which, for instance, geometrical and dynamic parameters are scaled by different factors). However, all the models are perfect replicas, which means that all the structural elements are scaled down: hat-section stringers, corrugated intertank sections, joints, etc. In some cases, different gravity conditions are simulated and tested, requiring the purposeful creation of shock-chord suspension systems. All of this work has required a substantial improvement of fabrication procedures: machining and chemical milling tolerances, curvature forming techniques, aluminium forgings, machining of complex ring frames, etc.

Some reports are dedicated to early stage spacecraft and landers testing. As a matter of fact, before encountering the hazardous space environment, a spacecraft is indeed subjected to extreme vibrations during launch and the boost phases. It is not feasible to design a spacecraft so that its natural frequencies are such that the structure does not respond to the booster inputs. Considering also that instrumentation and payloads are damaged by vibration conditions less severe than those expected during the flight plan, it is necessary to investigate suitable procedures to reduce the severity

of many resonant conditions. Testing of different lander designs is also performed, considering multilegged designs with different suspension systems. These vehicles, in fact, must land on irregular surfaces of unknown topology and must not overturn after landing. These are some of the reasons that led NASA engineers to test spacecraft, such as the Nimbus (Carden and Herr, 1964), and landers, such as the lunar module (Herr and Wayne Leonard, 1967; Blanchard, 1968) or the Viking spacecraft lander (Stubbs, 1971; McGehee and Stubbs, 1973).

A fundamental requirement of launch vehicles is a high operational reliability due to high costs and payload preservation, thus a reliable structural design is necessary for the launch vehicle to survive the shock and vibration environment encountered during the transportation to the launch site, construction on the launch pad, launch, and flight itself. Particularly, there are several phenomena that must be taken into account during the launch and flight phases: for instance, the fuel consumption and the resulting change in weight condition and sloshing. All these environments contain many sources of transient and quasi-steady-state excitations that may produce undesirable vibration response levels in the vehicle structure. Therefore, it becomes important to study the feasibility of using replica models in order to obtain vibration data necessary for the design of complex launch vehicle structures, control systems, clustered tank configurations, etc. Many works were dedicated to test launch vehicles, including a generic launch vehicle (Wissmann, 1968); Saturn SA-1 (Mixson and Catherine, 1964a; Mixson and Catherine, 1964b; Catherine, 1965); Titan III in A (Thompson, Jr., 1967), B (Peele, Thompson, Jr., and Pusey, 1968), and C (Morosow and Jaszlics, 1966) configurations; and Apollo-Saturn V (Leadbetter, Wayne Leonard, and John Brock, Jr., 1967; Adelman and Steeves, 1968; Catherines, 1968; Steeves and Catherines, 1968; Pinson and Wayne Leonard, 1969; Leadbetter, 1970; Peele, Wayne Leonard, and Leadbetter, 1970).

Large structures like spacecrafts, space stations, and deployable systems (such as antennas and solar sails) defy conventional testing because of their size and flexibility. Furthermore, the static preloads and deflections due to gravity are greater than those developed in orbit. Scaled models were used also to bypass these problems, for example, when testing Space Shuttle subcomponents (Thornton, 1971; Bernstein et al., 1974a; Bernstein et al., 1974b; Levy et al., 1974; Mason et al., 1974a; Mason et al., 1974b; Pinson, 1975; Zalesak, 1975; Leadbetter et al., 1976; Blanchard, Miserentino, and Leadbetter, 1977). Actually, NASA established a dedicated program, the dynamic scale model technology project, aimed at the development of model technology for space structures too large to be tested on ground in full-scale. The Space Station Freedom (Keith Belvin and Edighoffer, 1986b; Gronet et al., 1987; Shih, Chen, and Garba, 1987; McGowan, Edighoffer, and Wallace, 1990; McGowan, Jaeed, and Edighoffer, 1991; Davis et al., 1994), large antennas (Keith Belvin and Edighoffer, 1986a; Schroeder et al., 1989), and Pathfinder (Letchworth, McGowan, and Gronet, 1988) are the structures tested under this program.

Another NASA program, the in-space propulsion project, has consisted in tests on models of solar sails. These are thrust devices consisting of a membrane-based

structure, lightweight and large, made of gossamer, which convert solar pressure into thrust of a spacecraft. On the one hand, such solar sails can potentially provide low-cost propulsion and operate without the use of propellant allowing access to non-Keplerian orbits through a constant thrust; on the other hand, solar pressure is small, so the sails must have a significant size and, at the same time, a small enough system mass to achieve reasonable accelerations: to give an example, these sails can reach dimensions ranging from 200 to 10^4 m^2. It is, therefore, expected that ground demonstrations must be conducted at significantly smaller sizes. Thus, the limitations of ground facilities and costs force the use of scaled models in order to test numerically and experimentally (Canfield et al., 2004; Canfield, Peddieson, and Garbe, 2010; Murphy, Macy, and Gaspar, 2004; Gaspar et al., 2005; Gaspar et al., 2006) solar sails coupled with booms.

Solar sail-boom systems are an example of deployable structures, i.e., structures folded into several tight bundles for stowage that are propelled in specific directions in space at the beginning of the deployment phase. Also in this case, testing difficulties and costs require the use of scaled models. However, because of manufacturing limits (e.g., thickness control and accuracy), standard geometrical scaling cannot be used. Instead, Greschik et al. (Greschik, Mikulas, and Freeland, 1999) propose a constant thickness scaling, which entails the uniform scaling of the global dimensions while keeping the thickness constant. This work is then continued by Holland et al. (Holland et al., 2002), who explore the computational and experimental issues (FE model complexity, accuracy, and differences between analytical and experimental results) arising in the modeling and testing of scale models of inflatable structures.

Jackson and Fasanella (Jackson and Fasanella, 1999; Jackson and Fasanella, 2003) investigate fuselages crashworthiness, subjecting a 1/5-scale model to drop tower tests. The results highlight some events characteristic of size effects. In fact, both prototype and model subfloor sections exhibit the same damage modes, but the amount of relative damage and accelerations are greater in the prototype.

All these works prove that scaled models are useful to overcome experimental problems due to size, facility limits, and costs. Selecting with care the scale factors and the methods of manufacture, with a judicious evaluation of deviations from direct scaling duplications, replica models turn out to be technically and economically feasible to study complex structures.

Aeroelastic similitude

Aeroelastic testing aims at verifying the numerically predicted aeroelastic characteristics of an entire vehicle or a part of it. Generally, the scaled model must represent exactly the prototype dynamics matching, basically, mass and stiffness distributions (Molyneux, 1964; Hunt, 1973; French, 1990; Bisplinghoff, Ashley, and Halfman, 1996; French and Eastep, 1996). Examples of structures that need aeroelastic validation, in terms of flutter clearance, gust response, and so on, are flexible wing rotors, high and low aspect ratio wings, and new design aircrafts.

Typically, DA is the base of any similitude approach used in aeroelastic analysis; in fact, aeroelastic similitude is achieved matching the nondimensional parameters governing aerodynamics, the structural response, and their coupling. According to Bisplinghoff et al. (Bisplinghoff, Ashley, and Halfman, 1996), these nondimensional parameters are scale factors relating the static deflections and the modal behavior of the model with those of the prototype. Typically, the length scale - as the ratio of the allowable model span in the wind tunnel to the real wing span - is dictated by the facility dimensions (Pereira et al., 2007).

Molyneux (Molyneux, 1964) reports more details on the constraints of aeroelastic scaling. Particularly, two types of establishable similitudes are identified:

1. *Aerodynamic similitude*: Mach and Reynolds numbers must be kept and the bodies must be geometrically similar at the surface, that is, same shape, same incidences to the flow, and same static elastic deformations.

2. *Structural similitude*: by analyzing the force-deflection, vibration, and equilibrium equations, the following quantities must be maintained: ratio between stiffness and aerodynamic forces, stiffness distribution, reduced frequency, mass ratio, and Froude number.

The above constraints lead inevitably to many conditions to fulfill. However, in some cases, such as studies of elastic aeroelasticity (Heeg, Spain, and Rivera, 2004), some terms can be neglected because they are relevant only for dynamic phenomena (such as mass ratio). In other cases, like the study made by Hunt (Hunt, 1973) on flexible wing rotors when thermal effects are neglected, some compromises must be accepted: in the particular case of his work, Hunt states that the requirements on Mach and Frounde numbers cannot be fulfilled at the same time. Therefore, the scaling procedure can be applied only if one of these two conditions is relaxed.

A particular attention must be dedicated to the flow conditions (subsonic, transonic, etc.) when similitude is used.

If the full-scale flow is not wholly subsonic, the full-scale Mach number is retained, leading to a structural model with same mass density and same modulus of elasticity. On the other hand, the Froude number is retained when the dynamic phenomenon is characterized by a significant weight dependence or when high-speed flight is performed in low-speed facilities. In this case, the mass density is kept the same while the modulus of elasticity is lower, so that an arbitrary structure or a replica can be used.

It is clear that the structural aspect is mainly governed by material properties such as mass density and modulus of elasticity. Considering also the aerodynamic requirements, an alternative manner to define the conditions for aeroelastic scaling is to keep mass and stiffness distributions and, at the same time, the aerodynamic envelope unchanged (Bisplinghoff, Ashley, and Halfman, 1996; French, 1990). Consequently, the model must not necessarily resemble the internal structure of the full-scale prototype, allowing one to fabricate simpler structures, with noticeable money saving. In the

same investigation, Reynolds number conservation cannot be achieved at all, which means that the model cannot be tested at full-scale Reynolds number. Nonetheless, this number must be high enough to ensure the right type of viscous effects. Hunt (Hunt, 1973) makes an important remark on the experimental aspects: the dimensional tolerances are scaled with the same scale of linear dimensions, thus the quality of manufacture of the model is fundamental, as spurious dynamic effects may arise due to errors in manufacturing.

Many works in aeroelastic field are based on the coupling between scaling procedures and optimization techniques (French, 1990; French and Eastep, 1996; Richards et al., 2009; Ricciardi et al., 2012b; Ricciardi et al., 2014; Spada et al., 2017). In fact, keeping in mind the requirements for aeroelastic scaling, the error function to minimize may address the mass distribution, while the design requirements of the model (limits on deflections under static loading, natural frequencies, flutter speed, etc.) may be used as constraints.

French is the first who uses optimization procedures (French, 1990), aimed at designing a scaled model of a low aspect ratio wing made of anisotropic material. The typical assumptions made in aeroelasticity field, such as chordwise rigid wing and consequent beam-like response, are not applicable because they apply only for high aspect ratio wings made of metal. Therefore, in order to bypass this problem, French proposes an approach based on optimization techniques. Successively, French and Eastep (French and Eastep, 1996) break the optimization process into two steps: sizing the structural stiffness, first, and then sizing the mass distribution. This approach leads to good results; furthermore, it is suitable for every structure that can be discretized with an FE approach, and saves a lot of time otherwise required for the correct sizing of the model. Moreover, it provides an interesting perspective on automatic procedures when only structural influence coefficients are known.

Richards et al. (Richards et al., 2009) propose a variation of French's method (French, 1990; French and Eastep, 1996). The authors propose two scaling methodologies: one matches directly the modal response by updating mass and stiffness distributions simultaneously in a single optimization routine; the second updates mass and stiffness in two separate optimization loops. Actually, both the methods converge to an acceptable result; however, the single loop approach performs poorly when a gradient-based technique is used. In the authors' opinion, it would be much more effective if another search method, like genetic algorithms, is used. Conversely, the two-loops method proves to be computationally more efficient and more robust. However, the drawback of this technique is the requirement of additional information, namely displacement sets under given loads.

The method proposed by Richards et al. (Richards et al., 2009) is expanded by Ricciardi et al. (Ricciardi et al., 2012b), who include the match with nonlinear static deflections in the stiffness optimization loop. The implementation is successful and leads to a good evaluation of aeroelastic frequency, damping, and nonlinear static responses; however, the mass and stiffness decoupling introduces some issues. The procedure is further expanded (Ricciardi et al., 2014) by simultaneously designing

the vehicle elastic stiffness, geometric stiffness, and nonstructural mass. The work is based on the results obtained by Ricciardi et al. (Ricciardi et al., 2012b) and in a successive work (Ricciardi et al., 2012a) in which the authors develop an aeroelastic interface that loosely couples a custom vortex-lattice code with MSC-NASTRAN. Successively, Spada et al. (Spada et al., 2017) propose a nonlinear scaling methodology similar to the one due to Ricciardi et al. (Ricciardi et al., 2014), with the main difference that the scaling of stiffness and mass is performed in two different optimization loops.

Another set of works focuses on aeroservoelastic applications (Friedmann, Guillot, and Presente, 1997; Presente and Friedmann, 1998a; Presente and Friedmann, 1998b; Friedmann, 1999; Pototzky, 2002; Friedmann, 2004), mainly demonstrating that the typical aeroelastic scaling relations, developed for flutter, need to be extended when dealing with moder aeroelasticity, that is, when active control of aeroelastic stability, response problems, and extensive use of computer simulations (Baker, Westine, and Dodge, 1991) are introduced. For example, Friedmann and coworkers (Friedmann, Guillot, and Presente, 1997; Presente and Friedmann, 1998a; Presente and Friedmann, 1998b; Friedmann, 1999; Friedmann, 2004) aim to obtain scaling laws for aeroservoelastic problems emphasizing scaling requirements for actuator forces, hinge moments, and actuation power. These objectives are pursued under different flow conditions and for different control devices: subsonic flow (Friedmann, Guillot, and Presente, 1997; Presente and Friedmann, 1998a), compressible flow (Presente and Friedmann, 1998b), trailing edge flap (Friedmann, Guillot, and Presente, 1997; Presente and Friedmann, 1998a), and piezoelectric induced actuation (Presente and Friedmann, 1998b). Particularly, Friedmann (Friedmann, 2004), Presente and Friedmann (Presente and Friedmann, 1998b), and Friedmann (Friedmann, 1999) introduce a two-pronged approach that perfectly fits in the framework of modern aeroelasticity, as the classical approach is supported by parallel computer simulations playing the role of numerically derived "similarity solutions". These solutions are applied where innovative scaling laws are required (e.g., control power, control surfaces, and shock wave motion in transonic flows), so that on expanded or refined set of scaling laws is obtained.

Thermal similitude

Coutinho et al. (Coutinho, Baptista, and Rodrigues, 2016) refer to thermal similitude as an independent or complementary branch of structural similitude. For example, it has been used extensively in space structures modeling, as it is important to obtain experimental validations of the mathematical methods used for predicting the thermal performances of aircrafts and spacecrafts. As a matter of fact, aircrafts must be capable of withstanding the adverse effects of aerodynamic heating (high temperatures and rates of change) during their mission, while spacecrafts must keep temperature values in fairly narrow limits because of complex electronic equipment and instrumentation. This is not a trivial matter because the space environment is hazardous, exhibiting

high temperatures and significant gradients (for example, when space vehicles pass from sunlight to shadows and vice versa). Thermal control is acquired through proper design of the conductive and radiative heat-transfer paths between components in the vehicle, in conjunction with the control of the exterior radiative exchange of the vehicle with its environment. The thermal scaling can be easily derived by applying DA (which can be seen as an additional demonstration of the versatility of this method).

The environmental simulations are typically carried out in suitable structures, the "space chambers". Again, small models are required for the experimental tests as small test chambers appear to offer better environmental control and reliability. Thus, on the one hand, structural scaling must be executed; on the other hand, because of the characteristic problem under investigation, thermal characteristics must be scaled, too. Dictating a similitude in thermal terms means to have similar temperatures, temperature distribution, heat content, and heat flow.

The work of Vickers (Vickers, 1965) is of relevant importance as identifies two possible procedures to perform thermal scaling: temperature preservation and material preservation. While the former considers prototype and model with the same absolute temperature, the latter considers prototype and model made of the same materials. Another significant work is due to Watkins (Watkins, 1966), which derives and provides all possible sets of independent similitude ratios for thermal modeling in a simulated space environment. These ratios are defined by a computer program which applies DA on the physical quantities of interest (e.g., energy transfer from and to a single, elemental, and isothermal volume), using a matrix formulation of Buckingham's Π Theorem.

According to O'Sullivan (O'Sullivan, 1957), in an analysis of aerodynamic heating of aircraft, thermal similitude in terms of heat flow can be ensured if geometrical similitude is coupled with material preservation. Keeping the temperature, instead, thermal stresses and deformations are similar. Katzoff (Katzoff, 1963) demonstrates that all conditions for thermal similitudes cannot be satisfied simultaneously because of their complexity. An example is provided by thermal conductivity and heat capacity scaling. Rolling (Rolling, 1966) highlights that the temperature preservation method is a better choice because it allows material change, which makes possible the choice of a material suitable to comply with the similitude conditions. Moreover, Gabron (Gabron, 1966) states that temperature preservation requires the conservation of thermal paths. This requirements can be satisfied by effectively using material and geometric distortions (of the minor dimensions as the thickness of plates, shells, etc.). Maples and Scogin (Maples and Scogin, 1970) focus on thermal conduction and radiation under transient conditions and prove that thermal similitude can be applied to transient systems with internal generation. Shannon (Shannon, 1972) takes into account, in addition to radiation and conduction, also convection, demonstrating that it can be considered with both the preservation methods achieving adequate thermal similitudes.

However, the difficulties during thermal scaling are also an important point underlined by these works. The constraints on temperature or material introduce limits

on the properties and the possible length ratios for models. More generally, the pure adherence to thermal modeling laws is often experimentally unfeasible, due to the limited choice of materials, fabrication difficulties, and high costs. Gabron (Gabron, 1966) provides a clarifying example, concerning a 1/5-scale model of a Voyager-type spacecraft that is impractical to build due to the difficulties in fabricating small elements. Therefore, as shown in the same article, some spacecraft appendages are scaled-up. However, the results in terms of measured temperature are not very accurate.

2.4.2 Civil engineering

Even investigations on seismic response and performances of civil structures are affected by limitations in testing equipment. Usami and Kumar (Usami and Kumar, 1996) and Kumar (Kumar et al., 1997) discuss the aspects to consider in selecting a suitable set of scaling factors, procedure often complicated by the great number of possible sets. The authors show that the whole procedure can be divided into two distinct types depending on whether the scale factor is chosen for mass or time.

Kim et al. (Kim, Kwak, and Chang, 2004) give a relevant contribution to the topic. Deriving the scaling laws in the elastic range leads inevitably to discrepancies when studying the inelastic response of small scale models. The authors compare three scaling laws, based on mass, time, or acceleration, according to the importance of gravity, derived with DA. The authors conclude that, when using the same scale factors for length and force, the comparisons of pseudodynamic tests with the three similitude laws lead to inelastic responses which are practically coincident. Pseudodynamic tests on steel columns prove that these laws work well also in the inelastic domain. Moreover, they propose a modified similitude law which considers both a scale factor for length and a stiffness ratio, which is demonstrated to effectively simulate the seismic response of prototype structures.

Inelastic range makes similitude requirements based on geometry not suitable. Therefore, Kim et al. (Kim, Lee, and Chang, 2009), in order to overcome some problems related to the reduction of the scale factors, propose models with dissimilar materials to those of the prototype. This is why the authors modify the acceleration-based law, introduced in the previous work (Kim, Kwak, and Chang, 2004), into an equivalent multiphase similitude law which takes into account the material non-linearities. The equivalent modulus ratio and the peak strain ratio are the key parameters of the model. The derived law is implemented in a numerical algorithm reproducing a pseudodynamic test; the results prove that such a modified law is applicable to the seismic simulation tests. The investigation is completed with experimental tests of a 1/5 scale reinforced concrete model and its prototype. Results prove that a variable modulus ratio produces similar responses, while a constant one produces large errors because the strain level of the small scale model is not considered.

2.4.3 Impact engineering

An important contribution to the application of similitude in the field of impact engineering is provided by Atkins (Atkins, 1988). Focusing on non-scaling phenomena occurring in scaled problems of mechanical impact and fracture, the author develops an energy analysis according to which, when the problem presents a mixture of surface and volume effects, a perfect replica scaling is unfeasible. Unfortunately, such a mixture is present in the majority of problems.

By rigorously analyzing the governing equations and a detailed comparison between theory and test results, Atkins defines a non-dimensional parameter as the ratio between the energy involved in volume deformation and the energy involved into forming the crack surfaces. It is, therefore, a function of both material properties and the absolute size of the prototype. The scaling laws derived consider both the classical scale factors and the dimensionless parameter and explain why geometric scaling of energy fails in problems of combined flow and fracture.

Me-Bar (Me-Bar, 1997) follows the trail of Atkins (Atkins, 1988), dividing the impactor energy, lost during the penetration into two contributions: energy expended in surface and volume effects, respectively. The normalized impact energy involved in volume effects is the same in all scales, while the fraction of normalized energy involved in surface effects increases when the scale factors decrease. Therefore, a small structure absorbs more energy, a clear size effect. In this way, the method explains why scaling does not hold in ballistic configurations without knowledge of the constitutive relations of the several materials involved. Actually, for simple configurations and when just one material is present, non-scaling due to strain-rate effects can be considered. Instead, the method proposed by Atkins (Atkins, 1988) allows to evaluate the energy transfer interaction for a given material at any given scale, only if its constitutive relations and fracture.

Other theoretical studies involving, more generally, scaling of material failure are provided for linear elastic range (Atkins and Caddell, 1974; Mai and Atkins, 1978), plastic fracture (Atkins, 1988), nonlinear elastic range (Mai and Atkins, 1975), elasto-plastic materials (Atkins, Chen, and Cotterell, 1998; Atkins, 1999), and epoxy and polyether ether ketone composites (Kellas and Morton, 1992a). Bažant et al. provide an extensive treatise of failure scaling (Bažant, 1985; Bažant and Pfeiffer, 1988; Bažant and Kazemi, 1990; Bažant, Xi, and Reid, 1991a; Bažant, Xi, and Reid, 1991b; Bažant, 1993a; Bažant, 1993b), while the failure of quasi-brittle materials is experimentally investigated by van Vliet and van Mier (van Vliet and van Mier, 2000).

Westine and Mullin (Westine and Mullin, 1987) investigate experimentally hypervelocity impacts into semi-infinite, shielded targets. In this case, beyond the typical phenomena expected when impacts are involved, such as plastic flow, fragmentation, and spalling, other mechanical and thermal phenomena must also be taken into account (for example, melting and vaporization). The authors derive scaling laws suitable for both semi-infinite and complex, finite-size targets. Hypervelocity impacts are found to scale well for both replica and dissimilar materials models.

Other works go beyond the pure theoretical investigations, in which impact analysis is applied to tests on scaled models of casks, for shipping radioactive waste (Acquaro et al., 2010) or spent fuel elements (Quercetti, Müller, and Schubert, 2008). Also automotive fields finds useful help in scaled models (Holmes and Sliter, 1974; Lowe, Al-Hassani, and Johnson, 1974; Emori, 1973; Brownfield and Rogers, 1978). In fact, the response of an automobile in high speed crashes is complex: the intricate structure of an automobile undergoes large deformations, buckling, fracture, tearing, and joints deformation. The response also depends on other elements, such as impact velocity, angle of incidence, and the type of obstacle impacted by the car. Crashworthiness phenomena have analytical solutions developed only for simple cases and depend on empirically derived data, relying, therefore, strongly on experiments. Scaled-down models allow one to perform an acceptable number of experiments reducing the financial and temporal costs.

2.4.4 Naval and marine engineering

Similitude methods in naval and marine engineering are addressed toward two main applications: ocean structures, that can be studied in model basins, as well as the behavior of ships, typically during collisions.

An interesting perspective on several problems with scaling in marine environment is given by Kure (Kure, 1981). For instance, habitability is not a factor of secondary importance when dealing with offshore structures, which are subjected to loads easy to model as long as still water is considered. However, complex phenomena, such as wave loads and drifting forces, may also need to be considered. Moreover, oceanic environment is characterized by other types of phenomena: wind, waves, currents, and, in come particular applications, ice flows, continuous winter sea ice, and icebergs.

Concerning ships behavior, an interesting review by Calle and Alves (Calle and Alves, 2011) focuses on collision scenarios. As a matter of fact, ship collisions and grounding represent the majority of ship accidents and are cause, mainly, by human errors, ship failure, and harsh environment. Considering that, when the review was written, the global fleet had increased significantly in the number of ships, the risk of a collision had increased in parallel. Moreover, ship collisions lead to many serious damages, e.g., the degradation of marine environment (about 48% of the world fleet consists in tankers, therefore the risk of oil leakage is high), explosions, human losses, blocking of ship traffic, and permanent damage to ships. Thus, ship collisions are a serious and sensitive topic which collides with the enormous difficulty in setting up experimental collisions testing of prototypes, due to their too large sizes.

Nonetheless, there are many works on experimental testing of colliding ships (Blok and Dekker, 1979; Hagiwara, Takanabe, and Kawano, 1983; Ohtsubo, Kawamoto, and Kuroiwa, 1994; Lehmann and Peschmann, 2002; Tabri, Määttänen, and Ranta, 2008; Calle, Oshiro, and Alves, 2017; Oshiro et al., 2017; Aguiar et al., 2012) and, in all of them, the ships are scaled down, sometimes significantly [1/45 (Blok and

Dekker, 1979), 1/35 (Tabri, Määttänen, and Ranta, 2008), and 1/100 (Oshiro et al., 2017) scaled models]. What really jumps out from these works is the difficulty in realizing the experimental tests. For example, Hagiwara et al. (Hagiwara, Takanabe, and Kawano, 1983), aiming at estimating the energy involved in low energy collisions, simplify the model manufacturing by omitting some structural members, which invalidates the experimental results. Moreover, non-similarities in material failure appear. These manufacturing difficulties are remarked upon also by Ohtsubo et al. (Ohtsubo, Kawamoto, and Kuroiwa, 1994) and Calle et al. (Calle, Oshiro, and Alves, 2017). To give an example, interior welding is limited by restricted accesses. Fabrication of all the components would lead to a great complexity, disproportionate costs, and long times for assembly. Simplified geometries become, perforce, a necessity: only the main plates and stiffeners ae typically considered.

Finally, the solutions adopted by Lehmann and Peschmann (Lehmann and Peschmann, 2002) and Tabri et al. (Tabri, Määttänen, and Ranta, 2008) are quite interesting, since they use a rigid, bulbous bow as striker, instead of making a second, scaled-down ship model.

2.4.5 Rapid prototyping

According to Cho and Wood (Cho and Wood, 1997), between the 1980s and 1990s, various RP techniques emerged and advanced, as a consequence of the dramatic reduction of fabrication cost and time that this group of industrial techniques provides, so that at least twenty companies already commercialized diverse RP systems. Cho et al. (Cho, Wood, and Crawford, 1998b) highlight that, in the late 1990s, there was only limited literature about similitude methods applied to RP, most based on DA (Dornfeld, 1994; Mahn and Bayly, 1999; Steinchen, Kramer, and Kupfer, 2008), that just examine experimentally the test results (Dornfeld, 1994; Steinchen, Kramer, and Kupfer, 2008) and perform predictions of aluminium prototypes by means of impacted StereoLithography (SL) models (Mahn and Bayly, 1999).

However, Coutinho et al. (Coutinho, Baptista, and Rodrigues, 2016) report other works concerning RP, many of them related to wind tunnel testing: Springer (Springer, 1998) obtaines models with Fused Deposition Method (FDM) using ABS plastic or polyether ether ketone, SL, selective laser sintering, and laminated object manufacturing; Nadooshan et al. (Nadooshan, Daneshmand, and Aghanajafi, 2007) employ FDM with polycarbonate; Chuk and Thomson (Chuk and Thomson, 1998) compare times and costs of ten RP techniques in making wind tunnel models. However, the authors agree on the fact that such technologies are applicable for models as long as the loads are kept sufficiently low, because those parts made of plastic materials or metal powders do not provide enough structural integrity for testing.

A preliminary design and manufacturing technique is introduced by Dang-guo et al. (Dang-guo et al., 2011; Dang-guo et al., 2013), in order to improve the structural integrity of RP models and reduce the manufacturing period and cost. This technique is applied to hybrid high-speed wind-tunnel models with an internal frame and an

outer resin, fabricated, respectively, with a conventional method and SL. A similar method is already applied by Fujino et al. (Fujino, Oyama, and Omotani, 2003) to experimentally investigate the flutter characteristics of an over-the-wing engine mount configuration by using different scale models at different flow conditions.

Ziemian et al. (Ziemian, Ziemian, and Barker, 2010) present a different case of study. They investigate the correlation between the dynamic behavior of a full-scale steel prototype and a small-scale plastic model fabricated using FDM, in order to obtain baseline information on the dynamic response on the dynamic behavior on FDM plastic parts. The feasibility of the small-scale FDM models is assessed, by means of a shake-table test, comparing the experimental results with those of a full prototype study and with computational models.

Zhu et al. (Zhu et al., 2011) present a novel method to design and fabricate aeroelastic wing models for wind tunnel tests. It is based on SL and derives the model through a sequential design procedure of dimensional scaling, and stiffness and mass optimization. The test article used to test the approach is an aluminium wing box, scaled down to obtain the desired dynamic behavior data.

However, as reported by Coutinho et al. (Coutinho, Baptista, and Rodrigues, 2016), all these researches do not propose real innovations and do not try to bypass the characteristic problems of RP testing by changing approach. This path is taken by Cho and Wood (Cho and Wood, 1997), who propose the ESM and claiming that their approach is more suitable in solving distortion problems. Particularly, this work addresses the application of ESM to predict the deflection of an aluminium beam in two locations with a certain distance from the clamping point, then the investigation of a thermostructural problem in which some of the dimensionless parameters are not kept identical. ESM is then applied to an aluminium/nylon rod and to study the temperature transition of an aluminium/nylon mold (Cho, Wood, and Crawford, 1998b), and on a numerical slotted rod and a mold (Cho, Wood, and Crawford, 1998a); moreover, an error estimation of both DA and ESM results, with a numerical application to the study of thermal behavior of turbine blades, are performed (Cho, Wood, and Crawford, 1999). Then, three approaches to contruct the transformation matrix are extensively proposed (Dutson and Wood, 2002): a pseudo-inverse approach, diagonal matrix approach, and circulant matrix approach. Then, a numerical analysis of the deflection of a cantilever beam is exposed; the same application is repeated after introducing and advanced ESM, proposed to bypass the problems of specimen distortions. This novel method is applied also to the control of steady-state temperature of central processing unit surfaces. The advanced ESM is further applied to investigate the deflection of a cantilever beam with five holes subjected to a concentrated load at the tip (Dutson et al., 2003). Successively, a lumped ESM is introduced to link distorted systems made of more than one part (Cho et al., 2005); a numerical study is then performed of an archery bow, while an experimental investigation on a heat sink (to control the steady-state temperature of a central processing unit).

Chapter 3

Theoretical framework

The theoretical tools used in this thesis are introduced in this chapter. First, SAMSARA method is applied to the derivation of the similitude conditions and scaling laws related to the dynamic characteristics of the systems considered, namely natural frequencies, velocity response, and radiated acoustic power. Then, the main concepts behind machine learning, Artificial Neural Networks (ANN) and Principal Component Analysis (PCA) are provided. Finally, the main steps of the SOBI algorithm are briefly listed.

3.1 The similitude method: SAMSARA

In this section, SAMSARA method is applied in order to obtain the similitude conditions of the dynamic characteristics of 1D and 2D structures, namely beams and plates. In particular, plates are investigated in both the classic, thin configuration and sandwich one. The dynamic characteristics addressed by the application of SAMSARA are the natural frequencies, the velocity response, and the radiated acoustic power.

It is recalled that the scale factor of the generic parameter g are herein defined as Eq. 2.3, that is,

$$\lambda_g = \frac{\widehat{g}}{g},$$

where the hat symbol $\widehat{\ }$ describes the parameter of the model.

3.1.1 Similitude conditions and scaling laws of the natural frequencies

Scaling natural frequencies is the first step to take when similitude theory is applied to the analysis of the dynamic behavior of systems. In fact, knowing how natural frequencies change is fundamental for the reconstruction of the dynamic response, as well as the distortions in models may be already conveyed through such scaling.

The structures investigated in this thesis are beams, isotropic plates, and sandwich plates in similitude. Up to now, SAMSARA has not yet been applied to beams, that, even though they may be considered as "simple" structures, are an interesting starting

point because they are structural operators which do not generate distorted models. Conversely, plates may lead to models in partial similitude. This time, the mode shape is described by a couple of integer numbers which combination, and its succession, may change with the model.

The beams under analysis are simply supported, while the isotropic plates are studied with Clamped-Free-Clamped-Free (CFCF) boundary conditions [as the simply supported (De Rosa, Franco, and Meruane, 2015) and cantilever (Meruane, De Rosa, and Franco, 2015) configurations have already been investigated]. Finally, the sandwich plates are simply supported, too.

Table 3.1 summarizes all the scale factors introduced in this section.

Parameter	**Scale factor**
Beam length	$\lambda_L = \frac{\widehat{L}}{L}$
Bending stiffness	$\lambda_D = \frac{\widehat{D}}{D}$
Damping	$\lambda_\eta = \frac{\widehat{\eta}}{\eta}$
Elastic modulus	$\lambda_E = \frac{\widehat{E}}{E}$
Force	$\lambda_F = \frac{\widehat{F}}{F}$
Angular frequency	$\lambda_\omega = \frac{\widehat{\omega}}{\omega}$
Mass	$\lambda_M = \frac{\widehat{M}}{M}$
Mass density	$\lambda_\rho = \frac{\widehat{\rho}}{\rho}$
Panel length	$\lambda_a = \frac{\widehat{a}}{a}$
Panel thickness	$\lambda_h = \frac{\widehat{h}}{h}$
Panel width	$\lambda_b = \frac{\widehat{b}}{b}$
Poisson's ratio	$\lambda_\nu = \frac{\widehat{\nu}}{\nu}$
Velocity	$\lambda_V = \frac{\widehat{V}}{V}$

TABLE 3.1: List of the scale factors.

Scaling the natural frequencies of simply supported isotropic beams

The equation describing the propagation of a flexural wave in an undamped simply supported beam is (Fahy and Gardonio, 2007)

$$EI\frac{\partial^4 w}{\partial x^4} = -M\frac{\partial^2 w}{\partial t^2}, \tag{3.1}$$

where w is the displacement, x is the direction of the length of the beam, t is the time, E is the Young's modulus, I is the moment of inertia, and $M = \rho A$ is the mass per unit length (being ρ the mass density per unit volume and A the cross sectional area).

A progressive (incident) wave is assumed as solution, given by

$$w_i^+(x,t) = \widetilde{A} exp(-jk_b x) exp(j\omega t), \tag{3.2}$$

with $\widetilde{A}$ the complex amplitude of the wave at $x = 0$, j the imaginary unit, k_b the flexural wavenumber, ω the angular frequency.

The presence of the support on the right end of the beam generates a reflected, negative going wave (there is no transmitted wave, since the beam does not continue after the supports), with expression

$$w_r^-(x,t) = [\widetilde{B}_1 exp(jk_b x) + \widetilde{B}_2 exp(k_b x)] exp(j\omega t). \tag{3.3}$$

Applying the conditions associated with simply supported boundaries, then $\widetilde{B}_1 = -\widetilde{A}, \widetilde{B}_2 = 0$ (Fahy and Gardonio, 2007), therefore the beam displacement can be written as

$$w(x,t) = 2j\widetilde{A} sin(k_b x) exp(j\omega t). \tag{3.4}$$

These results show that the amplitude of the reflected wave equals that of the incident wave, and their relative phase is π. The returning wave is reflected once more when it reaches the left support, and so on. Under certain circumstances, the incident and reflected waves may have phase coincidence; in particular, since the wavenumber is the phase change per unit length, this happens in a beam when

$$k_b(2L) = n(2\pi), \tag{3.5}$$

where L is the length of the beam and n is the number of half waves along the x direction, or, equivalently,

$$k_b = \frac{n\pi}{L}. \tag{3.6}$$

Expliciting the flexural wavenumber, $k_b = (\omega^2 M/EI)^{1/4}$, the equation of the natural frequencies of a simply supported beam is

$$\omega_n = \frac{n^2\pi^2}{L^2}\sqrt{\frac{EI}{M}} \quad n = 1,2,\dots \quad . \tag{3.7}$$

Since similar systems are governed by the same set of equations, Eq. 3.7 can be analogously written, for any model, as

$$\widehat{\omega}_n = \frac{n^2\pi^2}{\widehat{L}^2}\sqrt{\frac{\widehat{E}\widehat{I}}{\widehat{M}}} \quad n = 1,2,\dots \quad . \tag{3.8}$$

Expliciting the scale factors, Eq. 3.8 becomes

$$\lambda_\omega \omega_n = \frac{n^2\pi^2}{\lambda_L^2 L^2}\sqrt{\frac{\lambda_E E \lambda_I I}{\lambda_M M}} \quad n = 1,2,\dots \quad . \tag{3.9}$$

Eqs. 3.7-3.8 are the same if the terms involving the scale factors on both sides of the Eq. 3.9 are equal, namely

$$\lambda_\omega = \frac{1}{\lambda_L^2}\sqrt{\frac{\lambda_E \lambda_I}{\lambda_M}}. \tag{3.10}$$

Eq. 3.10 represents the frequency scale factor of a simply supported beam made of isotropic material. Such a scale factor is an invariant, valid in all the frequency range, which allows the reconstruction of the natural frequencies of the prototype from those of the model, and vice versa, whatever the model. In fact, it is not associated to any similitude condition which limits its validity range. Any change in length, Young's modulus, inertia moment, or mass can be represented in terms of the associated scale factor. Even different cross-sectional shapes can be chosen, as the change in inertia moment are conveyed through the specific scale factor, λ_I. Therefore, simply supported beams do not generate any distorted model.

Under the assumption of unchanged material and cross section dimensions, $\lambda_E = \lambda_I = \lambda_M = 1$, therefore Eq. 3.10 becomes

$$\lambda_\omega = \frac{1}{\lambda_L^2}, \tag{3.11}$$

according to which only the length size affects the natural frequencies.

Scaling the natural frequencies of CFCF isotropic plates

The CFCF plates considered have clamped sides along the y direction. In order to derive the equation of the natural frequencies of such a peculiar boundary condition, it is possible to refer to the procedure provided by Warburton (Warburton, 1954). The plate equation is

$$\frac{\partial^4 w}{\partial x^4} + 2\frac{\partial^4 w}{\partial x^2 \partial y^2} + \frac{\partial^4 w}{\partial y^4} + \frac{12\rho(1-\nu^2)}{Eh^2}\frac{\partial^2 w}{\partial t^2} = 0, \tag{3.12}$$

where w is the plate displacement trasversal to the xy plane, x and y are the directions of length and width of the plate, ρ is the mass per unit volume, ν is the Poisson ratio. The displacement can be expressed as

$$w = W sin(\omega t), \tag{3.13}$$

In order to determine the amplitude W, energy considerations allow to write

$$\omega^2 = \frac{U_{max}}{\frac{\rho h}{2}\int_0^a \int_0^b W^2 dxdy}, \tag{3.14}$$

where U_{max} is the maximum potential energy, a and b are the length and width, respectively (the geometrical characteristics are schematically represented in Fig. 3.1). The term W can be explicited by means of Rayleigh-Ritz method, in which a series is assumed for it:

$$\sum_{\alpha}\sum_{\beta} A_{\alpha\beta}\theta_{\alpha}(x)\phi_{\beta}(y). \tag{3.15}$$

In Eq. 3.15, $\theta_{\alpha}(x)$ and $\phi_{\beta}(y)$ are beam functions representing the modes of a beam with a certain boundary condition at its ends; the coefficients $A_{\alpha\beta}$ make the value ω^2, given in Eq. 3.14, a minimum. The functions $\theta_{\alpha}(x)$ and $\phi_{\beta}(y)$ are used to describe the undulatory behavior in x and y directions of a plate having the same boundary conditions of the beams. To give an example, the waveform of the plate in x direction, for each position alongside y, is the same of the beam with axis in x direction and the boundary conditions of the plate.

For any boundary condition, substituting the proper expressions for $\theta_{\alpha}(x)$ and $\phi_{\beta}(y)$ (Warburton, 1954) into Eq. 3.12 and Eq. 3.14, the following expression for the natural frequencies of a plate is given by

$$\omega_{mn} = \frac{\gamma_{mn}^2}{a^2}\sqrt{\frac{Eh^2}{12\rho(1-\nu^2)}}, \tag{3.16}$$

where the term λ_{mn} is known as the dimensionless natural frequency parameter and it is a function of the boundary conditions, geometry, and Poisson's ratio:

$$\gamma_{mn}^2 = \pi^2\sqrt{G_m^4 + G_n^4\left(\frac{a}{b}\right)^2 + 2\left(\frac{a}{b}\right)^2[J_mJ_n + 2\nu(H_mH_n - J_mJ_n)]}. \tag{3.17}$$

The coefficients $G_m, G_n, H_m, H_n, J_n, J_n$ are dimensionless and depend on the modal pattern and on the boundary conditions. Such a modal pattern is described by the subscripts m and n, which chan represent both the number of half waves or nodal lines in x and y directions, respectively. In particular, Blevins (Blevins, 2016) reports the values, for each couple (m,n) of the six dimensionless coefficients, as a function of the half waves, while Warburton (Warburton, 1954) provides the same coefficients as functions of the number of nodal lines. It is worth remarking that, in the latter case, the index m starts from 2, while the n index starts from 0, as the free sides are those along the x direction, while the clamped sides are those along the y direction. Thus, since the clamped sides are always nodal lines, their number, along the x direction, is at least 2; conversely, the free sides are not nodal lines, therefore their number along the y direction is, at least, 0. For this reason (and since the formulation given by Blevins starts both m and n from 1), the formulation by Warburton is more complete and, therefore, is the one herein adopted. For sake of completeness, the coefficients proposed by Warburton are summarized in Tables 3.2-3.3.

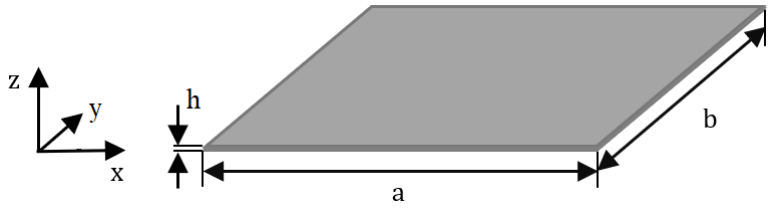

FIGURE 3.1: Geometrical characteristics of a rectangular panel.

m	$\mathbf{G_m}$	$\mathbf{H_m}$	$\mathbf{J_m}$
2	1.506	1.248	1.248
3, 4, 5, ...	$m-\frac{1}{2}$	$\left(m-\frac{1}{2}\right)^2\left[1-\frac{2}{\left(m-\frac{1}{2}\right)\pi}\right]$	$\left(m-\frac{1}{2}\right)^2\left[1-\frac{2}{\left(m-\frac{1}{2}\right)\pi}\right]$

TABLE 3.2: Coefficients in Eq 3.17 along the x direction.

n	$\mathbf{G_n}$	$\mathbf{H_n}$	$\mathbf{J_n}$
0	0	0	0
1	0	0	$\frac{12}{\pi^2}$
2	1.506	1.248	5.017
3, 4, 5, ...	$n-\frac{1}{2}$	$\left(n-\frac{1}{2}\right)^2\left[1-\frac{2}{\left(n-\frac{1}{2}\right)\pi}\right]$	$\left(m-\frac{1}{2}\right)^2\left[1+\frac{2}{\left(m-\frac{1}{2}\right)\pi}\right]$

TABLE 3.3: Coefficients in Eq 3.17 along the y direction.

As for the beam, also for plates the behavior of scaled-up or down models is governed by the same set of equations of the prototype, therefore, substituting Eq. 3.16 into Eq. 3.11, the natural frequencies of any CFCF model is given by:

$$\widehat{\omega}_{mn} = \frac{\pi^2}{\widehat{a}^2}\sqrt{\frac{\widehat{E}\widehat{h}^2}{12\widehat{\rho}(1-\widehat{\nu}^2)}}\times\ldots$$
$$\ldots\times\sqrt{G_m^4+G_n^4\left(\frac{\widehat{a}}{\widehat{b}}\right)^4+2\left(\frac{\widehat{a}}{\widehat{b}}\right)^2\left[J_mJ_n+2\widehat{\nu}(H_mH_n-J_mJ_n)\right]}. \quad (3.18)$$

Introducing the scale factors, Eq. 3.18 becomes:

$$\lambda_\omega\omega_{mn} = \frac{\pi^2}{\lambda_a^2 a^2}\sqrt{\frac{\lambda_E E\lambda_h^2 h^2}{12\lambda_\rho\rho(1-\lambda_\nu^2\nu^2)}}\times\ldots$$
$$\ldots\times\sqrt{G_m^4+G_n^4\left(\frac{\lambda_a a}{\lambda_b b}\right)^4+2\left(\frac{\lambda_a a}{\lambda_b b}\right)^2\left[J_mJ_n+2\lambda_\nu\nu(H_mH_n-J_mJ_n)\right]}. \quad (3.19)$$

Assuming unchanged material ($\lambda_E = \lambda_\rho = \lambda_\nu = 1$), Eqs. 3.16-3.19 are the same if

$$\lambda_\omega = \frac{\lambda_h}{\lambda_a^2} = \frac{\lambda_h}{\lambda_b^2} = \frac{\lambda_h}{\lambda_a \lambda_b}, \tag{3.20}$$

that are all valid at the same time only if

$$\lambda_a = \lambda_b. \tag{3.21}$$

Eq. 3.21 represents the similitude condition to fulfill in order to design model panels in complete similitude; according to this condition, the length and the width of the panel must scale in the same way. Thickness, on the other hand, is a free parameter. It can be equivalently rewritten as

$$\lambda_{\mathcal{AR}} = 1, \tag{3.22}$$

that is, the aspect ratio of the panel must not change.

In the particular case of the plate, if all the geometrical dimensions scale with the same scale factor ($\lambda_a = \lambda_b = \lambda_h = \lambda_l$), the model is called *replica*. The similitude condition is satisfied, and Eq. 3.20 reduces, inevitably, to

$$\lambda_\omega = \frac{1}{\lambda_l}. \tag{3.23}$$

If only length and width scale and such a scaling procedure fulfills the condition given in Eq. 3.21 ($\lambda_a = \lambda_b = \lambda_l$), then the model is called *proportional sides*; Eq. 3.20 reduces, in this case, to

$$\lambda_\omega = \frac{\lambda_h}{\lambda_l^2} \tag{3.24}$$

The fulfillment of the similitude condition makes Eqs. 3.23-3.24 univocal laws, working fine into all the frequency range, that allow to reconstruct the natural frequencies of the prototype. These frequencies appear different ranges in prototypes and models (generally, higher frequencies if the model is scaled-down, lower frequencies if the model is scaled-up), but, if the model is in complete similitude, the succession of the modes is kept. Therefore, the reconstruction is possible because the invariant λ_ω performs a remodulation in frequency, that is, switches the frequencies of the model back to those of the prototype, and vice versa.

If the similitude condition is not satisfied, then the model is called *avatar*; the geometrical parameters scale differently, therefore Eq. 3.20 does not reduce into an univocal scaling law, instead there are three of them:

$$\lambda_\omega = \frac{\lambda_h}{\lambda_a^2}, \tag{3.25a}$$

$$\lambda_\omega = \frac{\lambda_h}{\lambda_b^2}, \tag{3.25b}$$

$$\lambda_\omega = \frac{\lambda_h}{\lambda_a \lambda_b}. \tag{3.25c}$$

Eqs. 3.25 are not equivalent and, typically, none of them allows an accurate reconstruction of the dynamic response of the prototype, at least not in all the frequency range. This is due to the fact that, not adhering to the similitude condition, the mode succession is not retained and the scale factor is not able to keep track of this phenomenon. This also explains why beams do not generate avatars. In fact, being the beams 1D structures, the flexural wave travels just in one direction and the modes follow one another in frequency for increasing n: the modes succession is always the same and, therefore, it is always retained. Conversely, flexural waves travel in two directions in plates, thus the modes are given by combinations of the numbers of half waves in these directions; such a combination strongly depends on the aspect ratio. Therefore, even small changes in the aspect ratio - which means violating the similitude condition - may alter the succession of the modes and generate avatars.

Eqs. 3.25 always lead to discrepancies in the remodulation phase, and these discrepancies increase as the distortion increases (i.e., as the aspect ratio of the plates changes significantly). Occasionally, Eqs. 3.25 may give acceptable predictions, however it is not possible to know *a priori* which scaling laws return the best results, the best choice can be determined only after the application of the law. Thus, the deterministic procedure, consistent with the similitude laws, is lost.

It is interesting to note that Eqs. 3.20-3.21 are not only the similitude conditions and scaling laws for CFCF plates, but also those of simply supported and cantilever plates (De Rosa, Franco, and Meruane, 2015; Meruane, De Rosa, and Franco, 2015): they do not change if the boundary conditions change. This is not surprising, as similitude methods are based on the principle of dimensional homogeneity, for which both the LHS (Left Hand Side) and RHS (Right Hand Side) of an equation must have the same dimensions. Hence, even though the boundary conditions affect the reflection of the waves in a structure, therefore influencing the phase coincidence and the resonance, they do not have effects on the scaling laws and similitude conditions, since the structural operator is the same and it must keep the same dependencies with the same parameters. This concept can be extended to beams, too.

Scaling the natural frequencies of simply supported sandwich plates

The similitude conditions and scaling laws are derived for sandwich plates under simply supported conditions made of isotropic material (aluminium skins and aluminium

foam core). As demonstrated in Sec. 3.1.1, they do not change if the boundary conditions change, being based on dimensional homogeneity. Hence, simply supported plates are considered because they are more straightforward to manage analytically, with respect to free-free plates.

In order to derive the equation of natural frequencies of a simply supported isotropic sandwich plate which skins and core are made of isotropic material, it is possible to start with the equation of an orthotropic laminate. Assuming that there is no transverse load and rotatory inertia, this equation can be written as

$$D_{11}\frac{\partial^4 w}{\partial x^4}+2(D_{12}+2D_{66})\frac{\partial^4 w}{\partial x^2\partial y^2}+D_{22}\frac{\partial^4 w}{\partial y^4}+\rho_S\frac{\partial^2 w}{\partial t^2}=0, \tag{3.26}$$

where the several terms D_{ij} indicate the bending stiffnesses of the laminate, and $\rho_S = M/ab$ the mass density per unit area. Expressing the deflection in the form

$$w(x,y,t)=w(x,t)e^{j\omega t}, \tag{3.27}$$

and substituting into E. 3.26, returns

$$D_{11}\frac{\partial^4 w}{\partial x^4}+2(D_{12}+2D_{66})\frac{\partial^4 w}{\partial x^2\partial y^2}+D_{22}\frac{\partial^4 w}{\partial y^4}-\rho_S\omega^2 w=0. \tag{3.28}$$

The spatial part of Eq. 3.27 can be expressed as a double series written as

$$\sum_{m=1}^{\infty}\sum_{n=1}^{\infty}C_{mn}sin\left(\frac{m\pi a}{a}\right)sin\left(\frac{n\pi y}{b}\right), \tag{3.29}$$

that, under simply supported boundary conditions, becomes

$$w(x,y)=C_{mn}sin\left(\frac{m\pi x}{a}\right)sin\left(\frac{n\pi y}{b}\right). \tag{3.30}$$

The term C_{mn}, and the associated coefficients, are given in Berthelot (Berthelot, 2015).

Substituting Eq. 3.30 into Eq. 3.28 gives

$$\left[\frac{m^4\pi^4}{a^4}D_{11}+2\frac{m^2n^2\pi^2}{a^2b^2}(D_{12}+2D_{66})+\frac{n^4\pi^4}{b^4}D_{22}-\rho_S\omega^2\right]C_{mn}=0. \tag{3.31}$$

For nonzero values of C_{mn}, the following equation for the natural frequencies of an orthotropic plate is obtained:

$$\omega_{mn}=\frac{\pi^2}{a^2}\sqrt{\frac{1}{\rho_S}\left[m^4D_{11}+2m^2n^2\left(\frac{a}{b}\right)^2(D_{12}+2D_{66})+n^4\left(\frac{a}{b}\right)^4D_{22}\right]}. \tag{3.32}$$

Since the plate under investigation is an isotropic sandwich plate, it can be assumed that $D_{11}=D_{22}=D_{12}+2D_{66}=D$, therefore (Berthelot, 2015)

$$\omega_{mn} = \frac{\pi^2}{a^2}\sqrt{\frac{D}{\rho_S}}\sqrt{m^4 + 2m^2n^2\left(\frac{a}{b}\right)^2 + n^4\left(\frac{a}{b}\right)^4}, \tag{3.33}$$

The sandwich characteristic can be inserted into Eq. 3.33 by means of the bending stiffness. For isotropic sandwich plates, the bending stiffness can be expressed by separating the contribution of the skins from that of the core. According to Powell and Stephens (Powell and Stephens, 1966), the bending stiffness can be written as

$$D = \frac{E_f(h^3 - h_c^3)}{12(1-\nu_f^2)} + \frac{E_c h_c^3}{12(1-\nu_c^2)}, \tag{3.34}$$

in which the f and c subscripts describe the facing and core properties, respectively.

The equation for models, considering the bending stiffness given in Eq. 3.34 and expliciting the mass density per unit area, is:

$$\widehat{\omega}_{mn} = \frac{\pi^2}{\widehat{a}^2}\sqrt{\frac{\widehat{E}_f(\widehat{h}^3 - \widehat{h}_c^3)\widehat{a}\widehat{b}}{12\widehat{M}(1-\widehat{\nu}_f^2)} + \frac{\widehat{E}_c\widehat{h}_c^3\widehat{a}\widehat{b}}{12\widehat{M}(1-\widehat{\nu}_c^2)}} \times \ldots$$
$$\ldots \times \sqrt{m^4 + 2m^2n^2\left(\frac{\widehat{a}}{\widehat{b}}\right)^2 + n^4\left(\frac{\widehat{a}}{\widehat{b}}\right)^4}. \tag{3.35}$$

Introducing the scale factors, Eq. 3.35 can be written in terms of the prototype parameters as

$$\lambda_\omega\omega_{mn} = \frac{\pi^2}{\lambda_a^2 a^2}\sqrt{\frac{\lambda_{E_f}E_f(\lambda_h^3 h^3 - \lambda_{h_c}^3 h_c^3)\lambda_a a\lambda_b b}{12\lambda_M M(1-\lambda_{\nu_f}^2\nu_f^2)} + \frac{\lambda_{E_c}E_c\lambda_{h_c}^3 h_c^3\lambda_a a\lambda_b b}{12\lambda_M M(1-\lambda_{\nu_c}^2\nu_c^2)}} \times \ldots$$
$$\ldots \times \sqrt{m^4 + 2m^2n^2\left(\frac{\lambda_a a}{\lambda_b b}\right)^2 + n^4\left(\frac{\lambda_a a}{\lambda_b b}\right)^4}. \tag{3.36}$$

Eq. 3.36 is written under two assumptions. First, the number of half waves in x and y direction scale equally in both the prototype and model, which means $\lambda_m = \lambda_n = 1$. This assumption is not trivial, however the most reasonable choice for both scale factors is the same (unit) value. This is true for two reasons: the same mode shapes must be compared, thus the unit value; then, the scale factors are, basically, invariant terms, thus the value of both λ_m and λ_n must be fixed *a priori*.

Secondly, it is assumed that also the Poisson's ratios of both skins and core are the same between prototype and model (i.e., $\lambda_{\nu_f} = \lambda_{\nu_c} = 1$), which implies that the material may change but it will still be a metal or an alloy.

Hence, Eqs. 3.33-3.36 are the same if the following set of conditions holds:

$$\begin{cases} \lambda_a = \lambda_b \\ \lambda_h = \lambda_{h_c} \\ \lambda_{E_f} = \lambda_{E_c} \end{cases} . \tag{3.37}$$

Therefore, a complete similitude is obtained if length and width scale in the same way (as for the flat plate); new conditions appear, concerning the elastic moduli of skins and core, the total thickness and the core thickness. These are clearly associated with the sandwich configuration of the test article. It is interesting to notice that Eq. 3.36 would have brought likewise to the additional condition $\lambda_m = \lambda_n$, if it would have not been previously assumed.

Fulfilling the conditions given in Eq. 3.37 leads, as expected, to the definition of an univocal scaling law, that is

$$\lambda_\omega = \frac{1}{\lambda_l}\sqrt{\frac{\lambda_E \lambda_h^3}{\lambda_M}}, \tag{3.38}$$

where $\lambda_a = \lambda_b = \lambda_l$ and $\lambda_{E_f} = \lambda_{E_c} = \lambda_E$.

The considerations done for Eq. 3.24 in the case of CFCF plates still hold for Eq. 3.38: it allows to predict the natural frequencies of the prototype from those of the model (and vice versa) in the whole frequency range.

Not fulfilling the conditions given in Eq. 3.37 leads to avatars also for sandwich plates. There are several possible scaling law, depending on which condition is satisfied and which not. For instance, satisfying the conditions about Young's modulus and thickness ($\lambda_{E_f} = \lambda_{E_c} = \lambda_h = \lambda_{h_c} = 1$) leads to the following scaling laws (from Eq. 3.36:

$$\lambda_\omega = \frac{1}{\lambda_a}\sqrt{\frac{1}{\lambda_M}}, \tag{3.39a}$$

$$\lambda_\omega = \frac{1}{\lambda_b}\sqrt{\frac{1}{\lambda_M}}, \tag{3.39b}$$

$$\lambda_\omega = \sqrt{\frac{1}{\lambda_a \lambda_b \lambda_M}}. \tag{3.39c}$$

Also in this case, the several scale factors provided by Eqs. 3.39 do not work fine in all the frequency range.

However, it is possible to reduce the number of the similitude conditions if many parameters are grouped into just one parameter with physical meaning. In particular, considering the bending stiffness provided in Eq. 3.34 as a whole parameter, instead of expliciting it, the similitude conditions and the scaling law for a complete similitude reduce to Eq. 3.21 and

$$\lambda_\omega = \frac{1}{\lambda_l}\sqrt{\frac{\lambda_D}{\lambda_M}}, \tag{3.40}$$

respectively.

Therefore, only the first of the conditions listed in Eq. 3.37 remains, and the model is still a proportional sides. Now, the similitude condition completely coincides with those found for flat plates with CFCF, simply supported (De Rosa, Franco, and Meruane, 2015), and clamped on one side (Meruane, De Rosa, and Franco, 2015) boundary conditions. Thus, concerning plates, passing from a flat to a sandwich configuration does not affect the similitude conditions, only the scaling laws.

Since Eq. 3.40 directly involves the bending stiffness, it is possible to take into account changes of the material just by evaluating the corresponding scale factor λ_D, without adding other similitude conditions.

3.1.2 Scaling the velocity response

The velocity response of a generic linear system can be written as a summation of its vibration modes (Cremer, Heckl, and Petersson, 2005)

$$V(x_F,x_R;\omega) = j\omega F(\omega)\sum_{m=1}^{\infty}\sum_{n=1}^{\infty}\frac{\phi_{mn}(x_F)\phi_{mn}(x_R)}{\mu_{mn}(\omega_{mn}^2-\omega^2+j\eta\omega_{mn}^2)}, \tag{3.41}$$

where x_F is the excitation point, x_R the receiving point, both expressed in dimensionless coordinates, j the imaginary unit, ϕ_{mn} the mode shape of the mode of order (m,n), η the structural modal damping, and ω is the excitation frequency (not to be confused with ω_{mn}, which represents the natural frequency). The force $F(\omega)$ harmonic, acting at the point x_F according to

$$F(x_F;T) = F(\omega)\delta(x_{F0}-x_F)e^{j\omega T}, \tag{3.42}$$

in which δ denotes the Kronecker delta function, while T is the time.

Finally, the term μ_{mn} is the generalized mass. For a plate, it is expressed by

$$\mu_{mn} = \rho h\int_0^a\int_0^b \phi_{mn}^2(x,y)dxdy. \tag{3.43}$$

The term μ_{mn} is representative of the amount of mass participating to the mode of order (m,n) and it is a fraction of the total mass M (for example, it is $M/4$ when the plate is simply supported). Thus, its scaling can be taken into account in terms of the mass scale factor, λ_M.

Scaling the velocity response consists in the same procedure carried out for the natural frequencies. The model velocity response is

$$\widehat{V}(x_F,x_R;\widehat{\omega}) = j\widehat{\omega}\widehat{F}(\widehat{\omega})\sum_{m=1}^{\infty}\sum_{n=1}^{\infty}\frac{\phi_{mn}(x_F)\phi_{mn}(x_R)}{\widehat{\mu}_{mn}(\widehat{\omega}_{mn}^2-\widehat{\omega}^2+j\widehat{\eta}\widehat{\omega}_{mn}^2)}. \tag{3.44}$$

For structures in similitude, the excitation and acquisition points always act at the same relative dimensionless coordinates. The modes $\phi_{mn}(x_F)\phi_{mn}(x_R)$ are evaluated in the same non-dimensional coordinates, therefore, for a given mode shape,

their value does not change among the models. This implies that the mode shapes $\phi_{mn}(x_F)\phi_{mn}(x_R)$ do not need to be posed in similitude, whatever the model type.

Eq. 3.44 can be written in terms of the scale factors as

$$\lambda_V V(x_F,x_R;\lambda_\omega\omega) = j\lambda_\omega\omega\lambda_F F(\lambda_\omega\omega)\times\ldots \\ \ldots\times\sum_{m=1}^{\infty}\sum_{n=1}^{\infty}\frac{\phi_{mn}(x_F)\phi_{mn}(x_R)}{\lambda_M\mu_{mn}(\lambda_\omega^2\omega_{mn}^2-\lambda_\omega^2\omega^2+j\lambda_\eta\eta\lambda_\omega^2\omega_{mn}^2)}. \quad (3.45)$$

To derive the scaling law of velocity, it is assumed that the damping does not change among the models, $\lambda_\eta = 1$ [although this assumption should be implicit, because, as demonstrated in literature (De Rosa et al., 2012), constant damping is required between prototype and model]; this hypothesis is acceptable if the material and the boundary conditions do not change. Hence, the velocity scales according to the law

$$V(x_F,x_R;\omega) = \frac{\lambda_M\lambda_\omega}{\lambda_F}\widehat{V}(x_F,x_R;\lambda_\omega\omega). \quad (3.46)$$

Eq. 3.46 provides the scale factor of velocity. The frequency response of any model can be predicted into two steps: first, the amplitude of the response is scaled by means of the ratio $\frac{\lambda_M\lambda_\omega}{\lambda_F}$; then, the resonance peaks are aligned by means of the frequency remodulation $\lambda_\omega\omega$.

Eq. 3.46 has been derived without posing any similitude condition on the geometry, thus this equation would work fine for all the types of models. However, the distortion can be still conveyed by means of the frequency scale factor. This affects the reconstruction of the velocity response, as both the amplitude and frequency remodulation involve the frequency scale factor; moreover, when the system lacks of an univocal frequency scale factor, it also lacks of an univocal velocity scale factor.

For sake of completeness, also the mobility is considered:

$$Y(x_F,x_R;\omega) = \frac{V(x_F,x_R;\omega)}{F(\omega)} = j\omega\sum_{m=1}^{\infty}\sum_{n=1}^{\infty}\frac{\phi_{mn}(x_F)\phi_{mn}(x_R)}{\mu_{mn}(\omega_{mn}^2-\omega^2+j\eta\omega_{mn}^2)}, \quad (3.47)$$

and it is straightforward to demonstrate that it scales as

$$\lambda_Y = \frac{1}{\lambda_M\lambda_\omega}. \quad (3.48)$$

Eq. 3.48 clearly descends from Eqs. 3.46-3.47, therefore the same considerations hold.

3.1.3 Scaling the radiated acoustic power

The acoustic power radiated by a plate can be derived in terms of summation modes and elementary radiators. The former formulation requires the resolution of quadruple

integrals, which is a complex process. Thus, the approach with elementary radiators turns out to be more straightforward (Fahy and Gardonio, 2007).

Considering a baffled panel, it is divided into a grid of R rectangular elements, at the centres of which a velocity v_{er} acts. If the motion is time-harmonic, then the overall vibration of the panel can be described by the vector of complex amplitudes $\widetilde{V} = [\widetilde{V}_1, \widetilde{V}_2, \ldots, \widetilde{V}_R]^T$. A vector of pressures acting on each element can be analogously created, $\widetilde{p} = [\widetilde{p}_1, \widetilde{p}_2, \ldots, \widetilde{p}_R]^T$.

If the dimensions of each element are small with respect to both the structural and acoustic wavelength, the total radiated acoustic power can be written as the summation of the powers radiated by each element, namely

$$\Pi_{rad}(\omega) = \sum_{r=1}^{R} \frac{1}{2} A_e Re\{\widetilde{V}_r^* \widetilde{p}_r\} = \frac{S}{2R} Re\{\{\widetilde{V}^H\}\{\widetilde{p}\}\}, \tag{3.49}$$

where A_e and S are, respectively, the areas of each element and of the entire panel.

When $\sqrt{A_e} << \lambda$, the integral formulation of pressure due to Rayleigh (Rayleigh, 1896) can be written as

$$\widetilde{p}_i = \frac{j\omega\rho_0 A_e e^{-jkR_{ij}}}{2\pi R_{ij}} \widetilde{V}_j(x_j, z_j), \tag{3.50}$$

where R_{ij} is the distance between the centres of the i-th and j-th radiators. Rewriting Eq. 3.50 in vectorial form,

$$\{\widetilde{p}\} = [\widetilde{Z}]\{\widetilde{V}\}. \tag{3.51}$$

Thus, substituting Eq. 3.51 into Eq. 3.49, and rearranging the terms, the acoustic power radiated by an elastic surface at the radial frequency ω, having a normal velocity distribution $V(\omega)$, is given, in discrete coordinates, as (Fahy and Gardonio, 2007)

$$\Pi_{rad}(\omega) = \frac{\omega^2 \rho_0}{4\pi c_0} \{V(\omega)\}^H [A][R(\omega)][A]\{V(\omega)\}, \tag{3.52}$$

where the superscript H indicates the Hermitian matrix. The terms ρ_0 and c_0 are the air density and speed of sound, respectively. Assuming N_G grid points in total, $[A]$ is the $N_G \times N_G$ diagonal matrix of equivalent nodal areas

$$[A] = \begin{bmatrix} A_1 & 0 & \ldots & 0 \\ 0 & A_2 & \ldots & 0 \\ \vdots & \vdots & \ddots & \vdots \\ 0 & 0 & \ldots & A_{N_G} \end{bmatrix}. \tag{3.53}$$

For an homogeneous mesh, each equivalent nodal area A_i, corresponding to the generic i-th grid point, is

$$A_i = \frac{ab}{(N_x - 1)(N_y - 1)}, \tag{3.54}$$

where N_x and N_y are the numbers of grid points along the x and y directions, so that $N_x N_y = N_G$.

Finally, the matrix $[R(\omega)]$ is the radiation matrix, which elements are *sinc* functions:

$$[R(\omega)] = \begin{bmatrix} 1 & \frac{sin(kd_{1,2})}{kd_{1,2}} & \cdots & \frac{sin(kd_{1,N_G})}{kd_{1,N_G}} \\ \frac{sin(kd_{1,2})}{kd_{1,2}} & 1 & \cdots & \cdots \\ \vdots & \vdots & \ddots & \vdots \\ \frac{sin(kd_{1,N_G})}{kd_{1,N_G}} & \cdots & \cdots & 1 \end{bmatrix}, \tag{3.55}$$

where $k = \omega / c_0$ is the acoustic wavenumber and $d_{i,j}$ is the distance between the i-th and the j-th grid points.

The N_G grid points are the centres of the elementary radiators with equivalent nodal area A_i. The differences among the velocities in the centres and in the corners of the elementary radiator are negligible when the dimension of the element is small with respect to the acoustic wavelength (that is, $\sqrt{A_i} << \lambda$). Moreover, Eq. 3.55 returns acceptable results when the sides of the discrete radiator are much smaller than both the acoustic and modal wavelengths in the panel.

Until now, all the parameters considered, may they be scalar values (like geometrical or material characteristics) or vectors spanning a frequency band (like velocity), are scaled by means of single-valued scale factors. This is not the case of the radiation matrix, in which the element-wise model-to-prototype ratio would lead to a matrix made of different scale factors. For example, those along the diagonal are always equal to 1, because, by definition of *sinc* function, the diagonal elements of the matrix are always unitary. Instead, all the other elements scale differently because of the transformation caused by the *sinc* function. Thus, it is not possible to scale directly this function, which prevents from the derivation of a scaling law of the radiated acoustic power written only in terms of scale factors, as done for the frequency in Eq. (3.24) and the velocity in Eq. (3.46). However, the remodulation can still be performed by substituting the scale factors into the equation of the radiated acoustic power of the model (keeping in mind that constants as air density and the speed of sound do not need scaling). In particular, the argument of the *sinc* function is remodulated, instead of the function itself, obtaining

$$\widehat{\Pi}_{rad} = \frac{\lambda_\omega^2 \omega^2 \rho_0}{4\pi c_0} \{\lambda_V V(\lambda_\omega \omega)\}^H [\lambda_A A] [\widehat{R}(\lambda_\omega \omega)] [\lambda_A A] \{\lambda_V V(\lambda_\omega \omega)\}, \tag{3.56}$$

in which every element of the model radiation matrix scales as

$$\widehat{R}_{ij} = \frac{sin\left(\lambda_\omega \frac{\omega}{c_0} \lambda_d d_{i,j}\right)}{\lambda_\omega \frac{\omega}{c_0} \lambda_d d_{i,j}}. \tag{3.57}$$

As the panel dimensions change, the positions of the acquisition points change too, along with their relative distances. Therefore, because the velocity distributions $V(\omega)$ must act at the same grid points dimensionless coordinates of both prototype and model, the distance between them must scale in the same way of length and width, leading to the similitude condition for the radiated acoustic power

$$\lambda_d = \lambda_a = \lambda_b. \tag{3.58}$$

Thus, even though a scaling law of the radiated acoustic power has not been directly derived, a similitude condition has been found. Interestingly, this condition incorporates the similitude conditions of the natural frequencies of plates. Equivalently, Eq. 3.58 suggests that also the elementary radiators must scale keeping constant their aspect ratio, that is, as the plate itself.

3.2 Machine learning

Machine learning is a subset of Artificial Intelligence (AI) in which several disciplines converge, such as computational statistics, pattern recognition, image processing, data mining, adaptive algorithms, etc. Briefly, machine learning techniques allow to perform predictions in an automatic way by learning from a set of data and exploiting the information underneath. More precisely, machine learning methods provide to a computational device the capability to improve its performance on a specific task from data without being explicitly programmed. A formal definition is given by Mitchell (Mitchell, 1997), who writes

> A computer program is said to learn from experience E with respect to some class of tasks T and performance measure P, if its performance at tasks in T, as measured by P, improves with experience E.

Some of the tasks T that can be addressed by machine learning (Goodfellow, Bengio, and Courville, 2016) are: classification, classification with missing inputs, regression, transcription, machine translation, structured output, anomaly detection, synthesis and sampling, imputation of missing values, denoising, etc. The term P is a performance index representing the degree of success into executing the task; in most of the cases, it is a error to minimize, or a gain to maximize.

Machine learning is based on algorithms that derive models from sample inputs providing data-driven predictions and decisions. The fact that there is not an explicit algorithm, because the process is totally data-driven, confers to the approach a high versatility which allows its application in several research fields and kinds of problems.

Basically, the learning algorithm performs several iterations on a set of training data - called *training set* - generating an internal model which describes the behavior underlying this data. Each iteration aims at improving the performance index, that in this context is a training error to minimize. The central objective is to develop the capability of performing well on unseen data, that is, to generalize. Therefore, after each iteration, the internal model generated by the learning algorithm is tested on a *test set* in order to evaluate the test (or generalization) error. These sets of data are organized in features and observations. The features are the characteristics describing the phenomenon under investigation; sets composed of one value of each feature generate an observation.

Both the task T and performance index P define the type of experience E to be gained, that can be broadly separated into three groups:

- *Supervised learning*: the dataset contains features and each examples is described by a label;
- *Unsupervised learning*: the dataset contains features but the examples are not described by labels (it is very useful when the purpose is to find structure in data);
- *Reinforcement learning*: the algorithm interacts with a dynamic environment, generating a feedback loop between the learning algorithm and its experiences;

The range of machine learning methods is wide and diversified. Linear models, such as linear regression, Support Vector Machines (SVMs), etc., are simple, can be fit efficiently and reliably, and the solution is in closed form or with convex optimization; of course, they are limited to linear functions. Regression polynomials, on the other hand, help to derive empirical equations fitting experimental data; however, when data is limited, inconsistent, or it involves a large number of variables, it is difficult to generalize empirically. As a matter of fact, data is gathered in a multidimensional surface with complex and unknown underlying functional forms (Fu, Liang, and Li, 2007).

Among all these methods, ANNs constitute a powerful tool able to reconstruct the functional relationships between variables with nonlinear dependencies; they also work with noisy and/or time-varying data, and can produce solutions in short times (independently of the complexity of the problem). All these characteristics make ANNs an attractive method even if there are alternative techniques which can return more accurate results (Flood and Kartam, 1993). For this reason, a part of this work is dedicated to the investigation of the ANNs in similitude field.

3.2.1 Artificial Neural Networks (ANNs)

ANNs are a machine learning algorithm which trains and generalizes directly on the data set; they can work with complex, nonlinear functional relationships by learning from data obtained with analytical/numerical simulations or from experiments. Moreover, they are robust to noise and incomplete information.

ANNs are loosely inspired to human brain; they are called "networks" because they are composed of functions associated with a directed graph, as shown in Fig. 3.2, where the organization in layers is highlighted: input (orange), hidden (blue), and output (green) layers. Each one is made of several computational units, called nodes or neurons, in which the input is processed and transformed into an output. Particularly, the network shown in Fig. 3.2 is a fully connected network, as all the neurons of a layer are connected with all the neurons of the successive layer.

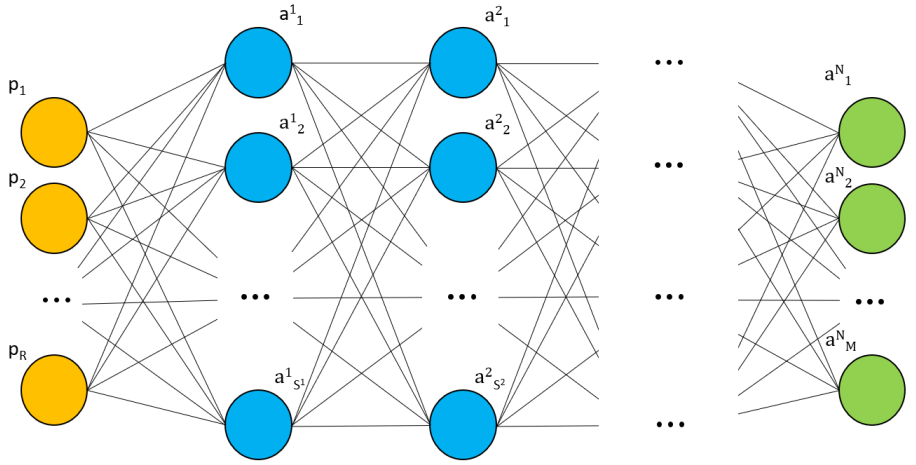

FIGURE 3.2: Scheme of an ANN.

The input processing into a neuron is shown in Fig. 3.3; it can be divided into two steps. Being a fully connected network, the neuron receives all the R inputs. Then, firstly (left part of the neuron), the net input of the neuron, n_j, is evaluated as (Hagan et al., 2014)

$$n_j = \sum_{i=1}^{R} \mathbf{W}\mathbf{p} + b_j, \tag{3.59}$$

where $\mathbf{W}$ is a matrix of adjustable parameters, called weights, b_j is another adjustable parameter, called bias, $\mathbf{p}$ is the vector of inputs, and R is the total number of inputs. Thus, the net input is a linear combination of inputs and weights, plus the bias.

Secondly (right part of the neuron), the net input is transformed into the output a_j by means of an activation function $f(\cdot)$, so that

$$a_j = f(n_j). \tag{3.60}$$

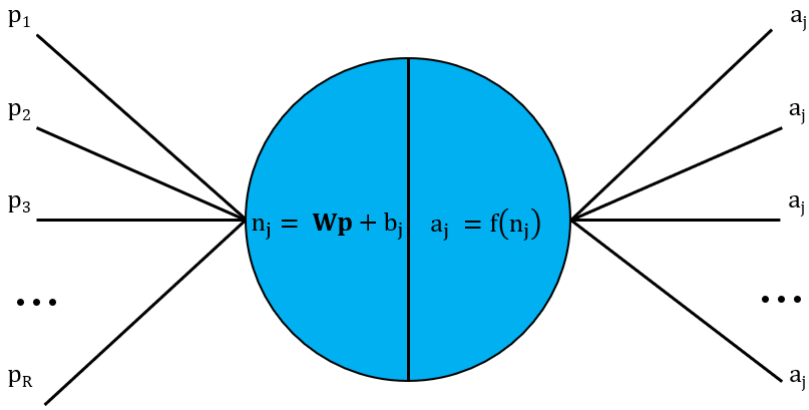

FIGURE 3.3: Scheme of an neuron (of the first hidden layer).

The activation function is used into the hidden and output layers. There is no transformation into the input layers, they simply "pass" the input to the first hidden layer.

The number of neurons of the input layer is equal to the number of input features, therefore the input vector has dimensions $R \times 1$. If the first hidden layer has more than one neuron, viz. S^1 neurons, then the weight matrix dimensions are $\mathbf{W}$ has $S^1 \times R$, while the bias vector b_j has $S^1 \times 1$ elements (i.e., a bias for each neuron). Therefore, both the net input $\mathbf{n}$ and output $\mathbf{a}$ vectors have dimensions $S^1 \times 1$. The output layer has as many neurons as the number of output features (say, D), thus the output vector has $D \times 1$ elements.

The input layer gathers all the inputs from the training set and transfers them to the successive layer, that is typically a hidden layer. These types of layers are fundamental, as they introduce the nonlinear behavior by means of the activation function. Then, the output of the first hidden layer becomes the input of the successive layer, that can be an output or a hidden layer. In the latter case, the operations executed in the first hidden layers are repeated. When data is passed to the output layer, it returns the final values of the internal model generated by the ANN.

If the calculations stop after a complete crossing of the network, then the ANN is called feedforward (because the data moves in one direction, from the input to the output layer). Alternatively, a backpropagation can be inserted, so that the final output is compared with the reference value (contained into the test set). The derivatives of the obtained error are evaluated with respect to weights and biases, following a backward path from the output to the input layers.

In this thesis, the transfer function chosen for the hidden layers is the hyperbolic tangent (also known as tangent sigmoid, Fig. 3.4):

$$a_j = tanh(n_j) = \frac{e^{n_j} - e^{n_j}}{e^{n_j} + e^{n_j}}. \tag{3.61}$$

It is a function defined in all $\mathbb{R}$, assuming values in the interval [-1, 1]; the passage from the $y < 0$ to the $y > 0$ region occurs with a smooth step, so that $y(0) = 0$. The internal model generated by the ANN is a function which develops, for each hidden layer, as many steps as the number of neurons. Each weight adjusts the steepness of the associated step, while the bias takes into account translation.

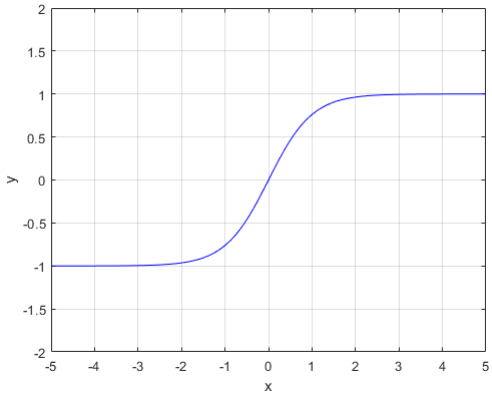

FIGURE 3.4: Hyperbolic tangent.

The transfer function of the output layer is a simple linear function

$$a_j = n_j, \tag{3.62}$$

since the output mapping is desired, no more transformations are wanted. Furthermore, this choice is in agreement with the universal approximation theorem (Hornik, Stinchcombe, and White, 1989; Cybenko, 1989), which states that a forward network with a linear output layer and at least one hidden layer with any squashing activation function (that is, a function that compresses the input into a small interval, such as the logistic or the tangent sigmoid) can approximate any continuous function on a closed and bounded subset of $\mathbb{R}^n$ from one finite-dimensional space to another without error, provided that the network has enough hidden units.

The performance index adopted in this thesis, for both training and test phases, is the Mean Squared Error (MSE), defined as

$$MSE = \frac{1}{N_E} \sum_{i=1}^{N_E} (t_i - a_i)^2, \tag{3.63}$$

where N_E is the total number of examples, t_i is the target output of the i-th example, and a_i is the output provided by the ANN, evaluated on the same example.

Another fundamental element is the learning algorithm; the one chosen is the Levenberg-Marquardt (Marquardt, 1963) one; it is a backpropagation algorithm, that is, the gradient of the error with respect to the weights is evaluated. The choice is

due to the fact that it is the fastest training method for multilayer networks with hundreds of weights and biases applied to function approximation problems (Hagan et al., 2014).

The weights at the step $k+1$ are evaluated as (Hagan et al., 2014)

$$\mathbf{w}_{k+1} = \mathbf{w}_k - [\mathbf{J}^T(\mathbf{w}_k)\mathbf{J}(\mathbf{w}_k) + \mu_k \mathbf{I}]^{-1}\mathbf{J}^T(\mathbf{w}_k)\mathbf{v}(\mathbf{w}_k), \tag{3.64}$$

where $\mathbf{J}$ is the Hessian matrix, $\mathbf{v}$ is the output error, and μ_k regulates the step amplitude.

The algorithm starts with a small value of μ_k. If the MSE does not decrease in a step, then this step is repeated with a greater value of μ_k, obtained by multiplying μ_k by a factor $\Theta > 1$. This operation should produce a smaller value of MSE, because a small step in the direction of the steepest descent is taken. If this happens, then μ_k is divided by Θ in the successive step. In this way, the amplitude of this new step decreases, the step is larger, and the convergence is accelerated. This ensures that the Levenberg-Marquardt algorithm is a very good compromise in terms of convergence velocity and guarantee (Hagan et al., 2014).

The iterations composing the Levenberg-Marquardt algorithm are the following (Hagan et al., 2014):

1. Presentation of the inputs, evaluation of the network output, estimation of the errors, associated with the q-th example, as $\mathbf{e}_q = \mathbf{t}_q - \mathbf{a}_q^M$, and of the performance index, $F(\mathbf{x})$.

2. Calculation of the Jacobian matrix, containing the second derivatives of the errors with respect to the weights, and of the sensitivities (derivatives of the errors with respect to the net input).

3. Application of Eq. 3.64.

4. Re-evaluation of the performance index using $\mathbf{w}_k + \Delta\mathbf{w}_k$. If the new index is smaller than that estimated in step 1, then the parameter μ is divided by Θ and the algorithm restarts from step 1; otherwise, μ is multiplied by Θ and the algorithm restarts from step 3.

In this thesis, Levenberg-Marquardt algorithm is coupled with Bayesian regularization, which helps to reduce the overfitting, hence improving the generalization. The Bayesian framework in ANNs assumes that the the weights w_{ij} and biases b_j are random variables. Therefore, the approach aims at evaluating the weights that maximize the conditional probability of the weights given the data.

There are several methods which objective is the selection of the regularization parameters (Hagan et al., 2014); the one herein chosen was developed by MacKay (MacKay, 1992) and puts the ANN training into the Bayesian framework abovementioned. The use of a Bayesian approach allows to use an ANN without a third set, called validation set, so that there are more examples at disposal for both the training and test sets.

$$||\mathbf{w}_i^1|| = 0.7(S^1)^{1/R}, \tag{3.65}$$

while the bias b_i is set to an uniform random value between $-||\mathbf{w}_i^1||$ and $||\mathbf{w}_i^1||$.

The training procedure adopts four, mutually exclusive, stopping criteria: maximum number of epochs, minimum MSE value, minimum error gradient, and maximum μ. The number of epochs indicates one complete pass through the training data (the whole training set, in the cases considered in this work); such a number is fixed equal to 1000, as, at this value, the test error has already stabilized or overfitting has already appeared (Hagan et al., 2014). The minimum error is set equal to a very small number, 10^{-16}; the minimum error gradient is 10^{-7}, while the maximum value of μ parameter is 10^{10}.

3.2.2 Principal Component Analysis (PCA)

The main reason why Principal Component Analysis (PCA) has been introduced is data visualization, since it allows to extract information from large quantities of data. This is very important, since the human eye and brain are a valuable pattern detection tool, however they can handle data only in low-dimensional space. PCA is a projection method which maps data to lower dimensional space with a linear transformation. This is possible since many data sets have points lying close to a manifold with less dimensions than the original data space (Bishop, 2006).

Basically, data is projected along directions called Principal Components (PCs), and they generate the principal subspace. It is possible to demonstrate, by maximizing variance or, equivalently, minimizing the error (Bishop, 2006), that the PCs $\mathbf{u}_i$ are the eigenvectors of the covariance matrix Σ, that is,

$$\Sigma \mathbf{u}_i = \psi_i \mathbf{u}_i, \tag{3.66}$$

where ψ_i is the eigenvalue corresponding to the eigenvector $\mathbf{u}_i$. Considering N_{obs} observations $\mathbf{x}_i$ of dimensionality H, with mean $\bar{\mathbf{x}}$, the covariance matrix is defined as

$$\Sigma = \frac{1}{N_{obs}} \sum_{i=1}^{N_{obs}} (\mathbf{x}_i - \bar{\mathbf{x}})(\mathbf{x}_i - \bar{\mathbf{x}})^T. \tag{3.67}$$

The first PC represents the maximum direction of maximum variability of the original data, which amount is represented by the corresponding eigenvalue. The successive PC, orthogonal to the first one, represents the second maximum contribution in variability of the data set, and so on.

By applying PCA, the data set has a reduced dimensionality H_{red}, with $H_{red} < H$. Both the variance maximization and error minimization approaches are intuitively explains in Fig. 3.5 for a simple case with data dimensionality $H = 2$ reduced to a principal subspace with $H_{red} = 1$ dimension and PC $\mathbf{u}_1$. Particularly, the search of the principal subspace is executed so that the variance of the orthogonal projections (green

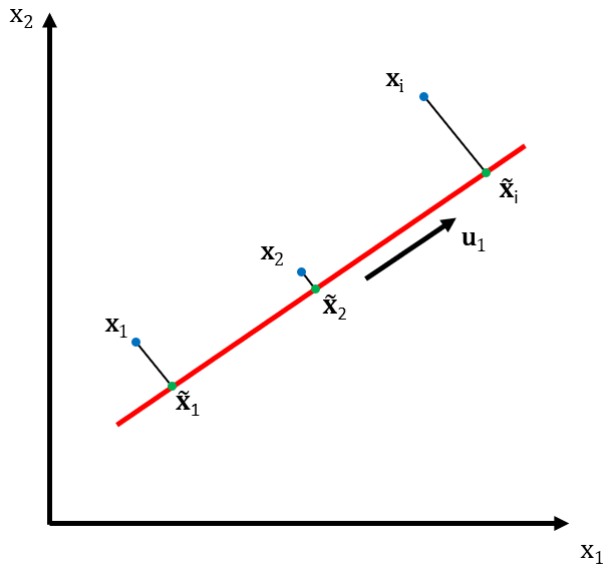

FIGURE 3.5: 2D data projected onto a 1D data by means of PCA.

dots $\tilde{\mathbf{x}}_i$) of the data (blue dots) $\mathbf{x}_i$ is maximized; alternatively, the error, represented by the blue lines, is minimized.

PCA turns out to be a fast and easy to compute method. Its capability of extracting the maximal information (in the sense of variance of projected data) is very helpful for cases with dimensionality problems.

3.3 SOBI algorithm

The SOBI algorithm further explained is used in Chapter 6 for determining the spectra of the exciting force. It is proposed by Jia et al. (Jia et al., 2020), who extend the work of McNeill and Zimmerman (McNeill and Zimmerman, 2008) to the prediction of random dynamic loads. The analytical details can be found in the referenced paper, providing them is outside the aims of this thesis, however it may be useful listing the computational steps, in order to give an idea of the involved parameters:

1. Obtain the structural responses in terms of time histories of point displacements.
2. Evaluate the PSD matrix of the structural responses.
3. Estimate of the modal matrix, modal damping ratio, and natural frequencies.
4. Calculate the PSD matrix of modal responses.
5. Evaluate the matrix $\mathbf{Z}_\phi(\omega)$ and the matrices of the modal loads PSD.
6. Estimate of the random dynamic load PSD matrix

The matrix $\mathbf{Z}_\phi(\omega)$ is a diagonal matrix which i-th element is

$$Z_i = \mu_i(\omega_i^2 - \omega^2 + j\eta_i\omega_i^2), \quad i = 1,2,...,N, \tag{3.68}$$

being N the total number of degrees of freedom. Eq. 3.68 can be easily recognized as the denominator of the transfer function.

Chapter 4

Experimental validation of scaling laws

This chapter concerns the validation of the scaling laws determined in Chapter 3. First, five CFCF flat plates in similitude are investigated, aiming at determining the natural frequencies and velocity response of the prototype. Then, three simply supported sandwich plates in similitude are studied; in this case, the radiated acoustic power of the prototype, in addition to the natural frequencies and velocity response, are determined.

Up to now, plates with CFCF boundary conditions have never been investigated, only with simply supported (De Rosa, Franco, and Meruane, 2015) and cantilever (Meruane, De Rosa, and Franco, 2015) conditions. This helps to demonstrate that the similitude conditions and scaling laws of plates do not depend of the boundary conditions.

Concerning sandwich structures, they have received little attention in similitude fields. Frostig and Simitses (Frostig and Simitses, 2004) investigate the buckling of sandwich plates with a soft core, while Yang et al. (Yang et al., 2013) focus on the size effects of sandwich plates subjected to low velocity impacts. Finally, Luo et al. (Luo et al., 2014b) try to determine the structure size interval for vibrating sandwich plates in similitude.

Basically, sandwich structures are three-layered media made of two thin and stiff face sheets bonded, or welded, to a relatively thick and low density core (Vinson, 1999). They are characterized by a high bending stiffness-to-weight ratio; their particular pattern allows to improve not only the mechanical efficiency, but also properties such as fire resistance, noise control, heating and cooling performances. Zenkert (Zenkert, 1995) provides more details; more recent insights on the vibroacoustic behavior are given in the review of D'Alessandro et al. **??**.

In recent years, metal foams have received great attention, as they possess a peculiar combination of properties, ranging from low specific weight and high stiffness-to-weight ratio, to high energy absorption capacity and good mechanical and acoustical damping. These characteristics make metal foams fitting for many applications, such as bare components to manufacture energy absorbers and silencers, as well as cores for sandwich configurations; more information is listed in the works of Bauhart (Bauhart,

2005) and Schwingel et al. (Schwingel et al., n.d.), which focus on automotive and aerospace engineering fields, respectively.

Metal foams are obtained by letting the liquid phase solidify and keeping, at the same time, the morphology of the foam. However, the manufacturing process is not fully controlled yet, which leads to randomized distributions of both mass and stiffness, as it strongly depends on the morphology of the pores of the metallic matrix, such as average size, shape, spatial distributions, etc. Therefore, due to the complexity of the system and the lack of complete design information, metallic foam sandwich structures require an extensive experimental evaluation in order to investigate their properties and potentialities, and how such a randomized distribution of mass and stiffness affects these properties. Such an experimental campaign may find advantages in the exploitation of similitude methods, since easier and less costly tests may be executed.

These are the main reasons behind the experimental tests herein illustrated. In Chapter 3 the derivation of two sets of conditions is described. A complete set, in which all the geometrical and material properties are explicited, and another, a reduced one, in which many parameters are gathered in just one term with physical meaning. The first set of similitude conditions and scaling laws is validated by performing an experimental modal analysis on three simply supported AFS plates models: the prototype, a proportional sides, and an avatar. The material characteristics are the same (in the framework of the material uncertainties previously mentioned), only the geometrical dimensions change so that the plate dimensions remain into the range of engineering significance. The size of the macrostructure - the whole panel - is never reduced so much to get closer to the size of the microstructure - the foam voids. Thus, it is reasonable to assume that the resulting size effects are negligible and do not affect both the scaling procedure and the dynamic response. Secondly, the tests reported in D'Alessandro et al. (D'Alessandro et al., 2014), performed on free-free sandwich plates, are used to validate the second set of similitude conditions and scaling laws, the reduced one. Particularly, the same prototype (with free-free conditions) is put in similitude with a proportional sides AFS plates with different core properties.

The first section of this chapter deals with the thin plates with CFCF boundary conditions, while the second reports the results for the AFS plates.

4.1 CFCF flat plates

All the flat plates are analyzed with the same boundary condition, that is clamped-free-clamped-free. The reference system is taken so that the long sides are those parallel to the x direction, while the short sides - that are the clamped ones - are parallel to the y direction. The plates are identified as a prototype (P), a replica (R), a proportional sides (PS), an avatar 1 (A1), and an avatar 2 (A2); they are shown in Fig. 4.1, while their geometrical and scaling characteristics are summarized in Table 4.1 (the scale factors are evaluated with respect to the prototype P as reported in Eq. 2.3). The material properties of the panels, used for both numerical and analytical simulations

in this chapter and in the remainder of the thesis, are listed in Table 4.2. The test articles exhibit slight differences in material properties, however they are not taken into account for the sake of simplicity (in order to assume that the scale factors of the material parameters reported in Table 4.2 are equal to 1).

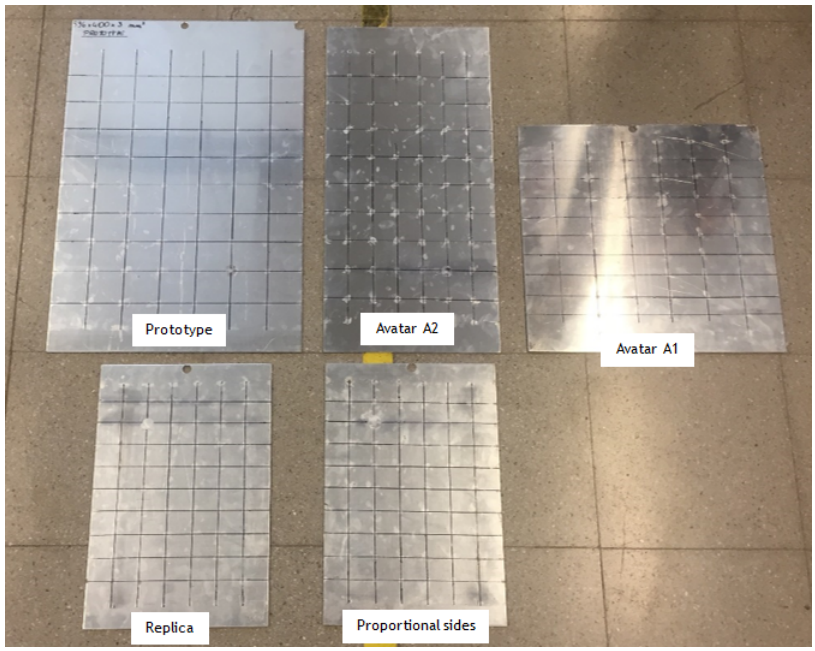

FIGURE 4.1: Flat plates in similitude.

	a [m]	b [m]	h [m]	λ_a	λ_b	λ_h
P	0.506	0.400	0.003	1.00	1.00	1.00
R	0.337	0.267	0.002	0.67	0.67	0.67
PS	0.337	0.267	0.003	0.67	0.67	1.00
A1	0.337	0.400	0.003	0.67	1.00	1.00
A2	0.500	0.280	0.002	0.99	0.70	0.67

TABLE 4.1: Geometrical and scaling characteristics of the flat plates in similitude.

Young's modulus, E	55×10^9 Pa
Mass density per unit volume, ρ	2723 kg/m^3
Poisson's ratio, ν	0.33
Damping loss factor, η	0.005

TABLE 4.2: Material characteristics assumed for the numerical and analytical simulations of flat plates.

An Experimental Modal Analysis (EMA) is executed on the plates, which are clamped horizontally, along the width, with bars bolted in three points (as shown in Fig. 4.2) and excited with an electrodynamic shaker, which is suspended above the plate with springs. The input signal is burst random; 8 PCB Piezotronics accelerometers return the output, i.e., the accelerations, in a frequency range 0-18840 rad/s, at frequency steps with amplitude equal to 2.30 rad/S (approximately 8197 spectral lines). The force and the acceleration are filtered with a Hanning window. Because a shaker is used, only one point is excited, with non-dimensional coordinates $(x_F, y_F) = (0.2000, 0.2875)$, while the response is measured in 88 acquisition points: 11 along the x direction, along the y direction. The non-dimensional coordinates of excitation and acquisition points are the same for all the plates.

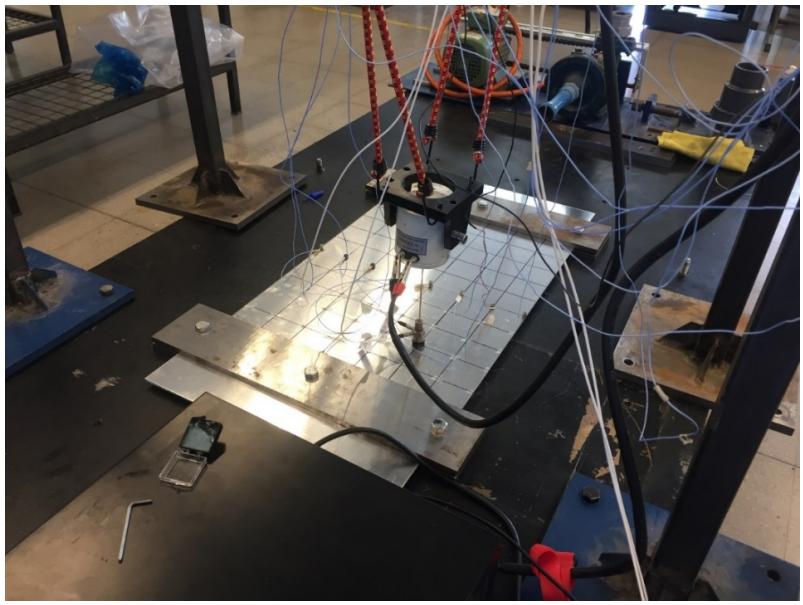

FIGURE 4.2: Experimental setup of a CFCF plate.

Once performed the tests, the results are compared with numerical simulations performed with NASTRAN, in which all the plates are modeled with the PSHELL property and QUAD elements. The numerical mesh replicates the experimental one. The colorbar reports the percentage of experimental-numerical correlation between the mode shapes. Red color indicates good correlation, green color represent medium values, while blue is typical of low correlation levels. The outcomes of these comparisons are shown in Fig. 4.3 and summarized in Tables 4.3-4.7 in terms of Modal Assurance Criterion (MAC), given by (Ewins, 2000)

$$MAC = \frac{|\{\psi_X^T\}\{\psi_A\}|^2}{(\{\psi_X^T\}\{\psi_X\})(\{\psi_A^T\}\{\psi_A\})}, \tag{4.1}$$

where ψ is the mode shape vector, and the subscripts X and A indicate the experimental and theoretical-analytical results, respectively.

In particular, the tables report, from left to right, the FEA mode number, the natural frequency numerically determined, the EMA mode number, the natural frequency experimentally determined, the percent discrepancy between the numerical and experimental natural frequency, and the percent MAC.

FEA	ω_{num} **[rad/s]**	**EMA**	ω_{exp} **[rad/s]**	**Diff. (%)**	**MAC (%)**
1	354.94	1	313.69	13.15	96.7
2	455.24	2	456.24	-0.22	95.1
3	904.32	4	965.11	-6.30	84.3
4	979.49	3	903.82	8.37	62.6
5	1125	5	1143.27	-1.60	95.7
6	1633.62	6	1672.99	-2.36	86.7
7	1861.52	8	2014.56	-7.60	88.9
8	1923.69	7	1827.67	5.25	67.2
9	2085.96	9	2135.45	-2.32	81.6
10	2581.14	11	2742.85	-5.90	75.5
11	2647.33	10	2620.64	1.02	72.8

TABLE 4.3: Experimental-numerical comparison, prototype; mean error: 0.13%.

FEA	ω_{num} **[rad/s]**	**EMA**	ω_{exp} **[rad/s]**	**Diff. (%)**	**MAC (%)**
1	533.49	1	540.20	-1.24	66.8
2	683.64	2	717.49	-4.71	72.4
3	1355.41	3	1422.67	-4.73	68
4	1472.16	4	1474.17	-0.14	67.6
5	1689.95	5	1744.08	-3.10	74.2
6	2451.15	6	2616.31	-6.31	75.9
7	2787.31	8	3099.74	-10.08	48.8
8	2891.25	7	2816.14	2.67	37.5
9	3134.10	9	3317.85	-5.54	52.3

TABLE 4.4: Experimental-numerical comparison, replica; mean error: -3.69%.

Fig. 4.3 shows that it is not possible to detect, experimentally, the same number of successive modes for all the plates; however, the first nine experimental natural frequencies and mode shapes are determined for all the models. The percent values of MAC are listed in Tables 4.3-4.7. In general, the numerical and experimental results show an acceptable correlation, except for some modes, which have not high MAC

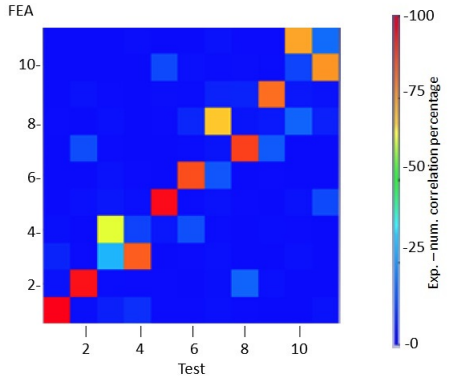

(A) Prototype

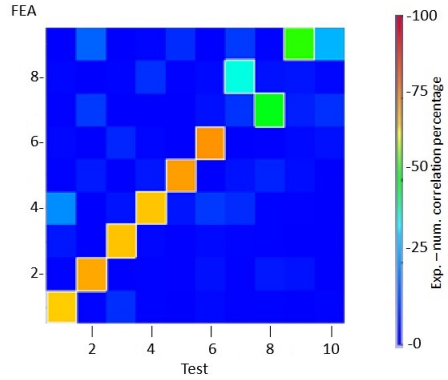

(B) Replica

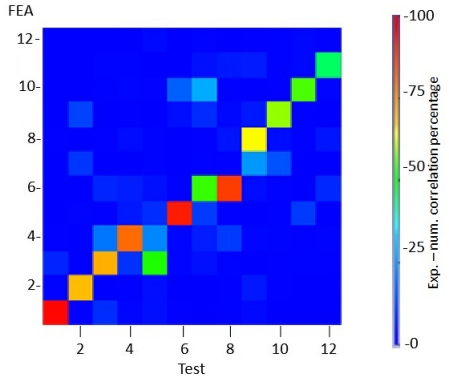

(C) Proportional sides

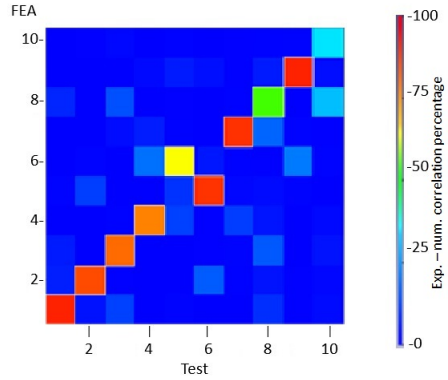

(D) Avatar 1

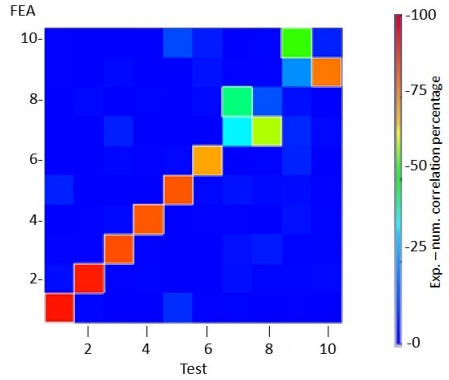

(E) Avatar 2

FIGURE 4.3: MAC between experimental and numerical results for the prototype (A), replica (B), proportional sides (C), avatar 1 (D), and avatar 2 (E).

FEA	ω_{num} [rad/s]	EMA	ω_{exp} [rad/s]	Diff. (%)	MAC (%)
1	799.88	1	817.28	-2.13	98.8
2	1024.46	2	1065.02	-3.81	69.3
3	2030.64	3	2153.60	-5.71	71.4
4	2206.35	4	2177.53	1.32	82.6
5	2531.78	6	2640.24	-4.11	95.4
6	3670.35	8	4032.14	-8.97	90.2
8	4330.94	9	4482.10	-3.37	64.3
9	4693.29	10	4904.30	-4.30	58.1
10	5791.23	11	6217.14	-6.85	54.1
11	5948.60	12	6386.76	-6.86	44.7

TABLE 4.5: Experimental-numerical comparison, proportional sides; mean error: -4.48%.

FEA	ω_{num} [rad/s]	EMA	ω_{exp} [rad/s]	Diff. (%)	MAC (%)
1	803.02	1	734.01	9.4	94.4
2	910.03	2	914.93	-0.54	87.8
3	1342.73	3	1396.48	-3.85	82.6
4	2214.64	4	2043.20	8.39	78.7
5	2250.19	6	2369.00	-5.01	91.6
6	2362.54	5	2336.16	1.13	63.9
7	2888.36	7	3057.79	-5.54	92.0
8	3693.96	8	3561.76	3.71	53.7
9	3827.35	9	3874.45	-1.22	94.4

TABLE 4.6: Experimental-numerical comparison, avatar 1; mean error: 0.72%.

FEA	ω_{num} [rad/s]	EMA	ω_{exp} [rad/s]	Diff. (%)	MAC (%)
1	241.47	1	218.98	10.26	96.7
2	364.68	2	370.33	-1.54	95.4
3	666.18	3	645.96	3.13	87.3
4	853.70	4	874.74	-2.41	85.4
5	999.46	5	1060.00	-5.71	86.0
6	1309.57	6	1324.44	-0.81	73.0
7	1525.54	8	1598.82	-4.59	59.6
8	1526.10	7	1549.59	-1.51	43.2
9	2169.17	10	2295.78	-5.51	80.5
10	2258.41	9	2158.12	4.65	52.8

TABLE 4.7: Experimental-numerical comparison, avatar 2; mean error: -0.40%.

percentage or same succession passing from the numerical simulation to the experimental test. In the latter case, the percentage reported in Tables 4.3-4.7 refer to the MAC evaluated for the experimental mode that best fits the numerical one.

There are several reasons behind these discrepancies, and the most relevant one is the realization of the boundary condition. In fact, the CFCF condition is not easy to setup as an homogeneous clamping must be assured. In this regard, aluminium strips, having the same thickness of the plate under investigation, are placed parallel to the clamped edges, in order to avoid a backward tilting of the bars. However, it is not possible to keep control of the clamping force for all the bolts; moreover, the clamping structure has its own flexibility which makes the condition not really clamped, even though the clamping force would be uniform.

Another reason behind the numerical-experimental discrepancies may be due to uncertainties on material properties. In fact, the numerical simulations are carried out with the same aluminium properties (those listed in Table 4.2) for all the models, although, as previously mentioned, the test articles exhibit slight variations in terms of Young's modulus and mass density. These variations are not considered for the sake of simplicity, so that material change is not introduced into the scaling laws (and in the creation of the training set in the further application of machine learning).

However, despite the experimental uncertainties, the tests show a correlation that is acceptable for the purpose of validating the scaling laws of natural frequencies and velocity response as derived by SAMSARA.

In this regard, the scaling laws given in Eq. 3.25 are used to predict the first nine natural frequencies of the prototype. The frequency scale factors, evaluated according to Eqs. 3.25, are summarized in Table 4.8, while the results are presented in Fig. 4.4

	Eq. 3.25a	**Eq. 3.25b**	**Eq. 3.25c**
Replica	1.50	1.50	1.50
Proportional sides	2.25	2.25	2.25
Avatar 1	2.25	1.00	1.50
Avatar 2	0.67	1.58	1.05

TABLE 4.8: Frequency scale factors of all the models given by Eqs. 3.25.

Table 4.8 shows how Eqs. 3.25 return the same scale factor for both replica and proportional sides, which are both true models, therefore the equations are equivalent; this happens since the similitude condition is satisfied, thus length and width scale equally. On the other hand, the same equations return different results when applied to both avatar 1 and 2, since length and width scale differently. Particularly, Eq. 3.25a provides the same scale factor for proportional sides and avatar 1, however it does not work fine for the latter, since it is a distorted model and each natural frequency scales differently and, generally, with scale factors different from those of the proportional sides. Eq. 3.25b applied to avatar 1 gives another proof of the wrong evaluation of a scale factor for partial similitudes, since the equation returns a value equal to 1, which

means that the natural frequencies do not change. A quick look at Fig. 4.4c shows that this is not true. In fact, the natural frequencies of the model and of the prototype are not the same, thus the scale factor must be, necessarily, different from 1.

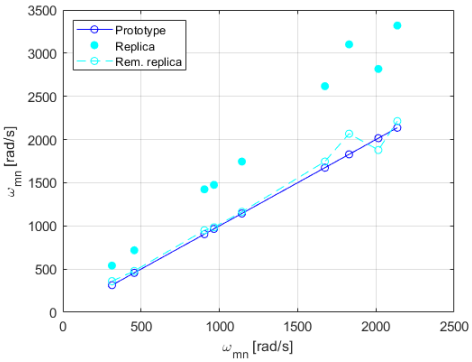

(A) Prototype-Replica

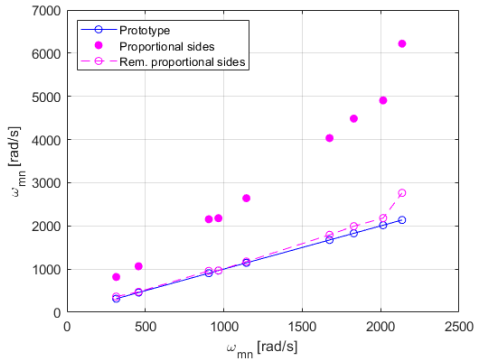

(B) Prototype-Proportional sides

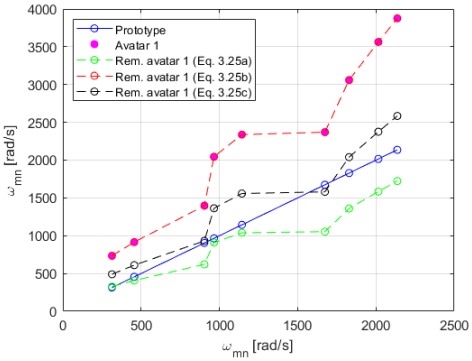

(C) Prototype-Avatar 1

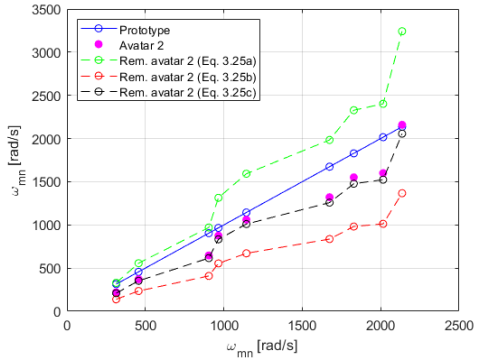

(D) Prototype-Avatar 2

FIGURE 4.4: Predictions of the prototype natural frequencies from different models: replica (A), proportional sides (B), avatar 1 (C), and avatar 2 (D).

Fig. 4.4 illustrates the reconstruction of the natural frequencies of the prototype, starting from each of the model considered, by using Eqs. 3.25. The natural frequencies of the prototype are reported on the horizontal axis, while those of the compared model are reported on the vertical axis. In all the figures, the blue line with empty dots is the prototype reference, each dot representing the natural frequency. The full colored dots represent the model natural frequencies, and the dashed line with empty dots represents the prediction of the prototype natural frequencies by means of the scaling laws. A successful prediction implies the latter curve overlapping the prototype curve.

Figs. 4.4a-4.4b illustrate the predictions from replica and proportional sides, respectively. Since Eqs. 3.25 return the same scale factor, there is just one remodulation (abbreviated to rem. in the figures) curve. In fact, Eqs. 3.25 reduce to Eq. 3.23 in the case of the replica, and to Eq. 3.24 in the case of the proportional sides. The

prediction is accurate for both the models; the slight decorrelation which appears with the last natural frequencies is due to the experimental uncertainties, not to the similitude method. Thus, the results agree with the similitude conditions and the change of thickness does not lead to non-scalable effects.

The predictions provided by avatars 1 and 2 are shown in Figs. 4.4c-4.4d. This time, there are three remodulation curves since Eqs. 3.25 return three different scale factors for each model (the reference equation of each curve is reported in the legend). Both the plots highlight how there is no scaling law which works well in all the frequency range. Eq. 3.25a seems to work fine in the range 200-500 rad/s for avatar 1, then in the range 900-1250 rad/s, however this is not enough to state that Eq. 3.25a allows an acceptable reconstruction of the prototype natural frequencies. The same holds for Eq. 3.25c, which frequency remodulation is close to the prototype values for the third and sixth natural frequencies. Eq. 3.25b fails the prediction in all the frequency range. Moreover, even even though more frequencies would have been well remodulated, a check on the mode would be mandatory, since, as written in Chapter 3, partial similitudes overturn the mode succession and this phenomenon is not taken into account by the scaling laws derived. Finally, all Eqs. 3.25 do not work well with avatar 2.

Concerning the reconstruction of the mobility, it develops into two steps: first, amplitude scaling, then frequency remodulation in order to align the resonance peaks. The amplitude scale factors are summarized in Table 4.9. There are no geometrical similitude conditions associated to mobility (or velocity) response, thus there is just one scaling law (Eq. 3.48 or, equivalently, Eq. 3.46). However, since the frequency scale factor appears into the mobility scaling law, there are as many mobility scale factors as the number of natural frequency scaling laws (Eqs. 3.25), even though the mobility scaling law (Eq. 3.48) is unique. These scale factors are summarized in Table 4.9

	Eq. 3.25a	**Eq. 3.25b**	**Eq. 3.25c**
Replica	2.23	2.23	2.23
Proportional sides	1.01	1.01	1.01
Avatar 1	0.30	0.67	0.44
Avatar 2	3.26	1.37	2.07

TABLE 4.9: Mobility scale factors of all the models given by Eqs. 3.25 and Eq. 3.48.

In order to validate the mobility scaling laws, the accelerance measurements are, first, transformed into mobility (dividing them by $j\omega$), then averaged on all the acquisition points. The results are shown in Figs. 4.5-4.8 for all the models.

Figs. 4.5-4.6 report the dynamic response of replica and proportional sides models, before (Figs. 4.5a-4.6a) and after (4.5b-4.6b) the remodulation process. In both cases, the reconstruction is acceptable; also here, the differences are due to experimental uncertainties. Instead, Figs. 4.7-4.8 show that even the dynamic response is

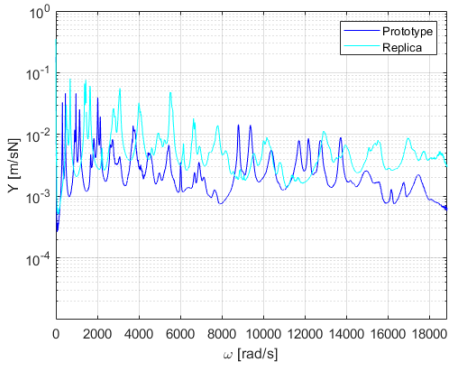

(A) Not remodulated.

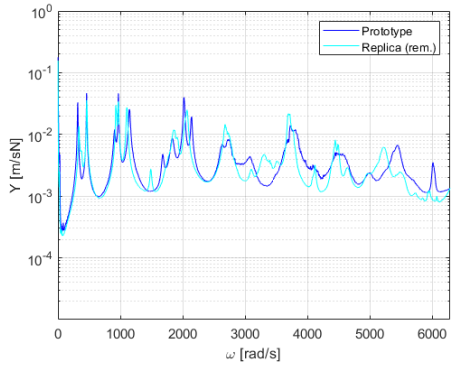

(B) Remodulated.

FIGURE 4.5: Comparisons between the spatially averaged mobilities of prototype and replica, before (A) and after (B) the remodulation.

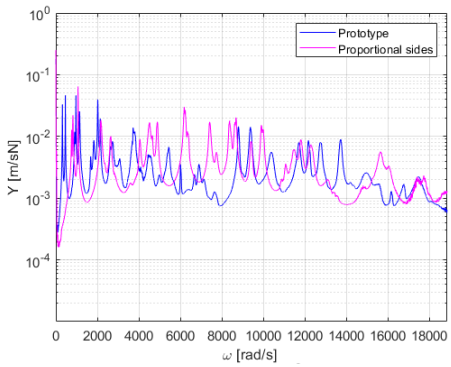

(A) Not remodulated.

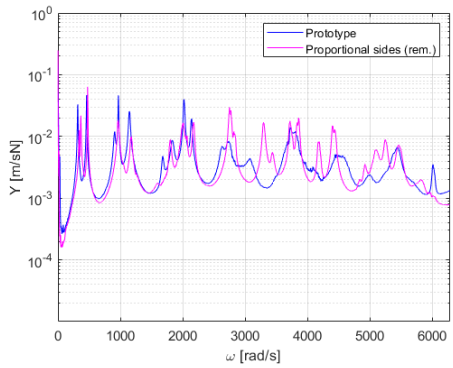

(B) Remodulated.

FIGURE 4.6: Comparisons between the spatially averaged mobilities of prototype and proportional sides, before (A) and after (B) the remodulation.

not predictable from avatars. In particular, Figs. 4.7a-4.8a report the prototype and model (avatar 1 and 2, respectively) mobility without remodulation, Figs. 4.7b-4.7d and 4.8b-4.8d the attempts of prediction with the scale factors given in Table 4.9. The lack of an univocal scale factor for the natural frequencies affects, first, the amplitude prediction, since the mobility scale factor depends on the frequency scale factor (Eq. 3.48); moreover, even the frequency remodulation is not accurate, because the natural frequencies are not well predicted. Therefore, the mobility predictions in Figs.4.7b-4.7d and 4.8b-4.8d are not satisfactory. The only positive aspect is that the prototype and predicted responses are still in the same range of values.

The scaling laws work not only for the spatially averaged responses, but also for

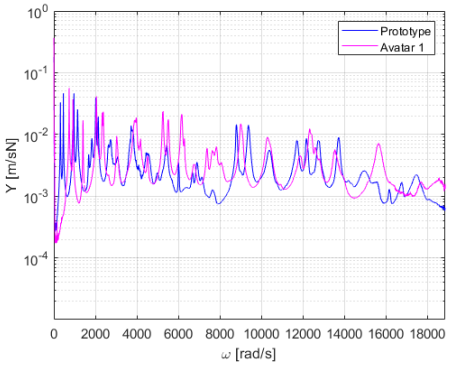

(A) Not remodulated.

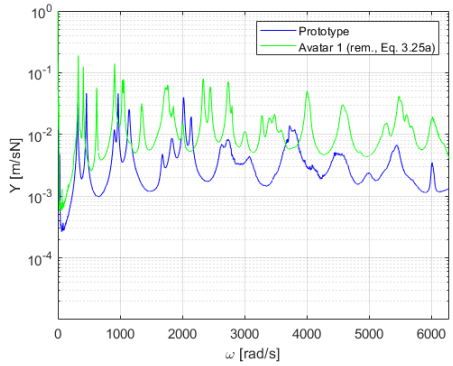

(B) Remodulated, eq. 3.25a.

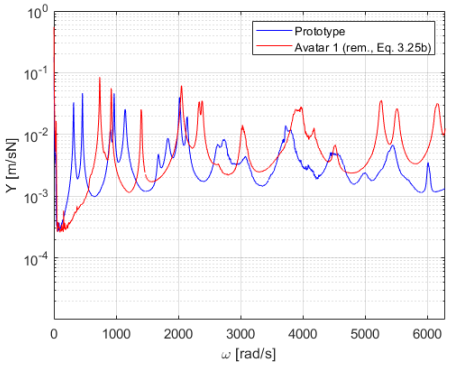

(C) Remodulated, eq. 3.25b.

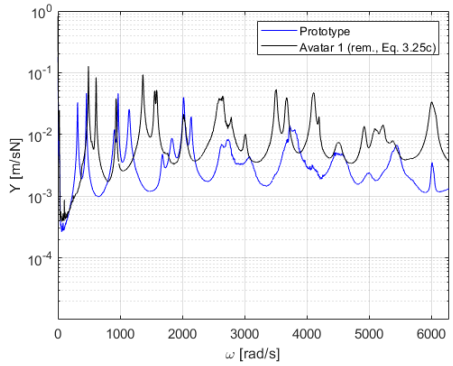

(D) Remodulated, eq. 3.25c.

FIGURE 4.7: Comparisons between the spatially averaged mobilities of prototype and avatar 1, before (A) and after (B)-(D) the remodulation.

the local responses. This is demonstrated in Figs. 4.10-4.13, which show the remodulated local mobility of three nodes (labeled 28, 54, and 67, which non-dimensional coordinates are reported in Table 4.10) of each model. The positions of the chosen acquisition points on the plates are shown in the top view of Fig. 4.14, obtained by means of FEMAP Graphical User Interface (GUI); the red circle indicates the excitation point, while the yellow circles indicate the acquisition points. Particularly, from Fig. 4.10 to Fig. 4.13, the remodulations of the replica, proportional sides, avatar 1 and 2 are shown, respectively. For sake of brevity, the avatars in Figs. 4.12-4.13 are remodulated only with Eq. 3.25a.

Again, as expected, the response is well reconstructed in the cases of replica and proportional sides, while it is not for both avatars, still returning inaccurate results in terms of mobility amplitude and frequency.

In conclusion, these tests validate the scaling laws determined for CFCF plates and underline that the prototype response can be reconstructed from the response of model in complete similitude, while this is not possible when the similitude is distorted.

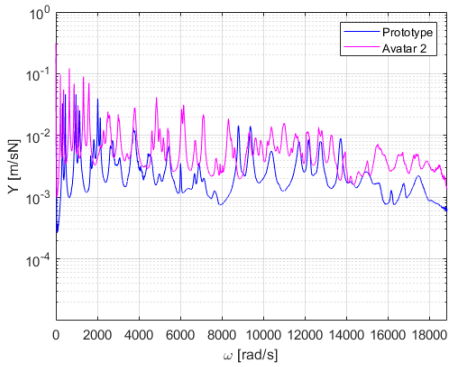

(A) Not remodulated.

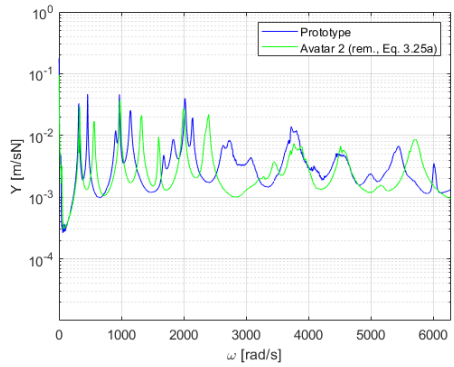

(B) Remodulated, eq. 3.25a.

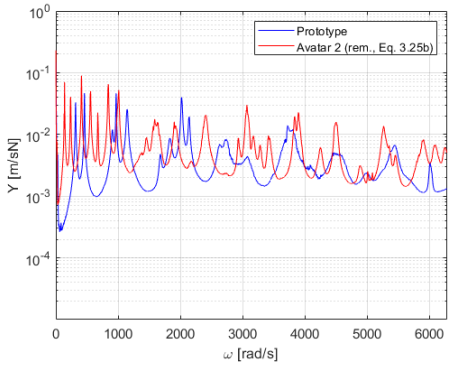

(C) Remodulated, eq. 3.25b.

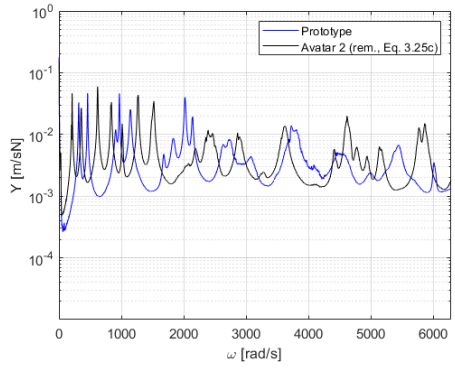

(D) Remodulated, eq. 3.25c.

FIGURE 4.8: Comparisons between the spatially averaged mobilities of prototype and avatar 2, before (A) and after (B)–(D) the remodulation.

	x_R	y_R
Node 28	0.300	0.572
Node 54	0.600	0.286
Node 67	0.800	0.715

TABLE 4.10: Nondimensional coordinates of the nodes 28, 54, and 67 in which the local response is evaluated.

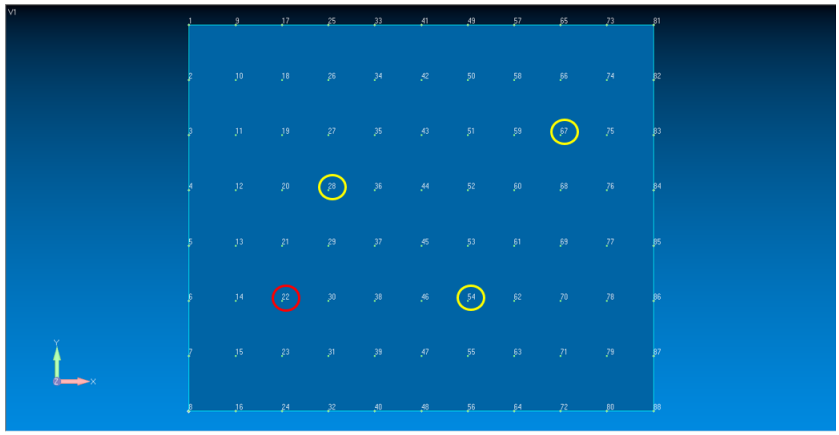

FIGURE 4.9: Top view of the plate with the 88 acquisition points numbered. The excitation point is indicated by the red circle, the acquisition points used for the evaluation of the local response are indicated by the yellow circles.

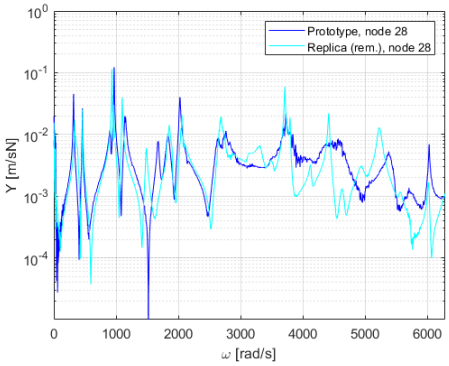

(A) Node 28.

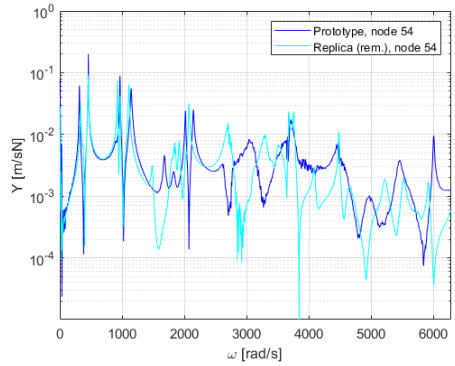

(B) Node 54.

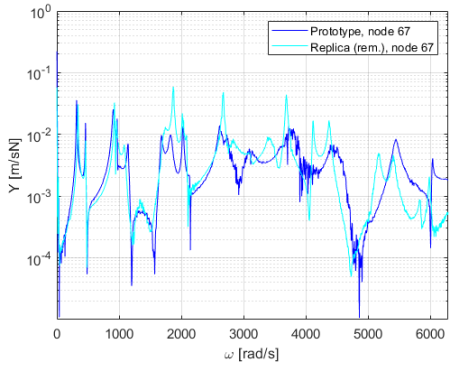

(C) Node 67.

FIGURE 4.10: Comparisons between the local mobilities of prototype and replica, node 28 (A), node 54 (B), node 67 (D).

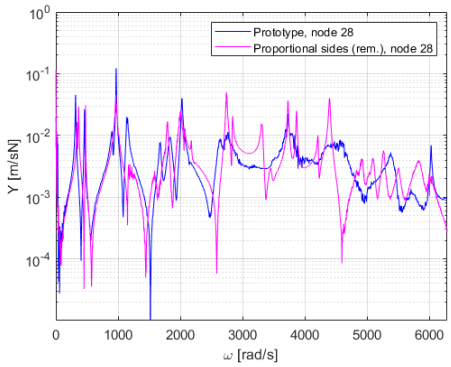

(A) Node 28.

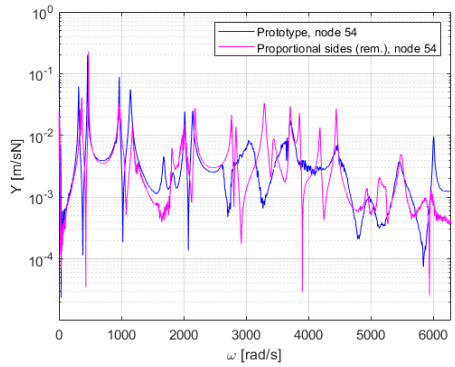

(B) Node 54.

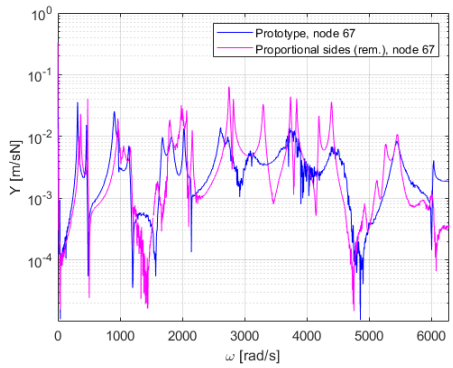

(C) Node 67.

FIGURE 4.11: Comparisons between the local mobilities of prototype and proportional sides, node 28 (A), node 54 (B), node 67 (C).

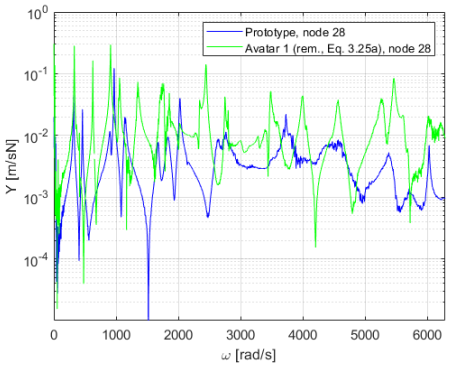

(A) Node 28.

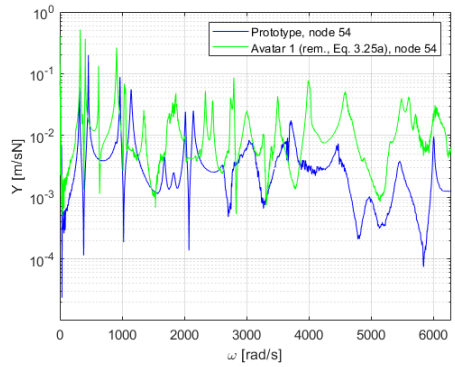

(B) Node 54.

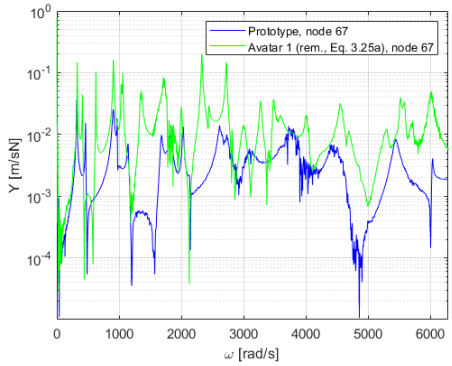

(C) Node 67.

FIGURE 4.12: Comparisons between the local mobilities of prototype and avatar 1, node 28 (A), node 54 (B), node 67 (C).

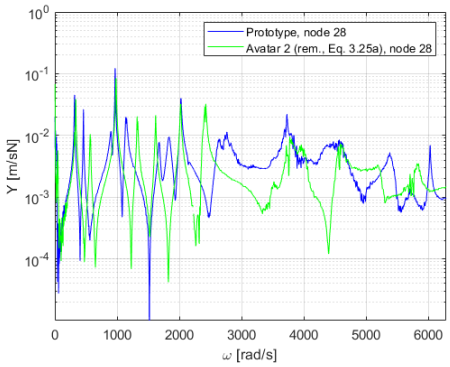

(A) Node 28.

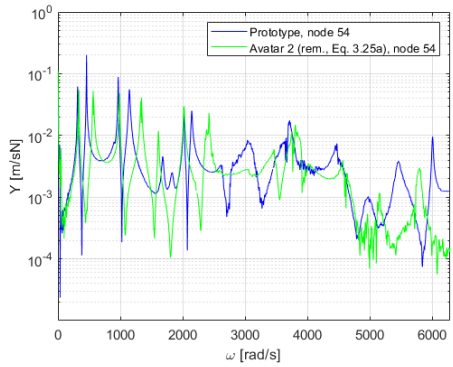

(B) Node 54.

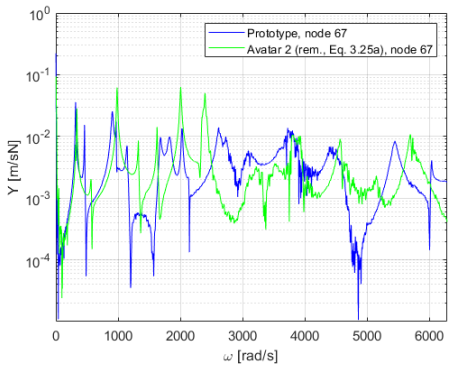

(C) Node 67.

FIGURE 4.13: Comparisons between the local mobilities of prototype and avatar 2, node 28 (A), node 54 (B), node 67 (C).

4.2 Simply supported sandwich plates

This section concerns the experimental tests performed on simply supported AFS panels. These plates are made of the same material and will be indicated as panels of type A. The models are a prototype (PA), a proportional sides (PSA), and an avatar (AA). Then, the prototype PA is put in similitude with a proportional sides model which core is made with an aluminium foam (plate of type B, thus PSB model), having free boundary conditions. The geometrical characteristics and their scale factors are summarized in Table 4.11. Table 4.12 reports the material characteristics of the facings, while Table 4.13 summarizes the core properties of both plates A and B [determined by D'alessandro et al. (D'Alessandro et al., 2014)].

	a [m]	**b [m]**	**h_f [m]**	**h_c [m]**	λ_a	λ_b	λ_{h_f}	λ_{h_c}
PA	0.656	0.476	0.001	0.008	1.00	1.00	1.00	1.00
PSA	0.558	0.405	0.001	0.008	0.85	0.85	1.00	1.00
AA	0.656	0.405	0.001	0.008	1.00	0.85	1.00	1.00
PSB	0.656	0.476	0.0006	0.0074	1.00	1.00	0.60	0.92

TABLE 4.11: Geometrical and scaling characteristics of the AFS plates in similitude.

Young's modulus, E_f	71×10^9 Pa
Mass density per unit volume, ρ_f	2700 kg/m^3
Poisson's ratio, ν_f	0.33

TABLE 4.12: Material characteristics of panels A and B facings.

Panel	**E_c [Pa]**	**ρ_c kg/m^3**	ρ_r	ν_c
A	6.48×10^9	600	0.222	0.31
B	3.43×10^9	390	0.144	0.31

TABLE 4.13: Material characteristics of panels A and B cores.

In particular, the fourth column of Table 4.13 lists the values of the relative foam density ρ_r, namely, the ratio between the foam density and the standard value of aluminium density (D'Alessandro et al., 2014). In the case considered, the change in relative density is due only to the quantity of voids, because the average cell size of the bubbles is unvaried and equal to 2 mm. Thus, the values listed in Table 4.13 are representative of an aluminium foam core with the given relative density and dimension of the voids.

First, the simply supported panels are experimentally tested in order to validate the similitude conditions given by Eq. 3.37 and the scaling laws in Eq. 3.39. Then, the free panels are tested in order to demonstrate that, gathering many parameters into

one with physical meaning, Eq. 3.40 still returns a true model, useful to reconstruct the behavior of the prototype.

Simply supported panels

The simply supported boundary conditions of the panels of type A is realized according to the instructions provided by Robin et al. (Robin et al., 2016); the test setup is shown in Fig. 4.14. Also in this case, the excitation is generated by an electrodynamic shaker, suspended above the models with springs, while the response is acquired by means of accelerometers. The frequency range, number of spectral lines and non-dimensional excitation and acquisition points are the same of the experiments made with the CFCF plates.

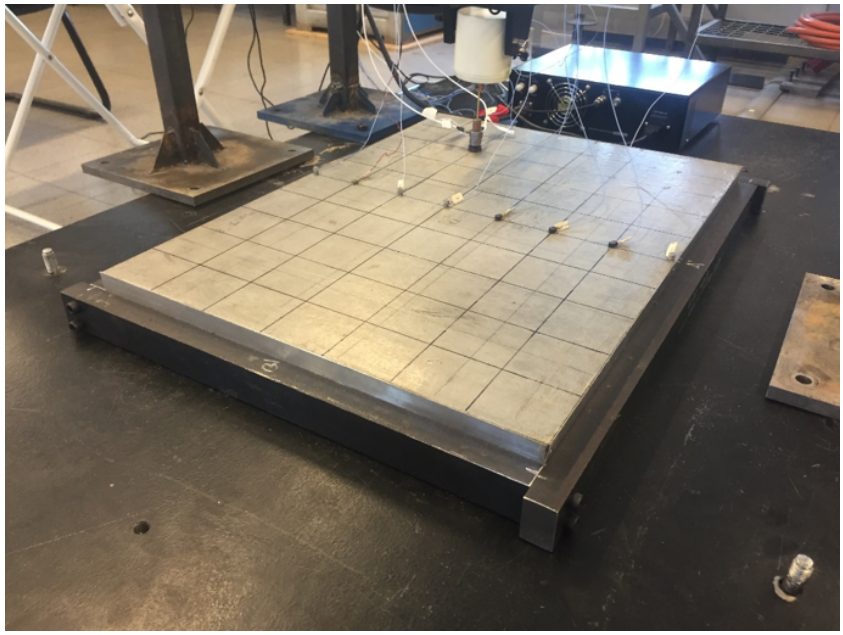

FIGURE 4.14: Experimental setup of the simply supported AFS panel.

The experimental results are then compared with numerical simulations obtained with NASTRAN. The PSHELL property is used to create a numerical model of the panel. The sandwich configuration is generated by describing the plates with a lay-up made by three layers: two skins and one core, having the geometrical and material properties reported in Tables 4.11-4.13. Thus, using a plane property, not a solid one, the mesh is generated with QUAD elements.

The experimental-numerical comparisons are reported in terms of MAC; they are summarized in Fig. 4.15 and Tables 4.14-4.16 and it is noticeable a very good correlation between the experimental and numerical results, with values assessing between 90% and 100%. Only the third and fourth mode of the avatar (Fig. 4.15c) have

MAC values around 60%. According to the results provided by D'Alessandro et al. (D'Alessandro et al., 2014), this may be due to the not homogeneous distribution of stiffness and mass in the core of the real plate. However, these results highlight that, generally, building the sandwich lay-up and using the PSHELL property is a satisfactory approach in modelling sandwich plates made of isotropic material.

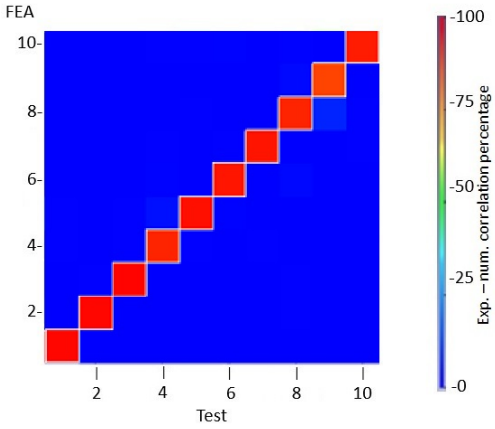

(A) Prototype.

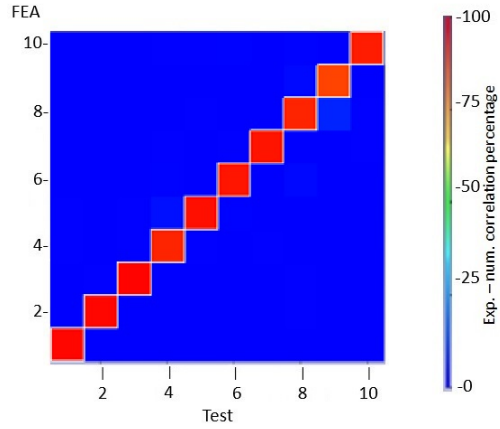

(B) Proportional sides.

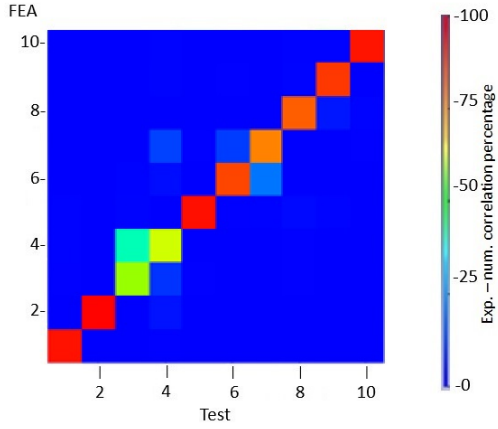

(C) Avatar.

FIGURE 4.15: MAC between experimental and numerical results for the prototype (A), proportional sides (B), avatar (C).

The panels of type A have same thickness and material properties. Only the planform changes, thus $\lambda_{E_f} = \lambda_{E_c} = \lambda_h = \lambda_{h_c} = 1$: the first two similitude conditions of Eq. 3.37 are satisfied. The frequency scale factors are then derived by means of Eq. 3.39. They are summarized in Table 4.18. As expected, Eqs. 3.39 return the same scale factor for the proportional sides A, being $\lambda_a = \lambda_b$; conversely, each law returns different scale factors when applied to the avatar, since $\lambda_a \neq \lambda_b$.

FEA	ω_{num} [rad/s]	EMA	ω_{exp} [rad/s]	Diff. (%)	MAC (%)
1	1208.08	1	1204.38	0.31	93.6
2	2443.04	2	2338.80	4.46	94.2
3	3581.92	3	3749.98	-4.48	99.0
4	4496.10	4	4600.98	2.28	98.4
5	4763.82	5	4780.40	-0.35	97.4
6	6746.60	6	6661.20	1.28	98.2
7	7323.74	7	7247.75	1.05	94.2
8	7452.48	8	7520.3	-0.91	90.4
9	8583.50	9	8610.51	-0.31	97.9
10	9500.38	10	9389.23	1.18	98.2

TABLE 4.14: Experimental-numerical comparison, prototype; mean error: 0.45%.

FEA	ω_{num} [rad/s]	EMA	ω_{exp} [rad/s]	Diff. (%)	MAC (%)
1	1658.57	1	1771.23	-6.36	99.0
2	3326.44	2	3473.47	-4.23	99.1
3	4929.41	3	5153.84	-4.36	99.5
4	6092.55	4	6336.59	-3.85	94.1
5	6508.12	5	6653.89	-2.19	97.5
6	9155.23	6	9133.87	0.24	96.5
7	9880.30	7	9913.61	-0.34	96.8
8	10217.09	8	10091.42	1.25	94.2
9	11709.97	9	11542.84	1.45	89.1
10	12817.70	10	12549.40	2.13	95.5

TABLE 4.15: Experimental-numerical comparison, proportional sides; mean error: -1.63%.

The results about the prediction of the natural frequencies are shown in Fig 4.16. Fig. 4.16a reports the remodulation from the proportional sides model. The remodulated curve overlaps the prototype curve, hence the prediction is accurate and Eq. 3.38 or, equivalently, Eq. 3.39, works fine. The reference and remodulated curves slightly diverge only after 7000 rad/s. This may be due to experimental uncertainties, as well as the effect of the voids contained into the aluminium foam, which lead to not homogeneous distributions of foam mass and stiffness. However, the difference is small and it cannot be ascribed to the similitude method for sure.

Fig. 4.16b shows three remodulated curves, one for each scale factor provided by Eqs. 3.39. No curve provides an accurate prediction in all the frequency range of interest. Only the first two natural frequencies seem to be recovered with a quite acceptable accuracy by all the scaling laws, with Eq. 3.39b working fine up to the third natural frequency. However, after 4000 rad/s all the curves diverge, with the

FEA	ω_{num} [rad/s]	EMA	ω_{exp} [rad/s]	Diff. (%)	MAC (%)
1	1518.21	1	1532.20	-0.90	96.9
2	2753.42	2	2816.12	-2.23	99.5
3	4796.46	3	4886.68	-1.85	58.4
4	4815.62	4	4932.30	-2.37	61.4
5	5966.70	5	6254.34	-4.60	97.6
6	7660.46	6	7588.20	0.95	88.6
7	7933.15	7	7704.44	2.97	78.6
8	10090.17	8	9621.44	4.87	84.6
9	10672.62	9	10283.06	3.79	91.0
10	11199.15	10	11104.27	0.86	96.8

TABLE 4.16: Experimental-numerical comparison, proportional sides; mean error: 0.15%.

	Eq.3.39a	Eq. 3.39b	Eq. 3.39c
Proportional sides A	1.38	1.38	1.38
Avatar	1.09	0.92	1.18

TABLE 4.17: Frequency scale factors of all the models given by Eqs. 3.39.

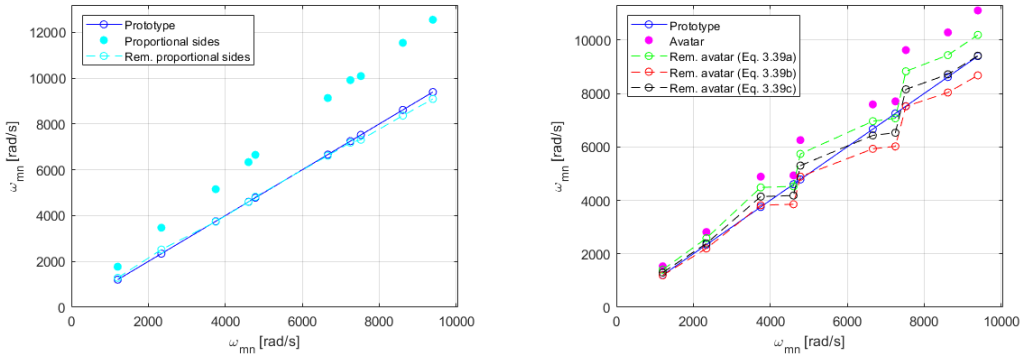

(A) Prototype–Proportional sides.

(B) Prototype–Avatar.

FIGURE 4.16: Predictions of the prototype natural frequencies from proportional sides (a) and avatar (b) models.

exception of that associated to Eq. 3.39c, which oscillates around the reference curve, then converges again, recovering the last two natural frequencies. However, also in this case, since the modes succession is not retained in avatars, even if some natural frequencies are well predicted it is not known each frequency to which mode is associated, therefore the reconstruction of an important information, associated with the spatial pattern of vibration, is lost.

Concerning FRF scaling, the scale factors for both proportional sides and avatar are reported in Table 4.18. Again, the proportional sides is characterized by an univocal mobility scale factor, while the avatars are associated with as many frequency scale factors as the number of scaling laws, leading to the same number of velocity scale factors.

	Eq. 3.39a	**Eq. 3.39b**	**Eq. 3.39c**
Proportional sides A	0.99	0.99	0.99
Avatar	1.08	0.92	1.00

TABLE 4.18: Mobility scale factors of all the models given by Eqs. 3.39 and Eq. 3.48.

The measured accelerance is transformed into mobility, then averaged on all the acquisition points. Fig. 4.17a reports the spatially averaged mobilities of both prototype and proportional sides model, in the range of frequencies covering the first ten resonance peaks of the prototype. The prototype and the only remodulated model curve match quite accurately (Fig. 4.17b), although small discrepancies in amplitude for the first three modes. Moreover, the slight error in predicting the natural frequencies, noticed in Fig. 4.16a, is observed in Fig. 4.17b, in which the last two resonance peaks are misaligned. The remodulation is acceptable up to 8000 rad/s. While the discrepancies in amplitude may be due to experimental uncertainties, the likely cause behind the slight shift of resonance peaks are those previously underlined, i.e., the not homogeneous distribution of mass and stiffness in the core.

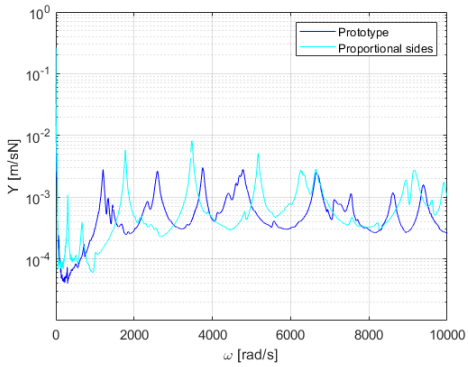

(A) Not remodulated.

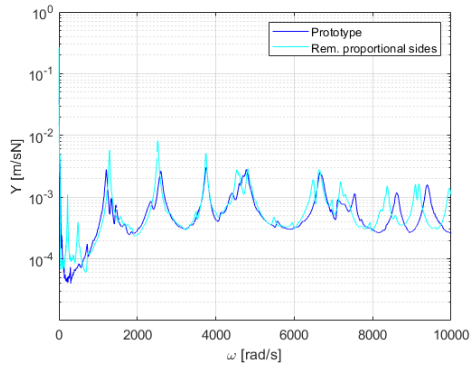

(B) Remodulated.

FIGURE 4.17: Comparisons between the spatially averaged mobilities of prototype and proportional sides model, before (A) and after (B) the remodulation.

The results obtained from avatars are shown in Fig. 4.18. Fig. 4.18a shows the mobilities of prototype and not remodulated avatar. No scale factor from Table 4.18 works fine, as Figs. 4.18b-4.18d demonstrate. All the reconstructions exhibit some

resonance peaks aligned, which correspond to the natural frequencies well predicted reported in Fig. 4.16b. Particularly, Eq. 3.39c seems to return a good prediction in terms of amplitude and frequency, especially by looking at the first resonance peak and the last two ones (in the range 8000-10000 rad/s). Thus, although some scaling laws seem to work fine in the specified frequency range, it is not possible to generalize this correspondence between scaling law and range to all the other avatars, defined with other scale factors (while it is possible, indeed, to generalize for proportional sides, because the scaling law is univocal and works fine in all the frequency range).

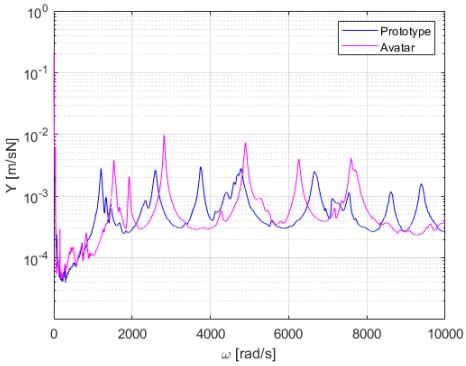

(A) Not remodulated.

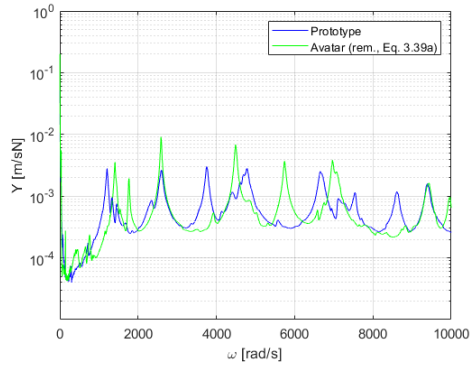

(B) Remodulated, Eq. (3.22a).

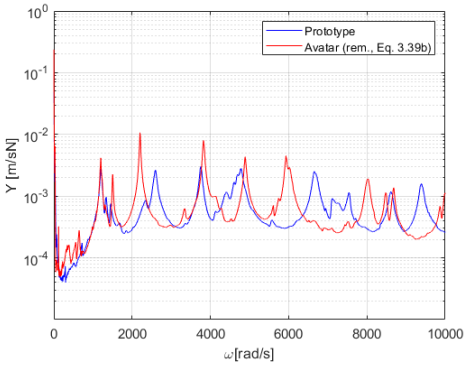

(C) Remodulated, Eq. (3.22b).

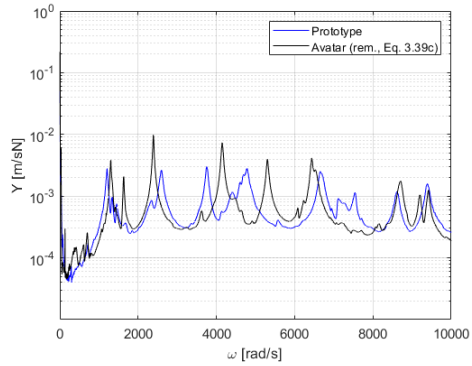

(D) Remodulated, Eq. (3.22c).

FIGURE 4.18: Comparisons between the spatially averaged mobilities of prototype and avatars, before (A) and after (B)-(D) the remodulation.

For sake of completeness, the remodulation of the local responses are shown also for these panels. The local acquisitions considered are the same of the CFCF models (refer to Fig. 4.11 and Table 4.13 for the non-dimensional coordinates). Fig. 4.19 reports the reconstruction from the proportional sides. in general, the same level of accuracy of the averaged response is retained, with an acceptable remodulation up to 8000 rad/s even for the local response.

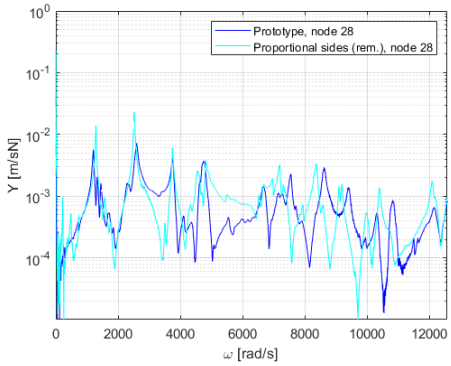

(A) Node 28.

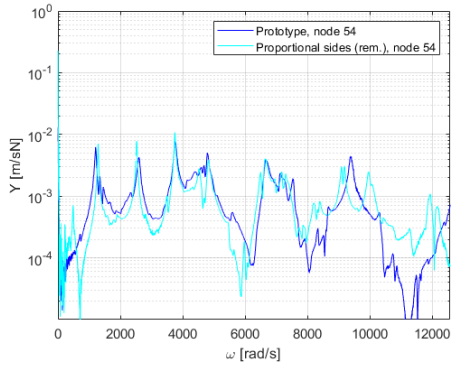

(B) Node 54.

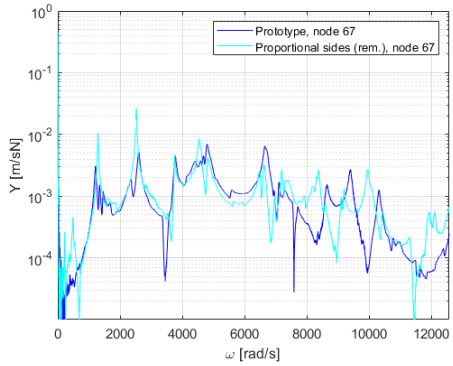

(C) Node 67.

FIGURE 4.19: Comparisons between the local mobilities of prototype and proportional sides AFS plates, node 28 (A), node 54 (54), and node (67).

The results obtained from the avatar are shown in Fig. 4.20; also here, only Eq. 3.39a is used to demonstrate that, even at local level, it is not possible to predict the response of the prototype.

About the evaluation of the radiated acoustic power, it is estimated by introducing the accelerometric measurements, transformed into velocity, into a MATLAB code implementing Eq. 3.52. As a matter of fact, the experimental mesh is such that the elements in which the panel is discretized have dimensions satisfying the requirements to apply Eq. 3.52, using the velocities measured at the corners of each element instead of the centers. The remodulation is carried out as described in section 3.1.3.

Fig. 4.21 reports the results obtained from the proportional sides. Firstly, it is noticeable a strong resemblance with the behavior of the mobilities, due to the direct involvement of velocity into Eq. 3.52. As specified in section 3.1.3, it is not possible to derive a scaling law for the radiated acoustic power written in discrete coordinates because of the radiation matrix; however, the prototype acoustic power can be reconstructed from that of the proportional sides. Therefore, the acoustic power of the

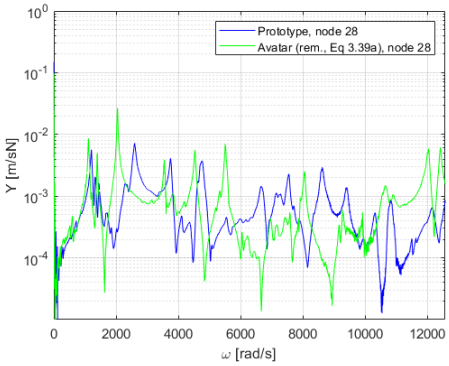

(A) Node 28.

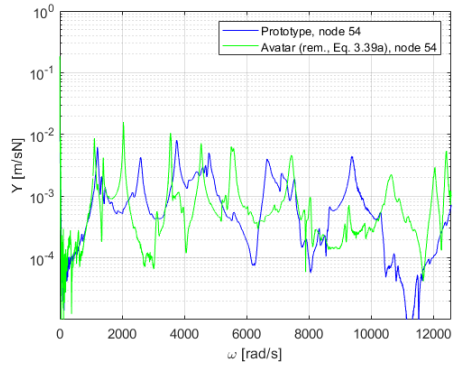

(B) Node 54.

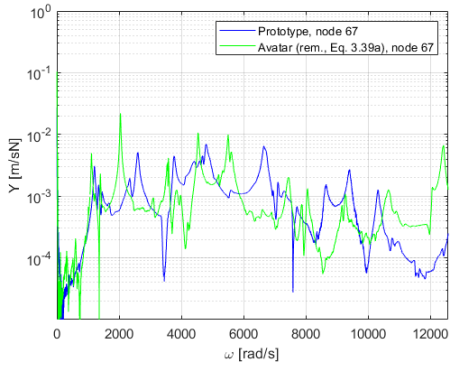

(C) Node 67.

FIGURE 4.20: Comparisons between the local mobilities of prototype and avatar AFS plates, node 28 (A), node 54 (54), and node (67).

proportional sides (Fig. 4.21a) can be remodulated (Fig. 4.21b): the predictions are acceptable and exhibit the same amplitude and frequency inconsistencies observed in the velocity reconstruction (Fig.4.17b) (since the correlation with mobility).

Analogously, Fig. 4.22 proves that the distortion introduced by not univocal frequency scaling laws, since affecting the mobility prediction, it also has influence on the reconstruction of the radiated acoustic power. Thus, three remodulated curves are obtained, as Figs. 4.22b-4.22d highlight, and some resonance peaks and amplitudes are well predicted in the same measure as shown in Figs. 4.18b-4.18d. However, no law allows a faithful prediction of the radiated acoustic power, yet.

4.2.1 Free-free panels

In order to validate the similitude condition and scaling law given by Eq. 3.21 and Eq. 3.40, the results of vibroacoustic experiments performed by Petrone et al. (Petrone et al., 2014), which experimental setup is shown in Fig. 4.23, are used. The prototype PA

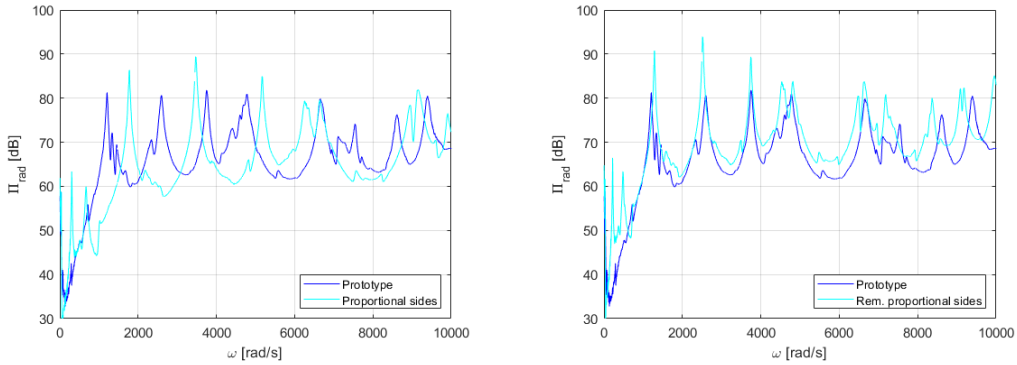

(A) Not remodulated. (B) Remodulated.

FIGURE 4.21: Comparisons between the radiated acoustic powers of prototype and proportional sides model, before (A) and after (B) the remodulation.

and the proportional sides model PSB are tested with free-free boundary conditions. This time, the geometrical (thickness, in particular) and material characteristics of the core (summarized in Tables 4.11-4.13), both of them affecting the bending stiffness. The bending stiffness, frequency and mobility scale factors are summarized in Table 4.19.

λ_D	0.47
λ_ω	0.88
λ_Y	1.88

TABLE 4.19: Bending stiffness, frequency, and velocity scale factors of the proportional sides B model.

Fig. 4.24 summarizes the remodulation of natural frequencies, spatially averaged mobility and radiated acoustic power.

The reconstruction of the natural frequencies is illustrated in Fig. 4.24a. There is an almost perfect overlap of the reference and remodulated curves; a slight divergence is noticeable also in this case, starting a little bit before 4000 rad/s, this time.

Figs. 4.24b-4.24c and Figs. 4.24d-4.24e show the spatially averaged mobilities and radiated acoustic power before and after the remodulation, respectively. There is a good match of the curves also in this case, although at around 4000 rad/s appears the expected misalignment of resonance peaks in both mobility and acoustic power. However, the frequency shift is restrained up to 7000 rad/s, as in the case of simply supported panels. Instead, the amplitude level is predicted accurately in all the frequency range. The recurrence of these shifts in a different set of experiments, in which other boundary conditions, similitude conditions, and scaling laws are considered, strengthens the idea that they may be attributed to the effect of mass and stiffness

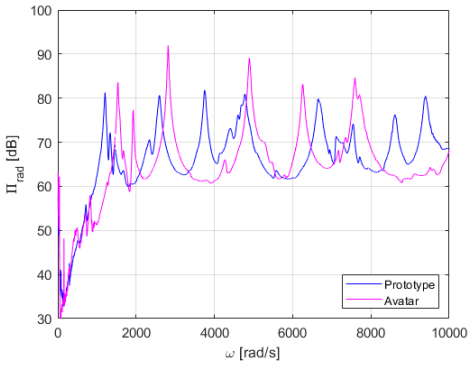

(A) Not remodulated.

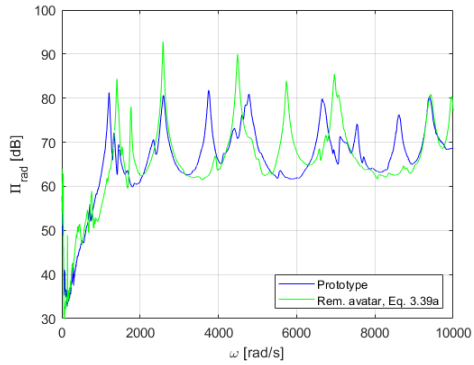

(B) Remodulated, Eq. 3.39a.

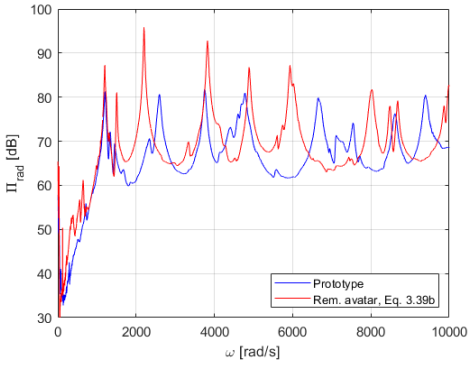

(C) Remodulated, Eq. 3.39b.

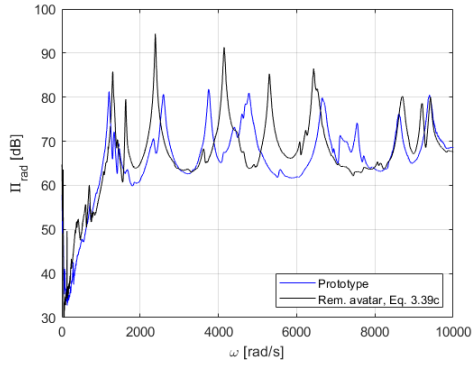

(D) Remodulated, Eq. 3.39c.

FIGURE 4.22: Comparisons between the radiated acoustic powers of prototype and avatar model, before (A) and after (B)-(D) the remodulation.

inhomogeneities in the core, instead of experimental uncertainties, which become relevant after 7000 rad/s.

The onset of the misalignments occurs around 7000 rad/s when investigating both panels A and B, which differ in material properties. It is reasonable to conclude that these shifts appear when the extent of the inhomogeneities, caused by the voids, become comparable with the structural wavelength.

Finally, these results demonstrate that Eqs.3.21-3.40 allow the definition of a true model, therefore the prediction of the natural frequencies is accurate, even when material changes occur.

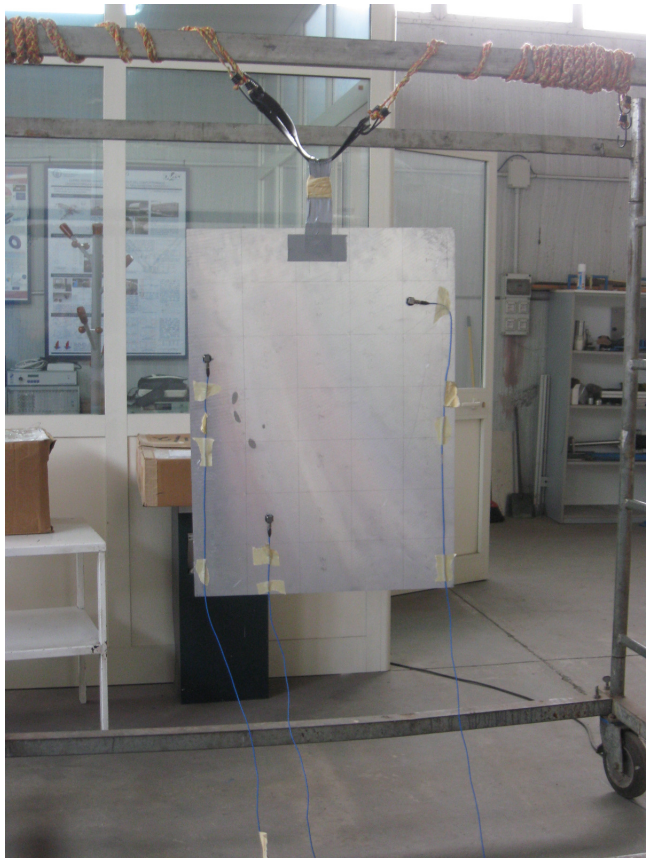

FIGURE 4.23: AFS plate with free-free boundary conditions.

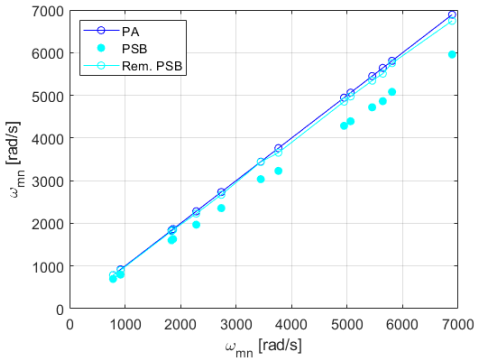

(A) Remodulation of the natural frequencies from PSB.

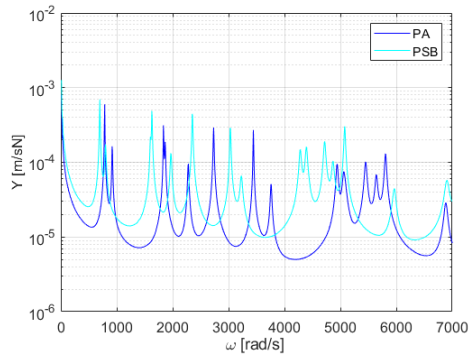

(B) PA and PSB spatially averaged mobility.

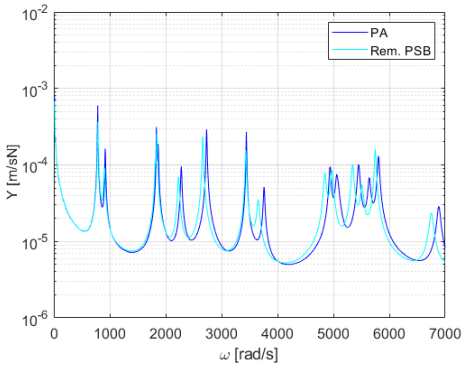

(C) PA and PSB remodulated spatially averaged mobility.

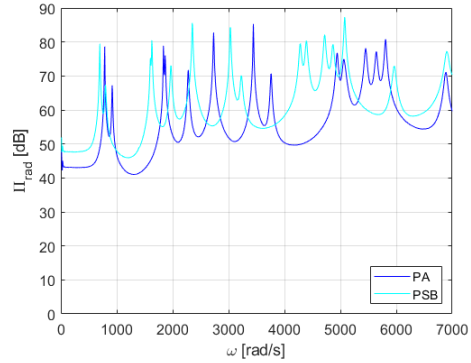

(D) PA and PSB radiated acoustic power.

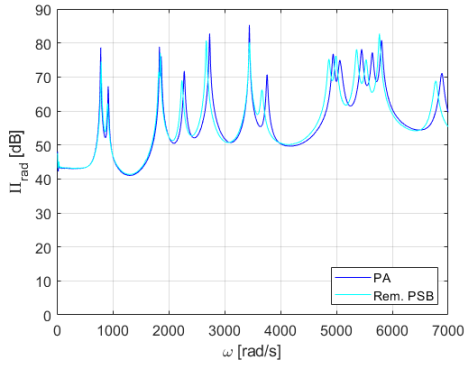

(E) PA and PSB remodulated radiated acoustic power.

FIGURE 4.24: Prediction of natural frequencies (a), mobility (b)-(c) and radiated acoustic power(d)-(e) from PSB.

Chapter 5

Application of machine learning methods to structures in similitude

The review provided in Chapter 2 shows how historical methods, such as DA and STAGE, are limited by the effort to derive, manually, similitude conditions and scaling laws for each system under analysis (although their wide use). On the other hand, methods like ASMA, SAMSARA, and SA prove that the will of the scientific community is to go beyond these limits, following two parallel paths: the resolution of complex problems (acoustic-elastic systems, multicomponent structures, etc.), and to reduce the effort of the analysts in deriving the similitude conditions and scaling laws by means of automated procedures by means of their implementation in an algorithm.

The results shown in Chapter 4 highlight the problems arising when the prototype reconstruction is based on distorted models. As a matter of fact, avatars are not only a modeling matter, they are a real issue due to several reasons, like manufacturing constraints (technical limitations, errors, etc.), or the dimensions of the experimental facilities that should house the model. An example is shown in Fig. 5.1, where the internal part of a longitudinally and orthogonally stiffened cylinder is shown. The broken lines highlight the misalignment of the stiffeners, which may lead to unforeseen behavior in all the frequency range.

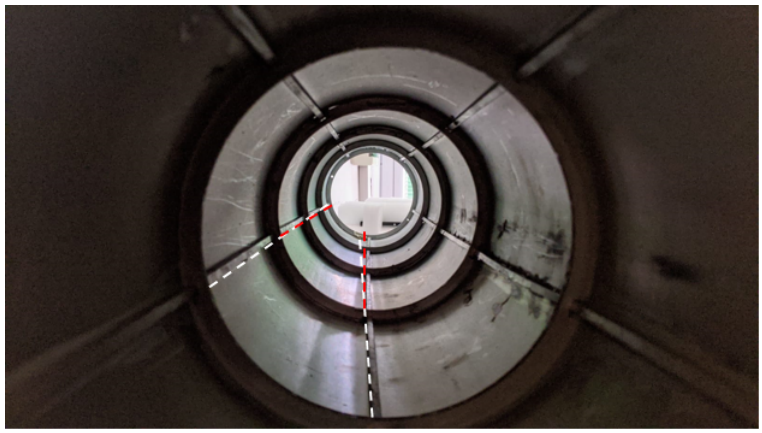

FIGURE 5.1: Stiffened cylinder with misaligned stiffeners.

All these matters, along with the impossibility of reconstructing the prototype behavior from avatars, may lead to unreliable predictions, as well as a waste of money and time. For these reasons, and since the classic similitude approach stops being deterministic when distorted models are involved, it is reasonable to investigate alternative techniques which allow to exploit the information provided by all types of models, may they be in complete or partial similitude. Thus, this chapter is dedicated to the investigation of the prediction capabilities of ANNs in similitude field.

The wide literature concerning the application of machine learning to vibration problems is the proof of its feasibility. Structural Health Monitoring (SHM) is one of the fields with a very high number of employments. Alves et al. (Alves et al., 2015) assess the structural modifications due to damage or any foreign event (like reinforcement procedures, different types of traffic loads, etc.) of a simply supported beam and a box girder bridge. The authors deal with a typical binary classification problem with damaged and undamaged classes. Particularly, they focus on two points: the possibility of dealing with classification problems using raw data (accelerations) acquired *in situ* by means of experimental tests, and the effects of environmental effects, such as changes in temperature. Different machine learning methods are used, such as Bayesian decision trees, ANNs, and Support Vector Machines (SVMs). One undamaged and five damaged (with holes of different diameters) beams are used for training; for the bridge, the training is carried out with data before and after reinforcement. Considering the temperature effects, the results improve, hence the definition of features when creating the training set is fundamental. Moreover, it is proven that, also using raw data, machine learning techniques are very efficient in determining the states of the structures.

Krishnakumar et al. (Krishnakumar, Jain, and Singru, 2015) focus on machinery maintenance. Being able to monitor systems would mean to generate accurate, quantitative information on the present condition of a machine, hence to optimally schedule maintenance achieving an optimum use of resources and cost reduction. Normal equation and ANNs are applied to monitor the mechanical conditions and derive the approximate time of functional failure of different parts of lathes. The training set uses data on noise and vibration (L- and g-peaks) as inputs, while the number of operating days is the output. The results show how this type of set leads to a good estimate for scheduling regular overall maintenance of lathes.

Damage assessment by means of ANNs is the aim of Meruane and Mahu (Meruane and Mahu, 2013), who exploit the changes in antiresonance frequencies, with respect to the intact case, as inputs and damage indices as outputs. The results highlight a well identified damage even though just antiresonance information is used.

Some works deal with the human response to noise. Sharp et al. (Sharp et al., 2013) classify unknown vibration signals (freight and passengers railway vibrations) so that exposure-human response relationships can be derived. A simple logistic regression model with gradient descent training algorithm is employed, which successfully separates unknown railway vibrations with a success percentage of 97%; moreover, useful exposure-response relationships are found.

FEM and ANNs are combined to predict the behavior of human auditory system by Wang et al. (Wang et al., 2017). FEs model the auditory canal and the ear tympanic membrane of a human ear, with the aim of studying their transmission behavior. The ear is excited by signals reproducing the noise of a vehicle (twenty noise signals measured under ten working conditions); Radial Basis Functions (RBFs) ANNs are used to reconstruct the nonlinear features of human auditory system and provide, as outputs, the A-weighted Sound Pressure Level (SPL) and the total values of loudness and sharpness. The method works fine, and it is general in terms of applications: it can be used not only to analyze the response to vehicle noise, but also for ear diseases diagnosis, hearing repair, etc., since the model can reflect the sound transfer mechanisms in human ear.

Kužnar et al. (Kužnar et al., 2012) address noise reduction for car passengers comfort. In fact, at high speeds, the noise is mainly generated by the air flow around a car and it prevails on other sources, such as engine, tires, etc. Aerodynamic improvement would lead to noise reduction, however mechanical design, aesthetics, and, more generally, time and money matters related to the number of experimental tests to perform in wind tunnels limit such an improvement. This opens the way to the prediction capabilities of machine learning techniques: the strong need to automate and speed up the process leads to the introduction of machine learning methods. Therefore, the authors employ a high number of techniques and their results are compared: the results prove that the aeroacoustic comfort field can significantly benefit a machine learning approach, leading to an improvement of engineers efficiency, shortening vehicle development cycles and development costs.

Wei et al. (Wei et al., 2019) demonstrate how the huge data acquired witih experimental testing can be profitably employed. In fact, the authors show that the data acquired by means of Laser Doppler Vibrometer (LDV) are suitable to create a data set to which machine learning methods can refer to. This data is used for vehicle identification (car, bus, etc.) by submitting it to several methods, like k-Nearest-Neighbor (kNN), Deep Belief Networks (DBNs), Convolutional Neural Networks (CNNs), etc. All the methods return acceptable results, neural networks above all.

An example of system identification is provided by Xu et al. (Xu et al., 2004), who aim at direct identification of structural parameters (stiffness and damping) in order to determine the structure state. Velocities and displacements are used as inputs of Back Propagation Artificial Neural Networks (BPANN). In particular, an emulator neural network models the time-domain behavior of a reference structure (having the same dimensions and topology of the object structure), while a parametric evaluation neural network is trained to identify the parameters of the object structure. This method proves to be resilient to noise, slow convergence, local minima, and it does not need an *a priori* knowledge of the undamaged structural parameters.

Valero and Alias (Valero and Alias, 2012) address noise source classification by testing different features (time domain, spectral domain, linear prediction, wavelet analysis) and machine learning techniques to understand which combination provides the best results. The objective is to successfully classify road vehicles (polluted by

other noise sources, such as railway and air transports, industrial, and traffic noises). It is shown that spectral features, combined with kNN, ANN and Gaussian Mixture Models (GMMs), prove to be the best combinations. Importantly, the article demonstrates that a hierarchical classification works fine, adding a 3% of success to the already high success percentage of classification (equal to 89.5%), gaining a performance equivalent to that acquired with Hidden Markov Models (HMMs). Moreover, hierarchical classification has two advantages: lower computational cost and observable states. By means of a listening test, it is demonstrated how machine learning outperforms the human ear in nose recognition of 12%.

In the framework of lifetime improvement of gas-turbine airfoils, Martin and Bestle (Martin and Bestle, 2018) address the automatic classification of eigenmodes bands of compressor airfoils in presence of fixation uncertainties, which lead to uncertainties in the stiffness of contact layers. Such indefiniteness of the boundary condition leads to a change in eigenmodes which does not allow their easy identification (at least with a low error rate). Thus, the authors apply several post-processing methods to raw data (the eigenmodes), like normalization and dimensionality reduction, then proceed to classification with BPNNs. The result exhibits less than 5% of cross-validated error.

To conclude this brief review on machine learning applied to vibroacoustic problems, the review due to Hossain et al. (Md et al., 2017) covers the applications to system identification based on inverse parametric approach and using ANNs. The articles reviewed concern input identification (vibration-inducing force identification, force involving factors identification) and system identification (mass, damping and stiffness identification, natural frequency and modal parameters identification, damage localization and quantification, mechanical properties identification), showing the huge amount of applications of machine learning on system identification, as well as the impressive number of different types of neural networks and data pre-processing methods. Another interesting review is provided by Bianco et al. (Bianco et al., 2019), reporting the main applications of machine learning in acoustics.

Although the wide range of applications of machine learning to vibration problems, they have not been applied yet to the analysis of systems in similitude, as far the authors know. Nonetheless, it would be interesting to understand if ANNs can use the information provided by all type of models - true and distorted - to predict the prototype response (or even the response of any other model) starting from the scaling characteristics. This may result very helpful in similitude field as ANNs may provide quick preliminary estimations of the dynamic response of models and, consequently, evaluate how much the distortions affect their behavior. This would lead to noticeable money and time savings, especially in those cases in which the experiments are hard or expensive to setup (like crashworthiness or other impact tests in which the breakage of the specimen is scheduled, as well as dynamic and acoustic investigations of fuselages, ship hulls, etc.) or the numerical simulations may require substantial computational efforts and are time consuming (such as the interaction between an elastic structure and a TBL, or other fluid-structure interaction problems).

On the other hand, it would be interesting to understand if it is possible to identify and quantify the distortion, starting from the dynamic characteristics. Such an analysis would complete the investigation concerning the potentialities of ANNs in similitude field. Moreover, it would suit peculiar scenarios in which only the analysis results are provided, while detailed information about the material and/or geometry may be totally or partially missing. However, this type of information is fundamental in similitude field, since great deformations and material changes [especially if composites are used (Simitses and Rezaeepazhand, 1993)] affect the dynamic response in the whole frequency range, while small distortions have a much greater influence when the modal overlap factor is high. Being able to determine the scaling characteristics of both geometrical and material parameters from the dynamic behavior would be useful to determine and quantify the distortion and, then, act on its source during the manufacturing procedure.

In general, a machine learning algorithm that generalizes well is a powerful tool to model systems in which it is not easy to understand the functional relationships between the dependent and the independent variable(s). After all, it is known that the human effort required to find patterns in data is limited and it becomes more difficult when the size of the data set increases (Bianco et al., 2019). There are machine learning techniques that are useful even when the data is subject to uncertainties or varies with the passage of time. Last, but not least, these methods may produce solutions in less than one seconds, independently of the complexity of the problem. This makes the approach attractive even when there are alternative techniques that can produce more accurate results (Flood and Kartam, 1993). However, machine learning methods should not be considered as an alternative to the conventional computational techniques, but as an efficient supplementary tool for various purposes because they reduce drastically the computational cost when excessive iterations are needed for convergence, there is a lack of analytical models due to the complexity of the problem, or reference data is quickly needed to validate the effectiveness of a new model.

These considerations make easy to understand why building systems that can learn from experience has been attractive for researchers of many fields, such as computer science, engineering, mathematics, physics, neuroscience, and cognitive science. Out of these activities a wide range of learning techniques has been derived and all of them have the potentialities to transform many scientific and industrial fields (Rasmussen and Williams, 2006).

However, many publications demonstrate how machine learning is affected by a widespread misuse. As noted by Flood and Kartam (Flood and Kartam, 1993), for example, many users tend to submit, almost blindly, a problem to Artificial Neural Networks (ANNs) hoping in an acceptable solution. Probably, the capability of machine learning to provide these solutions automatically encourage these habits. The operations and the effect of a number of internal parameters are often ignored, affecting negatively the model performance and the comparison among several machine learning models.

Nowadays, ANNs are not always appreciated since the architecture and the number of examples cannot be determined *a priori*. Many authors have tried to define, at least, boundaries on the architecture or the number of training examples, such as Hush and Horne (Hush and Horne, 1993), Huang and Huang (Huang and Huang, 1991), or Stathakis (Stathakis, 2009). All of them agree on the fact that the number of hidden neurons should be much more smaller than the number of training samples (otherwise the network would memorize the training set, without synthesizing the information hidden in data). However, the truth is that the right network can be defined only empirically, being strongly problem-dependent. Hush and Horne (Hush and Horne, 1993) suggest a trial-and-error methodical approach, in which one starts with the smallest possible network and increases the size gradually, until the performances improve significantly. Nonetheless, the architecture is just one side of the problem. In fact, if the system under analysis exhibits high variability, the number of training examples required increases and it is not always possible to produce a large enough statistical population to train the network (Castellini and Revel, 2000).

For these reasons, this work is executed so that the decisions about the architecture of ANNs are, as far as possible, made purposefully and with understanding of their consequences, by explaining the importance of all the features involved and showing the effects of their presence. The choice of each architecture and set of features is guided by performing a sensitivity analysis. In this way, a compromise between the "black box" and "model" approaches is carried out. Moreover, this phase is realized keeping an eye on the possibility of generating an experimental training set, for future laboratory applications. Although the results herein presented regard particular case studies, they may be considered as a guide on the topic for those that currently use (or intend to) ANNs in similitude field.

The training sets used further are generated analytically. In fact, building an experimental training set, where each example is a structural model on which laboratory tests must be performed, is unfeasible from both economical and working time points of view, no matter how simple the model is. The analyses are made by using the Deep learning Toolbox of MATLAB®. Since, as written in section 3.2.1, the weights are randomly initialized at each training, they are, therefore, different and the chosen architecture and training set can be only analyzed running several training and evaluating if (a) the errors exhibit oscillations or decrease smoothly, and (b) if the errors of subsequent training exhibit values with the same orders of magnitude. The training which satisfies these two points is considered to be stable and suitable for the task.

In this chapter, the potentialities of ANNs are investigated with a simple case of structures in similitude, namely, simply supported beams, which do not exhibit avatars. Then, a more complex case is considered, which is CFCF plates (in order to compare the generalization capabilities of the ANNs with the results obtained experimentally and described in Chapter 4). Two tasks are executed or both the structural operators: prediction of the dynamic characteristics starting from the scaling characteristics, and vice versa. Moreover, in the case of the plates, a thorough sensitivity analysis is executed, in order to derive the best architecture and to understand which

parameters provide more information about systems in similitude

5.1 Artificial Neural Networks applied to simply supported beams in similitude

As previously explained, ANNs are herein applied to simply supported beams in similitude to two cases. In Case 1, the input is the length scale factor, and the dynamic characteristics, in terms of the first ten natural frequencies, are the outputs. Case 2 concerns the prediction of the length scale factor by providing the first ten natural frequencies as input. This is, therefore a supervised regression problem.

There are several reasons why natural frequencies are chosen as representative of the dynamic characteristics in this investigation (and in the next one). Firstly, the length of the input/output pattern (depending on the case considered) would be limited. Then, they represent the global behavior of the structure and can be determined experimentally. Furthermore, knowing their scale factor is fundamental for both frequency and response remodulation. On the other hand, modal parameters such as mode shapes are not suitable for the analysis with ANNs because they would provide an excessively long input/output pattern. Moreover, since they are not posed in similitude, they would not provide interesting information about the type of model.

The data set is made of 31 models which scale factor ranges from 0.50 to 2.00 at steps amplitude of 0.05. The prototype is identified by the length scale factor $\lambda_L = 1$. For each model, the first ten natural frequencies are polluted with random noise having a Gaussian distribution. In fact, considering the noise as the consequence of the sum of many, independent but identically distributed external factors, then such a sum would obey a Gaussian distribution. This happens regardless the original distribution of each factor, according to the Central Limit Theorem (Mitchell, 1997). The parameters of this distribution are zero mean and standard deviation equal to 5%, since, in the case of the beams, there are no references about their value. This is done in an attempt of replicating the experimental error and demonstrate the robustness of ANNs in presence of noise. For both Case 1 and Case 2, the training set is made of 20 observations (out of 31), randomly sampled. The 85% is used for training, the remaining 15% for test phase. There is no validation set since the Bayesian approach is used.

The prototype beam has geometrical and material characteristics summarized in Table 5.1. All the models are scaled only geometrically in length; the cross sectional dimensions and material properties (aluminium) do not change (however, they may change without introducing further complications since another true model would be returned).

As highlighted in Chapter 3, beams do not generate avatars and the natural frequencies of two models are related by Eq. 3.11. Thus, this equation is the law that should be underneath the model generated by the ANN. Moreover, the models are described only by means of one scale factor, that is the length one. Therefore, this problem is relatively simple and does not need a particularly deep sensitivity analysis.

Length, L [m]	1.00
Cross-section sides, s [m]	0.025
Young's modulus, E [Pa]	70×10^{9}
Mass density, ρ [kg/m^3]	2700
Poisson's ratio, ν	0.30

TABLE 5.1: Geometrical and material characteristics of the prototype beam.

Case	**Architecture**	**No. of examples**	**Epochs**	**MSE$_{train}$**	**MSE$_{test}$**
Case 1	5–10	20	1000	390	8.374×10^{4}
Case 2	2–3	20	156	4.43×10^{-15}	4.43×10^{-4}

TABLE 5.2: Training characteristics for Case 1 (from length scale factor to natural frequencies) and Case 2 (from natural frequencies to length scale factor).

The training characteristics and results for the best training are summarized in Table 5.2. The table reports, from the left to the right column, the case under analysis, the architecture, the number of examples for both training and test phases, the number of epochs (that is, the number of times the entire training set is used), and the train and test MSEs. The maximum number of epochs allowed is 1000, as it has been noticed that it is a value at which, typically, the errors have stabilized or overfitting has already shown up . The architecture columns is indicated in terms of neurons of hidden layers (therefore, the number of neurons of both input and output layer are omitted). For example, the Case 1 has architecture 5–10, which means that the neural network has two hidden layers, the first with 5 neurons, the second with 10 neurons.

Case 1 exhibits high values of training and test MSE and an architecture more complex than that used for Case 2. This is due to the fact that ten outputs are predicted and that the training examples are polluted by noise, which leads to an increase of the MSE between the real output and the estimated one.

Fig. 5.2 shows the training and test errors for Case 1. After a first phase of assessment, the training error decreases and stabilizes around 400, while the test error is stabilized around 10^4.

The results returned by the ANN are shown in Fig. 5.3; four different models are considered (not contained into the training set, of course), with length scale factors equal to 0.90, 1.35, 1.55, and 1.75. The red dots, representing the predictions provided by the ANN, are very close to the reference line, implying that the ANN can reconstruct the natural frequencies with an acceptable accuracy and, moreover, it is robust to noise.

Case 2 exhibits a less complex architecture and smaller training and test MSE. The evolution of the errors is illustrated in Fig. 5.4. The training error exhibits a decreasing behavior, reaching very low values around the order of magnitude 10^{-15}. The test error decreases smoothly, too, stabilizing around 10^{-4}

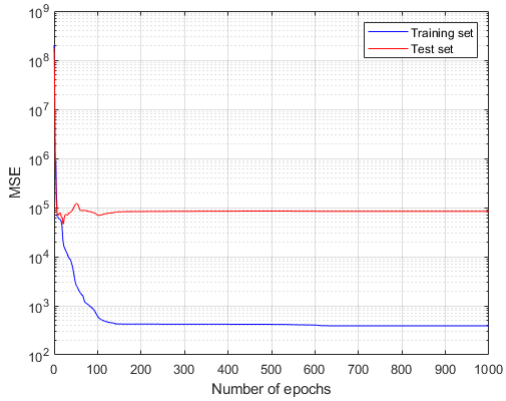

FIGURE 5.2: Training and test errors for Case 1.

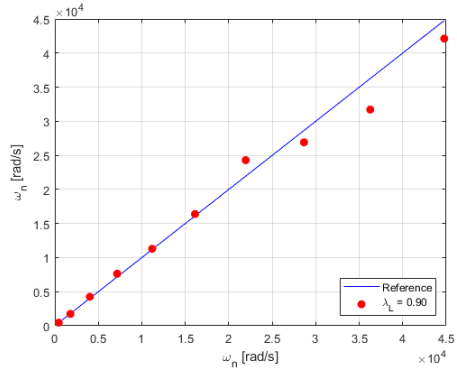

(A) $\lambda_L = 0.90$.

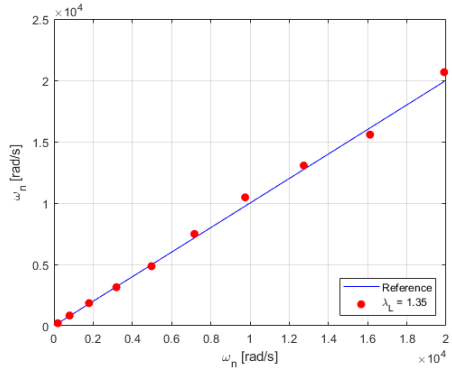

(B) $\lambda_L = 1.35$.

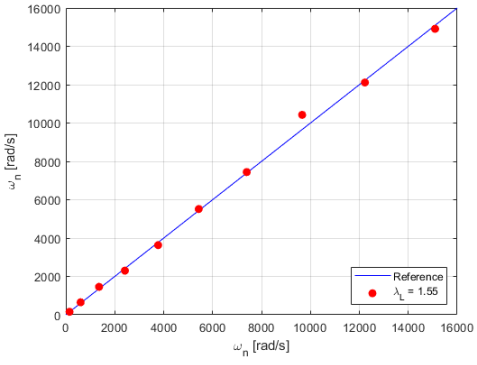

(C) $\lambda_L = 1.55$.

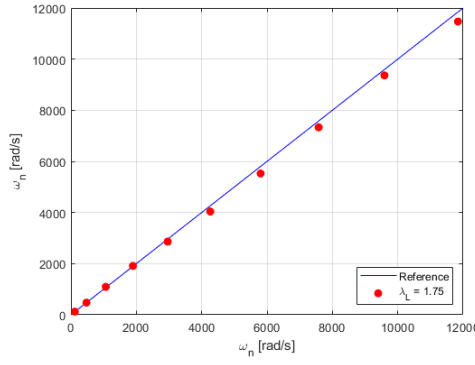

(D) $\lambda_L = 1.75$.

FIGURE 5.3: Prediction of the natural frequencies of simply supported beams with $\lambda_L = 0.90$ (A), $\lambda_L = 1.35$ (B), $\lambda_L = 1.55$ (C), and $\lambda_L = 1.75$ (D).

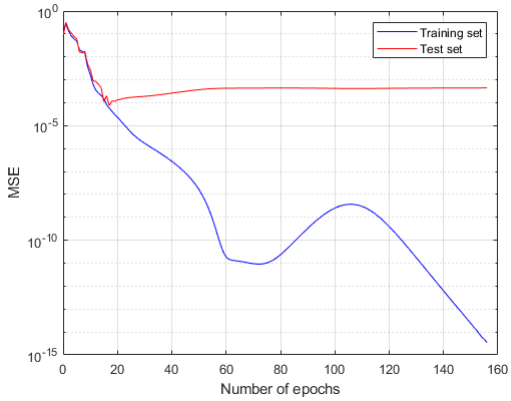

FIGURE 5.4: Training and test errors for Case 2.

These considerations on the errors are confirmed by Fig. 5.5, showing the prediction of the length scale factors of five models. In this case, it is the input to be polluted with noise. Nonetheless, the predictions are very good, returning errors smaller than 0.05, that is the sampling step used to generate the training set.

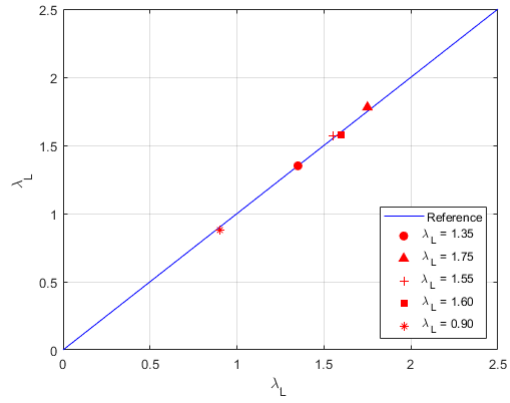

FIGURE 5.5: Predictions of the length scale factors for five models.

5.2 Artificial Neural Networks applied to CFCF plates in similitude

In this section, ANNs are applied to CFCF plates in similitude, using the experimental results, discussed in Chapter 4, to validate the outputs of the network.

The architecture, the input features, and the number of training examples are identified, qualitatively, by means of a sensitivity analysis. The procedure applied is the trial-and-error one, suggested by Hush and Horne (Hush and Horne, 1993). Each

training example, i.e., each plate, is characterized in terms of length, width, and thickness scale factors (referenced with respect to the prototype). The natural frequencies and FRFs of models with geometrical scale factors ranging from 0.50 to 1.50 (with steps equal to 0.05) are evaluated, for a total of 9,261 models. From this data set, several training sets are created. All of them are made of a common basis, constituted by a set of examples describing the boundaries of the input space in order to bypass the risk of extrapolation (Hagan et al., 2014). Then, other examples are randomly sampled from the set. The 85% of the examples are used for the training phase, the remaining 15% for test. Since there is no validation set, the samples are distributed between the sets in order to improve both the training and test phases. Also these subsets are created randomly at each training, then standardized with respect to their mean value and standard deviation.

This section is divided into two subsections. The first concerns the prediction of the dynamic characteristics, in terms of natural frequencies, of plates in similitude when the scaling characteristics used in input are characterized in terms of geometrical scale factors (length, width, and thickness). The second section deals with the prediction of the scale factors by starting from the dynamic characteristics.

5.2.1 Prediction of the natural frequencies starting from the scaling characteristics

For this task, the geometrical scale factors are the inputs, while the natural frequencies are the outputs to predict. The experimental results reported in Chapter 4 are used as reference to test the performances of the ANN. For all the experimental models, at least the first nine natural frequencies are available, therefore the ANN is used to predict these frequencies.

A first data set is analytically generated and without noise pollution, and the sensitivity analysis performed on this set is summarized in Fig. 5.6 and Table 5.3. Particularly, Fig. 5.6 illustrates how the training (Fig. 5.6a) and test (Fig. 5.6b) MSEs, reported on the vertical axes, change with different output combinations (on the horizontal axes). Each dot on the curves corresponds to the MSE, averaged on three different training. Four different architectures are investigated.

Basically, two different types of output are considered. First, single natural frequencies, to investigate if ANNs are able to predict natural frequencies of increasing order with the same level of accuracy or not. Then, combinations of natural frequencies are considered. In the following plots, a vertical black broken line divides the outcomes obtained from single natural frequencies from those obtained with groups of them.

Table 5.3 is a good reference for a better understanding of Fig. 5.6, as it gathers the better architectures for the cases shown in the figure. The table summarizes the characteristics of the most simple networks returning an acceptable prediction for several output types (listed in the first column), which may be single natural frequencies

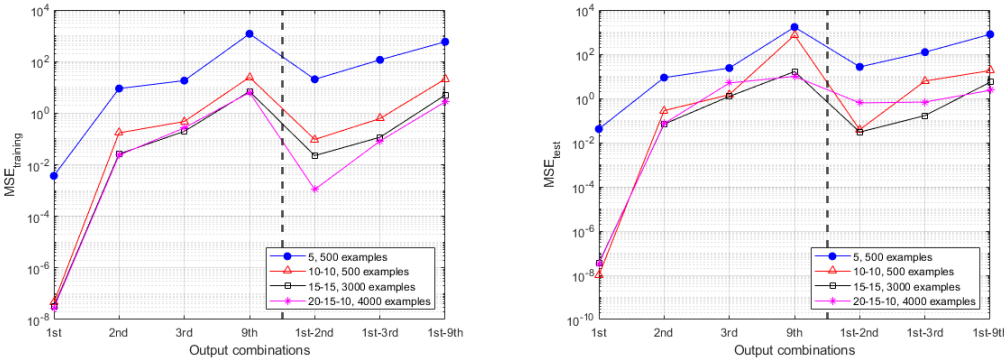

(A) Training error.

(B) Test error.

FIGURE 5.6: Training (A) and test (B) MSEs from the sensitivity analyses on the ANN architecture. Data without noise.

or successions of them. The choice of a particular architecture is due to the fulfillment of both the requirements for a stable training, previously described. Then, the architecture, the number of examples, and the training and test errors are reported.

Output type	**Hidden layers architecture**	**No. of examples examples**	**MSE_{train}**	**MSE_{test}**
1st natural frequency	5	500	0.0037	0.0413
2nd natural frequency	10–10	500	0.1720	0.2790
3rd natural frequency	15–15	3000	0.1970	1.2300
9th natural frequency	20–15–10	4000	6.3000	9.9500
1st–2nd natural frequencies	10–10	500	0.0953	0.0383
1st–3rd natural frequencies	15–15	3000	0.1160	0.1670
1st–9th natural frequencies	20–15–10	4000	2.7500	2.3300

TABLE 5.3: Results of sensitivity analysis on ANN architecture. The vertical black broken line separates the single output training from those with multiple outputs. Data without noise.

By looking at Fig. 5.6, the blue line represents the error obtained by the simplest architecture, consisting in one hidden layer having 5 neurons, trained with 500 examples. The first natural frequency is well predicted by the ANN, with satisfying values of training and test errors equal to 0.037 and 0.0413, respectively (Table 5.3). However, it does not perform so well with the following frequencies, as well as combinations of them, since the increasing error prevents from an acceptable prediction. Such an increase in predicting the natural frequencies with order higher than the first may be due to an excessive simplicity of the model generated by the ANN. Thus, in order to achieve better performances, the architecture must be complicated. However, adding more hidden layers and neurons may lead to overfitting, since the more complex model of the ANN turns out to be built *ad hoc* on the data points and, therefore,

lacking of good generalization capabilities. This problem can be mitigated with an increase of the number of training examples (Hagan et al., 2014). The sensitivity analysis is executed on the basis of a trade-off between more complicated architectures and the addition of more samples.

As a consequence, passing to an ANN with two hidden layers, each one with 10 neurons, and trained by 500 examples (red line), the error is lower than the previous case for both the first and second natural frequencies. Nonetheless, the ANN with one hidden layer and 5 neurons would be chosen to predict the first natural frequency since it is less complicated and, in principle, it returns an acceptable prediction requiring less computational resources and time. However, also in this case, the architecture performs poorly on the successive natural frequencies and combinations of them.

These considerations hold for the prediction of the successive natural frequencies: for instance, 3000 examples and a 15–15 ANN (that is, two hidden layers with 15 neurons each, as indicated in Table 5.3) are necessary to predict only the third natural frequency, while a 20–15–10 ANN, trained with 4000 examples, is needed to predict the ninth natural frequency, as the training and test errors are equal to 6.30 and 9.95 (Table 5.3). On the one hand, the number of training examples is prohibitive, especially in the perspective of generating an experimental training set; on the other hand, such a great number is necessary to avoid overfitting.

Thus, the left half of the plots in Fig. 5.6 shows that, once the architecture and the number of training examples are fixed, it becomes harder, for an ANN, the prediction of the natural frequencies as the frequency order increases. A possible reason may be the characterization of the models just in terms of geometrical scale factors, since such a description may result poor when higher order frequencies are considered. Moreover, the increasing complexity leads to a higher number of samples, which makes an experimental training set unrealizable.

However, the purpose of this investigation is to predict the first nine natural frequencies all together, therefore the sensitivity analysis is executed with combinations of natural frequencies, too. The outcomes of such a study are shown in the right part of the plots in Fig. 5.6, in which successions of natural frequencies are considered. It is possible to notice that, when combinations of natural frequencies are taken into account, the most suitable architecture is the one that works fine with the higher order frequency of the entire set under consideration. For instance, in the case of the 1st-2nd natural frequencies combination, the best network is that used for just the second natural frequency (10–10 neurons and 500 examples). In the case 1st-3rd natural frequencies, the network that works fine is that used for the third frequency alone (15–15 neurons and 3000 examples), and so on. It is reasonable to conclude that the higher order frequency fixes a lower boundary on the best architecture. Of course, more complicated networks would work even better, at least until overfitting occurs.

The same sensitivity analysis is performed with the same training set, this time polluted with random noise (applied only to the natural frequencies) in order to reproduce the experimental uncertainty. This step has a double objective: to compare these

results with the predictions provided by the not polluted training set and the experimental results, and to demonstrate the robustness of ANNs to noise. This time, the parameters of the distributions are evaluated on the basis of the experimental-numerical differences, illustrated in Chapter 4, between natural frequencies. Since the noise must replicate the experimental error on the evaluation of the natural frequencies, the parameters of the Gaussian distribution used to model this noise are evaluated on the basis of the error obtained during the experimental phase. It is estimated as the difference between the experimental natural frequencies and those obtained numerically. Thus, the mean and standard deviation of the Gaussian distribution are equal to μ = -0.0151 and standard deviation $\sigma = 0.0519$, respectively.

The results of this sensitivity analysis are summarized in Fig. 5.7 and Table 5.4. The considerations developed for the training set without noise are valid also for this case: high order frequencies require more complicated architectures and more examples. When output combinations are considered, its the lower boundary is fixed by the best architecture working fine with the single higher order frequency of the combination analysed.

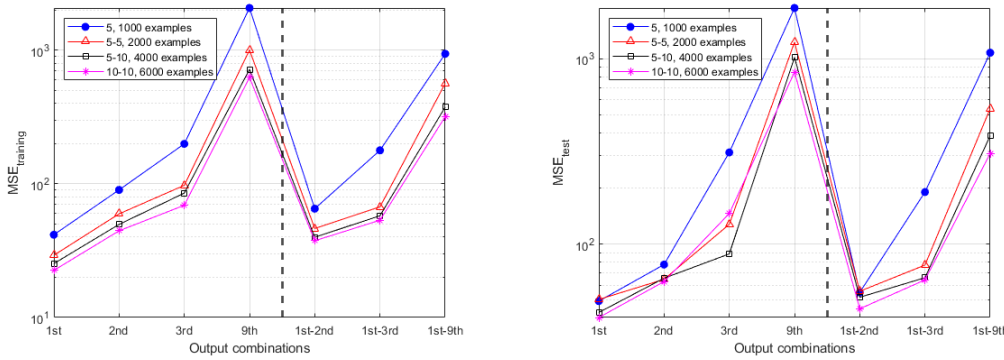

(A) Training error.

(B) Test error.

FIGURE 5.7: Training (A) and test (B) MSEs from the sensitivity analyses on the ANN architecture. The vertical black broken line separates the single output training from those with multiple outputs. Data with noise.

The results show how, passing from not noisy to noisy data, the architecture must change even though the same output type is considered. In fact, polluted data generates overfitting more easily than not polluted data, since casual patterns (i.e., structures in data seemingly organized which are, actually, random) generated by noise may be interpreted as regularities by the ANN, resulting in a model, tailored on these fake regularities, that does not reflect the actual behavior underlying the data (Mitchell, 1997).

As a matter of fact, Baum and Haussler (Baum and Haussler, 1988) confirm that an excessively complicated network would be surely capable of overfitting since it

Output type	Hidden layers architecture	No. of training examples	MSE_{train}	MSE_{test}
1st natural frequency	5	1000	41.60	49.30
2nd natural frequency	5–5	2000	59.60	64.60
3rd natural frequency	5–10	4000	85.20	88.60
9th natural frequency	10–10	6000	624.70	848.50
1st–2nd natural frequencies	5–5	2000	46.30	55.70
1st–3rd natural frequencies	5–10	4000	57.70	65.90
1st–9th natural frequencies	10–10	6000	317.70	309.10

TABLE 5.4: Results of sensitivity analysis on ANN architecture. Data with noise.

would perform an exact interpolation of the training data, without leaving any possibility to the existence of errors. Such a network may be seen as a stiff one, which leads for sure to overfitting in presence of noise.

Polluted data require a more flexible network, capable of providing a robust approximation instead of interpolation. Therefore, when working with noisy data, all the typical countermeasures against overfitting must be applied: namely, less complex architecture (thus, less hidden layers and less hidden neurons), and a greater number of training examples).

According to the results of these sensitivities analyses (Tables 5.3 and 5.4), the most suitable architectures to predict the first nine natural frequencies are those with 20–15–10 hidden neurons and 4000 examples when the data is not noisy, and 10–10 hidden neurons with 6000 examples when noise is considered. On the one hand, the number of hidden neurons is not very high, resulting in relatively simple neural networks; on the other hand, a lot of training examples are needed, especially in the case with noise.

The suitability of these architectures is proved by the final values of the errors, but also by the stable training, underlined by the evolution of MSE with the number of epochs in Fig. 5.8. In both cases, the error decreases quite smoothly, without exhibiting wild oscillations. In particular, the training on the set without noise stops when the maximum number of epochs is reached, as the learning algorithm works on analytical data and the error decreases epoch after epoch, as illustrated in Fig. 5.8a. On the other hand, Fig. 5.6b illustrates that polluted data prevents the error from decreasing too much, assessing at a quite constant value which enables the minimum error gradient stopping criterion.

The predictions provided by the ANN are summarized in Fig. 5.9. The black line is the analytical reference obtained with Eq. 3.16; the blue empty triangles represent the predictions of the ANN when the training set is not polluted by noise, the red stars represent the ANN predictions in the case of noisy data, and the black circles represent the natural frequencies determined experimentally.

Firstly, since, in most of the cases, the experimental frequencies are not very far from the black reference line implies that the analytical model, used to generate the

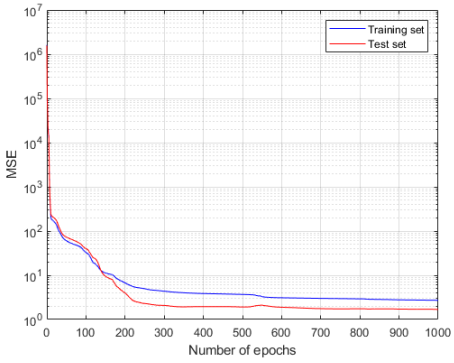

(A) Training and test MSEs. Training set without noise.

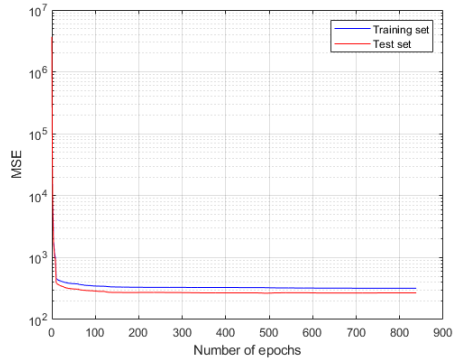

(B) Training and test MSEs. Training set with noise.

FIGURE 5.8: Training and test MSEs in the case of data without (A) and with (B) noise.

training set, works fine and the differences may be due to experimental uncertainties. Then, the blue triangles lie on the reference line, therefore the predictions of the ANN using the not noisy training set practically coincide with the analytical results: the ANN is able to give very accurate predictions when the data is without noise. However, also the predictions provided in the case of polluted data set are very close to the reference line. The proximity between the experimental results and the "polluted predictions" allow to conclude that the experiments validate the results provided by the ANN. Moreover, it is interesting to notice that, starting from data having the same level of uncertainty of the experimental results, it is possible to achieve predictions with the high level of accuracy characterizing the ANN predictions.

It is possible to conclude that, according to the results, when providing the scaling characteristics as input, ANNs can predict quite accurately a certain range of natural frequencies for systems in similitude, even with noisy data. It is, therefore, reasonable to think that ANNs can perform with the same level of accuracy even when using experimental training set, if the tests are well executed and, above all, if the number of examples is high enough. However, the results in Table 5.4 indicate that the number of training example is prohibitive if the training set to create is experimental. A different characterization in input of the models may help, for example adding material characteristics or changing the boundary conditions, as well as predicting less natural frequencies (Hagan et al., 2014; Bishop, 2006; Mitchell, 1997).

5.2.2 Model identification

As already stated, avatars are an actual problem due to manufacturing constraints or errors. Hence, an important question is whether it is possible to identify, by means of the dynamic response, if a model is true or distorted.

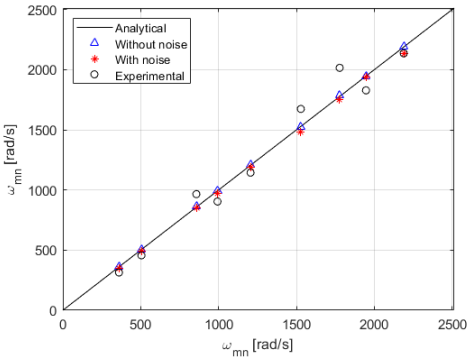

(A) Prototype.

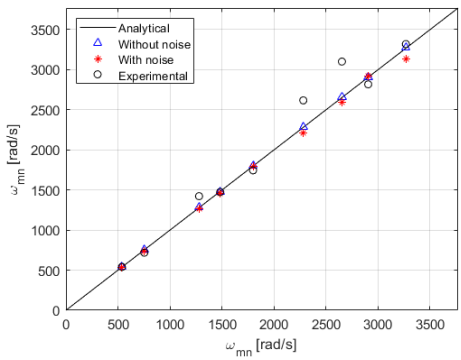

(B) Replica.

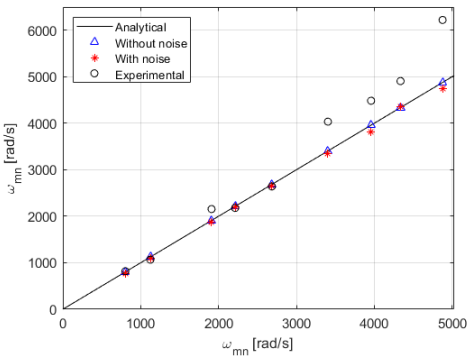

(C) Proportional sides.

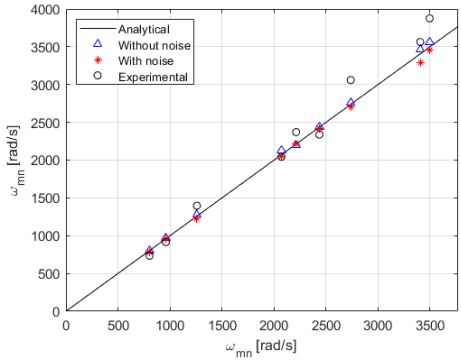

(D) Avatar 1.

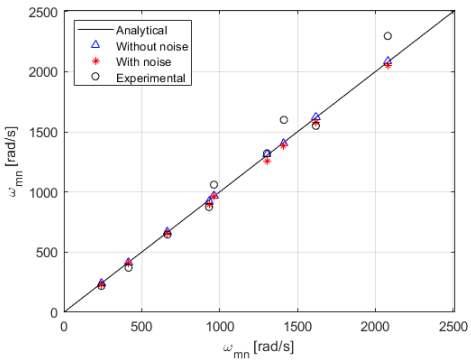

(E) Avatar 2.

FIGURE 5.9: ANN predictions with polluted and not training set for the prototype (A), replica (B), proportional sides (C), avatar 1 (D), and avatar 2 (E).

The model identification task, however, is investigated as a regression task. In fact, in case of classification a somewhat equally distributed amount of each class (replica, proportional sides, and avatars, in this case) should be needed in the training set. Since

the set is made of models which length, width and thickness scale factors range from 0.50 to 1.50 at steps of 0.05, the occurrences of replica and proportional sides models would be too low for an acceptable training, moreover being outnumbered by the amount of avatar examples. The number of replica and proportional sides models may be replenished using other values of scale factors, but, in order to reach an acceptable amount, it would involve models scaled with factors without any engineering sense (for example, equal to 10), also unfeasible to create experimentally.

For these reasons, the model identification is faced as a regression task, with the purpose of modeling the functions of length, width, and thickness scale factors and check whether the relationships between the scale factors, which identify the type of model, are kept or not. The final objective is not so much to predict with extreme accuracy the values of the scale factors, but to keep the relationships among them so that the type of model is identified.

The sensitivity analysis performed in the previous task is repeated, more focused, this time, on which kind of features should be used as input to characterize the models at best. In the following, only the main steps of the path that leads to the final architecture, in order to provide a cumbersome presentation.

A first attempt consists in providing, as input, the analytical, not noisy first nine natural frequencies. The training characteristics are summarized in Table 5.5. The predictions made with the first architecture, which has the lowest training and test errors, are reported in Table 5.6.

Architecture	**No. of examples**	**MSE_{train}**	**MSE_{test}**
5	500	0.0422	0.0491
5–5	1000	0.456	0.0552
15	2000	0.0509	0.0533
20–15–10	8000	0.0531	0.0561

TABLE 5.5: MSEs of different architectures for the model identification problem.

	True (λ_a, λ_b, λ_h)	**Predicted (λ_a, λ_b, λ_h)**
Prototype	1.00, 1.00, 1.00	1.17, 1.20, 1.43
Replica	0.67, 0.67, 0.67	0.90, 0.93, 1.30
Proportional sides	0.67, 0.67, 1.00	0.73, 0.75, 1.30
Avatar 1	0.67, 1.00, 1.00	0.75, 1.27, 1.48
Avatar 2	1.00, 0.70, 0.67	1.45, 1.02, 1.47

TABLE 5.6: Predictions of length, width and thickness scale factors. Architecture: 5. Number of training examples: 500. Data without noise.

First of all, Table 5.9 shows that it is not possible to go below a certain threshold of MSE, even though networks of incresing complexity are used. Then, the results in

Table 5.6 highlight that, with the order of magnitude of error reported in Table 5.9, the predictions are not so good. In fact, the percent error ranges from 8% (length scale factor of proportional sides) to 119% (thickness scale factor of avatar 2). The prediction of the scale factors results to be disastrous and the model identification fails totally.

From the error that does not goes beyond a certain value to the consequent bad performances, the main reason is due to the fact that, even though nine features are given in input, they are nine variations of the same characteristic. The natural frequencies of different order change, more or less, in the same way across the models, i.e., decreasing if the length or the width (or both together) increase, increasing if the thickness increases, etc. Therefore, adding more and more natural frequencies of different order does not add a significant amount of information that the ANN can exploit during the learning phase. Other parameters are needed to characterize the plates in similitude.

In addition to natural frequencies, the FRF is another fundamental and characteristic feature of dynamic response. However, the processing of such an information is not lacking of ambiguities.

Firstly, one should decide whether to keep the same frequency range or the same number of modes. In the first case, care must be taken of processing the FRFs in order to have the same number of spectral lines, referring to the same frequency. However, this means that, changing the model, also the number of resonant modes in a given bandwidth, namely, the modal density (Fahy and Gardonio, 2007), changes, increasing or decreasing according with the material and geometrical properties of the models. Conversely, the number of modes can be retained, which implies that the frequency range and the spectral lines change with the model. Furthermore, local responses strongly depend from the acquisition and excitation points, thus one should gather the local FRFs evaluated at the same non-dimensional coordinates.

Moreover, another problem is placed by the dimension of the training set. Assuming that each model would be described by the spatially averaged FRF, it is characterized by a large number of points, which implies a large number of input neurons (since each point would correspond to an input neuron). Therefore, the information contained into the FRFs must be exploited in another way.

For this reason, PCA is introduced, as the whole FRF curve can be synthesized by few representative numbers, that are the PCs eigenvalues, as suggested by Zang and Imregun (Zang and Imregun, 2001).

However, before using the PCA, the FRFs must be evaluated. While polluting the natural frequencies is a "easy", because a simple shift in frequency is simulated by increasing or decreasing the value of the natural frequency, such a task is not so straightforward for an FRF. In fact, to the shift in frequency of the resonance peaks other factors should be added, like errors in amplitude, missing or splitting peaks, etc. This is why the FRFs are evaluated analytically with Eq. 3.47 without adding any noise source. The analytical FRFs are therefore estimated with excitation and acquisition points having the same non-dimensional coordinates used for the experimental

tests described in Chapter 4. In order to compare the same type of information, the frequency ranges vary according to the model in order to always consider nine resonance peaks.

Not all the PCs are necessary, only those containing most of the variance of the system. The amount of information conveyed by the PCs can be quantified by means of the normalized cumulative sum of all the eigenvalues. Such a normalized sum up to the i-th eigenvalue is given by

$$E_{\xi,i} = \frac{\sum_{j=1}^{N_{\xi,i}} \xi_j}{\Xi}, \tag{5.1}$$

where $N_{\xi,i}$ is the number of eigenvalues up to the i-th one, ξ_j is the j-th eigenvalue, and Ξ is the the sum of all the eigenvalues.

The normalized cumulative sum of several models is plotted as a function of the number of eigenvalues in Fig. 5.10. The figure highlights that, after 11 eigenvalues, the 99% of variance threshold is reached (the 11th eigenvalue is indicated with a black circle).

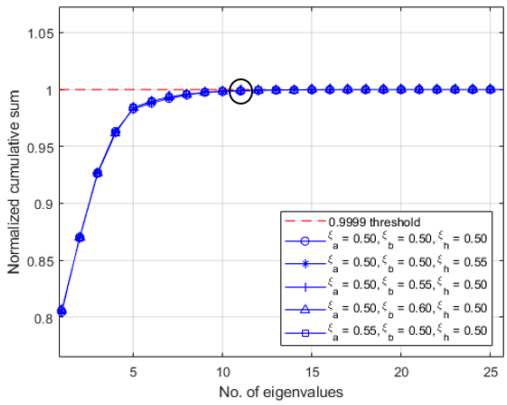

FIGURE 5.10: Normalized cumulative sum of PCs eigenvalues. The black circles indicates the 11th eigenvalue.

The evolution of performances are summarized in Tables 5.7-5.8. In order to underline how the training performances change, several combinations of input features, applied to ANNs with the same architecture, are shown. This architecture is the final one, chosen after several trials, with an architecture 5–7 and 200 examples.

Table 5.7 is shown just to demonstrate that ANNs trained with PCs eigenvalues alone are susceptible of the same problem arisen with ANNs trained only with the natural frequencies. A reduction of the error is indubitable. However, the price for a significant reduction of the error is to use many features, as the the third and fourth rows display. Thus, the considerations made with the natural frequencies as input features still hold in this case: providing the same type of information, which change in the same way, brings limited information to the ANN.

Input combinations	MSE_{train}	MSE_{test}
1st PC eigenvalue	0.0532	0.0566
1st-2nd PC eigenvalues	0.442	0.0502
1st-3rd PC eigenvalues	0.0399	0.0425
1st-11th PC eigenvalues	0.0187	0.0222

TABLE 5.7: Training performances with several combinations of PCs eigenvalues used as inputs. Architecture: 5–7. No. of examples: 200.

Considering the combination of different input types leads to better results, as highlighted by Table 5.8. Three characteristic parameters of dynamic response are considered: the natural frequencies, the PCs eigenvalues, and the modal density. In particular, modal density is evaluated in a fixed bandwidth, which covers the 0–15700 rad/s range. Such a choice is not casual, since this is the range in which the first nine modes of the smallest model ($\lambda_a = 0.50$, $\lambda_b = 0.50$, $\lambda_h = 0.50$) are contained. In this way, the resonance peaks move further as the dimensions of the models change, and the modal density varies accordingly.

Input combinations	MSE_{train}	MSE_{test}
Modal density	0.13	0.131
1st PC eigenvalue + 1st natural frequency	0.0143	0.0436
1st PC eigenvalue + 1st-2nd natural frequencies	6.77×10^{-5}	1.29×10^{-4}
1st PC eigenvalue + 1st-2nd natural frequencies + modal density	7.64×10^{-5}	6.45×10^{-5}

TABLE 5.8: Training performances with several combinations of input features. Architecture: 5–7. No. of examples: 200.

Table 5.8 highlights that the modal density is a poor feature to describe the models: both the training and test MSEs are high. In fact, modal density does not change very much among the models. Combining different types of features, instead, returns better results. For example, the training carried out with the first natural frequency and the first PC eigenvalue exhibits a reduction in training and test errors equal to 73.1% and 18.04%, respectively, with respect to the case with just one eigenvalue (Table 5.7). Adding the second natural frequency gives even better results, with an error decrease equal to 99.53% and 99.70% with respect to the case involving the first natural frequency and the first PC eigenvalue.

The best performances, which combine the lower number of features and the best performance index, are obtained by combining the first PC eigenvalue, the first two natural frequencies and the modal density. In fact, although the training error increases of 11.4% (still remaining quite low, equal to 7.64×10^{-5}) with respect to the case without the modal density, the test error is halved, reaching the value of 6.45×10^{-5}. Therefore, a feature like the modal density, which performs poorly when used alone, stabilizes the generalization when used in combination with other features. Thus, this set

	True (λ_a, λ_b, λ_h)	**Predicted (λ_a, λ_b, λ_h)**
Prototype	1.00, 1.00, 1.00	1.00, 1.00, 1.00
Replica	0.67, 0.67, 0.67	0.67, 0.67, 0.65
Prop. sides	0.67, 0.67, 1.00	0.66, 0.66, 1.00
Avatar 1	0.67, 1.00, 1.00	0.67, 1.00, 1.00
Avatar 2	0.99, 0.70, 0.67	0.99, 0.70, 0.67

TABLE 5.9: Predictions of the scale factors of the experimental plates. Architecture: 5–7. No. of examples: 200.

of input features is chosen, and the training and test performances are shown in Fig. 5.11. They are very smooth, without excessive oscillations.

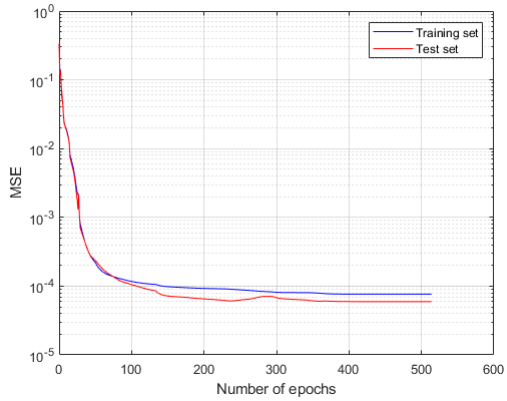

FIGURE 5.11: Training and test MSEs for a 5–7 ANN, with 200 training examples.

The network trained with these inputs and architecture is used to predict the scale factors of the experimental plates. The results are reported in Table 5.9. The prototype is perfectly identified. There is a slight difference in the prediction of length and width scale factors in the case of the proportional sides, but they are still the same, so the model can be still identified as proportional sides. For both the avatars, the predictions are exact. Concerning the replica, the thickness scale factor deviates of 3% from the real scale factor. The error is not high *per se*, but it prevents the model identification.

To have an idea on the general performances of the network, it can be tested on all the others models. For this purpose, maps of the percent error are generated for the three scale factors. They are illustrated in Fig. 5.12. The output space of the problem under investigation is reported in each figure. All the points are identified by the values of length, width, and thickness scale factors along the x, y, and z axes, respectively, and a color. This color is representative of the relative percent error made by the ANN on the prediction of a scale factor. The black dots indicate the points used in the training set and must not be predicted.

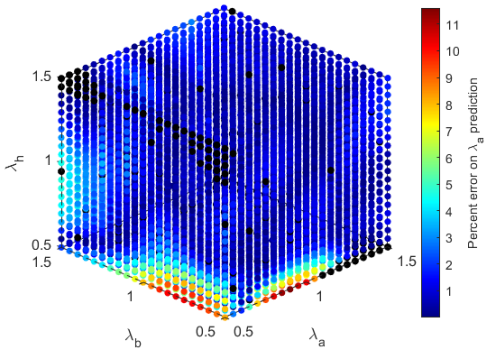

(A) Prediction error on λ_a.

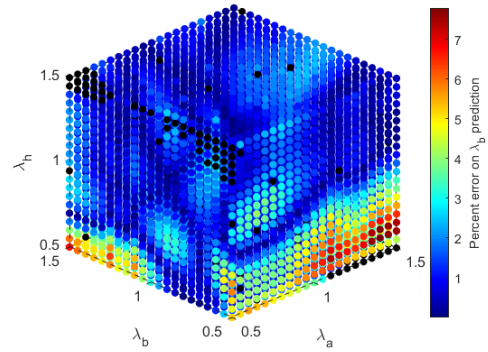

(B) Prediction error on λ_b.

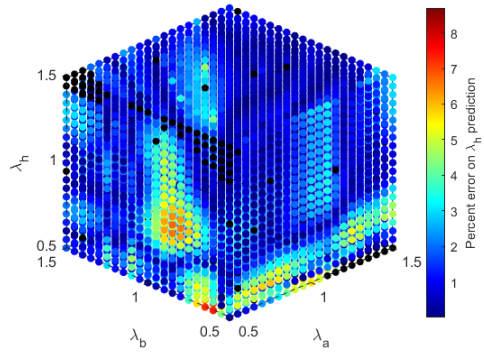

(C) Prediction error on λ_h.

FIGURE 5.12: Maps of the prediction percent relative errors made on λ_a (a), λ_b (b), λ_h (c).

In particular, Figs. 5.12a-5.12c illustrate the percent error made on the prediction of the length, width, and thickness scale factors, respectively. The error on the prediction of a generic scale factor λ_g is evaluated as

$$\%Err_{\lambda_g} = \frac{|\lambda_{g_{ref}} - \lambda_{g_{pred}}|}{\lambda_{g_{ref}}} \times 100, \tag{5.2}$$

where $\lambda_{g_{ref}}$ is the reference value, and $\lambda_{g_{pred}}$ is the value predicted by the ANN.

An example may help to clarify the read of Fig. 5.12. Let us consider the point having coordinates (λ_a, λ_b, λ_h) = (0.50, 1.00, 0.50) and how the error changes when moving parallel to the λ_h axis. Such a point exhibits an error almost equal to 8% (colored in red) in Fig. 5.12a, which concerns the evaluation of the error on the scale factor λ_a. Moving along the λ_h direction, the error decreases, assessing around 2%-3% (light blue and blue colors), which means that the scale factor $\lambda_a = 0.50$, associated with the same value λ_b = 1.00, but changing values of λ_h, is predicted better.

The same considerations can be carried out for Fig. 5.12b, which shows the prediction errors of the scale factor λ_b. The point (λ_a, λ_b, λ_h) = (0.50, 1.00, 0.50) indicates an error nearly equal to 4% (light green dot) in the estimation of the value λ_b = 1.00, which decreases at almost 1% (blue color) while moving along the λ_h direction.

Finally, similar reasoning can be carried out about Fig. 5.12c, in which the error on the scale factor λ_h is represented. An error between 1%-2% (blue color) is given for the point (λ_a, λ_b, λ_h) = (0.50, 1.00, 0.50). Moving along the vertical direction, λ_h changes and the prediction error on the corresponding value of λ_h ranges between 1%-3% (colored in blue).

In general, the errors are very low in all the cases, oscillating in the 1%-2% interval. For each scale factor there is a region of higher error, in which peaks of 7%-11% are reached, as in the case of the scale factor λ_a (Fig. 5.12a). These values may lead to wrong conclusions during the model identification, since, for example, a replica may be confused with a proportional sides. Moreover, it is not possible to predict which region is going to exhibit the higher error, since these areas are training sensitive. The only information about the error is provided by the MSE. However, the points with the higher error are limited in number, thus an acceptable prediction is guaranteed for the majority of the scale factors.

In conclusion, ANNs prove to provide acceptable predictions of the scale factors. Although the model identification is not completely successful, as Table 5.9 shows, the predicted scale factors are never too far from the real ones. More importantly, this analysis demonstrates that a mindful characterization of the systems in similitude leads to a significant reduction of the number of training examples. Instead of using many features of the same type, it is better to pick few different ones. Even though this application is analytical, the actual possibility of reducing the number of samples required for the training and test phases opens the way to the creation of an experimental training set.

Chapter 6

Support of dynamic measurements through similitude formulation

The works listed in Chapter 2 shows that some authors, like Simitses and Rezaeepazhand (Simitses and Rezaeepazhand, 1993), investigate different combinations of scale factors in order to determine the distorted model returning the best prototype prediction. Luo et al. (Luo et al., 2016b), on the other hand, aim at deriving a distorted scaling law which returns predictions within a certain discrepancy range (fixed *a priori*). These types of studies are almost mandatory since not always experimental facilities can house models, as well as some similitude conditions may require the realization of geometrical dimensions beyond the capabilities of today's technology. In this regard, manufacturing errors must not be underestimated. However, both the approach and the results are addressed towards the final comparison with the prototype behavior.

As illustrated in Chapter 4, it is expected that, when the similitude conditions are satisfied, the prototype curve and the model remodulated curve overlap. Thus, as already proposed by Franco et al. (Franco et al., 2019), it is theoretically possible to employ similitude theory may provide information about the quality of the experimental tests, typically affected by uncertainties, random noise and errors due to other sources, by observing the outcome of the remodulation process.

According to this idea, the range of applications of similitude methods widens, being applicable to purposes other than the typical ones reported in literature (namely, predict the behavior of the full-scale model, Chapter 2). The fact that the curves of two models in complete similitude are bound to overlap when the conditions are fulfilled, can be used to support experimental measurements polluted by uncertainties, to provide a criterion to decide whether a laboratory experiment is acceptable or not, and understand to which extent noisy or missing data have an influence on the remodulation process.

For instance, let us consider a campaign of experimental tests on a particular structure which turns out to be polluted by noise. Before repeating the whole set of experiments (with its own financial and temporal costs) or taking decisions and drawing conclusions on the behavior of the structure on the basis of the results obtained, it

would be useful to perform a remodulation and compare it with a set of reference measurements, considered reliable, executed on a structure of the same type but different dimensions. The analysis of the level of discrepancy between the reference curves and the remodulated ones may help to take a final decision concerning the non-acceptance of the results. This procedure may be even more useful when alternative validation methods, like analytical solutions or numerical simulations, are missing or take too much time, as the remodulation takes few seconds.

Hence, in this chapter SAMSARA method is applied in order to corroborate the measurements obtained by means of a DIC test on two AFS panels, in complete similitude, excited by a shaker. The objective is to demonstrate that similitude methods help to establish whether a set of measurements is reliable or not, by comparing the experimental measurements of systems in similitude with different levels of noise.

There are some works in literature that deal with the reconstruction of the response from experimental data and the validation of measurements in presence of noise, but none of them relies on similitude theory. Chen et al. (Chen et al., 2019) propose a method for expanding the dynamic response from a sparse set of points to a much larger set without utilizing a FE model. Successively, Chen et al. (Chen, Avitabile, and Dodson, 2020) propose a function to check the consistencies of measurements to all of the data of the entire set.

DIC cameras are extensively used to analyse the estimate the structural stress and analyze vibrational behavior. In fact, they allow to quickly collect high-density spatial information from structures remotely. This reveals to be an advantage in all those cases in which contact sensors may induce mass-loading effects (like in the case of lightweight structures), or the large scale of the test article implies long sessions of intensive human work and results time consuming. Recently, Sarrafi (Sarrafi et al., 2018) have applied Phase-based Motion Estimation (PME) and video magnification to execute an Operational Modal Analysis (OMA) on turbine blades, aiming at executing vibration-based SHM. Recently, Zhihui et al. (Zhihui et al., 2020) have combined DIC and Element-Free Galerkin (EFG) to characterize the strain field and extracting the stress intensity factor of a surface crack.

However, DIC measurements are bounded by intrinsic limitations, that are the sources of uncertainties, such as the precision of the cameras and the errors. First of all, camera precision is linked to the pixel dimension: the displacement of a point can be registered only if it crosses the borders of the pixel. Concerning the errors, there exist two types (Siebert et al., 2007a; Siebert et al., 2007b): correlation and calibration errors. The latter impacts the reconstruction of the 3D coordinates of the points, while the former can be divided into two more contributions: statistical and systematical errors. Statistical noise is influenced by several environmental conditions, ranging from the intrinsic camera noise, to the photon shot noise, different illumination conditions between the cameras, image intensity contrast, and spatial contrast of the stochastic pattern covering the surface of the test article. On the other hand, systematical errors are mainly related to situations in which the facets do not reflect the effective complexity of the real present transformation, such as curved specimen or lens distortion.

Methods to reduce the errors are the subject of many works. For instance, Jones et al. (Jones et al., 2019) propose X-ray imaging instead of optical imaging when the refraction of visible light, due to density gradients between DIC cameras and the test article (caused by smoke, flame, heated object, shock waves due to explosions, etc.) generates a substantial error that can invalidate the measurement itself. Li et al. (Li, Wang, and Duan, 2019) investigate the discrepancy between the order of the real deformation and that of the applied mapping function in experimental tests involving DIC cameras.

However, even though the accurate calibration and correlation procedures used nowadays, and the reduction methods widely proposed in literature, not all the error sources (like the statistical noise) present in DIC techniques are under the control of the analyzer, therefore not all the results provided by a DIC acquisition system can be used. Hence, these results may need some post-processing to reconstruct the vibrational responses.

In this chapter, the responses are directly extracted from the experimental measurements provided by the DIC camera or with the aid of a SOBI (Second-Order Blind Identification) algorithm (Jia et al., 2020). In particular, the SOBI algorithm and SAMSARA are applied to numerical plates to understand to which extent the noise affects the performances of the methods. Then, SOBI algorithm is used on experimental data to reconstruct the spectra of the excitation forces and to estimate the scale factor of force amplitude. Finally, SAMSARA is used to validate the DIC measurements by overlapping the prototype and proportional sides curves.

The flowchart in Fig. 6.1 summarizes the details of the work concerning the management of the experimental data. The rectangular red frames are assigned to experimental procedure and results, those rounded blue are associated to numerical/analytical procedures and results.

The experimental displacement time histories, provided by DIC cameras, along with the natural frequencies experimentally determined with accelerometric tests previously performed, are given as input to the SOBI algorithm, which extracts the spectra of the excitation forces. This helps to understand whether the input information is coherently retained into noisy data and derive the scale factor of the force amplitude. It is used further to calculate the velocity scale factor, which allows the remodulation in both frequency and amplitude of the velocity curves, analytically evaluated starting from the displacement fields provided by DIC measurements and the experimental natural frequencies, according to Eq. 3.41. This allows to determine if the experimental estimation of the displacements for each mode is acceptable or not. In conclusion, the same operation is performed with the mobility (estimated with Eq. 3.47), then compared with the accelerometric observations, in order to understand if all the analytical calculations carried out are, in general, correct and coherent.

In the following, the approach described is initially applied to results numerically derived for sake of completeness and clarity. Data is polluted with random Gaussian noise to investigate the effect of uncertainties on the results. Then, the procedure is

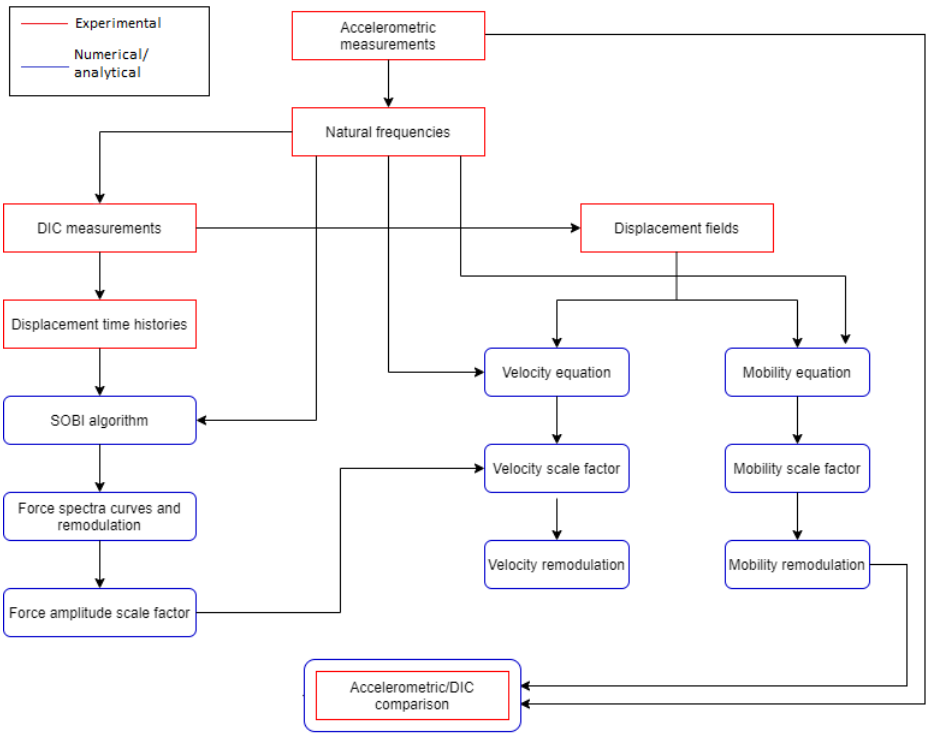

FIGURE 6.1: Work flowchart.

applied to a real, more complex, laboratory case involving the AFS simply supported plates.

6.1 Numerical simulations

The numerical simulations are carried out on two simply supported thin aluminium plates in complete similitude: a prototype (P) and a proportional sides (PS). The geometrical details and the mass of each plate are summarized in Table 6.1, while the material properties, that are the same for both the models, are reported in Table 6.2. The scale factors are summarized in Table 6.3; they are estimated on the basis of the geometrical and material properties of the models, as well as Eqs. 3.24-3.46 assuming that Poisson's ratio and damping do not change. This is an acceptable hypothesis if the material properties and the boundary conditions are the same for both the models.

	a [m]	**b [m]**	**h [m]**	**M [kg]**
P	0.656	0.476	0.003	2.53
PS	0.558	0.405	0.003	1.83

TABLE 6.1: Geometrical characteristics and mass of the prototype and the proportional sides.

Young's modulus, E	71GPa
Mass density, ρ	2700 kg/m^3
Poisson's ratio, ν	0.33
Structural loss factor, η	0.001

TABLE 6.2: Material properties.

Length, λ_a	0.85
Width, λ_b	0.85
Thickness, λ_h	1.00
Mass, λ_M	0.72
Natural frequency, λ_ω	1.38
Velocity, λ_V	1.01

TABLE 6.3: Scale factors of the proportional sides model.

The numerical plates are modeled with PSHELL property and QUAD elements. The mesh is made by 88 points (11 along the x direction, 8 along the y direction). The plates are excited with several sinusoidal forces, applied once at time, with frequencies equal to the natural frequencies of the test articles. The force amplitudes are equal to 2 N and 1 N, respectively. The force PSD S_{FF} can be evaluated as

$$S_{FF} = \frac{F(\omega)F^*(\omega)}{\Delta f}, \tag{6.1}$$

where $F(\omega)$ is the force spectrum, $F^*(\omega)$ is the force spectrum complex conjugate, and Δf is the frequency spacing. Assuming the same frequency resolution ($\lambda_{\Delta_f} = 1$), the force amplitude, i.e. $Re\{F(\omega)\}$, scales as

$$\lambda_{S_{FF}} = \lambda_F^2. \tag{6.2}$$

Therefore, the scale factors of the force amplitude and the PSD are $\lambda_F = 0.5$ and $\lambda_{S_{FF}} = 0.25$.

The SOBI algorithm is used to derive the PSD of the force from the displacements of the plates. If the the PSD curves remodulate according to the scale factor, then the similitude holds and the algorithm is reliable. It is reasonable to assume that this procedure can be applied even for cases in which not all the information about the excitation is known.

Therefore, the force PSD associated with the first two modes are evaluated. For each mode, the time history of the displacement of each point is polluted with random Gaussian noise with 1%, 5%, and 10% of standard deviation σ, so that the effect of an increasing level of uncertainty is investigated.

With reference to the steps listed in Section 3.3, the structural responses needed in step 1 are numerically derived, then noise is added. The modal matrix of step 3 is estimated with the Joint Approximated Diagonalization (JAD) of the whitened response covariance matrix (Belouchrani et al., 1997).

The results of the PSD remodulation at the first natural frequency are summarized in Fig. 6.2. Each figure is made of three curves. The force PSD of the prototype is represented by the blue curve, the PSD of the proportional sides by the red curve, the PSD of the proportional sides remodulated in frequency and amplitude by the yellow curve. In each figure, a small box displays a zoom on the peaks. All the figures demonstrate that the amplitude remodulations carried out with the scale factors predicted are accurate. However, passing from 1% (Fig. 6.2a) to 10% (Fig. 6.2c) of standard deviation, there is a sensitive decrease in PSD amplitude. Therefore, the noise induces a loss of information which explicates in terms of underestimated amplitude. Nonetheless, the scaling procedure is still valid.

Moreover, the results displayed in Fig. 6.2 make clear that the SOBI algorithm can extrapolate coherent information even though the measurements are noisy. The input frequency is set on the basis of the natural frequencies of the plates, hence the remodulation procedures generate curves that are accurately aligned in frequency because the models are in complete similitude. The important information of these plots is not so much the overlap itself, which is expected because the proportional sides is a true model, but the fact that the overlapping curves are reconstructed by noisy measurements and that, despite this, they scale accordingly to the same scale factor. This implies that the input information is kept and it is not distorted.

For sake of completeness, the same procedure is carried out when the excitation frequency is equal to the second natural frequency. The results are reported in Fig. 6.3 and confirm the previous ones: the remodulation works fine, although the noise leads to underestimated amplitudes.

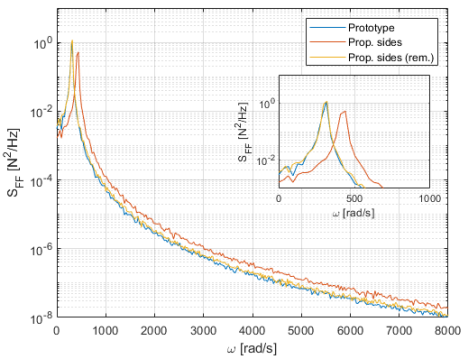

(A) $\sigma = 1\%$.

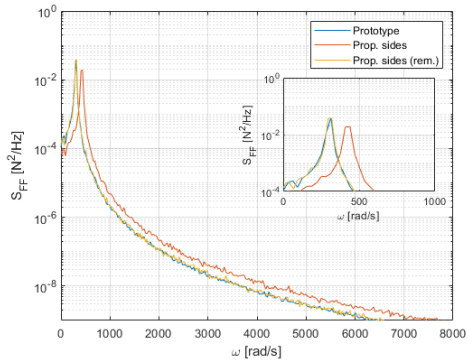

(B) $\sigma = 5\%$.

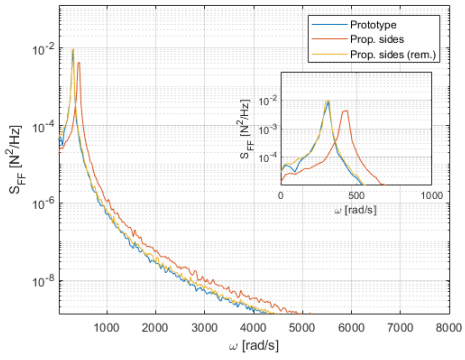

(C) $\sigma = 10\%$.

FIGURE 6.2: Remodulation of the spatially averaged force PSD, first natural frequency (P: 303.45 rad/s; PS: 424.59 rad/s); noise standard deviation equal to 1% (A), 5% (B), and 10% (C).

Therefore, Figs. 6.2-6.3 demonstrate that, by means of the SOBI algorithm, the excitation signal can be extracted from a set of polluted data. On the one hand, such a signal is affected by the noise, in fact the PSD amplitude is underestimated; on the other hand, the information extracted is coherent enough to follow the scaling procedure.

Successively, Eq. 3.46 is used to evaluate the velocity response. Also the mode shapes ϕ_{mn} are polluted with random Gaussian noise at three different standard deviations (1%, 5%, and 10%), so that the impact of uncertainties are analyzed also on the reconstruction of the frequency response. As in the previous case, the main aim is verify the overlap of the velocity curves after the scaling procedure.

The results obtained at the first resonance frequency are shown in Fig. 6.4. When the level of noise is low, the remodulation is accurate (Fig. 6.4a). However, the more data becomes polluted, the more discrepancies in amplitude begin to appear (Fig. 6.4b), increasing significantly when the noise is high (Fig. 6.4c).

These outcomes are corroborated by applying the same procedure to the second

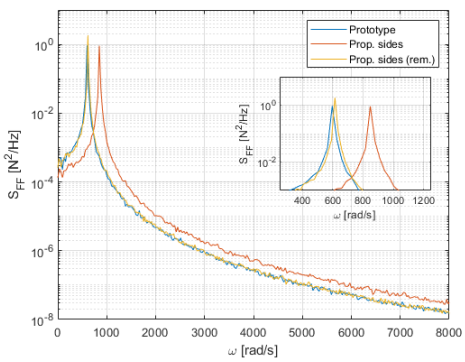

(A) $\sigma = 1\%$.

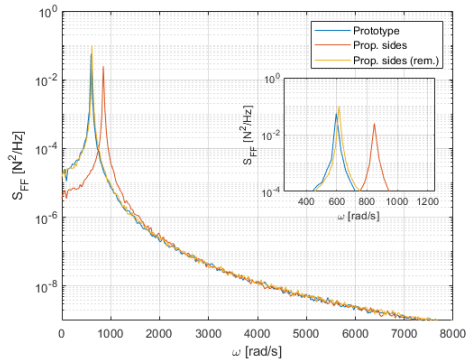

(B) $\sigma = 5\%$.

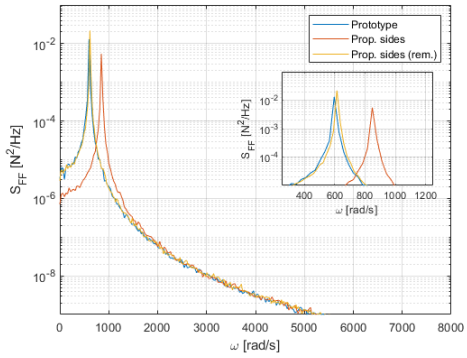

(C) $\sigma = 10\%$.

FIGURE 6.3: Remodulation of the spatially averaged force PSD, second natural frequency (P: 602.88 rad/s; PS: 852.89 rad/s); noise standard deviation equal to 1% (A), 5% (B), and 10% (C).

mode, as shown in Fig. 6.5. The pollution due to noise affects the remodulation also in this case.

Thus, with respect to the reconstruction of excitation force spectra, the presence of noise affects much more the evaluation of velocity response, impairing the scaling process if the uncertainty level is too high.

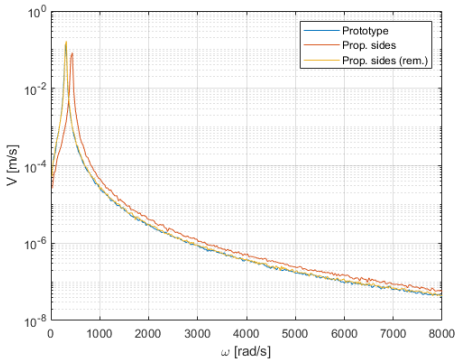

(A) $\sigma = 1\%$.

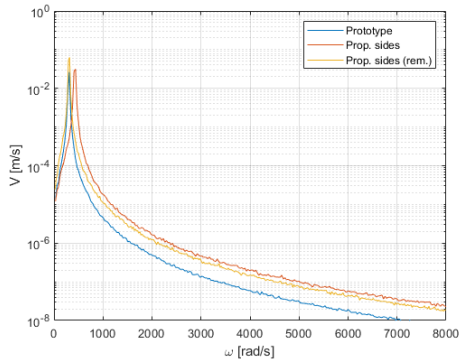

(B) $\sigma = 5\%$.

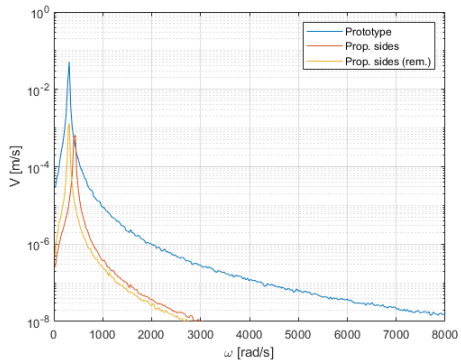

(C) $\sigma = 10\%$.

FIGURE 6.4: Remodulation of the spatially averaged velocity, first natural frequency (P: 303.45 rad/s; PS: 424.59 rad/s); noise standard deviation equal to 1% (A), 5% (B), and 10% (C).

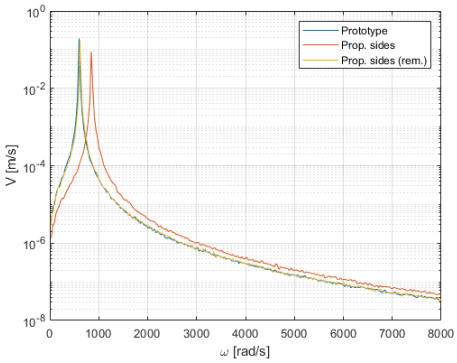

(A) $\sigma = 1\%$.

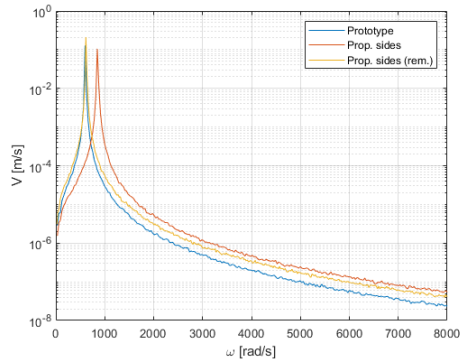

(B) $\sigma = 5\%$.

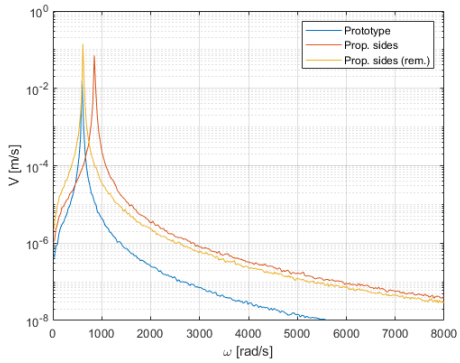

(C) $\sigma = 10\%$.

FIGURE 6.5: Remodulation of the spatially averaged velocity, second natural frequency (P: 602.88 rad/s; PS: 852.89 rad/s); noise standard deviation equal to 1% (A), 5% (B), and 10% (C).

6.2 Experimental tests

The test articles of the experimental tests are two AFS plates with simply supported boundary conditions. Table 6.4 summarizes the geometrical characteristics and masses. The material properties of the skin are the same of those listed in Table 6.2; the properties of the core are listed in Table 6.5; they were obtained by D'Alessandro et al. (D'Alessandro et al., 2014) by means of Ashby's laws. It must be underlined that the foam core is not homogeneous because of the random distribution voids, which generates an inhomogeneous distribution of mass and stiffness. However, the material properties reported in Table 6.5 refer to the equivalent, uniform material with relative density equal to 0.222. For this reason, during the scaling procedure, the core is treated as an isotropic, homogeneous material, characterized by the Young's modulus, mass density, and Poisson's ratio listed in the table. The scale factors are the same of the thin plates used for the numerical simulations, therefore they are summarized in Table 6.3.

	a [m]	**b [m]**	**h_f [m]**	**h_c**	**M [kg]**
P	0.656	0.476	0.001	0.008	3.20
PS	0.558	0.405	0.001	0.008	2.34

TABLE 6.4: Geometrical characteristics and mass of the prototype and the proportional sides.

Young's modulus, E_c	6.48 GPa
Mass density, ρ_c	600 kg/m^3
Poisson's ratio, ν_c	0.31
Relative density, ρ_r	0.222

TABLE 6.5: Aluminium foam core material properties.

6.2.1 Experimental setup

The experimental setup and test articles are shown in Fig. 6.6 and 6.7, respectively. The displacements are captured by two high-speed synchronized cameras connected to DIC software, corresponding to the Q450 high-speed DIC system by Dantec Dynamics. The maximum acquisition frequency of the cameras is 7530 frames per second at a resolution of 1 megapixel; the displacement precision is equal to 0.02 pixels. Each acquisition consists of 1000 samples. No averaging is adopted. The frequency range covers up to 31,400, already considering the Nyquist Theorem, thus the bandwidth of interest is 0–15,700 rad/s. The cameras are arranged in stereoscopic configuration, so that each point of the plate is focused on a specific pixel in the image plane of each camera. A stochastic texture is applied to both prototype and proportional

sides, therefore the plates surfaces result as an indistinguishable pattern to both cameras. The image of the first camera is subdivided into several subimages, the so-called facets, used by the correlation algorithm which determines a suitable transformation of each facet, matching the homologous area in the second camera image. Executing this procedure for every loading step of the object under test, it is possible to follow the facet deformation during all the experiment (Siebert et al., 2007a; Siebert et al., 2007b).

FIGURE 6.6: Experimental setup.

A signal generator produces the excitation waveform, then passed to an amplifier and an electrodynamic shaker which excites the plate. The points of measurement are determined by overlapping a virtual grid to the image of the test article, which is contained into a frame known as mask. The mask separates the area of measurement from the background and indicates which part of the field of view must undergo the measurement procedure. The dimensions of the grid elements and facets are determined on the basis of a trade-off among several matters (Becker et al., 2006; Siebert et al., 2007b).

In first place, the more dense the grid is, the better the spatial resolution of the variable under investigation (that, in this case, is the displacement). On the other hand, this leads to an increasing computational effort and required memory space, since there would be more grid points to process. Reducing the number of points would reduce the computational and memory burden, although the displacements would be described more coarsely.

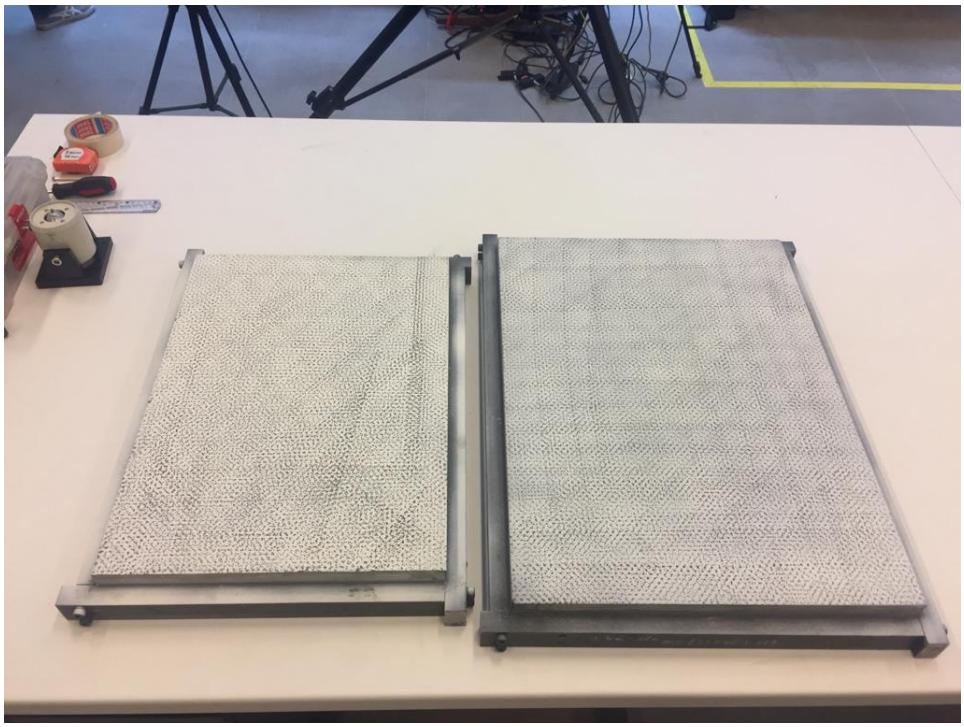

FIGURE 6.7: Experimental plates with speckle patterns for DIC analysis.

The statistical error previously introduced is directly linked to the facet size, since the error decreases with the square root of the number of facet pixels as the facet dimensions reduces. However, the results of the measurement are evaluated as mean values for each fact, hence the spatial resolution is too low if the facet dimensions decrease too much.

Taking into account all these aspects, the resulting trade-off leads to choose, for both prototype and proportional sides model, a virtual grid made of 30x44 square elements, with a total of 1345 grid points. The grid element and the facets of the prototype have dimensions of 20x20 and 23x23 pixels, respectively. Since it is fundamental to compare the displacements of homologous points, if the DIC cameras frame the same portion of the panel, then the grid spacing and facets dimensions must be scaled down accordingly to the geometrical dimensions of the plates, i.e., with a scale factor equal to 0.85. In this way, the grid elements have dimensions 17x17, while the facets are set to 21x21.

The excitation point of the plates has non-dimensional coordinates (0.2000, 0.2875); the load is a sinusoidal force at a specific frequency (the natural frequencies of the plate, previously evaluated by means of EMA). The prototype and the proportional sides are excited with the same waveform but with different and unquantified amplifier gain.

6.2.2 Reconstruction of excitation spectra

An example of the measured displacement is displayed in Fig. 6.8. The plot shows a noticeable noise, mainly due to the contactless characteristic of the procedure itself, but also to the precision of the DIC cameras. The AFS panels have a high stiffness-to-weight ratio, and the simply supported boundary conditions adds an artificial stiffness. In addition, the displacement magnitude decreases as the resonance order increases. All these factors contribute to the generation of small displacements which values may assess below the DIC camera precision. Considering the contribution of the sources of statistical errors, too, the level of noise becomes noticeable, as pictured in Fig. 6.8. As a consequence, the raw measurements cannot be used directly, and post-processing is needed.

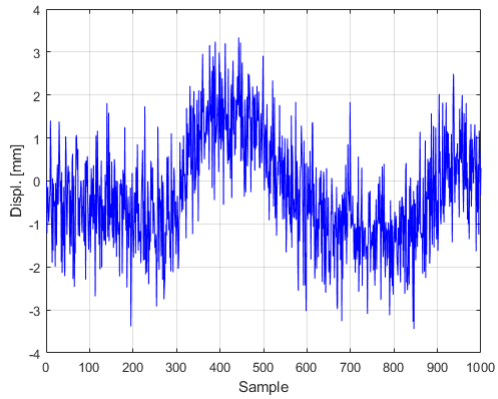

FIGURE 6.8: Displacement of the point no. 100 of the prototype, mode 1 (1350 rad/s).

Concerning the excitation, only the waveform - which is sinusoidal - is a certain information. The gain of the amplifier is unknown, hence the force amplitude is unknown, too. The SOBI algorithm is, therefore, to determine the spectra of the input forces. In fact, as shown in Section 6.1, the input information underlying the measured displacement time histories is retained and this information is coherent enough to follow the scaling procedure. Hence, it would be possible, as a rule of thumb, to derive the scale factor of both force PSD and amplitude by overlapping the prototype curve and the curve of the proportional sides after the frequency remodulation.

With reference to the list provided in Section 3.3, the time histories required in step 1 are experimentally gathered by means of DIC measurements. The structural loss factor, for the AFS panels, is set to 0.02 (D'Alessandro et al., 2014).

The spatially averaged PSD of the excitation force is shown in Fig. 6.9 for the first three excitation frequencies. In order to determine the scale factor of the force PSD, the curves of the proportional sides model (the red curves) are first remodulated only in frequency, then the values of the PSDs are compared at homologous points in frequency. For this purpose, 30 points are selected for each curve (mainly clustered

around the resonance peak), then the scale factor for each point is evaluated. The mean value of the force PSD scale factor, obtained by averaging on all the points and all the excitation frequencies, is $\lambda_{S_{FF}} = 0.67$, which returns very good amplitude scaling, as the remodulated curves (the yellow ones) illustrate.

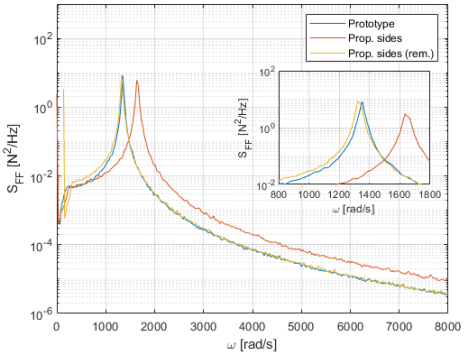

(A) Mode 1 (P: 1350 rad/s; PS 1645 rad/s.

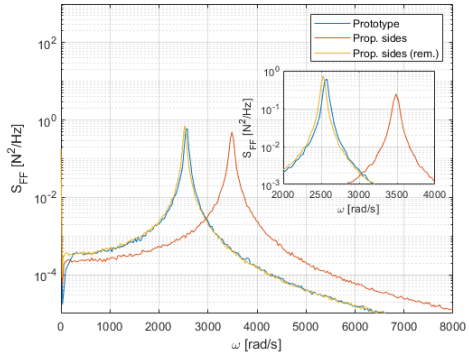

(B) Mode 2 (P: 2562 rad/s; PS 3485 rad/s.

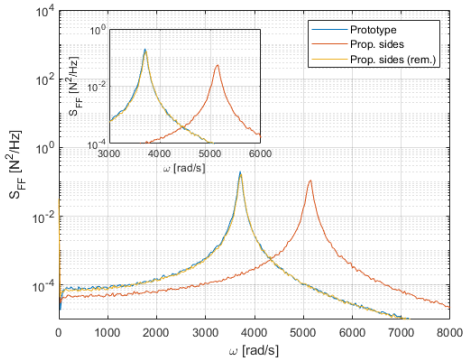

(C) Mode 3 (P: 3705 rad/s; PS 5130 rad/s.

FIGURE 6.9: Remodulation of the spatially averaged force PSD for mode 1 (A), mode 2 (B), and mode 3 (C).

Fig. 6.9 shows that the SOBI algorithm can return coherent information about the excitation even though the sources of experimental uncertainties.

As already seen in Chapter 4, the inhomogeneity of the foam leads to slight discrepancies in frequency between the prototype and the remodulated curve of the model. These discrepancies begin to be noticeable from the fourth resonance on, and they increase as the frequency increases. this is the reason why only the first three resonance peaks are used to evaluate the force PSD scale factor. In fact, the missing overlap would have prevented the direct comparison of homologous points in frequency. Moreover, it wil be demonstrated further that these modes are the only ones well identified for both prototype and proportional sides, therefore they are considered as the most reliable for extracting the input scaling characteristics.

Fig. 6.9 also shows that the amplitude of the PSDs decreases in frequency, even though the excitation amplitude is the same for each model. Probably, this is due to the decreasing value of displacements, when moving to further modes, which become less recognizable to the DIC acquisition system.

6.2.3 Reconstruction of the velocity response

The force spectra determined in the previous section are reliable enough to estimate the force amplitude and inserting it into Eq. 3.41 and reconstruct, analytically, the velocity response. All the parameters required are known: the modal mass (Eq. 3.43), natural frequencies, and the mode shapes ϕ_{mn}, the latter provided by DIC measurements as displacement fields.

From the force PSD scale factor, the force amplitude scale factor is estimated; it is equal to $\lambda_F = 0.82$ and, by means of Eq. 3.46, it returns a velocity scale factor equal to $\lambda_V = 1.00$.

Fig. 6.10 illustrates the displacement fields of both prototype (Fig. 6.10a) and proportional sides (Fig. 6.10b), and the reconstruction and remodulation of the velocity curves (Fig. 6.10c). Both the displacement fields exhibit a good representation of the first mode shape. Substituting the normalized values of these displacements into Eq. 3.41 leads to the velocity curves of Fig. 6.10c. As before, the frequency remodulation returns a satisfying overlap of the peak frequency, however this is a consequence of SAMSARA, since the models are in complete similitude. The frequency remodulation alone does not give important information on the experimental result. What is important, instead, is the amplitude level of the prototype, which is reconstructed accurately. This happens because the mode shapes are well reconstructed, and also because the normalized values of displacements are coherent between the prototype and the proportional sides. Thus, the velocity curves demonstrate that the experimental information is reliable and that the measurement is executed successfully.

These considerations are strengthened by the results obtained with the second mode, shown in Fig. 6.11. Also in this case, the remodulated curve matches accurately the prototype curve (Fig. 6.11c) in amplitude. As the mode shapes of the prototype (Fig. 6.11a) and proportional sides (Fig. 6.11b), demonstrate, this happens because the displacement fields are recognizable and their normalized values are coherent between the models.

When the modes become less identifiable, then the amplitude remodulation shows some discrepancies. For example, considering the fourth mode, the prototype mode shape (Fig. 6.12a) is quite clear, while that of the proportional sides is not (Fig. 6.12b) (even though the right side of the displacement map exhibits some peaks that may be associated with the right lobe of the mode). The remodulation procedure highlights the lack of an identifiable spatial pattern, and the consequent absence of coherence between the local displacements, as the prototype velocity curve and its reconstruction do not overlap well (Fig. 6.12c).

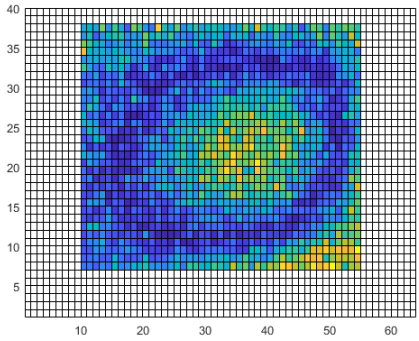

(A) Mode 1 (Prototype mode shape).

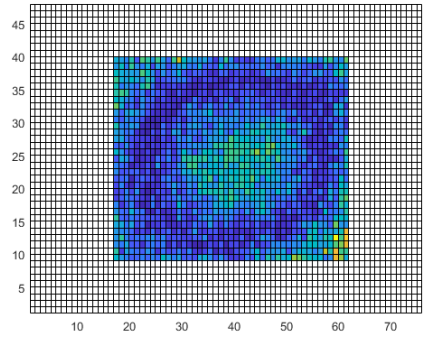

(B) Mode 2 (Proportional sides mode shape).

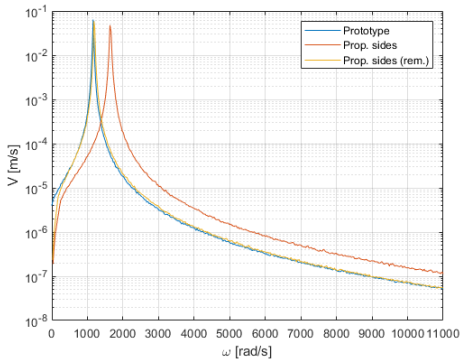

(C) Velocity curves.

FIGURE 6.10: Mode shapes and velocity remodulation of the first mode (P: 1350 rad/s); PS: 1645 rad/s).

The outcomes worsen when the mode shapes are not identified at all. The sixth mode is a fitting example, illustrated in Fig. 6.13. The velocity scaled curves are totally different, exhibiting discrepancies higher than one order of magnitude (Fig. 6.13c). In fact, the mode shapes of both prototype (Fig. 6.13a) and proportional sides (Fig. 6.13b) are not identified at all. The plate displacements become smaller as the frequency increases, confusing with the noise. As a consequence, the displacement field displays totally uncorrelated values.

These results prove that, provided a reference test article - namely, the prototype - which behavior is known, if a model fulfilling the similitude conditions is tested, then the similitude theory helps to understand the quality of an experiment polluted by noise and to validate it.

6.2.4 Reconstruction of mobility

The mobility can be reconstructed with Eq. 3.48, with an amplitude scale factor equal to $\lambda_Y = 0.99$. By doing so, the dynamic response of the plates is derived without

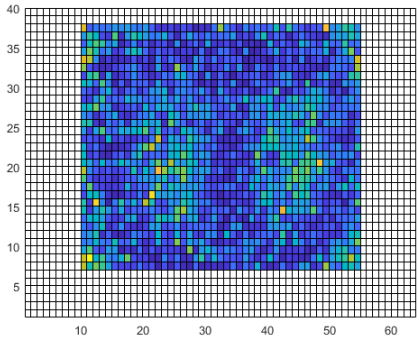

(A) Mode 2 (Prototype mode shape).

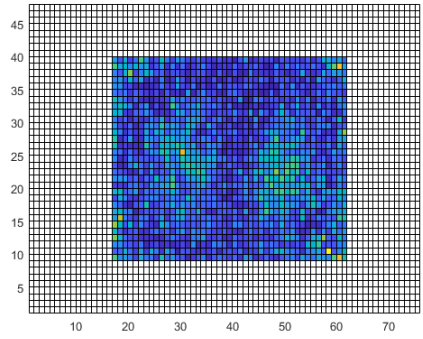

(B) Mode 2 (Proportional sides mode shape).

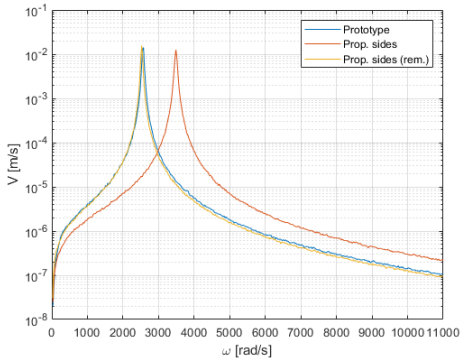

(C) Velocity curves.

FIGURE 6.11: Mode shapes and velocity remodulation of the second mode (P: 2562 rad/s); PS: 3845 rad/s).

directly involving the force spectra obtained with the SOBI algorithm. This is a useful alternative approach, in case of problems in deriving the force PSD.

The curve remodulations of the modes previously investigated are gathered in Fig.6.14. These plots confirm the results shown up to now: the quality of the remodulation can tell which mode is well reconstructed and which is not.

Fig. 6.14 is more than a simple reproposition of Figs. 6.10-6.13. In fact, the reconstructions of the mobility can be overlapped to the experimental results described in Chapter 4, in order to check the quality of the data post-processing from DIC measurements. These comparisons are shown in Fig. 6.15.

With reference to Fig. 6.16, too, illustrating the experimental mode shapes of the third and fifth modes (not yet shown), the prototype curves in Fig. 6.15a exhibit a very good match between the accelerometric and DIC measurements. The first five modes are well predicted, since the spatial patterns are reasonably reconstructed (Figs. 6.16a-6.16b), in agreement with the fact that the mode shapes are well recognized by DIC cameras. The sixth mode instead, is not identified well, and this affects the mobility

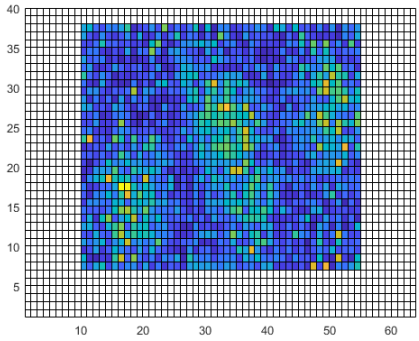

(A) Mode 4 (Prototype mode shape).

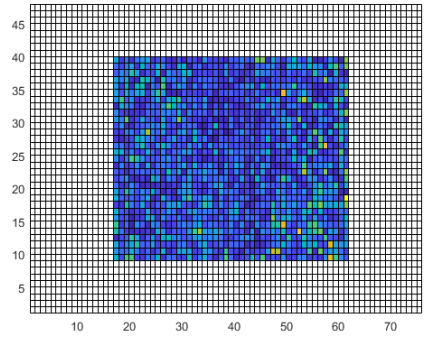

(B) Mode 4 (Proportional sides mode shape).

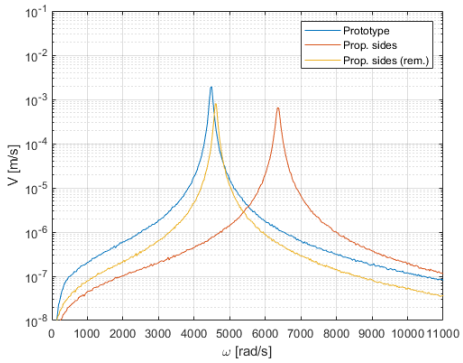

(C) Velocity curves.

FIGURE 6.12: Mode shapes and velocity remodulation of the fourth mode (P: 4477 rad/s); PS: 6355 rad/s).

reconstruction, shown by the underestimated resonance peak.

These considerations are confirmed by the comparisons between the accelerometric and DIC measurements of the proportional sides (Fig. 6.16b). The good evaluation of the first three resonance peaks is in agreement with the identification of the associated mode shapes. However, from the fourth mode on, the peaks are underestimated.

For sake of completeness, the correlation between the experimental mode shapes of prototype and proportional sides is shown in Fig. 6.17 in terms of MAC. The correlation percentage confirms the results seen until now. The first modes of prototype and proportional sides exhibit the higher correlation, upholding that the DIC system captures this mode satisfactorily. The second and third mode shapes follow in order of decreasing correlation, since the cameras roughly identify the form of the mode, but noise becomes noticeable. The fourth, fifth, and sixth mode do not exhibit any correlation, although some shapes are well identified in one model (for example, the fourth and fifth modes of the prototype), they are not in the other. The remaining comparisons return MAC values approximately equal to zero, except for the 4th-1st

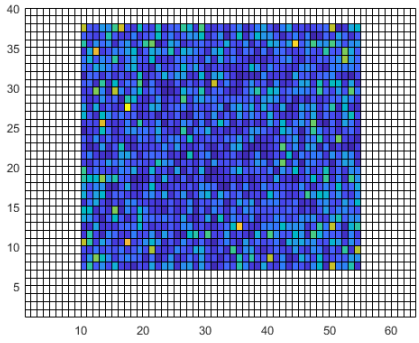

(A) Mode 6 (Prototype mode shape).

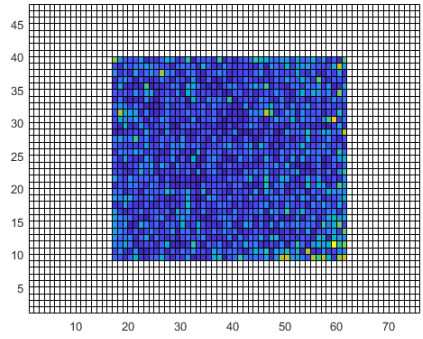

(B) Mode 6 (Proportional sides mode shape).

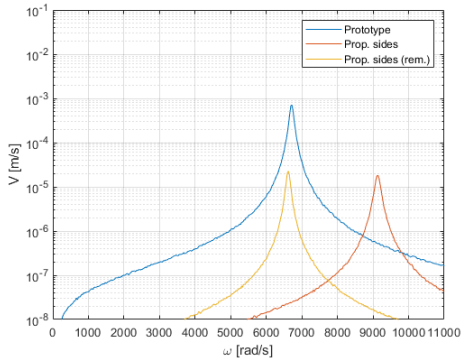

(C) Velocity curves.

FIGURE 6.13: Mode shapes and velocity remodulation of the sixth mode (P: 6707 rad/s); PS: 9124 rad/s).

and 5th-4th couples of prototype and proportional sides. However, these values of correlation are comprised in the range 10%-0%, and can be considered as outcomes due to noise.

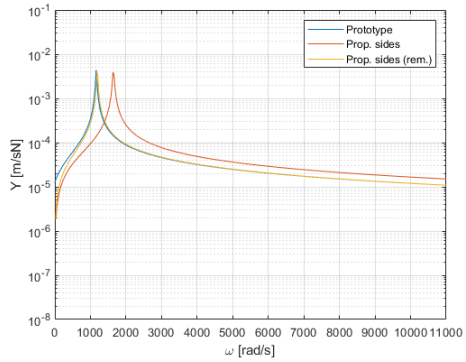

(A) Mode 1 (P: 1350 rad/s; PS: 1645 rad/s).

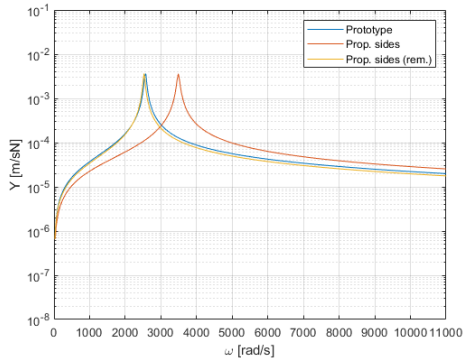

(B) Mode 2 (P: 2562 rad/s; PS: 3845 rad/s).

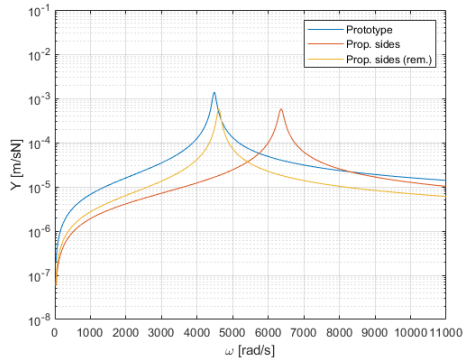

(C) Mode 4 (P: 4477 rad/s; PS: 6355 rad/s).

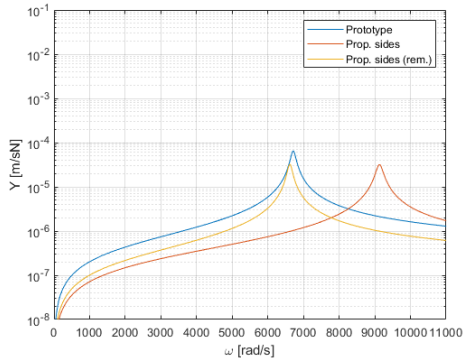

(D) Mode 6 (6707 rad/s; PS: 9124 rad/s).

FIGURE 6.14: Mobility remodulation curves of the first (A), second (B), fourth (C), and sixth (D) mode.

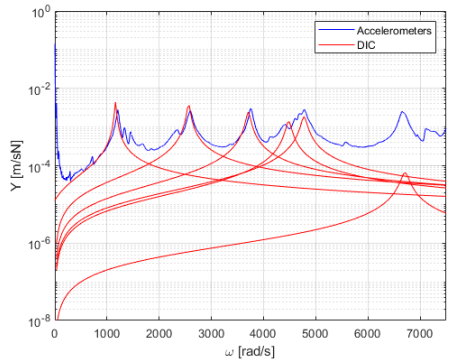

(A) Prototype.

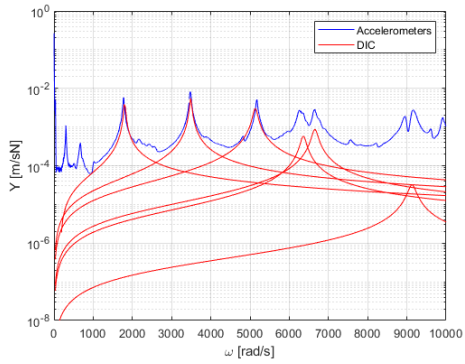

(B) Proportional sides.

FIGURE 6.15: Comparisons between the accelerometric and DIC measurements of spatially averaged mobility.

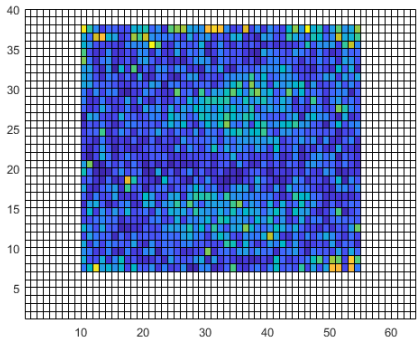

(A) Prototype mode 3, 3705 rad/s.

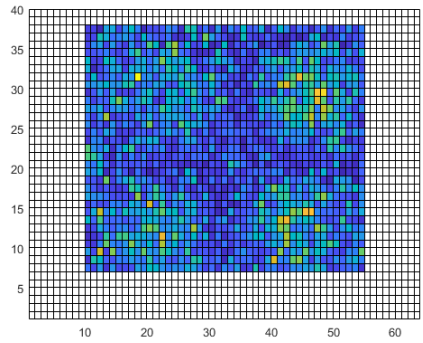

(B) Prototype mode 5, 4772 rad/s.

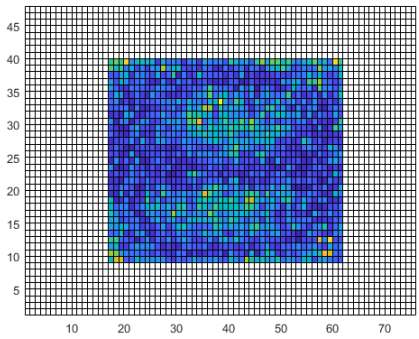

(C) Proportional sides mode 3, 5130 rad/s.

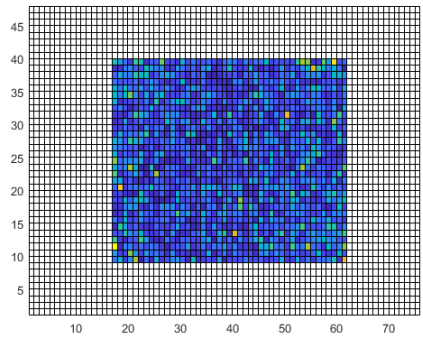

(D) Proportional sides mode 5, 6650 rad/s.

FIGURE 6.16: Spatial patterns of the third and fifth mode shapes of both prototype and proportional sides.

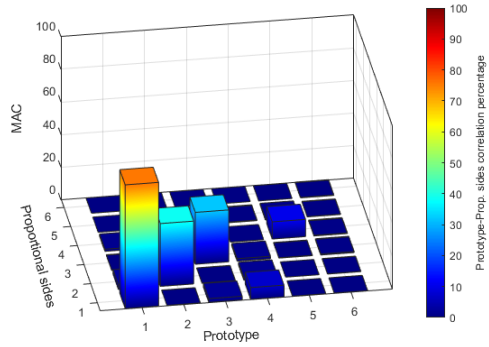

FIGURE 6.17: MAC between the experimental mode shapes of prototype and proportional sides.

Chapter 7

Conclusions and further research

7.1 Conclusions

The review provided in Chapter 2 has proven that similitude methods are an interesting and useful tool for many kinds of problems (free and forced vibrations, buckling, and impact problems), as well as for many engineering fields (aerospace, civil, naval engineering, etc.)

Even though the first methods are still applied, the continuous proposals of new methodologies highlights the will of scientific community to go beyond the typical limits (for instance, the analytical effort when deriving the similitude conditions). A general trend can be foreseen. On the one hand, the constantly increasing computational resources push towards procedures that can be implements in an algorithm; on the other hand, new methods try to solve more complex problems, like acoustic-elastic systems or multicomponent structures.

However, these analytical/numerical considerations must not distract the attention from the main purpose of similitude theory, that is, overcoming the problems related to full-scale testing, which is fundamental for investigating real structures without the simplifications of computer simulations (absence of noise, perfect boundary conditions, etc.).

In order to demonstrate not only the effectiveness of similitude conditions and scaling laws, but also their range of validity, the results of experimental tests on CFCF thin plates and simply supported AFS plates are reported in Chapter 4. Concerning the CFCF plates, the tests confirm that, fulfilling the similitude conditions, the reconstruction of the prototype response, in terms of natural frequencies and frequency response function, is quite accurate (except for some inconsistencies due to experimental uncertainties).

In the case of sandwich plates, a complete and a reduced set of similitude conditions are derived. While the former is used to study simply supported AFS plates, the latter is applied to the same type of plates with free-free boundary conditions. Complete similitudes are achieved in both the cases, and the similitude conditions and scaling laws are the same, independently of the boundary conditions. Of course, they can be applied among models with the same boundary conditions, not among systems which do satisfy the similitude conditions but have different boundary conditions. The

experiments show that true models allow to predict the vibroacoustic characteristics of the prototype with an acceptable degree of accuracy. However, some errors generates from the inhomogeneous distribution of stiffness and mass of the aluminium foam core, which may acquire increasing importance as the frequency becomes higher. This source of uncertainties affects the natural frequencies, therefore the reconstruction of the FRF and radiated acoustic power, too.

For both structural configurations, namely, thin and sandwich plates, the avatars prove that none of the scaling laws work satisfactorily in the frequency range of interest; maybe a law is able to catch a natural frequency or a resonance peak, but it is not possible to generalize such a scaling law-frequency range correspondence to all the avatars.

Unfortunately, almost in all experimental applications, partial similitude may be the best one can hope for, since they are not just an analytical matter, but also the result of manufacturing constraints (methods limitations, errors, etc.). Adding non-scaling phenomena, like size effects, which affect important properties of the specimens in terms of strength and load-bearing, makes the picture even more complicated. Moreover, the problem of partial similitudes cannot be generalized, as each system is sensitive to different parameters; to give an example, the aspect ratio affects panels, while cylinders are influenced by length and radius, damping is a key factor in modal approaches, strain-rate sensitivity has an important effect in impact problems (and more general data, such as material changes or excitation sources, is not taken into account).

It may be interesting trying to understand if it is possible to exploit, in any manner, avatars or, more generally, the information provided by all the types of models. This has led to the application of machine learning techniques, ANNs in particular. In Chapter 5, the potentialities of ANNs are investigated on simply supported beams in similitude, in first place, and CFCF thin plates, then. The prediction of dynamic characteristics from scaling parameters and the reconstruction of the scale factors from dynamic characteristics are performed for both the cases.

Concerning the beams, the results are very good, since the neural networks return prediction with high accuracy even if the training set is polluted with numerical noise. However, simply supported beams are a relatively simple case, as the system does not generate avatars and the target function is not complicated to "reconstruct". As a consequence, the system characterization does not require a strong diversification of input features: length scale factor and ten natural frequencies are enough to describe the system.

When dealing with plates, instead, a thorough sensitivity analysis is required, in order to identify the best architecture and the number of training examples. The results underline that, when there is no noise in the training data, the ANNs can be pushed up to very complex architectures, predicting the natural frequencies with great accuracy. Good results are achievable with noisy data, too, although there is a noticeable increase of number of training examples. This problem is relatively reduced when performing the task of model identification, since the possibilities of characterizing

the models are wider, therefore allowing the choice of different input features. As a consequence, less complex ANNs and less examples are required, simplifying the training phase.

The robustness to noise is undoubtedly helpful in case experimental data is used as training examples. Actually, a possible future step would be to use directly the results of experiments, although the creation of an acceptable experimental training set may be unfeasible for several reasons, ranging from financial costs to temporal and human-work efforts.

However, ANNs do have some implicit disadvantages, basically related to the lack of control on training and an *a priori* identification of the architecture, which has defied, until now, any attempt of boundaries definition. Nonetheless, the sensitivity analysis executed demonstrated that these disadvantages can be smoothed, highlighting that critical thinking is the key when using machine learning methods and analyzing their results. Hence, ANNs are an useful tool as they can be used with any type of data and can help to exploit the big amount of information obtainable from numerical simulations or experimental tests, to reduce the number of runs with consequent time saving, and to provide quick results when reference solutions are needed.

The last activity is reported in Chapter 6 and deals with the investigation of similitude methods as a mean to support noisy experimental measurements. For this purpose, the displacements of two AFS plates in complete similitude are observed with a DIC acquisition system. The response is reconstructed analytically, starting from the experimental measurement, since the acquisitions are strongly polluted by noise. The displacement in time is given as input to a SOBI algorithm, which returns the spectra of the input excitations. In this way, the input information is reconstructed, its coherence is checked, and a velocity scale factor is estimated, so that the velocity remodulation can be executed. Reconstructing the velocity response peak by peak, it is demonstrated that the model curves overlap accurately when the DIC measurements are able to identify the mode shapes. When just one spatial pattern is not sufficiently recognized, the remodulation exhibits noticeable discrepancies.

For sake of completeness, this procedure is carried out with mobility, too, then overlapped to the accelerometric measurements shown in Chapter 4 to check whether the analytical reconstruction is consistent. Also in this case, the accelerometric/DIC measurements comparison returns good matches only for the resonances corresponding to the identified modes. In the other cases, the peak values are seriously underestimated.

In conclusion, the similitude results are coherent with the quality of the experimental measurements. Similitude methods turn out to be an interesting tool for understanding if a set of measurements is reliable or not, especially in the light of an expanding set of approaches which allow to extrapolate the information hidden in polluted observations. The main obstacle, now, which may prevent a wider application of similitude as validation tool is that the complete similitude is mandatory

7.2 Further research

The results of this thesis show that further research on systems in similitude can take different paths. Distortions may be seen as manufacturing variabilities, or perturbations of a system with respect to a reference state that affects the responses [the works (Cunefare and De Rosa, 1999; De Rosa et al., 2007) can give a better idea]. Further research should concentrate on classical similitude theory, by proposing similitude conditions and scaling laws in which the parameters are re-arranged in different groups, physically meaningful, such as the structural wavenumber, since it is representative of the wavenumber. On the other hand, the application of machine learning in this thesis opens the way to other types of procedures, as CNNs or RNNs (Recurrent Neural Networks), SVM or Gaussian Processes. The choice spectrum is quite wide and can be partially driven by the type of target and data at disposal.

A new method has recently been proposed, which aims at reconstructing the response of a system, starting from that of a reference one. This method is called VOODOO (Versatile Offset Operator for the Discrete Observation of Objects) and the first results, concerning the reconstruction of the displacement of two plates, show that an exact evaluation of the frequency response is achieved (De Rosa et al., 2021). These results are promising indeed, as, in similitude terms, the linear transformation matrix which links the systems allows to move from the response of the prototype to that of the model (which is an avatar), and vice versa; moreover, similitude conditions and scaling laws are not directly involved. Investigations on the properties of the transformation matrix and the possibility to widen the range of applications are ongoing.

Last, but not least, research efforts should be addressed towards the definition of a metric of similitude degree; some examples are provided in Chapter 2 (De Rosa, Franco, and Meruane, 2015; Meruane, De Rosa, and Franco, 2015), yet their results are not always satisfying. The definition of such a metric would open the way to other, new approaches to similitude, based on the minimum/maximum distance between a model and a reference, as well as the minimization/maximization of an error/gain function referring to the metric itself.

Appendix A

Reference tables

Three reference tables will follow in order to provide a useful synopsis to the interested readers. They report the methods, Table A.1, and the test-articles, Table A.2, respectively. The last one, Table A.3, presents the references for complex structures and other application fields.

Method	References
DA	Rayleigh, 1915; Goodier and Thomson, 1944; Goodier, 1950; Murphy, 1950; Langhaar, 1951; Charlton, 1954; O'Sullivan, 1957; Ezra, 1962; Katzoff, 1963; Carden and Herr, 1964; Jones, 1964; Mixson and Catherine, 1964a; Mixson and Catherine, 1964b; Pankhurst, 1964; Adkins, 1965; Catherine, 1965; Chao and Wedekind, 1965; Folkman, Baldwin, and Wainwright, 1965; Gabron and Johnson, 1965; Gukhman, 1965; Jones and Harrison, 1965; Kline, 1965; Fowle, Gabron, and Vickers, 1966; Gabron, 1966; Morosow and Jaszlics, 1966; Shih, 1966; Watkins, 1966; Herr and Wayne Leonard, 1967; Leadbetter, Wayne Leonard, and John Brock, Jr., 1967; Thompson, Jr., 1967; Adelman and Steeves, 1968; Blanchard, 1968; Catherines, 1968; Peele, Thompson, Jr., and Pusey, 1968; Steeves and Catherines, 1968; Wissmann, 1968; Wolowicz, Bowman, Jr., and Gilbert, 1968; Pinson and Wayne Leonard, 1969; Rolling, Murray, and Marshall, 1969; Leadbetter, 1970; Maples and Scogin, 1970; Peele, Wayne Leonard, and Leadbetter, 1970; Soedel, 1971; Stubbs, 1971; Thornton, 1971; Shannon, 1972; Emori, 1973; Hunt, 1973; Marshall and Foster, 1973; McGehee and Stubbs, 1973; Bernstein et al., 1974a; Bernstein et al., 1974b; Holmes and Sliter, 1974; Levy et al., 1974; Lowe, Al-Hassani, and Johnson, 1974; Mason et al., 1974a; Mason et al., 1974b; Pinson, 1975; Zalesak, 1975; Leadbetter et al., 1976; Blanchard, Miserentino, and Leadbetter, 1977; Brownfield and Rogers, 1978; Cagliostro, Florence, and Abrahamson, 1979; Tennyson et al., 1981; Duffey, Cheresh, and Sutherland, 1984; Krayterman and Sabnis, 1984; Keith Belvin and Edighoffer, 1986b; Westine and Mullin, 1987; Letchworth, McGowan, and Gronet, 1988; Morton, 1988; Jackson and Fasanella, 1989; French, 1990; Jackson, 1990; Magness and Farrand, 1990; McGowan, Edighoffer, and Wallace, 1990; Baker, Westine, and Dodge, 1991; McGowan, Jaeed, and Edighoffer, 1991; Swanson, Smith, and Qian, 1991; Kellas and Morton, 1992a; Moradi and Parsons, 1992; Anderson, Jr., Mullin, and Kuhlman, 1993; Wen and Jones, 1993; Dornfeld, 1994; Pintado and Morton, 1994; French and Eastep, 1996; Usami and Kumar, 1996; Friedmann, Guillot, and Presente, 1997; Kumar et al., 1997; Rosenberg, Kreif, and Dekel, 1997; Singer, Arbocz, and Weller, 1997; Wereley and Kamath, 1997; Christoforou and Yigit, 1998; Presente and Friedmann, 1998a

DA (continued)	Presente and Friedmann, 1998b; Zhao, 1998; Greschik, Mikulas, and Freeland, 1999; Friedmann, 1999; Harris and Sabnis, 1999; Jackson and Fasanella, 1999; Zhao, 1999; Alves and Oshiro, 2006a; Alves and Oshiro, 2006b; Jiang et al., 2006; Oshiro and Alves, 2007; Yigit and Christoforou, 2007; Neuberger, Peles, and Rittel, 2007a; Neuberger, Peles, and Rittel, 2007b; Sutherland and Guedes Soares, 2007; Szirtes, 2007; McKown, Cantwell, and Jones, 2008; Quercetti, Müller, and Schubert, 2008; Steinchen, Kramer, and Kupfer, 2008; Yulong, Yongkang, and Pu, 2008; Christoforou and Yigit, 2009; Kim, Lee, and Chang, 2009; Oshiro and Alves, 2009; Richards et al., 2009; Acquaro et al., 2010; Canfield, Peddieson, and Garbe, 2010; Gang, Wang, and Su, 2010; Ramu, Prabhu Raja, and Thyla, 2010; Sabour and Bhat, 2010; Oshiro et al., 2011; Liu, Zhou, and Herrin, 2011; Tan, 2011; Bond et al., 2012; Ciappi et al., 2012; Kuneš, 2012; Oshiro and Alves, 2012; Ricciardi et al., 2012b; Zohuri, 2012; Mazzariol and Alves, 2013; Ramu, Prabhu Raja, and Thyla, 2013; Wan and Cesnik, 2013; Yang et al., 2013; Gauchìa et al., 2014; Mazzariol and Alves, 2014; Noam, Dolinski, and Rittel, 2014; Ricciardi et al., 2014; Zai et al., 2015; Mazzariol, Oshiro, and Alves, 2016; Xu et al., 2016; Saito and Kuwana, 2017; Spada et al., 2017; Zohuri, 2017; He et al., 2020
STAGE	Hu, 2000; Li and Jones, 2000; Hilburger, Rose, and Starnes, Jr., 2001; Sonin, 2001; Holland et al., 2002; Pototzky, 2002; Cartmell, Ziegler, and Neill, 2003; Jackson and Fasanella, 2003; Canfield et al., 2004; Kline, 1965; Szucs, 1980; Qian et al., 1990; Rezaeepazhand and Simitses, 1993; Simitses and Rezaeepazhand, 1993; Simitses and Rezaeepazhand, 1995; Rezaeepazhand, Simitses, and Starnes, Jr., 1995a; Rezaeepazhand, Simitses, and Starnes, Jr., 1995b; Rezaeepazhand, Simitses, and Starnes, Jr., 1996a; Rezaeepazhand, Simitses, and Starnes, Jr., 1996b; Rezaeepazhand and Simitses, 1997; Simitses, Rezaeepazhand, and Sierakowski, 1997; Tabiei, Sun, and Simitses, 1997; Chouchaoui and Ochoa, 1999; Chouchaoui, Parks, and Ochoa, 1999; Simitses, Starnes Jr, and Rezaeepazhand, 2000; Simitses, 2001; Ungbhakorn, 2001; Singhatanadgid and Ungbhakorn, 2002; Wu, Cartmell, and Whittaker, 2002; Singhatanadgid and Ungbhakorn, 2003; Ungbhakorn and Singhatanadgid, 2003a; Ungbhakorn and Singhatanadgid, 2003b; Ungbhakorn and Singhatanadgid, 2003c; Wu, 2003; Heeg, Spain, and Rivera, 2004; Friedmann, 2004; Frostig and Simitses, 2004; Kim, Kwak, and Chang, 2004

STAGE (continued)	Ambur et al., 2005; Singhatanadgid and Ungbhakorn, 2005; Wu, 2005; Wu, 2006; Ungbhakorn and Wattanasakulpong, 2007; Singhatanadgid and Na Songkhla, 2008; Torkamani, Jafari, and Navazi, 2008; Rezaeepazhand and Wisnom, 2009; Torkamani et al., 2009; Ungbhakorn and Singhatanadgid, 2009; Rezaeepazhand and Yazdi, 2011; Yazdi and Rezaeepazhand, 2011a; Yazdi and Rezaeepazhand, 2011b; Kuneš, 2012; Yazdi and Rezaeepazhand, 2012; Luo et al., 2013; Shokrieh and Askari, 2013; Yazdi, 2013; Luo et al., 2014a; Luo et al., 2014b; Luo et al., 2014c; Luo et al., 2014d; Zhu et al., 2014; Asl et al., 2015; Balawi, Shahid, and Mulla, 2015; Luo et al., 2015; Luo et al., 2016b; Asl et al., 2016a; Asl et al., 2016b; Asl et al., 2017a; Asl et al., 2017b; Asl et al., 2017c; Asl et al., 2017d; Zhu et al., 2017; Asl et al., 2018
EM	Kasivitamnuay and Singhatanadgid, 2005; Ungbhakorn and Singhatanadgid, 2009; Kasivitamnuay and Singhatanadgid, 2017
ASMA	De Rosa et al., 1997; Martini, De Rosa, and Franco, 2004; De Rosa, Franco, and Mace, 2005; De Rosa and Franco, 2008a; De Rosa and Franco, 2008b; De Rosa and Franco, 2010; Li, 2010a; Li, 2010b; De Rosa, Franco, and Polito, 2015; Robin, De Rosa, and Berry, 2016
SAMSARA	De Rosa, Franco, and Polito, 2011; De Rosa et al., 2012; De Rosa, Franco, and Polito, 2012; De Rosa and Franco, 2015; De Rosa, Franco, and Meruane, 2015; Meruane, De Rosa, and Franco, 2015; De Rosa, Petrone, and Franco, 2016; Petrone et al., 2017; Franco et al., 2019; Berry et al., 2020; Franco et al., 2020
ESM	Cho and Wood, 1997; Cho, Wood, and Crawford, 1998a; Cho, Wood, and Crawford, 1998b; Cho, Wood, and Crawford, 1999; Dutson and Wood, 2002; Dutson et al., 2003; Cho et al., 2005
SA	Luo et al., 2015; Adams, Bös, and Melz, 2016; Adams et al., 2018

TABLE A.1: Reference table of similitude methods.

Test article	References
Beam	Morton, 1988; Jackson and Fasanella, 1989; Jackson, 1990; Magness and Farrand, 1990; Sorensen et al., 1991; Anderson, Jr., Mullin, and Kuhlman, 1993; Drazetic et al., 1994; Pintado and Morton, 1994; De Rosa et al., 1997; Rosenberg, Kreif, and Dekel, 1997; Christoforou and Yigit, 1998; Zhao, 1998; Zhao, 1999; Wu, Cartmell, and Whittaker, 2002; Oshiro and Alves, 2004; Kasivitamnuay and Singhatanadgid, 2005; Wu, 2005; Alves and Oshiro, 2006a; Alves and Oshiro, 2006b; Carrillo and Cantwell, 2008; McKown, Cantwell, and Jones, 2008; Viot et al., 2008; Christoforou and Yigit, 2009; Oshiro and Alves, 2009; De Rosa and Franco, 2010; Ramu, Prabhu Raja, and Thyla, 2010; Oshiro et al., 2011; Oshiro and Alves, 2012; Ramu, Prabhu Raja, and Thyla, 2013; Balawi, Shahid, and Mulla, 2015; De Rosa, Franco, and Polito, 2015; Zai et al., 2015; Asl et al., 2016b; Mazzariol, Oshiro, and Alves, 2016; Asl et al., 2016a; Asl et al., 2017a; Asl et al., 2017b; Asl et al., 2017c; Asl et al., 2017d; Kasivitamnuay and Singhatanadgid, 2017; Asl et al., 2018

Unstiffened plate	Goodier and Thomson, 1944; Duffey, Cheresh, and Sutherland, 1984; Krayterman and Sabnis, 1984; Cheng and Lesueur, 1990a; Cheng and Lesueur, 1990b; Qian et al., 1990; Simitses and Rezaeepazhand, 1992; Rezaeepazhand and Simitses, 1993; Simitses and Rezaeepazhand, 1993; Wen and Jones, 1993; Rezaeepazhand, Simitses, and Starnes, Jr., 1995a; Rezaeepazhand, Simitses, and Starnes, Jr., 1995b; Simitses and Rezaeepazhand, 1995; Christoforou and Yigit, 1998; Zhao, 1998; Nettles, Douglas, and Estes, 1999; Hu, 2000; Simitses, 2001; Ungbhakorn, 2001; Singhatanadgid and Ungbhakorn, 2002; Singhatanadgid and Ungbhakorn, 2003; Ungbhakorn and Singhatanadgid, 2003c; Wu, 2003; Martini, De Rosa, and Franco, 2004; Jacob et al., 2004; Oshiro and Alves, 2004; Schleyer, Hsu, and White, 2004; Ambur et al., 2005; De Rosa, Franco, and Mace, 2005; Kasivitamnuay and Singhatanadgid, 2005; Singhatanadgid and Ungbhakorn, 2005; Wu, 2005; Alves and Oshiro, 2006a; Alves and Oshiro, 2006b; Wu, 2006; Yigit and Christoforou, 2007; Neuberger, Peles, and Rittel, 2007a; Neuberger, Peles, and Rittel, 2007b; Sutherland and Guedes Soares, 2007; Carrillo and Cantwell, 2008; De Rosa and Franco, 2008a; De Rosa and Franco, 2008b; McKown, Cantwell, and Jones, 2008; Singhatanadgid and Na Songkhla, 2008; Viot et al., 2008; Yulong, Yongkang, and Pu, 2008
Unstiffened plate (continued)	Christoforou and Yigit, 2009; Neuberger, Peles, and Rittel, 2009; Oshiro and Alves, 2009; Rezaeepazhand and Wisnom, 2009; De Rosa and Franco, 2010; Li, 2010a; Li, 2010b; Snyman, 2010; De Rosa, Franco, and Polito, 2011; Rezaeepazhand and Yazdi, 2011; Yazdi and Rezaeepazhand, 2011a; Yazdi and Rezaeepazhand, 2011b; Bachynski, Motley, and Young, 2012; Ciappi et al., 2012; Oshiro and Alves, 2012; Yazdi and Rezaeepazhand, 2012; Luo et al., 2013; Shokrieh and Askari, 2013; Mazzariol and Alves, 2014; Luo et al., 2014c; Noam, Dolinski, and Rittel, 2014; Zhu et al., 2014; Asl et al., 2015; Balawi, Shahid, and Mulla, 2015; De Rosa, Franco, and Meruane, 2015; Meruane, De Rosa, and Franco, 2015; Luo et al., 2015; Adams, Bös, and Melz, 2016; Luo et al., 2016a; Luo et al., 2016b; Mazzariol, Oshiro, and Alves, 2016; Xiaojian et al., 2016; Xu et al., 2016; Adams et al., 2018; Franco et al., 2019; Berry et al., 2020; Franco et al., 2020; He et al., 2020

Stiffened plate	Mazzariol et al., 2010; Coutinho, Baptista, and Rodrigues, 2018
Sandwich plate	Frostig and Simitses, 2004; Yang et al., 2013; Luo et al., 2014b
Unstiffened cylinder	Cheng and Lesueur, 1990a; Cheng and Lesueur, 1990b; Swanson, Smith, and Qian, 1991; Moradi and Parsons, 1992; Hamada and Ramakrishna, 1995; Rezaeepazhand, Simitses, and Starnes, Jr., 1996a; Rezaeepazhand, Simitses, and Starnes, Jr., 1996b; Simitses, Rezaeepazhand, and Sierakowski, 1997; Rezaeepazhand and Simitses, 1997; Tabiei, Sun, and Simitses, 1997; Chouchaoui and Ochoa, 1999; Chouchaoui, Parks, and Ochoa, 1999; Ungbhakorn and Singhatanadgid, 2003a; Ungbhakorn and Singhatanadgid, 2003b; Jiang, Wang, and Zhang, 2006; Oshiro and Alves, 2007; Tarfaoui et al., 2007; Ungbhakorn and Wattanasakulpong, 2007; De Rosa, Franco, and Polito, 2012; Qin et al., 2012; Mazzariol and Alves, 2013; Yazdi, 2013; Luo et al., 2014a; Luo et al., 2014d; De Rosa and Franco, 2015
Stiffened cylinder	Sato, Vecchio, and Andre, 1989; Hilburger, Lovejoy, and Thornburgh, 2012; De Rosa and Franco, 2015; Yu and Li, 2016; Petrone et al., 2017

TABLE A.2: Reference table of test articles.

Engineering field	References
Aerospace engineering	O'Sullivan, 1957; Katzoff, 1963; Carden and Herr, 1964; Jones, 1964; Mixson and Catherine, 1964a; Mixson and Catherine, 1964b; Adkins, 1965; Catherine, 1965; Chao and Wedekind, 1965; Folkman, Baldwin, and Wainwright, 1965; Gabron and Johnson, 1965; Jones and Harrison, 1965; Fowle, Gabron, and Vickers, 1966; Gabron, 1966; Morosow and Jaszlics, 1966; Shih, 1966; Watkins, 1966; Herr and Wayne Leonard, 1967; Leadbetter, Wayne Leonard, and John Brock, Jr., 1967; Thompson, Jr., 1967; Steeves and Catherines, 1968; Blanchard, 1968; Catherines, 1968; Peele, Thompson, Jr., and Pusey, 1968; Adelman and Steeves, 1968; Wissmann, 1968; Wolowicz, Bowman, Jr., and Gilbert, 1968; Pinson and Wayne Leonard, 1969; Rolling, Murray, and Marshall, 1969; Leadbetter, 1970; Maples and Scogin, 1970; Peele, Wayne Leonard, and Leadbetter, 1970; Stubbs, 1971; Thornton, 1971; Shannon, 1972; Hunt, 1973; Marshall and Foster, 1973; McGehee and Stubbs, 1973; Bernstein et al., 1974a; Bernstein et al., 1974b; Levy et al., 1974; Mason et al., 1974a; Mason et al., 1974b; Pinson, 1975; Zalesak, 1975; Leadbetter et al., 1976; Blanchard, Miserentino, and Leadbetter, 1977; Tennyson et al., 1981; Keith Belvin and Edighoffer, 1986a; Keith Belvin and Edighoffer, 1986b; Gronet et al., 1987; Shih, Chen, and Garba, 1987; Letchworth, McGowan, and Gronet, 1988; Schroeder et al., 1989; French, 1990; McGowan, Edighoffer, and Wallace, 1990; McGowan, Jaeed, and Edighoffer, 1991; Davis et al., 1994; Bisplinghoff, Ashley, and Halfman, 1996; French and Eastep, 1996; Friedmann, Guillot, and Presente, 1997; Wereley and Kamath, 1997; Presente and Friedmann, 1998a; Presente and Friedmann, 1998b; Friedmann, 1999; Greschik, Mikulas, and Freeland, 1999; Jackson and Fasanella, 1999; Horta and Kvaternik, 2000; Holland et al., 2002; Pototzky, 2002; Cartmell, Ziegler, and Neill, 2003; Jackson and Fasanella, 2003; Canfield et al., 2004; Friedmann, 2004; Heeg, Spain, and Rivera, 2004; Murphy, Macy, and Gaspar, 2004; Laue, Case, and Moore, 2005; Gaspar et al., 2005; Gaspar et al., 2006; Richards et al., 2009; Canfield, Peddieson, and Garbe, 2010; Sabour and Bhat, 2010; Bond et al., 2012; Ricciardi et al., 2012b; Wan and Cesnik, 2013; Ricciardi et al., 2014; Spada et al., 2017

Civil engineering	Usami and Kumar, 1996; Kumar et al., 1997; Kim, Kwak, and Chang, 2004; Kim, Lee, and Chang, 2009; Yu et al., 2010
Impact engineering	Emori, 1973; Holmes and Sliter, 1974; Lowe, Al-Hassani, and Johnson, 1974; Brownfield and Rogers, 1978; Westine and Mullin, 1987; Atkins, 1988; Hamada and Ramakrishna, 1995; Me-Bar, 1997; Jiang et al., 2006; Carrillo and Cantwell, 2008; Quercetti, Müller, and Schubert, 2008; Acquaro et al., 2010
Naval engineering	Blok and Dekker, 1979; Kure, 1981; Hagiwara, Takanabe, and Kawano, 1983; Brunette and Goldsmith, 1990; Ohtsubo, Kawamoto, and Kuroiwa, 1994; Vassalos, 1999; Lehmann and Peschmann, 2002; Wang, Yang, and Liu, 2007; Tabri, Määttänen, and Ranta, 2008; Calle and Alves, 2011; Aguiar et al., 2012; Calle, Oshiro, and Alves, 2017; Oshiro et al., 2017
Rapid Prototyping	Dornfeld, 1994; Cho and Wood, 1997; Chuk and Thomson, 1998; Springer, 1998; Mahn and Bayly, 1999; Cho, Wood, and Crawford, 1998a; Cho, Wood, and Crawford, 1998b; Cho, Wood, and Crawford, 1999; Dutson and Wood, 2002; Fujino, Oyama, and Omotani, 2003; Dutson et al., 2003; Cho et al., 2005; Nadooshan, Daneshmand, and Aghanajafi, 2007; Steinchen, Kramer, and Kupfer, 2008; Ziemian, Ziemian, and Barker, 2010; Dang-guo et al., 2011; Zhu et al., 2011; Dang-guo et al., 2013

TABLE A.3: Reference table of engineering application fields.

Appendix B

Articles, conferences, and collaborations

B.1 Peer reviewed articles

[1] Casaburo, A., Petrone, G., Franco, F., De Rosa, S. (2019). "A Review of Similitude Methods for Structural Engineering". In: *Applied Mechanics Reviews*, 71(3), pp. 0.30802-1–0.30802-32, doi: 10.1115/1.4043787.

[2] Casaburo, A., Petrone, G., Meruane, V., Franco, F., De Rosa, S. (2019). "Prediction of the Dynamic Behavior of Beams in Similitude Using Machine Learning Methods". In: *Aerotecnica Missili e Spazio*, 98, pp. 283-291, doi: 10.1007/s42496-019-00029-y.

[3] Casaburo, A., Petrone, G., Franco, F., De Rosa, S. (2020). "Similitude Theory Applied to Plates in Vibroacoustic Field: a Review up to 2020". In: *Progress in Scale Modeling, an Internationl Journal*, 1(1), doi: 10.13023/psmij.2020.03.

[4] Casaburo, A., Petrone, G., Meruane, V., Franco, F., De Rosa, S. (2021). "The Vibroacoustic Behaviour of Aluminium Foam Sandwich Panels in Similitude". In: *Journal of Sandwich Structures and Materials*, doi: 10.1177/1099636220986759.

[5] De Rosa, S., Franco, F., Petrone, G., Casaburo, A., Marulo, F., (2021). "A Versatile Offset Operator for the Discrete Observation of Objects". In: *Journal of Sound and Vibration*, 500, doi: 10.1016/j.jsv.2021.116019.

[6] Casaburo, A., Petrone, G., Meruane, V., Franco, F., De Rosa, S. (2021). "Support of Dynamic Measurements through Similitude Formulations". In: *Experimental Techniques*, doi: 10.1007/s40799-021-00457-1.

[7] Casaburo, A., Petrone, G., Meruane, V., Franco, F., De Rosa, S. (2021). "Evaluation of Plates in Similitude by Experimental Tests and Artificial Neural Networks". In: *Proceedings of the Institution of Mechanical Engineers, Part C: Journal of Mechanical Engineering Science*, accepted.

B.2 Conferences

Adams, C., Casaburo, A., Bös, J., Petrone, G., Franco, F., De Rosa, S., Melz, T., "A Comparison Between Similitude Methods for Frequency Response Analyses of Vibrating Structures", presented at Colloquium on Irregular Engineering Oscillations and Signal Processing, 10-12 September, 2018, Hamburg (Germany).

Casaburo, A., Petrone, G., Franco, F., De Rosa, S., "Application of Pattern Recognition and Machine Learning Methods to Identify Vibrating Systems in Similitude", presented at RASD 2019, 13th International Conference on Recent Advances in Structural Dynamics, 15-17 April 2019, Lyon (France).

Casaburo, A., Petrone, G, Franco, F., De Rosa, S., "Application of Machine Learning Methods to Structural Similitudes", presented at ISCVS12, 11th International Symposium on Vibrations of Continuous Systems, July 28-August 2, 2019, Corvara in Badia (Italy).

Casaburo, A., Petrone, G., Meruane, V., Franco, F., De Rosa, S., "Prediction of the Dynamic Behavior of Plates in Similitude Using Machine Learning Methods", presented at AIDAA XXV International Congress, 9-12 September 2019, Rome (Italy).

Casaburo, A., Petrone, G., Meruane, V., Franco, F., De Rosa, S., "Investigation of th Artifical Neural Networks Capabilities Applied to Vibrating Plates in Similitude", presented at MEDYNA 2020: 3rd Euro-Mediterranean Conference on Structural Dynamics and Vibroacoustics, 17-19 February 2020, Naples (Italy).

Casaburo, A., Petrone, G., Meruane, V., Franco, F., De Rosa, S., "Evaluation of Plates in Similitude by Experimental and Machine Learning Techniques", presented at ISMA 2020, International Conference on Noise and Vibration Engineering, 7-9 September, 2020, Leuven (Belgium).

Casaburo, A., Magliacano, D., Petrone, G., Franco, F., De Rosa, S., "Optimitzing the Acoustic Properties of a Meta-material Using Machine Learning Techniques", presented at Inter-Noise 2021, 50th International Congress and Exposition on Noise Control Engineering, 1-5 August, Washington, DC (US).

Tavasso, F., Casaburo, A., Petrone, G., Franco, F., De Rosa, S., "A Linear Transformation for the Reconstruction of the Response Between Systems in Similitude", presented at AIDAA XXV International Congress, August 31-September 3 2021, Pisa (Italy).

B.3 Research activity collaborations

October 2020 - January 2021: remote collaboration (due to COVID pandemic) with Ecole Centrale de Lyon, under the supervision of Prof. M. Ichchou. Activity: analysis of advanced methods for the reconstruction of the response of systems in similitude.

September- October 2019: Visiting researcher at Facultad de Ciencias Fisicas y Matematicas (Universidad de Chile) at Santiago, Chile, in collaboration with Prof. V. Meruane. Activity: application of DIC techniques to systems in similitude.

March-April 2019: Visiting researcher at Facultad de Ciencias Fisicas y Matematicas (Universidad de Chile) at Santiago, Chile, in collaboration with Prof. V. Meruane. Activity: experimental measurements and application of machine learning methods to systems in similitude.

Bibliography

Acquaro, D. et al. (2010). "Numerical and experimental analysis of the impact of a nuclear spent fuel cask". In: *Nuclear Engineering and Design* 240.4, pp. 706–712.

Adams, C., J. Bös, and T. Melz (2016). "A scaling method for vibrating structures using global sensitivity analysis". In: 45th International Congress and Exposition on Noise Control Engineering: Towards a Quieter Future, INTER-NOISE 2016. Hamburg, Germany, pp. 5411–5420.

Adams, C. et al. (2018). "Scaling laws obtained from a sensitivity analysis and applied to thin vibrating structures". In: *Mechanical Systems and Signal Processing* 110, pp. 590–610.

Adelman, H. M. and E. C. Steeves (1968). *Vibration analysis of a 1/40-scale dynamic model of Saturn V– launch-platform–umbilical-tower configuration*. Tech. rep. NASA TN D–4871. Washington (DC), USA: National Aeronautics and Space Administration.

Adkins, D. L. (1965). "Scaling of transient temperature distributions of simple bodies in a space chamber". In: 65–660. AIAA Thermophysics Specialist Conference. Monterey (CA), USA.

Aguiar, V. S. et al. (2012). "Experimental and numerical analysis of container stack dynamics using a scaled model test". In: *Ocean Engineering* 39, pp. 24–42.

Alves, M. and R. E. Oshiro (2006a). "Scaling impacted structures when the prototype and the model are made of different materials". In: *International Journal of Solids and Structures* 43, pp. 2744–2760.

— (2006b). "Scaling the impact of a mass on a structure". In: *International Journal of Impact Engineering* 32, pp. 1158–1173.

Alves, V. et al. (2015). "Structural modification assessment using supervised learning methods applied to vibration data". In: *Engineering Structures* 99, pp. 439–448.

Ambur, D. R. et al. (2005). "Scaling the non-linear impact response of flat and curved composite panels". In: 46th AIAA/ASME/ASCE/AHS/ASC Structures, Structural Dynamics and Materials Conference. Austin (TX), USA, pp. 1–15.

Anderson, Jr., C., S. Mullin, and C. Kuhlman (1993). "Computer simulations of strain-rate effects in replica scale model penetration experiments". In: *International Journal of Impact Engineering* 13.1, pp. 35–52.

Asl, M. et al. (2016a). *Similitude analysis of the strain field for loaded composite I–beams emulating wind turbine blades*. Ed. by B. D. Davidson, J. G. Ratcliffe, and M. W. Czabaj. Williamsburg (VA), USA.

Asl, M. E. et al. (2015). "Predicting the vibration response in subcomponent testing of wind turbine blades". In: *Special Topics in Structural Dynamics, Volume 6*. Ed. by R. Allemang. Springer, Cham.

— (2016b). "Similitude analysis of composite I–beams with application to subcomponent testing of wind turbine blades". In: *Experimental and Applied Mechanics, Volume 4*. Ed. by C. Sciammarella, J. Considine, and P. Gloeckner. Proceedings of the Society for Experimental Mechanics Series. Springer, Cham.

— (2017a). "Experimental and theoretical similitude analysis for flexural bending of scaled-down laminated I–beams". In: *Composite Structures* 176, pp. 812–822.

— (2017b). "Similitude analysis of the frequency response function for scaled structures". In: *Model Validation and Uncertainty Quantification, volume 3*. Ed. by R. Barthorpe et al. Conference Proceedings of the Society fro Experimental Mechanics Series. Springer, Cham.

— (2017c). "Similitude analysis of thin-walled composite I–beams for subcomponent testing of wind turbine blades". In: *Wind Engineeering* 41.5, pp. 297–312. URL: https://doi.org/10.1177/0309524X17709924.

— (2017d). "Vibration prediction of thin-walled composite I–beams using scaled models". In: *Thin-Walled Structures* 113, pp. 151–161. URL: https://doi.org/10.1016/j.tws.2017.01.020.

— (2018). "Scaled composites I–beams for subcomponent testing of wind turbine blades: an experimental study". In: *Mechanics of Composite and Multi-functional Materials, Volume 6*. Ed. by P. Thakre, R. Singh, and G. Slipher. Conference Proceedings of the Society for Experimental Mechanics Series. Springer, Cham.

Atkins, A. G. (1988). "Scaling combined plastic flow and fracture". In: *Int. J. Mech. Sci.* 30.3–4, pp. 173–191.

— (1999). "Scaling laws for elastoplastic fracture". In: *International Joouornal of Fracture* 95, pp. 51–65.

Atkins, A. G. and R. M. Caddell (1974). "The laws of similitude and crack propagation". In: *International Journal of Mechanical Sciences* 16, pp. 541–548.

Atkins, A. G., Z. Chen, and B. Cotterell (1998). "The essential work of fracture and J_R curves for the double cantilever beam specimen: an examination of elastoplastic crack propagation". In: *Proceedings of the Royal Society of London*. Vol. 454. 1971. The Royal Society, pp. 815–833.

Bachynski, E. E., M. R. Motley, and Y. L. Young (2012). "Dynamic hydroelastic scaling of the underwater shock response of composite marine structures". In: *Journal of Applied Mechanics* 79.1, pp. 014501–014507.

Baker, W. E., P. S. Westine, and F. T. Dodge (1991). *Similarity methods in engineeting dynamics: theory and practice of scale modeling. Revised ed.* Amsterdam, Netherlands: Elsevier.

Balawi, S., O. Shahid, and M. Al Mulla (2015). "Similitude scaling laws - Static and dynamic behaviour beams and plates". In: *Procedia Engineering* 114, pp. 330–337.

Bauhart, J. (2005). "Aluminium foams for lighter vehicles". In: *International Journal of Vehicle Design* 37.2–3, pp. 114–125.

Baum, E. B. and D. Haussler (1988). "What size net gives valid generalization?" In: *Neural Computation* 1.1, pp. 151–160.

Bažant, Z. P. (1985). "Fracture in concrete and reinforced concrete". In: *Mechanics of Geomaterials*. Ed. by Z. P. Bažant. Hoboken (NJ), USA: John Wiley & Sons Ltd.

— (1993a). "Scaling laws in mechanics of failure". In: *Journal of Engineering Mechanics* 119.9, pp. 1828–1844.

— (1993b). "Size effect in blunt fracture: concrete, rock, metal". In: *Journal of Engineering Mechanics* 110.4, pp. 518–535.

Bažant, Z. P. and M. T. Kazemi (1990). "Size effect in fracture of ceramics and its use to determine fracture energy and effective process zone length". In: *Journal of the American Ceramic Society* 73.7, pp. 1841–1853.

Bažant, Z. P. and P. A. Pfeiffer (1988). "Determination of fracture energy from size effect and brittleness number". In: *ACI Materials Journal* 84.6, pp. 463–480.

Bažant, Z. P., Y. Xi, and S. G. Reid (1991a). "Statistical size effect in quasi-brittle structures: I. Is Weibull theory applicable?" In: *Journal of Engineering Mechanics* 117.11, pp. 2609–2622.

— (1991b). "Statistical size effect in quasi-brittle structures: I. Is Weibull theory applicable?" In: *Journal of Engineering Mechanics* 117.11, pp. 2623–2640.

Becker, T. et al. (2006). "Error estimations of 3D digital image correlation measurments". In: *Proc. of SPIE* 6341. DOI: 10.1117/12.695277.

Belouchrani, A. et al. (1997). "A blind source separation techinque using second-order statistics". In: *IEEE Transactions on Signal Processing* 45.2, pp. 434–444.

Bernstein, M. et al. (1974a). *Development of technology for fluid-structure interaction modeling of a 1/8-scale dynamic model of the shuttle external tank (ET). Volume I: Technical report*. Tech. rep. NASA CR–132549. Washington (DC), USA: National Aeronautics and Space Administration.

— (1974b). *Development of technology for fluid-structure interaction modeling of a 1/8-scale dynamic model of the shuttle external tank (ET). Volume II: Supporting data, Appendixes A through B*. Tech. rep. NASA CR–132549. Washington (DC), USA: National Aeronautics and Space Administration.

Berry, A. et al. (2020). "Similitude laws for the sound radiation of flat orthotropic flexural panels". In: *Journal of Sound and Vibration* 489. DOI: https://doi.org/10.1016/j.jsv.2020.115636.

Berthelot, JM. (2015). *Mechanical behaviour of composite materials and structures, 3rd edition*. Les Clousures, Chemin des Horts, Vallouise (FR): Jean-Marie Berthelot.

Bianco, M. J. et al. (2019). "Machine learning in acoustics: theory and applications". In: *Journal of the Acoustical Society of America* 146.5, pp. 3590–3628. DOI: 10.1121/1.5133944.

Bishop, C. M. (2006). *Pattern recognition and machine learning*. New York (NY), USA: Springer.

Bisplinghoff, R., H. Ashley, and R. Halfman (1996). *Aeroelasticity*. New York: Dover Publications.

Blanchard, U. J. (1968). *Evaluation of a full-scale lunar-gravity simulator by comparison of landing-impact tests of a full-scale and a 1/6-scale model*. Tech. rep. NASA TN D–4474. Washington (DC), USA: National Aeronautics and Space Administration.

Blanchard, U. J., R. Miserentino, and S. A. Leadbetter (1977). *Experimental investigation of the vibration characteristics of a model of an asymmetric multielement space shuttle*. Tech. rep. NASA TN D–8448. Washington (DC), USA: National Aeronautics and Space Administration.

Blevins, R. D. (2016). *Formulas for dynamics, acoustics and vibration*. John Wiley and Sons.

Blok, J. J. and J. N. Dekker (1979). "On hydrodinamic aspects of ship collision with rigid or non-rigid structures". In: Offshore Technology Conference. Houston (TX), USA, pp. 2683–2698.

Bluman, G. W. and J. D. Cole (1974). *Similarity methods for differential equations*. New York (NY), USA: Springer-Verlag.

Bond, V. et al. (2012). "Aeroelastic scaling of a joined wing for nonlinear geometric stiffness". In: *AIAA Journal* 50.3, pp. 513–522.

Brownfield, H. A. and D. O. Rogers (1978). *Analysis of 30 mph frontal barrier utilizing half-scale metal models*. Tech. rep. SAE paper no. 780366.

Brunette, H. and W. Goldsmith (1990). "Propellant-driven anchoring in rock: results from initial scaling tests". In: *International Journal of Impact Engineering* 9.1, pp. 51–69. URL: https://doi.org/10.1016/0734-743X(90)90022-N.

Buckingham, E. (1914). "On physically similar systems, illustrations of the use of dimensional equations". In: *Physical review* 4.4, pp. 345–376.

Cagliostro, D. J., A. L. Florence, and G. R. Abrahamson (1979). "Scale modelling in LMFBR safety". In: *Nuclear Engineering and Design* 55.2, pp. 235–247.

Calle, M. A. G. and M. Alves (2011). "Ship collision: a brief survey". In: 21st Brazilian Congress of Mechanical Engineering. Natal (RN), Brazil.

Calle, M. A. G., R. E. Oshiro, and M. Alves (2017). "Ship collision and grounding: scaled experiments and numerical analysis". In: *International Journal of Impact Engineering* 103, pp. 195–210.

Canfield, S. L., J. Peddieson, and G. Garbe (2010). *Similarity rules for scaling solar sail systems*. Tech. rep. Technical Rreport M10–0055. National Aeronautics and Space Administration.

Canfield, S. L. et al. (2004). "Similarity rules for scaling solar sail systems". In: Solar sail technology and application conference (SSTAC). Greenbelt (MD), USA, pp. 1–10.

Carden, H. D. and R. W. Herr (1964). *A study on the effectiveness of various methods of vibration reduction on simplified scale models of the Nimbus spacecraft*. Tech. rep. NASA TN D–2418. Washington (DC), USA: National Aeronautics and Space Administration.

Carrillo, J. G. and W. J. Cantwell (2007a). "A comparison of ply-level and sublaminate-level scaling of fibre-metal laminates with in-plane dimensions". In: *Advanced Composites Letters* 16.6, pp. 233–236. DOI: 10.1177/096369350701600604.

— (2007b). "Scaling effects in the tensile behavior of fiber-metal laminates". In: *Composites Science and Technology* 67, pp. 1684–1693.

— (2008). "Scaling effects in the low velocity impact response of fiber-metal laminates". In: *J. Reinf. Plat. Compos.* 27, pp. 893–907.

Cartmell, M. P., S. W. Ziegler, and D. S. Neill (2003). "On the performance prediction and scale modelling of a Motorised Momentum Exchange Tether". In: *AIP Conference Proceedings*. Ed. by M. S. El-Genk. Space Technology and Applications International Forum - STAIF 2003, pp. 571–579.

Casaburo, A. et al. (2019). "A review of similitude methods for structural engineering". In: *Applied Mechanics Reviews* 71.3. DOI: 10.1115/1.4043787.

— (2020). "Similitude theory applied to plates in vibroacoustic field: a review up to 2020". In: *Progress in Scale Modeling, and International Journal* 1, pp. 1–13. DOI: https://doi.org/10.13023/psmij.2020.03.

Castellini, P. and G. M. Revel (2000). "An experimental technique for structural diagnostic based on laser vibrometry and neural networks". In: *Shock and Vibration* 7, pp. 381–397.

Catherine, J. J. (1965). *Torsional vibration characteristics of a 1/5-scale model of Saturn SA-1*. Tech. rep. NASA TN D–2745. Washington (DC), USA: National Aeronautics and Space Administration.

Catherines, J. J. (1968). *Experimental vibration characteristics of a 1/40-scale dynamic model of the Saturn V– launch–umbilical-tower configuration*. Tech. rep. NASA TN D–4870. Washington (DC), USA: National Aeronautics and Space Administration.

Chao, B. T. and G. L. Wedekind (1965). "Similarity criteria for thermal modeling of spacecraft". In: *Journal of Spacecraft and Rockets* 2.2, pp. 146–152.

Charlton, T. M. (1954). *Model analysis of structures*. New York: John Wiley and Sons.

Chen, Y., P. Avitabile, and J. Dodson (2020). "Data consistency assessment function (DCAF)". In: *Mechanical Systems and Signal Processing* 141. DOI: https://doi.org/10.1016/j.ymssp.2020.106688.

Chen, Y. et al. (2019). "Non-model based expansion from limited points to augmented set of points using Chebyshev polynomials". In: *Experimental Techniques* 43.5, pp. 521–543.

Cheng, L. and C. Lesueur (1990a). "Preliminary study on vibroacoustic model scaling of a structure coupled to an acoustic cavity". In: *J. Acoustique* 3, pp. 349–359.

— (1990b). "Vibroacoustic model scaling with dissipation effects". In: *Journal de Physique Colloques* 51.C2, pp. C2–213 –C2–216.

Cho, U. and K. Wood (1997). "Empirical similitude method for the functional test with rapid prototypes". In: Symposium for Solid Freeform Fabrication. DOI: 10.15781/T2JD4Q88T.

Cho, U., K. L. Wood, and R. H. Crawford (1998a). "Novel empirical similarity method for the reliable product test with rapid prototypes". In: *Proceedings of DETC '98*. 1998 ASME Design Engineering Technical Conference. Atlanta (GE), USA, pp. 1–14.

— (1998b). "Online functional testing with rapid prototypes: a novel empirical similarity method". In: *Rapid Prototyping Journal* 4.3, pp. 128–138.

— (1999). "Error measures for functional product testing". In: *Proceedings of DETC '99*. 1999 ASME Design Engineering Technical Conference. Las Vegas (NE), USA, pp. 1–13.

Cho, U. et al. (2005). "An advanced method to correlate scale models with distorted configurations". In: *Journal of Mechanical Design* 127, pp. 78–85.

Chouchaoui, O. and O. O. Ochoa (1999). "Similitude study for a laminated cylindrical tube under tensile, torsion, bending, internal and external pressure. Part I: governing equations". In: *Composite Structures* 44, pp. 221–229.

Chouchaoui, O., P. Parks, and O. O. Ochoa (1999). "Similitude study for a laminated cylindrical tube under tensile, torsion, bending, internal and external pressure. Part II: scale models". In: *Composite Structures* 44, pp. 231–236.

Christoforou, A. P. and A. S. Yigit (1998). "Effect of flexibility on low velocity impact response". In: *Journal of Sound and Vibration* 217.3, pp. 563–578.

— (2009). "Scaling of low-velocity impact response in composite structures". In: *Composite Structures* 91, pp. 358–365.

Chuk, R. N. and V. J. Thomson (1998). "A comparison of rapid prototyping techniques used for wind tunnel model fabrication". In: *Raid Prototyping Journal* 4, pp. 185–96.

Ciappi, E. et al. (2012). "Analysis of the scaling laws for the turbulence driven panel responses". In: *Journal of Fluids and Structures* 32, pp. 90–103. URL: https://doi.org/10.1016/j.jfluidstructs.2011.11.003.

Coutinho, C. P., A. J. Baptista, and J. D. Rodrigues (2016). "Reduced scale models based on similitude theory: A review up to 2015". In: *Engineering Structures* 119, pp. 81–94.

— (2018). "Modular approach to structural similitude". In: *International Journal of Mechanical Sciences* 135, pp. 294–312.

Cremer, L., M. Heckl, and B.A.T. Petersson (2005). *Structure-borne sound. Structural vibrations and sound radiation at audio frequencies, 3rd edition*. Springer.

Cunefare, K. A. and S. De Rosa (1999). "The sensitivity of structural acoustic response to attachment feature scale representation". In: *Journal of Acoustic Society of America* 106.6, pp. 3384–3393.

Cybenko, G. (1989). "Approximation by superpositions of a sigmoidal function". In: *Mathematics of Control, Signal, and Systems* 2, pp. 303–314.

D'Alessandro, V. et al. (2014). "Modeling of aluminium foam sandwich panels". In: *Smart Structures and Systems* 13.4, pp. 615–636.

Dang-guo, Y. et al. (2011). "A preliminary design and manufacturing study of hybrid lightweight high-speed wind-tunnel models". In: *Rapid Prototyping Journal* 17, pp. 45–54.

Dang-guo, Y. et al. (2013). "Design and manufacture methods of rapid prototyping wind-tunnel models based on photopolymer-resin". In: *Rapid Prototyping Journal* 17.1, pp. 20–7. DOI: 10.1108/13552541311292691.

Davis, D. A. et al. (1994). *Conceptual design and analysis of a dynamic scale model of the Space Station Freedom*. Tech. rep. NASA Contractor Report 4598. Washington (DC), USA: National Aeronautics and Space Administration.

De Rosa, S. and F. Franco (2008a). "A scaling procedure for the response of an isolated system with high modal overlap factor". In: *Mechanical Systems and Signal Processing* 22, pp. 1549–1565.

— (2008b). "Exact and numerical responses of a plate under a turbulent boundary layer excitation". In: *Journal of Fluids and Structures* 24, pp. 212–230.

— (2010). "On the use of the asymptotic scaled modal analysis for the time-harmonic structural analysis and for the prediction of coupling loss factors for similar systems". In: *Mechanical Systems and Signal Processing* 24, pp. 455–480.

— (2015). "Analytical similitudes applied to thin cylindrical shells". In: *Advances in aircraft and spacecraft science* 2.4, pp. 403–425.

De Rosa, S., F. Franco, and B. R. Mace (2005). "The asymptotic scaled modal analysis for the response of a 2-plate assembly". In: XVIII AIDAA National Congress. Volterra (PI), Italy.

De Rosa, S., F. Franco, and V. Meruane (2015). "Similitudes for structural response of flexural plates". In: *Proceedings of the Institution of Mechanical Engineers Part C, Journal of Mechanical Engineering Science* 230.3, pp. 174–188.

De Rosa, S., F. Franco, and T. Polito (2011). "Structural similitudes for the dynamic response of plates and assemblies of plates". In: *Mechanical Systems and Signal Processing* 25, pp. 969–980.

— (2012). "SAMSARA for thin cylindrical shells". In: Noise and Vibration: Emerging Methods (NOVEM 2012), pp. 048–1–048–12.

— (2015). "Partial scaling of finite element models for the analysis of the coupling between short and long structural wavelengths". In: *Mechanical Systems and Signal Processing* 52–53, pp. 722–740.

De Rosa, S., G. Petrone, and F. Franco (2016). "Similitudes for acoustic volumes: analytical model for the response". In: 45th International Congress and Exposition on Noise Control Engineering: Towards a Quieter Future, INTER-NOISE 2016. Hamburg, Germany, pp. 3416–3424.

De Rosa, S. et al. (1997). "First assessment of the scaling procedure for the evaluation of the damped structural response". In: *Journal of Sound and Vibration* 204.3, pp. 540–548.

De Rosa, S. et al. (2007). "Applicazione dell'algebra agli intervalli alla risposta strutturale". In: XIX Congresso Nazionale AIDAA. Forlì, Italy.

De Rosa, S. et al. (2012). "A similitude for structural acoustic enclosures". In: *Mechanical Systems and Signal Processing* 30, pp. 330–342.

De Rosa, S. et al. (2021). "A versatile offset operator for the discrete observation of objects". In: *Journal of Sound and Vibration*. DOI: 10.1016/j.jsv.2021.116019.

Dornfeld, W. H. (1994). "Direct dynamic testing of stereolithographic models". In: International Gas Turbine, Aeroengine Congress, and Exposition. The Hague, Netherlands, pp. 1–6.

Drazetic, P. et al. (1994). "Applying non-direct similitude technique to the dynamic bending collapse of rectangular section tubes". In: *International Joiurnal of Impact Engineering* 15.6, pp. 797–814.

Duffey, T. A., M. C. Cheresh, and S. H. Sutherland (1984). "Experimental verification of scaling laws for punch-impact-loaded structures". In: *International Journal of Impact Engineering* 2.1, pp. 103–117.

Dutson, A. J. and K. L. Wood (2002). "Foundations and applications of the Empirical Similitude Method (ESM)".

Dutson, A. J. et al. (2003). "Application of similitude techniques to functional testing of rapid prototypes". In: *Rapid prototyping Journal* 9.1, pp. 6–13.

Emori, R I. (1973). "Scale models of automobile collisions with breakaway obstacles". In: *Experimental Mechanics* 63.9, pp. 64–69.

Ewins, D. J. (2000). *Modal testing: theory, practice and application, 2nd edition*. Eastbourne (UK): Wiley.

Ezra, A. A. (1962). "Similitude requirements for scale model determination of shell buckling under impulsive pressures". In: *Collected papers on instability of shell structures*. N63–10804. Washington (DC), USA: NASA, pp. 661–669.

Fahy, F. and P. Gardonio (2007). *Sound and structural vibration. Radiation, transmission and response, 3rd edition*. Academic Press.

Flood, I. and N. Kartam (1993). "Neural networks in civile engineering. I: principles and understanding". In: *Journal of Computing in Civil Engineering* 8.2, pp. 131–148.

Folkman, N. R., F. L. Baldwin, and J. B. Wainwright (1965). "Tests on a thermally scaled model space station in a simulated solar environment". In: 65–658. AIAA Thermophysics Specialist Conference. Monterey (CA), USA: AIAA.

Fowle, A. A., F. Gabron, and J. M. F. Vickers (1966). "Thermal scale modeling of spacecraft: an experimental investigation". In: *Journal of Spacecraft and Rockets* 3.4, pp. 577–581.

Franco, F. et al. (2019). "Similitude laws for the structural response of flat plates under a turbulent boundary layer excitation". In: *Mechanical Systems and Signal Processing* 129, pp. 590–613.

Franco, F. et al. (2020). "Structural response of stiffened plates in similitude under a turbulent boundary layer excitation". In: *Journal of Fluids and Structures* 98. DOI: https://doi.org/10.1016/j.jfluidstructs.2020.103119.

French, M. (1990). "An application of structural optimization in wind tunnel model design". In: 31st AIAA/ASME/ASCE/AHS/ASC Structures, Structural Dynamics, and Materials Conference. Long Beach (CA), USA: AIAA, pp. 127–134.

French, M. and F. E. Eastep (1996). "Aeroelastic model design using parameter identification". In: *Journal of Aircraft* 33.1.

Friedmann, P. P. (1999). "Rotary-wing aeroelastic scaling and its implications for the adaptive-materials-based actuation". In: *Proc. SPIE 3668, Smart Structures and Materials 1999: Smart Structures and Integrated Systems*. 1999 Symposium on Smart Structures and Materials. Newport Beach (CA), USA, pp. 60–79.

— (2004). "Aeroelastic scaling for rotary-wing aircraft with applications". In: *Journal of Fluids and Structures* 19.5, pp. 635–650.

Friedmann, P. P., D. Guillot, and E. Presente (1997). "Adaptive control of aeroelastic instabilities in transonic flow and its scaling". In: *Journal of Guidance, Control and Dynamics* 20.6, pp. 1190–1199.

Frostig, Y. and G. J. Simitses (2004). "Similitude of sandwich panels with a 'soft' core in buckling". In: *Composites: Part B* 35, pp. 599–608.

Fu, J. Y., S. G. Liang, and Q. S. Li (2007). "Prediction of wind-induced pressures on a large gymnasium roof using artificial neural networks". In: *Computers and Structures* 85, pp. 179–192.

Fujino, M., H. Oyama, and H. Omotani (2003). "Flutter characteristics of an over the wing engine mount business jet configuration". In: 44th AIAA/ASME/ASCE/AHS structures, structural dynamics, and materials conference. Norfolk (VA), USA, pp. 1–12.

Gabron, F. (1966). *Thermal scale modeling techniques for Voyager-type spacecraft*. Tech. rep. C–66326–0. Pasadena (CA), USA: Jet Propulsion Laboratory.

Gabron, F. and R. W. Johnson (1965). *Thermal scale modeling of the temperature control model of Mariner Mars 64*. Tech. rep. CR–70178. Pasadena (CA), USA: A. D. Little, Inc for Jet Propulsion Laboratory.

Galilei, G. and J. Weston (1730). *Mathematical discourses concerning two new sciences relating to mechanicks and local motion: in four dialogues*. London: Printed for John Hooke, at the Flower-de-Luce Against St. Dunstan's Church in Fleet-Street.

Gang, X., D. Wang, and X. Su (2010). "A new similitude analysis method for a scale model test". In: *Key Engineering Materials* 439–440, pp. 704–709.

Gaspar, J. L. et al. (2005). "Testing of a 20-meter solar sail system". In: 53rd JANNAF propulsion meeting. Monterey (CA), USA.

Gaspar, J. L. et al. (2006). "Testing of a 10-meter quadrant solar sail". In: IMAC - XXIV conference and exposition on structural dynamics. Sant Louis (MO), USA.

Gauchìa, A. et al. (2014). "Methodology for bus structure torsion stiffness and natural vibration frequency prediction based on a dimensional analysis approach". In: *International Journal of Automotive Technology* 15.3, pp. 451–461.

Goodfellow, I., Y. Bengio, and A. Courville (2016). *Deep learning*. Cambridge (MA), USA: The MIT Press.

Goodier, J. N. (1950). *Dimensional analysis*. New York: John Wiley and Sons.

Goodier, J. N. and W. T. Thomson (1944). *Applicability of similarity principles to structural models*. Tech. rep. NACA Technical Report CR-4068. Washington (DC), USA: National Advisory Committee for Aeronautics.

Greschik, G., M. M. Mikulas, and R. E. Freeland (1999). "The nodal concept of deployment and the scale model testing of its application to a membrane antenna". In: AIAA–99–1523. American Institute of Aeronautics and Astronautics, pp. 2546–2554.

Gronet, M. J. et al. (1987). *Preliminary design, analysis, and costing of a dynamic scale model of the NASA Space Station*. Tech. rep. NASA Contractor Report 4068. Washington (DC), USA: National Aerospace and Space Administration.

Gukhman, A. A. (1965). *Introduction to the theory of similarity*. New York: Academic Press.

Hagan, M. T. et al. (2014). *Neural networks design, 2nd edition*. USA: Martin Hagan.

Hagiwara, K., H. Takanabe, and H. Kawano (1983). "A proposed method of predicting ship collision damage". In: *Int. J. Impact Engng.* 1.3, pp. 257–279.

Hamada, H. and S. Ramakrishna (1995). "Scaling effects in the energy absorption of carbon-fiber/PEEK composite tubes". In: *Composites Science and Technology* 55, pp. 211–221.

Harris, H. G. and G. M. Sabnis (1999). *Structural modeling and experimental techniques*. Boca Raton (FL), USA: CRC Press.

He, F. et al. (2020). "A similitude for the middle-frequency vibration response of satellite solar array based on the wave coupling hybrid finite element-statistical energy analysis method". In: *Proceedings of the Institution of Mechanical Engineers, Part C: Journal of Mechanical Engineering Science* 234.18, pp. 3560–3570.

Heeg, J., C. V. Spain, and J. A. Rivera (2004). "Wind tunnel to atmospheric mapping for static aeroelastic scaling". In: 45th AIAA/ASME/ASCE/AHS/ASC Structures, Structural Dynamics and Materials Conference. Palm Springs (CA), USA, pp. 1–13.

Herr, R. and H. Wayne Leonard (1967). *Dynamic model investigation of touchdown stability of lunar-landing vehicles*. Tech. rep. NASA TN D–4215. Washington (DC), USA: National Aeronautics and Space Administration.

Hilburger, M. W., A. E. Lovejoy, and R. P. Thornburgh (2012). "Design and analysis of subscale and full-scale buckling-critical cylinders for launch vehicle technology development". In: 53rd AIAA/ASME/ASCE/AHS/ASC Structures, Structural Dynamics and Materials Conference. Honolulu (HI), USA, pp. 1–48.

Hilburger, M. W., C. A. Rose, and J. H. Starnes, Jr. (2001). "Nonlinear analysis and scaling laws for noncircular composite structures subjected to combined loads". In: 42nd AIAA/ASME/ASCE/AHS/ASC Structures, Structural Dynamics and Materials Conference. Seattle (WA), USA, pp. 1–15.

Holland, D. B. et al. (2002). "Geometric scaling properties of inflatable structures for use in space solar power generation". In: 43rd AIAA/ASME/ASCE/AHS/ASC

Structures, Structural Dynamics and Materials Conference. Denver (CO), USA, pp. 1–10.

Holmes, B. S. and G. Sliter (1974). *Scale modeling of vehicle crashes - Techniques, applicability, and accuracy; cost effectiveness*. Tech. rep. SAE paper no. 740586.

Hornik, K., M. Stinchcombe, and H. White (1989). "Multilayer feedforward networks are universal approximators". In: *Neural Networks* 2, pp. 303–314.

Horta, L. G. and R. G. Kvaternik (2000). *A historical perspective on dynamics testing at the Langley Research Center*. Tech. rep. NASA/TM–2000–210295. Washington (DC), USA: National Aeronautics and Space Administration.

Hu, Y. Q. (2000). "Application of response number for dynamic plastic response of plates subjected to impulsive loading". In: *International Journal of Pressure Vessels and Piping* 77, pp. 711–714.

Huang, SC. and YF. Huang (1991). "Bounds on the number of hidden neurons in multilayer perceptrons". In: *IEEE Transactions on Neural Networks* 2.1, pp. 47–55.

Hunt, G. K. (1973). *Aero-elastic models of helicopter rotors*. Tech. rep. CP 1245. London, United Kingdom: Procurement Executive, Ministry of Defence, Aeronautical Research Council.

Hush, D. R. and B. G. Horne (1993). "Progress in supervised neural networks. What's new since Lippmann". In: *IEEE Signal Processing Magazine* 10.1, pp. 8–39.

Jackson, K. E. (1990). *Scaling effects in the static and dynamic response of graphite-epoxy beam-columns*. Tech. rep. NASA Technical Memorandum 102697, AVSCOM TR–90–B–006. Washington (DC), USA: National Aeronautics and Space Administration.

— (1993). "Workshop on scaling effects in composite materials and structures". In: NASA Conference Publication 3271. Proceedings of a workshop sponsored by the National Aeronautics et al. Hampton (VA), USA.

Jackson, K. E. and E. L. Fasanella (1989). *Scaling effects in the static large deflection response of graphite-epoxy composite beams*. Tech. rep. NASA Technical Memorandum 101619, AVSCOM Technical Memorandum 89–B–006. Washington (DC), USA: National Aeronautics and Space Administration.

— (1999). *Crashworthy evaluation of a 1/5-scale model composite fuselage concept*. Tech. rep. NASA/TM–1999–209132, ARL–MR–441. Washington (DC), USA: National Aeronautics and Space Administration.

— (2003). "Comparisons of the impact responses of a 1/5-scale model and a full-scale crashworthy composite fuselage section". In: American Helicopter Society 59th Annual Forum. Phoenix (AZ), USA.

Jacob, N. et al. (2004). "Scaling aspects of quadrangular plates subjected to localised blast loads - Experiments and predictions". In: *International Journal of Impact Engineering* 30, pp. 1179–1208.

Jia, Y. et al. (2020). "Prediction of random dynamic loads using second-order blind source identification algorithm". In: *Proc. IMechE part C: Journal of Mechanical Engineering Science* 234.9, pp. 1720–1732.

Jiang, P., W. Wang, and G. J. Zhang (2006). "Size effects in the axial tearing of circular tubes during quasi-static and impact loadings". In: *International Journal of Impact Engineering* 32, pp. 2048–2056.

Jiang, P. et al. (2006). "Experimental investigation into scaling laws for conical shells struck by projectiles". In: *International Journal of Impact Engineering* 32, pp. 1284–1298.

Johnson, D. P. et al. (1998). "Scaling effects in sublaminate-level scaled composite laminates". In: *AIAA Journal* 36.3, pp. 441–446.

Johnson, D. P. et al. (2000). "Size effects in scald fiber composites under four-point flexure loading". In: *AIAA Journal* 38.6, pp. 1047–1054.

Johnson, W. (1972). *Impact strength of materials*. London, UK: Edward Arnold (Publishers) Limited.

Jones, B. P. (1964). "Thermal similitude studies". In: *Journal of Spacecraft and Rockets* 1.4, pp. 364–369.

Jones, B. P. and J. K. Harrison (1965). *A set of experiments in thermal similitude*. Tech. rep. NASA TM X-53346. Huntsville (AL), USA: National Aeronautics and Space Administration.

Jones, E. M. C. et al. (2019). "X-ray stereo digital image correlation". In: *Experimental Techniques* 44.2, pp. 159–174.

Jones, N. (1989). *Structural impact*. Cambridge, UK: Cambridge University Press.

Kasivitamnuay, J. and P. Singhatanadgid (2005). "Application of an energy theorem to derive a scaling law for structural behaviors". In: *Thammasat. Int. J. Sc. Tech.* 10.4, pp. 33–40.

— (2017). "Scaling laws for displacement of elastic beam by energy method". In: *International Journal of Mechanical Sciences* 128–129, pp. 361–367.

Katzoff, S. (1963). *Similitude in thermal models of spacecraft*. Tech. rep. NASA TN D–1631. Washington (DC), USA: National Aeronautics and Space Administration.

Keith Belvin, W. and H. E. Edighoffer (1986a). "15 meter hoop-column antenna dynamics: test and analysis". In: First NASA/DOD CSI Technology Conference. Norfolk (VA), USA: National Aeronautics and Space Administration, pp. 167–185.

— (1986b). *Experimental and analytical generic space station dynamic models*. Tech. rep. NASA Technical Memorandum 87696. Washington (DC), USA: National Aeronautics and Space Administration.

Kellas, S. and J. Morton (1992a). *Scaling effects in angle-ply laminates*. Tech. rep. NASA Contractor Report 4423. Washington (DC), USA: National Aeronautics and Space Administration.

— (1992b). "Strength scaling in fiber composites". In: *AIAA Journal* 30.4, pp. 1074–1080.

Kim, N. S., Y. H. Kwak, and S. P. Chang (2004). "Pseudodynamic tests on small-scale steel models using te modified similitude law". In: 13th World Conference of Earthquake Engineering. Vancouver (BC), Canada, p. 3360.

Kim, N. S., J. H. Lee, and S. P. Chang (2009). "Equivalent multi-phase similitude law for pseudodynamic test on small scale reinforced concrete models". In: *Eingineering Structures* 31, pp. 834–846.

Kline, S. J. (1965). *Similitude and approximation theory*. NY: McGraw-Hill.

Krayterman, B. and G. M. Sabnis (1984). "Similitude theory: plates and shells analysis". In: *Journal of Engineering Mechanics* 110.9, pp. 1247–1263.

Krishnakumar, N., V. Jain, and P. M. Singru (2015). "Development of predictive model for vibroacoustic condition monitoring of lathe". In: *Journal of Vibroengineering* 17.1, pp. 229–242.

Kumar, S. et al. (1997). "Pseudodynamic testing of scaled models". In: *Journal of Structural Engineering* 123.4, pp. 524–526.

Kuneš, J. (2012). *Similarity and modeling in science and engineering*. Cambridge, United Kingdom: Cambridge International Science Publishing Ltd and Springer.

Kure, K. (1981). "Model tests with ocean structures". In: *Applied Ocean Research* 3.4, pp. 171–176.

Kužnar, D. et al. (2012). "Improving vehicle aeroacoustics using machine learning". In: *Engineering Applications of Artificial Intelligence* 25.5, pp. 1053–1061.

Langhaar, H. L. (1951). *Dimensionless analysis and theory of models*. New York: John Wiley and Sons.

Laue, G., D. Case, and J. Moore (2005). "Fabrication and deployment testing of solar sail quadrants for a 20-meter solar sail ground test system demonstration". In: 41st AIAA/ASME joint propulsion conference and exhibit. Tucson (AZ), USA, pp. 1–16.

Laws, N. and G. J. Dvorak (1988). "Progressive transverse cracking in composite laminates". In: *Journal of Composite Materials* 22.10, pp. 900–916.

Leadbetter, S. A. (1970). *Application of analysis and models to structural dynamic problems related to the Apollo-Saturn V launch vehicle*. Tech. rep. NASA TN D–5831. Washington (DC), USA: National Aeronautics and Space Administration.

Leadbetter, S. A., H. Wayne Leonard, and E. John Brock, Jr. (1967). *Design and fabrication considerations for a 1/10-scale replica model of the Apollo/Saturn*. Tech. rep. NASA TN D–4138. Washington (DC), USA: National Aeronautics and Space Administration.

Leadbetter, S. A. et al. (1976). *Vibration characteristics of a 1/8-scale dynamic models of the space-shuttle solid-rocket boosters*. Tech. rep. NASA TN D–8158. Washington (DC), USA: National Aeronautics and Space Administration.

Lehmann, E. and J. Peschmann (2002). "Energy absorption of the steel structure of ships in the event of collisions". In: *Marine Structures* 15, pp. 429–441.

Letchworth, R., P. E. McGowan, and M. J. Gronet (1988). "Space station: a focus for the development of structural dynamic scale model for large flexible space structures". In: AIAA/ASME/ASCE/AHS 29th SDM conference (not included in proceedings). Williamsburg (VA), USA, pp. 121–130.

Levy, A. et al. (1974). *Development of technology for modeling of a 1/8-scale dynamic model of the shuttle solid rocket booster (SRB)*. Tech. rep. Technical Report NASA

CR–132492. Washington (DC), USA: National Aeronautics and Space Administration.

Li, BJ., BQ. Wang, and DP. Duan (2019). "Displacement measurement errors in digital image correlation due to displacement mapping function". In: *Experimental Techniques* 43.4, pp. 445–456.

Li, Q. M. and N. Jones (2000). "On dimensionless numbers for dynamic response of structural members". In: *N. Archive of Applied Mechanics* 70.245, pp. 245–254.

Li, X. (2010a). "A scaling approach for the prediction of the high-frequency mean responses of vibrating systems". In: *J. Acoust. Soc. Am.* 127.5, EL209–EL214.

— (2010b). "Scaling for the ensemble statistics prediction of a random system subjected to harmonic excitations". In: *J. Acoust. Soc. Am.* 127.5, EL203–EL208.

Liu, J., L. Zhou, and D. W. Herrin (2011). "Demonstration of vibro-acoustic reciprocity including scale modeling". In: *SAE Technical Papers* 2011-01-1721. DOI: 10.4271/2011-01-1721.

Lowe, W. T., S. T. S. Al-Hassani, and W. Johnson (1974). "Impact behaviour of small scale model motor coaches". In: *Proceedings of the Institution of Mechanical Engineers* 186.36, pp. 409–419.

Luo, Z. et al. (2013). "Study of the structure size interval of incomplete geometrically similitude model of the elastic thin plates". In: *Journal of Measurements in Engineering* 1.4, pp. 207–218. URL: https://www.jvejournals.com/article/14666.

Luo, Z. et al. (2014a). "Determination method of dynamic distorted scaling laws and applicable structure size intervals of a rotating thin-wall short cylindrical shell". In: *Proceedings of the Institution of Mechanical Engineers, Part C: Journal of Mechanical Engineering Science* 229.5, pp. 806–817.

Luo, Z. et al. (2014b). "Determination method of the structure size interval of dynamically similar models for predicting vibration characteristics of the isotropic sandwich plates". In: *Journal of Vibroengineering* 16.2, pp. 608–622. URL: https://jvejournals.com/article/14742.

Luo, Z. et al. (2014c). "Determination method of the structure size intervals of dynamic distorted model of elastic cantilever thin plate". In: *Advances in Mechanical Engineering* 2014, pp. 1–10. DOI: 10.1155/2014/791047.

Luo, Z. et al. (2014d). "The dynamic similitude design of a thin-wall cylindrical shell with sealing teeth and its geometrically distorted model". In: *Advances in Mechanical Engineering* 7.2, pp. 1–12.

Luo, Z. et al. (2015). "The similitude design method of thin-walled annular plates and determination of structural size intervals". In: *Proceedings of the Institution of Mechanical Engineers, Part C: Journal of Mechanical Engineering Science* 230.13, pp. 2158–2168. URL: https://doi.org/10.1177/0954406215592055.

Luo, Z. et al. (2016a). "Dynamic similitude design method of the distorted model on variable thickness cantilever plates". In: *Applied Sciences* 6.228, pp. 1–15.

Luo, Z. et al. (2016b). "The dynamic similitude design method of thin walled structures and experimental validation". In: *Shock and Vibration* 2016, pp. 1–11.

Macagno, E. O. (1971). "Historico-critical review of dimensional analysis". In: *J. Franklin Inst.* 292, pp. 391–402.

Mace, B. (2003). "Statistical energy analysis, energy distribution models and system modes". In: *Journal of Sound and Vibration* 264, pp. 391–409.

MacKay, D. J. C. (1992). "Bayesian interpolation". In: *Neural Computation* 4, pp. 415–447.

Magness, L. and T. Farrand (1990). "Deformation behavior and its relationship to the penetration performance of high density KE penetrator materials". In: Proceedings of 1990 Army Science Conference. Durham (NC), USA.

Mahn, J. P. and P. V. Bayly (1999). "Impact testing of stereolithographic models to predict natural frequencies". In: *Journal of Sound and Vibration* 224.3, pp. 411–430.

Mai, Y. W. and A. G. Atkins (1975). "Scale effects and crack propagation in non-linear elastic structures". In: *International Journal of Mechanical Sciences* 17, pp. 673–675.

— (1978). "Crack propagation in non-proportionally scaled elastic structures". In: *International Journal of Mechanical Sciences* 20, pp. 437–449.

Maples, D. and J. V. Scogin (1970). *Thermal modeling with internal generation*. Tech. rep. NGR–10–001–068. Huntsville (AL), USA: Marshall Space Flight Center.

Marquardt, D. W. (1963). "An algorithm for least-squares estimation of nonlinear parameters". In: *J. Soc. Indust. Appl. Math.* 11.2, pp. 431–441.

Marshall, K. N. and W. G. Foster (1973). *Space Shuttle thermal scale modeling application study*. Tech. rep. TP–3613. Sunnyvale (CA), USA: Lockheed Missiles & Space Company.

Martin, I. and D. Bestle (2018). "Automated eigenmode classification for airfoils in the presence of fixation uncertainties". In: *Engineering Applications of Artificial Intelligence* 67, pp. 187–196.

Martini, L., S. De Rosa, and F. Franco (2004). "The structural response of a three plate assembly by Scaled Finite Element Method". In: Proceedings of ISMA. Leuven, Belgium, pp. 1539–1554.

Mason, P. W. et al. (1974a). *Analytical and experimental investigation of a 1/8-scale dynamic model of the shuttle orbiter. Volume I-Summary report*. Tech. rep. Technical Report NASA CR–132488. Washington (DC), USA: National Aeronautics and Space Administration.

— (1974b). *Analytical and experimental investigation of a 1/8-scale dynamic model of the shuttle orbiter. Volume II-Technical report*. Tech. rep. Technical Report NASA CR–132489. Washington (DC), USA: National Aeronautics and Space Administration.

Mazzariol, L. M. and M. Alves (2013). "Experimental study on scaling of circular tubes subjected to dynamic axial crushing using models of different materials". In: 22nd International Congress of Mechanical Engineering (COBEM 2013). Ribeirão Preto (SP), Brazil, pp. 8065–8074.

Mazzariol, L. M. and M. Alves (2014). "Scaling of the impact of a mass on a plate using models of different materials". In: 4th International Conference on Impact Loading of Lightweight Structures. Cape Town, South Africa, pp. 1275–1289.

Mazzariol, L. M., R. E. Oshiro, and M. Alves (2016). "A method to represent impacted structures using scaled models made of different materials". In: *International Journal of Impact Engineering* 90, pp. 81–94.

Mazzariol, L. M. et al. (2010). "Scaling of stiffened panels subjected to impact loading". In: *Mecánica Comput. Vol XXIX*. Ed. by E. Dvorkin, M. Goldscmit, and M. Storti. Iberian-Latin-American congresso on computational methods in engineering. Buenos Aires, Argentina, pp. 1275–1289.

McGehee, J. R. and S. M. Stubbs (1973). *Experimental validation of a landing-dynamics computer program for legged spacecraft landers*. Tech. rep. NASA Technical Note TN D–7301. Hampton (VA), USA: National Aeronautics and Space Administration.

McGowan, P. E., H. E. Edighoffer, and J. W. Wallace (1990). *Development of an experimental space station model for structural dynamics research*. Tech. rep. NASA Technical Memorandum 102601. Washington (DC), USA: National Aeronautics and Space Administration.

McGowan, P. E., M. Jaeed, and H. E. Edighoffer (1991). *Status of DSMT research program*. Tech. rep. NASA Technical Memorandum 102764. Washington (DC), USA: National Aeronautics and Space Administration.

McKown, S., W. J. Cantwell, and N. Jones (2008). "Investigation of scaling effects in fiber-metal laminates". In: *Journal of Composite Materials* 42.9/2008, pp. 865–888.

McNeill, S. I. and D. C. Zimmerman (2008). "A framework for blind modal identification using joint approximate diagonalization". In: *Mechanical Systems and Signal Processing* 22, pp. 1526–1548.

Md, S. H. et al. (2017). "Artificial neural networks for vibration based inverse parametric identifications: A review". In: *Applied Soft Computing* 52, pp. 203–219.

Me-Bar, Y. (1997). "A method for scaling ballistic penetration phenomena". In: *Int. J. Impact Engng.* 19.9–10, pp. 821–829.

Meruane, V., S. De Rosa, and F. Franco (2015). "Numerical and experimental results for the frequency response of plates in similitude". In: *Proceedings of the Institution of Mechanical Engineers, Part C: Journal of Mechanical Engineering Science* 230.18, pp. 3212–3221. DOI: https://doi.org/10.1177/0954406215610148.

Meruane, V. and J. Mahu (2013). "Damage assessment of a beam using artificial neural networks and antiresonant frequencies". In: *Special Topics in Structural Dynamics, Volume 6*. Ed. by R. Allemang et al. New York (NY), USA: Springer New York, pp. 217–224.

Mitchell, T. M. (1997). *Machine learning*. New York (NY), USA: McGraw Hill Education.

Mixson, J. S. and J. J. Catherine (1964a). *Comparison of experimental vibration characteristics obtained from a 1/5-scale model and from a full-scale Saturn SA-1*. Tech. rep. NASA TN D–2214. Washington (DC), USA: National Aeronautics and Space Administration.

— (1964b). *Experimental lateral vibration characteristics of a 1/5-scale model of Saturn SA-1 with an eight-cable suspension system*. Tech. rep. NASA TN D–2214. Washington (DC), USA: National Aeronautics and Space Administration.

Molyneux, W. G. (1964). *Aeroelastic modeling*. Tech. rep. 353. RAE.

Moradi, B. and I. D. Parsons (1992). "Dimensional analysis of buckling of stiffened composite shells". In: *Journal of Engineering Mechanics* 118.3, pp. 557–574.

Morosow, G. and I. J. Jaszlics (1966). *Titan III 20 percent dynamic model characteristics - Comparison of theory and experiment*. Tech. rep. Technical Report AFFDL–TR–66–80. Denver (CO), USA: Air Force Fliight Dynamics Laboratory.

Morton, J. (1988). "Scaling of impact-loaded carbon-fiber composites". In: *AIAA Journal* 26.8, pp. 989–994.

Murphy, D. M., B. Macy, and J. L. Gaspar (2004). "Demonstration of a 10-m solar sail system". In: 45th AIAA/ASME/ASCE/AHS/ASC Structures, Structural Dynamics and Materials Conference. Palm Springs (CA), USA, pp. 1–10.

Murphy, G. (1950). *Similitude in engineering*. New York: Ronald Press.

Nadooshan, A. A., S. Daneshmand, and C. Aghanajafi (2007). "Application of RP technology with polycarbonate material for wind tunnel model fabrication". In: *Int. J. Mech. Industr. Sci. Eng.* 1.8, pp. 371–376.

Nettles, A. T., M. J. Douglas, and E. E. Estes (1999). *Scaling effects in carbon/epoxy laminates under transverse quasi-static loading*. Tech. rep. NASA/TM–1999–209103. Washington (DC), USA: National Aeronautics and Space Administration.

Neuberger, A., S. Peles, and D. Rittel (2007a). "Scaling the response of circular plates to large and close range spherical explosions. Part I: air-blast loading". In: *International Journal of Impact Engineering* 34, pp. 859–873.

— (2007b). "Scaling the response of circular plates to large and close range spherical explosions. Part II: buried charges". In: *International Journal of Impact Engineering* 34, pp. 874–882.

— (2009). "Springback of circular clamped armor steel plates subjected to spherical air-blast loading". In: *International Journal of Impact Engineering* 36, pp. 53–60.

Noam, T., M. Dolinski, and D. Rittel (2014). "Scaling dynamic failure: a numerical study". In: *International Journal of Impact Engineering* 69, pp. 69–79.

Nurick, G. N. and J. B. Martin (1989a). "Deformation of thin plates subjected to impulsive loading–A review. Part I: theoretical considerations". In: *International Journal of Impact Engineering* 8.2, pp. 159–170.

— (1989b). "Deformation of thin plates subjected to impulsive loading–A review. Part II: experimental studies". In: *International Journal of Impact Engineering* 8.2, pp. 171–186.

Nyquist, H. (1928). "Certain topics in telegraph transmission theory". In: *Transactions of the American Institute of Electrical Engineers* 47.2, pp. 617–644.

Ohtsubo, H., Y. Kawamoto, and T. Kuroiwa (1994). "Experimental and numerical research on ship collision and grounding of oil tankers". In: *Nuclear Engineering and Design* 150, pp. 385–396.

Oshiro, R. E. and M. Alves (2004). "Scaling impacted structures". In: *Archive of Applied Mechanics* 74, pp. 130–145.

— (2007). "Scaling of cylindrical shells under axial impact". In: *International Journal of Impact Engineering* 34, pp. 89–103.

— (2009). "Scaling structures subject to impact loads when using a power law constitutive equation". In: *International Joournal of Solids and Structures* 46, pp. 3412–3421.

— (2012). "Predicting the behaviour of structures under impact loads using geometrically distorted scaled models". In: *Journal of the Mechanics and Physics of Solids* 60, pp. 1330–1349.

Oshiro, R. E. et al. (2011). "Experimental study of scaled T cross–section beams subjected to impact load". In: 21st Brazilian Congress of Mechanical Engineering. Natal (RN), Brazil.

— (2017). "Experimental study of collision in scaled naval structures". In: *International Journal of Impact Engineering* 110, pp. 149–161.

O'Sullivan, W. J. (1957). *Theory of aircraft structural models subject to aerodynamic heating and external loads*. Tech. rep. Technical Note 4115. Langley Field (VA), USA: National Advisory Committee for Aeronautics.

Pankhurst, R. C. (1964). *Dimensional analysis and scale factors*. New York (NY), USA: Chapman and Hall.

Peele, E. L., W. M. Thompson, Jr., and C. G. Pusey (1968). *A theoretical and experimental investigation of the three-dimensional vibration characteristics of a scaled model of an asymmetrical launch vehicle*. Tech. rep. NASA TN D–4707. Washington (DC), USA: National Aeronautics and Space Administration.

Peele, E. L., H. Wayne Leonard, and S. A. Leadbetter (1970). *Lateral vibration characteristics of the 1/10-scale Apollo/Saturn V replica model*. Tech. rep. NASA TN D–5778. Washington (DC), USA: National Aeronautics and Space Administration.

Pereira, P. et al. (2007). "Aeroelastic scaling and optimization of a joined-wing aircraft concept". In: 3rd AIAA MultiDisciplinary Design Optimization Specialists Conference. Honolulu (HI), USA: AIAA, pp. 1–13.

Petrone, G. et al. (2014). "Numerical and experimental investigations on the acoustic power radiated by aluminium foam sandwich panels". In: *Composite Structures* 118, pp. 170–177.

Petrone, G. et al. (2017). "Structural similitudes of stiffened cylinders". In: *Mathematics and Mechanics of Solids*. DOI: https://doi.org/10.1177/1081286517745722.

Pinson, L. D. (1975). *Analytical and experimental vibration studies of a 1/8-scale shuttle orbiter*. Tech. rep. NASA TN D–7964. Washington (DC), USA: National Aeronautics and Space Administration.

Pinson, L. D. and H. Wayne Leonard (1969). *Longitudinal vibration characteristics of a 1/10-scale Apollo/Saturn V replica model*. Tech. rep. NASA TN D–5159. Washington (DC), USA: National Aeronautics and Space Administration.

Pintado, P. and A. Morton (1994). "On the scaling of impact loaded composite beams". In: *Composite Structures* 27, pp. 357–365.

Polsinelli, J. and M. Levent Kavvas (2016). "A comparison of the modern Lie scaling method to classical scaling techniques". In: *Hydrl. Earth Syst. Sci.* 20, pp. 2669–2678.

Pototzky, A. S. (2002). "Scaling laws applied to a modal formulation of the aeroservoelastic equations". In: 43rd AIAA/ASME/ASCE/AHS/ASC Structures, Structural Dynamics, materials Conference, and Exhibit. Denver (CO), USA: AIAA, pp. 1–11.

Powell, C. A. and D. G. Stephens (1966). *Vibrational characteristics of sandwich panels in a reduced-pressure environment*. Tech. rep. Technical Report NASA TN D-3549. Hampton (VA), USA: National Aeronautics and Space Administration.

Presente, E. H. and P. P. Friedmann (1998a). "Aeroservoelasticity in compressible flow and its scaling laws". In: 43rd AIAA/ASME/ASCE/AHS/ASC Structures, Structural Dynamics, materials Conference, and Exhibit. Denver (CO), USA: AIAA, pp. 1705–1720.

— (1998b). "Aeroservoelasticity in subsonic flow and associated scaling laws". In: 43rd AIAA/ASME/ASCE/AHS/ASC Structures, Structural Dynamics, materials Conference, and Exhibit. Denver (CO), USA: AIAA, pp. 190–202.

Qian, Y. et al. (1990). "An experimental study of scaling rules for impact damage in fiber composites". In: *Journal of Composite Materials* 24.5, pp. 559–570.

Qin, G. et al. (2012). "Similitude analysis on mechanical parameters of thin walled shells". In: *Advanced Engineering Forum* 2–3, pp. 139–144. DOI: https://doi.org/10.4028/www.scientific.net/AEF.2-3.936.

Quercetti, T., K. Müller, and S. Schubert (2008). "Comparison of experimental results from drop testing of spent fuel package design using full scale prototype model and reduced scale model". In: *Packaging, Transport, Storage & Security of Radioactive Material* 19.4, pp. 197–202. DOI: 10.1179/174651008X362575.

Ramu, M., V. Prabhu Raja, and P. R. Thyla (2010). "Development of structural similitude and scaling laws for elastic models". In: *International Journal of Manufacturing Engineering* 9, pp. 67–69.

— (2013). "Establishment of structural similitude for elastic models and validation of scaling laws". In: *KSCE Journal of Civil Engineering* 17.1, pp. 139–144.

Rasmussen, C. E. and C. K. I. Williams (2006). *Gaussian processes for machine learning*. Cambridge (MA), USA: The MIT Press.

Rayleigh, L. (1896). *The Theory of Sound, 2nd Ed.* New York (NY), USA.

— (1915). "The principle of similitude". In: *Nature* 95, pp. 66–8.

Rezaeepazhand, J. and G. J. Simitses (1993). *Design of scaled down models for stability and vibration studies*. Tech. rep. NASA Technical Report 194687. National Aeronautics and Space Administration.

Rezaeepazhand, J. and G J. Simitses (1997). "Structural similitude for vibration response of laminated cylindrical shells with double curvature". In: *Composites part B* 28B.3, pp. 195–200.

Rezaeepazhand, J., G. J. Simitses, and J. H. Starnes, Jr. (1995a). "Design of scaled down models for stability of laminated plates". In: *AIAA Journal* 33.3, pp. 515–519.

— (1995b). "Use of scaled-down models for predicting vibration response of laminated plates". In: *Composite Structures* 30, pp. 419–426.

— (1996a). "Design of scaled down models for predicting shell vibration response". In: *Journal of Sound and Vibration* 195.2, pp. 301–311.

— (1996b). "Scale models for laminated cylindrical shells subjected to axial compression". In: *Composite Structures* 34, pp. 371–379.

Rezaeepazhand, J. and M. R. Wisnom (2009). "Scaled models for predicting buckling of delaminated orthotropic beam-plates". In: *Composite Structures* 90, pp. 87–91.

Rezaeepazhand, J. and A. A. Yazdi (2011). "Similitude requirements and scaling laws for flutter prediction of angle-ply composite plates". In: *Composites: Part B*, pp. 51–56.

Ricciardi, A. P. et al. (2012a). "High fidelity nonlinear aeroelastic analysis for scaled vehicle design". In: 14th AIAA/ISSMO Multidisciplinary Analysis and Optimization Conference. AIAA, pp. 1–11.

Ricciardi, A. P. et al. (2012b). "Nonlinear aeroelastic scaling of a joined-wing aircraft". In: 53rd AIAA/ASME/ASCE/AHS/ASC Structures, Structural Dynamics, and Materials Conference. Honolulu (HI), USA: AIAA, pp. 1–12.

Ricciardi, A.P. et al. (2014). "Nonlinear aeroelastic-scaled-model optimization using equivalent static loads". In: *J. Aircr.* 51.6, pp. 1842–1851.

Richards, J. et al. (2009). "Design of a scaled RPV for investigation of gust response of joined-wing sensorcraft". In: 50th AIAA/ASME/ASCE/AHS/ASC Structures, Structural Dynamics, and Materials Conference. Palm Springs (CA), USA: AIAA, pp. 1–14.

Rittel, D., ZG. Wang, and M. Merzer (2006). "Adiabatic shear failure and dynamic stored energy of cold work". In: *Physical Review Letters* 96.6, pp. 075502–1–075502–4.

Robin, O., S. De Rosa, and A. Berry (2016). "Similitudes for the structural response and radiated power from plates". In: 45th International Congress and Exposition on Noise Control Engineering: Towards a Quieter Future, INTER-NOISE 2016. Hamburg, Germany, pp. 5421–5430.

Robin, O. et al. (2016). "A plane and thin panel with repreentative simply supported boundary conditions for laboratory vibroacoustic tests". In: *Acta Acustica United with Acustica* 102, pp. 170–182.

Rolling, R. E. (1966). *Thermal scale modeling in a simulated space environment*. Tech. rep. NAS 8–11152. Palo Alto (CA), USA: Lockheed Missiles & Space Company.

Rolling, R. E., D. O. Murray, and K. N. Marshall (1969). *Limitations in thermal modeling*. Tech. rep. 6–78–69–41. Palo Alto (CA), USA: Lockheed Missiles & Space Company.

Rosen, R. (1989). "Similitude, similarity and scaling". In: *Landscape Ecology* 3.3–4, pp. 207–216.

Rosenberg, Z., R. Kreif, and E. Dekel (1997). "A note on the geometric scaling of long-rod penetration". In: *International Journal of Impact Engineering* 19.3, pp. 277–283.

Sabour, M. H. and R. B. Bhat (2010). "Thermal scale modeling by FEM and test". In: *Journal of Aerospace Engineering* 23.1, pp. 24–33.

Saito, K. and K. Kuwana (2017). "Scale modeling vibro-acoustics". In: *Acoust. Sci. & Tech.* 38.3, pp. 113–119.

Sarrafi, A. et al. (2018). "Vibration-based damage detection in wind turbine blades using phase-based motion estimation and motion magnification". In: *Journal of Sound and Vibration* 421, pp. 301–311.

Sato, J. A., F. J. Vecchio, and H. M. Andre (1989). "Scale-model testing of reinforced concrete under impact loading conditions". In: *Canadian Journal of Civil Engineering* 16.4, pp. 459–466.

Schleyer, G. K., S. S. Hsu, and M. D. White (2004). "Scaling of pulse loaded mild steel plates with different edge restraint". In: *International Journal of Mechanical Sciences* 46, pp. 1267–1287.

Schroeder, L. C. et al. (1989). *Near-field testing of the 15-meter hoop-column antenna*. Tech. rep. NASA Technical Memorandum 4073. Washington (DC), USA: National Aeronautics and Space Administration.

Schwingel, D. et al. (n.d.). "Aluminium foam sandwich structures for space applications". In: *Acta Astronautica* 61 (), pp. 326–330.

Shannon, R. L. (1972). *A thermal scale modeling study for Apollo and Apollo applications*. Tech. rep. D180–15048–1. Seattle (WA), USA: National Aeronautics and Space Administration.

Sharp, C. et al. (2013). "Analysis of railway vibration signals using supervised machine learning for the development of exposure-response relationships". In: *The Journal of Acoustical Society of America* 133.5.

Shi, X. H. and Y. G. Gao (2001). "Generalization of response number for dynamic plastic response of shells subjected to impulsive loading". In: *International Journal of Pressure Vessels and Piping* 78, pp. 453–459.

Shih, C. (1966). "Thermal similitude of manned spacecraft". In: 66–22. AIAA 3rd Aerospace Sciences Meeting. New York (NY), USA.

Shih, C. F., J. C. Chen, and J. A. Garba (1987). *Verification of large beam-type space structures*. Tech. rep. NASA TM–4073. Pasadena (CA), USA: National Aeronautics and Space Administration.

Shokrieh, M. M. and A. Askari (2013). "Similitude study of impacted composite under buckling loading". In: *J. Eng. Mech.* 139.10, pp. 1334–1340.

Siebert, T. et al. (2007a). "Error estimations in digital image correlations technique". In: *Applied Mechanics and Materials*. DOI: https://doi.org/10.4028/www.scientific.net/AMM.7-8.265.

— (2007b). "High-speed digital image correlation: error estimations and applications". In: *Optical Engineering* 46.5, pp. 0.51004–051004.

Simitses, G. J. (2001). "Structural similitude for flat laminated surfaces". In: *Composite Structures* 51, pp. 191–194.

Simitses, G. J. and J. Rezaeepazhand (1992). *Structural similitude and scaling laws for laminated beam-plates*. Tech. rep. NASA Grant NAG–1–1280. Washington (DC), USA: National Aeronautics and Space Administration.

— (1993). "Structural similitude for laminated structures". In: *Composites Engineering* 3.7–8, pp. 751–765.

— (1995). "Structural similitude and scaling laws for buckling of cross-ply laminated plates". In: *Journal of Thermoplastic Composite Materials* 8, pp. 240–251.

Simitses, G. J., J. Rezaeepazhand, and R. L. Sierakowski (1997). "Scaled models for laminated cylindrical shells subjected to external pressure". In: *Mechanics of Composite Materials and Structures* 4.3, pp. 267–280.

Simitses, G. J., J. H. Starnes Jr, and J. Rezaeepazhand (2000). "Structural similitude and scaling laws for plates and shells: a review". In: 41st AIAA/ASME/ASCE/AHS/ASC Structures, Structural Dynamics, Materials Conference, and Exhibit. Atlanta (GA), USA, pp. 1–11.

Singer, J., I. Arbocz, and T. Weller (1997). *Buckling experiments*. Chickester, England: John Wiley and Sons.

Singhatanadgid, P. and A. Na Songkhla (2008). "Experimental investigation into the use of scaling laws for predicting vibration responses of rectangular thin plates". In: *Journal of Sound and Vibration* 311, pp. 314–327.

Singhatanadgid, P. and V. Ungbhakorn (2002). "Scaling laws for vibration response of anti-symmetrically laminated plates". In: *Structural Engineering and Mechanics* 14.3, pp. 1–20.

— (2003). "Buckling similitude invariants of symmetrically laminated plates subjected to biaxial loading". In: *Composite Structures* 59.4, pp. 455–465.

— (2005). "Scaling laws for buckling of polar orthotropic annular plates subjected to compressive and torsional loading". In: *Thin-Walled Structures* 43, pp. 1115–1129.

Skudrzyk, E. J. (1966). "Vibrations and sound radiation of complex vibratory systems". In: *Underwater Acoustics, Volume 2*. Ed. by V. Albers. Scientific Affairs Committee of NATO and Penn State. Denmark, pp. 297–350.

Snyman, I. M. (2010). "Impulsive loading events and similarity scaling". In: *Engineering Structures* 32, pp. 886–896.

Soedel, W. (1971). "Similitude approximations for vibrating thin shells". In: *The Journal of Acoustical Society of America* 49.5 (Part 2), pp. 1535–1541.

Sonin, A. A. (2001). *The physical basis of dimensional analysis*. Cambridge, MA: Department of Mechanical Engineering, MIT.

Sorensen, B. R. et al. (1991). "High velocity penetration of steel targets". In: *International Journal of Impact Engineering* 11.1, pp. 107–119.

Spada, C. et al. (2017). "Nonlinear aeroelastic scaling of high aspect-ratio wings". In: *Aerospace Science and Technology* 63, pp. 363–371.

Springer, A. M. (1998). *Application of rapid prototyping methods to high speed wind tunnel testing*. Tech. rep. NASA TP–1998–208396. Huntsville (AL), USA: National Aeronautics and Space Administration.

Stathakis, D. (2009). "How many hidden layers and nodes?" In: *International Journal of Remote Sensing* 30.8, pp. 2133–2147.

Steeves, E. C. and J. J. Catherines (1968). *Lateral vibration characteristics of a 1/40-scale dynamic model of Apollo-Saturn V launch vehicle*. Tech. rep. NASA TN D–4872. Washington (DC), USA: National Aeronautics and Space Administration.

Steinchen, W., B. Kramer, and G. Kupfer (2008). "Photoelastic investigation using new STL-resins". In: Solid freeform fabrication symposium. Austin (TX), USA, pp. 204–12.

Sterrett, S. G. (2002). "Physical model and fundamental laws: using one piece of the world to tell about another". In: *Mind and Society* 3, pp. 51–66.

— (2009). "Similarity and dimensional analysis". In: *Handbook of the philosophy of science, volume 9: Philosophy of technology and the engineering sciences*. Ed. by A. Meijers. Amsterdam, Netherlands: Elsevier, pp. 799–824.

— (2014). "The morals of model-making". In: *Studies in history and philosophy of science* 46, pp. 31–45.

— (2015a). "Experimentation on analogue models". In: *Springer hanbook of model-based science*. Ed. by L Magnani and T. Bertolotti. Berlin, Germany: Springer International Publishing.

— (2015b). "Physically similar systems: a history of the concept". In: *Springer hanbook of model-based science*. Ed. by L Magnani and T. Bertolotti. Berlin, Germany: Springer International Publishing.

Sterrett, S.G. (2005). "Models of machines and models of phenomena". In: *International Studies in the Philosophy of Science* 20.1, pp. 69–80.

Stubbs, S. M. (1971). *Investigation of technique for conducting landing-impact tests at simulated planetary gravity*. Tech. rep. NASA TN D–6459. Washington (DC), USA: National Aeronautics and Space Adminsitration.

Sutherland, L. S. and C. Guedes Soares (2007). "Scaling of impact on low fibre-volume glass-polyester laminates". In: *Composites: Part A* 38, pp. 307–317.

Swanson, S. R., N. L. Smith, and Y. Qian (1991). "Analytical and experimental strain response in impact of composite cylinders". In: *Composite Structures* 18, pp. 95–108.

Szirtes, T. (2007). *Applied dimensional analysis and modeling 2nd ed.* Oxford, United Kingdom: Elsevier Butterworth-Heinemann.

Szucs, E. (1980). *Similitude and modelling*. Amsterdam, Netherlands: Elsevier.

Tabiei, A., J. Sun, and G. J. Simitses (1997). "Scaling laws of cylindrical shells under lateral pressure". In: *AIAA Journal: Techincal Notes* 35.10, pp. 1669–1671.

Tabri, K., J. Määttänen, and J. Ranta (2008). "Model-scale experiments of symmetric ship collisions". In: *J. Mar. Technol.* 13, pp. 71–84.

Tan, Q. M. (2011). *Dimensional analysis with case studies in mechanics*. Berlin: Springer-Verlag.

Tarfaoui, M. et al. (2007). "Scale and size effects on dynamic response and damage of glass/epoxy tubular structures". In: *Journal of Composite Materials* 41, pp. 71–84. URL: https://doi.org/10.1177/0021998306065287.

Tennyson, R. C. et al. (1981). "Study of crashworthiness of light aircraft structures". In: 22nd Structures, Structural Dynamics and Materials Conference. Atlanta (GA), USA, pp. 276–285.

Thompson, Jr., W. M. (1967). *An investigation of the response of a scaled model of a liquid-propellant multistage launch vehicle to longitudinal excitation*. Tech. rep. NASA TN D–3975. Washington (DC), USA: National Aeronautics and Space Administration.

Thornton, E. A. (1971). *Vibration analysis of a 1/15 scale dynamic model of a space shuttle configuration*. Tech. rep. NASA CR–111984. Norfolk (VA), USA: National Aeronautics and Space Administration.

Torkamani, S., A. A. Jafari, and H. M. Navazi (2008). "Scaled down models for free vibration analysis of orthogonally stiffened cylindrical shells using similitude theory". In: 26th International Congress of the Aeronautical Sciences. Anchorage (AK), USA: ICAS, pp. 3458–3469.

Torkamani, S. et al. (2009). "Structural similitude in free vibration of orthogonally stiffened cylindrical shells". In: *Thin-Walled Structures* 47, pp. 1316–1330.

Ungbhakorn, V. (2001). "A new approach for establishing structural similitude for buckling of symmetric cross-ply laminated plates subjected to combined load". In: *Thammasat. Int. J. Sc. Tech.* 6.3, pp. 55–60.

Ungbhakorn, V. and P. Singhatanadgid (2003a). "Scaling law and physical similitude for buckling and vibration of antisymmetric angle-ply laminated cylindrical shells". In: *International Journal of Structural Stability and Dynamics* 3.4, pp. 567–583.

— (2003b). "Similitude and physical modeling for buckling and vibration of symmetric cross-ply laminated circular cylindrical shells". In: *Journal of Composite Materials* 37.19, pp. 1697–1712.

— (2003c). "Similitude invariants and scaling laws for buckling experiments on antisymmetrically laminated plates subjected to biaxial loading". In: *Composite Structures* 59, pp. 455–465.

— (2009). "A scaling law for vibration response of laminated curved shallow shells by energy approach". In: *Mechanics of Advanced Materials and Structures* 16, pp. 333–344.

Ungbhakorn, V. and N. Wattanasakulpong (2007). "Structural similitude and scaling laws of anti-symmetric cross-ply laminated cylindrical shells for buckling and

vibration experiments". In: *International Journal of Structural Stability and Dynamics* 7.4, pp. 609–627.

Usami, T. and S. Kumar (1996). "Damage evaluation in steel box columns by pseudodynamic tests". In: *Journal of Structural Engineering* 122.6, pp. 635–642.

Valero, X. and F. Alias (2012). "Hierarhical clasification of environmental noise sources considering the acoustic signature of vehicle pass-bys". In: *Archives of Acoustics* 37.4, pp. 423–434.

van Vliet, M. R. A. and J. G. M. van Mier (2000). "Experimental investigation of size effect in concrete and sandstone under uniaxial tension". In: *Engineering Fracture Mechanics* 65, pp. 165–188.

Vassalos, D. (1999). "Physical modelling and similitude of marine structures". In: *Ocean Engineeering* 26, pp. 111–1232.

Vickers, J. M. F. (1965). "Thermal scale modeling". In: *Astronautics and Aeronautics*, pp. 34–39.

Vinson, J. R. (1999). *The behavior of sandwich structures of isotropic and composite materials*. Lancaster (PA), USA: Taylor and Francis Publishing Co.

Viot, P. et al. (2008). "Scale effects on the response of composite structures under impact loading". In: *Engineering Fracture Mechanics* 75, pp. 2725–2736.

Vlot, A. (2001). *Fiber Metal Laminates: an introduction*. Dordrecht: Kluwer Academia.

Wan, Z. and C. E. S. Cesnik (2013). "Geometrically nonlinear aeroelastic scaling for very flexible aircraft". In: 54th AIAA/ASME/ASCE/AHS/ASC Structures, Structural Dynamics, and Materials Conference. Boston (MA), USA: AIAA, pp. 1–15.

Wang, S., G. Yang, and N. Liu (2007). "Investigation of acoustic scale effects and boundary effects for the similitude model of underwater complex shell structure". In: *Journal of Marine Science and Application* 6.1, pp. 31–35.

Wang, Y. S. et al. (2017). "Acoustic behavior prediction for low-frequency sound quality based on finite element method and artificial neural network". In: *Applied Acoustics* 122, pp. 62–71.

Warburton, G. B. (1954). "The vibration of rectangular plates". In: *Proceedings of the Institution of Mechanical Engineers* 168.19, pp. 371–381.

Watkins, J. R. (1966). *Sets of similarity ratios for thermal modeling*. Tech. rep. NASA TN D–3452. Huntsville (AL), USA: National Aeronautics and Space Administration.

Wei, J. et al. (2019). "Vehicle engine classification using normalized tone-pitch indexing and neural computing on short remote vibration sensing data". In: *Expert Systems with Applications* 115, pp. 276–286.

Wen, H. M. and N. Jones (1993). "Experimental investigation of the scaling laws for metal plates struck by large masses". In: *Int. J. Impact Engng.* 13.3, pp. 485–505.

Wereley, N. M. and G. M. Kamath (1997). "Bringing relevance to freshman aerospace engineering: demonstration of model scale Comanche helicopter lag mode damper". In: *International Journal of Engineering Education* 13.5, pp. 369–375.

Westine, P. S. and S. A. Mullin (1987). "Scale modeling of hypervelocity impact". In: *International Journal of Impact Engineering* 5, pp. 693–701.

Wisnom, M. R. and J. W. Atkinson (1997). "Reduction in tensile and flexural strength of unidirectional glass fibre-epoxy with increasing specimen size". In: *Composite Structures* 38.1–4, pp. 405–411.

Wissmann, J. W. (1968). *Dynamic stability of space vehicles-Structural dynamics model testing*. Tech. rep. NASA CR–1195. Washington (DC), USA: National Aeronautics and Space Administration.

Wolowicz, C. H., J. S. Bowman, Jr., and W. P. Gilbert (1968). *Similitude requirements and scaling relationships as applied to model testing*. Tech. rep. NASA Technical Paper 1435. National Aeronautics and Space Administration.

Wu, J. J. (2003). "The complete-similitude scale models for predicting the vibration characteristics of the elastically restrained flat plates subjected to dynamic loads". In: *Journal of Sound and Vibration* 268, pp. 1041–1053.

— (2005). "Dynamic analysis of a rectangular plate under a moving load using scale beams and scaling laws". In: *Computers and Structures* 83, pp. 1646–1658.

— (2006). "Prediction of the dynamic characteristics of an elastically supported full-size flat plate from those of its complete-similitude scale model". In: *Computer and Structures* 84, pp. 102–114.

Wu, J. J., M. P. Cartmell, and A. R. Whittaker (2002). "Prediction of the vibration characteristics of a full-scale structure from those of a scale model". In: *Computer and Structures* 80, pp. 1461–1472.

Xiaojian, Z. et al. (2016). "A scaling procedure for panel vibro-acoustic response induced by turbulent boundary layer". In: *Journal of Sound and Vibration* 380, pp. 165–179.

Xu, B. et al. (2004). "Direct identification of structural parameters from dynamic responses with neural networks". In: *Engineering Applications of Artificial Intelligence* 17.8, pp. 931–943.

Xu, Z. et al. (2016). "An experimental and numerical study on scaling effects in the low velocity impact response of CFRP laminates". In: *Composite Structures* 154, pp. 69–78.

Yang, F. J. et al. (2013). "Scaling effects in the low velocity impact response of sandwich structures". In: *Composite Structures* 99, pp. 97–104.

Yazdi, A. A. (2013). "Prediction flutter boundaries of laminated cylindrical shells using scaling laws". In: *Journal of Aerospace Engineering* 27.1.

Yazdi, A. A. and J. Rezaeepazhand (2011a). "Accuracy of scale models for flutter prediction of cross-ply laminated plates". In: *Journal of Reinforced Plastics and Composites* 30.1, pp. 45–52.

— (2011b). "Structural similitude for flutter of delaminated composite beam-plates". In: *Composites Structures* 93, pp. 1918–1922.

— (2012). "Applicability of small-scale models in prediction flutter pressure of delaminated composite beam-plates". In: *International Journal of Damage Mechanics* 22.4, pp. 590–601.

Yigit, A. S. and A. P. Christoforou (2007). "Limits of asymptotic solutions in low-velocity impact of composite plates". In: *Composite Structures* 81, pp. 568–574.

Young, Y. L. (2010). "Dynamic hydroelastic scaling of self-adaptive composite marine rotors". In: *Composite Structures* 92, pp. 97–106.

Yu, H. et al. (2010). "Shaking table test numerical analysis of a 1:12 scale model of a special concentrically braced steel frame with pinned connections". In: *Earthquake Engineering and Engineering Vibration* 9.1, pp. 51–63.

Yu, W. and Z. L. Li (2016). "Structural similitude for prestressed vibration and buckling of eccentrically stiffened circular cylindrical panels and shells by energy approach". In: *International Journal of Structural Stability and Dynamics* 16.10, pp. 1550074–1–1550074–23.

Yulong, L., Z. Yongkang, and X. Pu (2008). "Study of similarity law for bird impact on structure". In: *Chinese Journal of Aeronautics* 21, pp. 512–517.

Zai, B. A. et al. (2015). "Prediction of vibration characteristics in beam structure using sub-scale modeling with experimental validation". In: *Chinese Journal of Mechanical Engineering* 28.5, pp. 928–933.

Zalesak, J. (1975). *Modal coupling procedures adapted to NASTRAN analysis of the 1/8-scale shuttle structural dynamics model. Volume I - Technical Report*. Tech. rep. NASA CR–132666. Washington (DC), USA: National Aeronautics and Space Administration.

Zang, C. and M. Imregun (2001). "Structural damage detection using artificial neural networks and measured FRF data reduced via principal component analysis". In: *Journal of Sound and Vibration* 242.5, pp. 813–827.

Zenkert, D. (1995). *An introduction to sandwich construction*. West Midlands, UK: EMAS Publications.

Zhao, Y. P. (1998). "Suggestion of a new dimensionless number for dynamic plastic response of beams and plates". In: *Archive of Applied Mechanics* 68.7–8, pp. 524–538.

— (1999). "Similarity consideration of structural bifurcation buckling". In: *Forschung in Ingenieurwesen* 65, pp. 107–112.

Zhihui, Z. et al. (2020). "A hybrid DIC-EFG method for strain field characterization and stress intensity factor evaluation of a fatigue crack". In: *Measurement* 154.

Zhu, W. et al. (2011). "Design and fabrication of stereolithography-based aeroelastic wing models". In: *Rapid Prototyping Journal* 17.14, pp. 298–307.

Zhu, Y. et al. (2014). "Determination method of the structure size intervals of dynamically similar models for predicting vibration characteristics of the coated thin plates". In: *Proceedings of the Institution of Mechanical Engineers, Part C: Journal of Mechanical Engineering Science* 229.1, pp. 59–68. DOI: 10.1177/0954406214532243.

Zhu, Y. et al. (2017). "Similitude design for the vibration problems of plates and shells: A review". In: *Front. Mech. Eng.* 12.2, pp. 253–264.

Ziemian, C., R. Ziemian, and E. Barker (2010). "Shake-table simulation study of small scale layered models". In: *Rapid Prototyping Journal* 16, pp. 4–11.

Zohuri, B. (2012). *Dimensional analysis and self-similarity methods for engineers and scientists*. Switzerland: Springer International Publishing.

Zohuri, B. (2017). *Dimensional analysis beyond the Pi Theorem*. Switzerland: Springer International Publishing.